Biocatalytic Strategies for Sustainable Epoxy Polymer Degradation and Synthesis

Vom Promotionsausschuss der
Technischen Universität Hamburg
zur Erlangung des akademischen Grades

Doktor-Ingenieur (Dr.-Ing.)

genehmigte Dissertation (Monografie)

von
Leon Klose

aus
Salzgitter

2026

Prüfungskomitee

Erstgutachter: Prof. Dr. Andreas Liese
Zweitgutachterin: Prof. Dr.-Ing. Kerstin Kuchta
Vorsitzende: Prof. Dr. Anna-Lena Heins

Prüfungsdatum

22. Mai 2026

TORE Identifier

DOI: https://doi.org/10.15480/882.17190
Handle: https://hdl.handle.net/11420/63200

ORCID iD

https://orcid.org/0000-0001-5139-591X

Creative Commons Lizenzvereinbarung

We live in a twilight world.

Acknowledgments

First and foremost, I want to thank Prof. Dr. Andreas Liese for giving me the opportunity to pursue my PhD in his institute. From the very beginning, I appreciated the welcoming atmosphere he created in the group. What I valued most, however, was the freedom he gave me to follow my own ideas and shape my research independently. His trust and support throughout this journey meant a great deal to me and influenced this work in more ways than one.

Furthermore, I would like to thank Prof. Dr.-Ing. Kerstin Kuchta for taking the time to review this thesis as second examiner, and Prof. Dr. Anna-Lena Heins for chairing the examination committee.

A big thank you goes to all my cooperation partners who contributed to this project: Prof. Dr. Garabed Antranikian, Dr. Barbara Klippel, and Dr.-Ing. Neele Meyer-Heydecke (CBBS); Prof. Dr.-Ing. Bodo Fiedler and M.Sc. Melissa Walter (Institute of Polymer and Composites, TUHH); Prof. Dr. Wolfgang Streit, Dr. Pablo Peréz-García, and Dr. Sasipa Wongwattanarat (Universität Hamburg); Prof. Dr. Nigel Scrutton and Dr. Mohamed Amer (Future BRH); and Dr. Camille Carré and Stéphane Bechtel (Airbus). I also want to specifically thank Dr. Filipe Hobi Bordon Sosa from the University of Aveiro for the COSMO-RS simulations.

To my colleagues Marlene, Luca, Grit, Marie, Giovanni, and Florian - thank you for welcoming me to the ITB and making my time there so enjoyable. A special thanks to Marie, who took the time to proofread this manuscript and gave me really valuable feedback.

To Anna and Maren - thank you for keeping the lab running and for your great practical help.

I also want to thank everyone who worked with me as a trainee or student: Margarita, Quentin, Bruno, Hala, Lennart, Michele, Martin, and Adrian, as well as Wilhelm, Denizhan, Robert, and Lisa. Your energy and dedication in the lab contributed significantly to making this thesis a reality.

To my parents, grandparents, my brother, and the rest of the family - thank you for your steady support, for motivating and encouraging me.

And finally, to Laura - thank you for everything. For being there on the tough days, for celebrating the small wins with me, and for your endless patience.

Abstract

Epoxy resins are widely used for their excellent mechanical properties. In contrast, they pose significant sustainability challenges due to their petrochemical origin and highly crosslinked, non-degradable structure. Within the framework of this dissertation two primary challenges in the context of sustainable epoxy thermosets were addressed. First, the investigation of the enzymatic degradation of highly crosslinked epoxy resins cured with aromatic amines. By employing a laccase-mediator system inspired by lignin degradation, the normally inert, densely crosslinked polymer network was rendered susceptible to oxidation. This approach paves the way for a mild, environmentally benign breakdown of an otherwise robust thermoset. Second, a bio-based synthesis route was developed for epoxidized thermoset monomers using the renewable resource linseed oil. Through a chemoenzymatic epoxidation of the unsaturated plant oils, sustainable epoxy precursors were produced as alternatives to conventional petroleum-derived monomers. The purification and curing performance of these monomers were evaluated, demonstrating that fully bio-based epoxy matrices can be achieved. Both strategies share the overarching goal of improving the sustainability of epoxy materials. By addressing end-of-life degradation and the utilization of renewable feedstocks, this work contributes to advancing thermoset polymers with reduced environmental impact.

Contents

List of Figures

List of Tables

Abbreviations

ABTS	2,2'-azino-bis(3-ethylbenzothiazoline-6)-sulfonic acid
AN	acid number
ANOVA	analysis of variance
ATR	attenuated total reflection
ATR-FTIR	attenuated total reflection fourier-transform infrared spectroscopy
BA	butyric acid
BET:GLY	betaine:glycerol
BET:SOR	betaine:sorbitol
BPA	bisphenol A
CA	caffeic acid
CALB	lipase from *Candida antarctica*
CEE	chemoenzymatic epoxidation
CFRP	carbon-fiber reinforced polymer
ChCl:BET	choline chloride:betaine
ChCl:DMF	choline chloride:dimethylformamide
ChCl:EG	choline chloride:ethylene glycol
ChCl:FA	choline chloride:formic acid
ChCl:LA	choline chloride:lactic acid
ChDHC	choline dihydrogen citrate
ChDHC:ERY	choline dihydrogen citrate:erythritol
ChDHC:XYL	choline dihydrogen citrate:xylitol
CI	carbonyl index
COSMO-RS	conductor-like screening model for real solvents
CV	cyclic voltammetry
DBEGA	bisphenol A diglycidyl ether
DES	deep eutectic solvent
DMF	dimethylformamide
DMSO	dimethyl sulfoxide

DO	dissolved oxygen
DoE	design of experiments
DSC	differential scanning calorimetry
EEW	epoxy equivalent weight
EI	electron ionization
EIS	electrochemical impedance spectroscopy
ELO	epoxidized linseed oil
EN	epoxy number
EP	epoxy polymer
ET	electron transfer
EtOAc	ethyl acetate
EVO	epoxidized vegetable oil
FA	ferulic acid
FFA	free fatty acid
FTIR	fourier-transform infrared spectroscopy
GC	gas chromatography
GC-FID	gas chromatography coupled flame ionization detector
GC-MS	gas chromatography coupled mass spectrometry
HAT	hydrogen atom transfer
HBA	hydrogen bond acceptor
HBD	hydrogen bond donor
HPLC	high-performance liquid chromatography
ID	inner diameter
IHM	indirect hard modeling
IV	iodine value
LacF	laccase from *Funalia trogii*
LacMT	Novozym 51003 from *Myceliophthora thermophila*

LacTV	laccase from *Trametes versicolor*
LacU	laccase of undisclosed origin
LMS	laccasemediator system
LO	linseed oil
M-MIPA	4,4'-methylenebis(2-isopropyl-6-methylaniline)
MB	Michlers base
MDEA	4,4'-methylenebis(2,6-diethylaniline)
MDSC	modulated differential scanning calorimetry
MIR	mid-infrared spectroscopy
NHE	normal hydrogen electrode
NIR	near-infrared spectroscopy
NMR	nuclear magnetic resonance spectroscopy
NNBT	*N*,*N*-bis(2-hydroxypropyl)-*p*-toluidine
OD	outer diameter
PA	polyamide
PAM	polyacrylamide
PAN	poly-acrylonitrile
PE	polyethylene
PET	polyethylene terephthalate
PLA	polylactic acid
PLS	partial least squares regression
PP	polypropylene
PRO:MA	proline:malic acid
PU	polyurethanes
PVC	polyvinylchloride
RBR	rotating bed reactor
RMSEC	root mean square error of calibration
RMSECV	root mean square error of cross-validation
RTM6	resin transfer mold 6 resin

SA	stearic acid
TEAB	tetraethylammonium bromide
TEMPO	2,2,6,6-tetramethylpiperidinyloxyl
TGA	thermogravimetric analysis
TGMDA	*N*,*N*,*N*',*N*'-tetraglycidyl-4,4'-methylenebisbenzenamine
TIC	total ion chromatogram
TOL	toluene
UPO	unspecific peroxygenase
UV/VIS	ultraviolet-visible light
VA	violuric acid
ZCl:FA	zinc chloride:formic acid

Symbols

Symbol	Description	Unit
A	Pure component infrared reference spectrum	
AN	Acid number	$\mathrm{mg \cdot g^{-1}}$
c	General concentration / Concentration-dependent infrared spectrum coefficient	$\mathrm{mol \cdot L^{-1}}$ /
d	Distance (e.g., electrode spacing)	cm
δ	bending (deformation) vibration	-
ΔH	Enthalpy of curing	$\mathrm{J \cdot g^{-1}}$
E	Absorbance (extinction)	
$E_{1/2}$	Half-wave potential	V
$E_{\mathrm{Ag/AgCl\ vs.\ NHE}}$	Potential difference between Ag/AgCl and normal hydrogen electrode	V
$E_{\mathrm{p,\ anode}}$	Anodic peak potential	V
$E_{\mathrm{P,\ cathode}}$	Cathodic peak potential	V
$E_{\mathrm{vs.\ NHE}}$	Potential against normal hydrogen electrode	V
EEW	Epoxy equivalent weight	$\mathrm{g \cdot mol^{-1}}$
EN	Epoxy number	$\mathrm{g \cdot 100\ g^{-1}}$
ε	Residual error	
ε_λ	Molar extinction coefficient	$\mathrm{L \cdot mol^{-1} \cdot cm^{-1}}$
$[E]$	Enzyme concentration	$\mathrm{mol \cdot L^{-1}}$
$[E]_0$	Initial enzyme concentration	$\mathrm{mol \cdot L^{-1}}$
$[ES]$	Enzymesubstrate complex	$\mathrm{mol \cdot L^{-1}}$
IV	Iodine value	$\mathrm{g \cdot 100\ g^{-1}}$
K_M	MichaelisMenten constant	$\mathrm{mol \cdot L^{-1}}$
k	Rate constant	$\mathrm{min^{-1}}$
λ	Wavelength	nm
$\ln \gamma_\infty$	Natural logarithm of the activity coefficient at infinite dilution	
m	Mass	g
MW	Molecular weight	$\mathrm{g \cdot mol^{-1}}$
n	Number of electrons / reaction order	

Symbols – Continued from previous page.

Symbol	**Description**	**Unit**
ν	stretching vibration	
pH	Acidity	
$P_{\text{org./aq.}}$	Distribution coefficient (organic/aqueous)	
s	Superimposed infrared spectrum	
S	Sampling site	-
$[S]$	Substrate concentration	$\text{mol}\cdot\text{L}^{-1}$
σ	Surface polarization charge density (COSMO-RS) / Electric conductivity	$\text{e}\cdot\text{Å}^{-2}$ / $\text{mS}\cdot\text{cm}^{-1}$
t	Time	s
T	Temperature	řC
v	Reaction rate	$\text{mol}\cdot\text{L}^{-1}\cdot\text{s}^{-1}$
v_{max}	Maximum reaction rate	$\text{mol}\cdot\text{L}^{-1}\cdot\text{s}^{-1}$
V	Volume	mL
vvm	Volume of gas per volume of liquid per minute	min^{-1}
w	Mass fraction	

1 Introduction

Because of their exceptional properties such as low cost, high mechanical stability, and chemical resistance, synthetic polymers, which play an extensive role in lightweight construction efforts, became indispensable materials. However, their poor recyclability and biodegradability stands in strong contrast to their widespread use and performance [1]. In 2023 alone, 413.8 Mt of polymers were synthesized while the global plastic production is projected to reach 884 Mt in 2050 [2, 3]. In contrast, only 9 % of the 8300 Mt produced between 1950 and 2018 were recycled and only 10 % of those underwent more than one lifecycle. Roughly 71 % of all plastic waste is either landfilled or released into the environment, as shown in Figure 1.1 [4, 5].

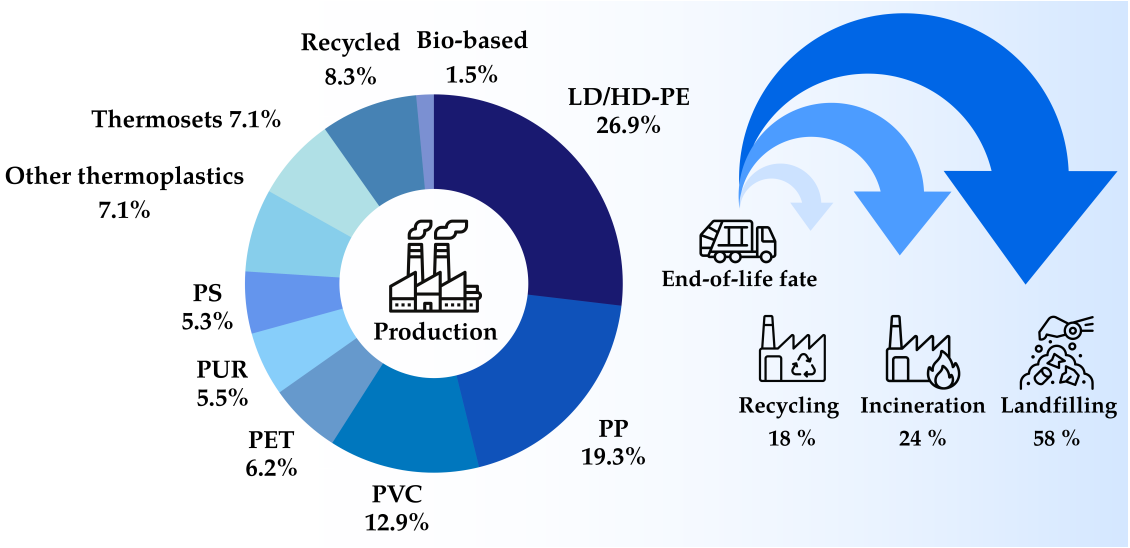

Figure 1.1 Production volume (status 2021) and end-of-life fate of plastics (status 2017) (adapted with changes from Klose et al. (2023) [6]); LD/HD-PELow-density/High-density polyethylene, PPPolypropylene, PVCPolyvinyl chloride, PETPolyethylene terephthalate, PURPolyurethane, PSPolystyrene.

The German governments lightweight construction strategy claims that mitigating climate change requires technologies which allow a transition towards resource-conserving value creation as well as sustainable and resilient raw-material supply. In this context, the strategy aims to reduce material and energy consumption via innovative lightweight construction materials in the automotive, aerospace, mechanical and plant engineering, energy, and construction industries. Especially recycling

and reuse are part of the material-efficient and sustainable lightweight construction strategy [7].

> *The goal must be closed raw material cycles that feed the valuable and sometimes rare materials back into the production process. There is still a need for research and development in this field. [...]*
> *Approaches from the industrial bioeconomy, for example, come into consideration. In the industrial bioeconomy, products and processes based on fossil raw materials are being replaced by new biobased products, production processes and business models.* - [7]

High-performance composite materials, particularly carbon-fiber reinforced polymers (CFRPs), play a pivotal role in realizing lightweight construction goals. Among them, epoxy-based materials offer advantages such as low weight, high strength, durability, corrosion and fatigue resistance, which make them key matrix materials in aerospace, wind energy, and automotive applications [8]. Although epoxy polymers accounted for only 7.1 % of global synthetic polymer production in 2021, their industrial relevance is increasing [9]. On the other hand, recycling CFRPs is energetically and economically desirable, but conventional mechanical, chemical, and thermal recycling methods often destroy fiber integrity or involve toxic reagents [10, 11]. These limitations have drawn attention to biotechnological strategies. While enzymatic depolymerization of polyethylene terephthalate (PET) has seen substantial advances, epoxy thermosets, due to their dense, crosslinked aromatic network and hydrophobicity, remain among the most recalcitrant and unexplored materials [6, 12]. Nevertheless, recent progress in biocatalytic degradation of hard-to-degrade materials such as polyethylene (PE) or polypropylene (PP), using oxidative enzymes such as fungal laccases, has shown that partial depolymerization under mild conditions might be achievable [13, 14, 15].

In parallel, complementary approaches aim to reduce future waste by improving the sustainability of epoxy materials at the production stage. Epoxidized vegetable oils (EVOs), particularly epoxidized linseed oil (ELO), have emerged as promising renewable alternatives to bisphenol-based resins [16]. Owing to its high degree of

unsaturation, linseed oil (LO) enables a high oxirane content and is therefore suitable for crosslinkable thermoset production [17]. However, conventional epoxidation methods typically require hazardous reagents and yield acidic waste streams [18]. In contrast, chemoenzymatic epoxidation (CEE), based on lipase-catalysed *in situ* peracid formation, offers a scalable and milder alternative that avoids the use of strong acids as oxidants [19]. Recent studies show that ELO-based formulations, when cured with biobased crosslinkers such as citric acid, yield polymer networks with thermal and curing properties comparable to conventional epoxies, while introducing hydrolytically cleavable ester bonds that may enhance biodegradability [20].

2 Theoretical Background

2.1 Epoxy Polymers and Their Composites

Epoxy polymers (EPs) have gained major importance in many industrial applications as their outstanding combination of physical and chemical properties can generally not be found in any other plastic materials. The term epoxy resin by strict definition refers to monomeric or oligomeric molecules which contain more than one epoxy group and in practice is falsely used to describe cured EP systems which might contain no to very few epoxy groups [21].

EP exhibit many unique properties which make them a standard option for various industrial applications where they are used as adhesives, sealants and coatings [22]. The good adhesion properties of EPs stem from the presence of polar groups in the polymer structure [23]. Crosslinked EPs come with high mechanical strength and toughness as well as chemical, moisture and corrosion resistance [24]. Thus, they are used in the construction industry to protect steel parts from corrosion, to support concrete structures and as matrix materials for composites, giving them major importance for the aerospace and automotive industry [25, 26, 27]. Also, the polymerization reaction does not release any volatile products and only shows low contraction during this process, making it advantageous compared to unsaturated polyester resins. Additionally, a variety of different material properties can be reached using different epoxy monomers and co-monomers. Therefore, EP can form materials with glass transition temperatures T_g ranging from $-15\,$řC (rubber-like) to $220\,$řC (glass-like) [28]. The glass transition temperature refers to the temperature at which an amorphous material changes from a solid or glass-like state into a viscous or rubber-like state [29]. EP have a high dielectric strength, a low dielectric constant and high thermal resistance, making them an important material for the electronic industry, where they are used as encapsulants and potting materials, especially for high-frequency and high-voltage applications [30, 31].

2.1.1 Thermoset Epoxy Polymer Synthesis

Thermoset polymers consist out of one large macromolecule of covalently bonded repeating units. Flow will not be possible unless the covalent bonds are destroyed by

e.g., high temperature [32]. The polymer network is formed by the polymerization of different monomer molecules, where one monomer reactant possesses at least two reactive groups. To generate certain material properties, commercial thermosetting resins can contain many different monomer molecules with different functionalities [33, 34]. During the polymerization and crosslinking reaction of the different monomer molecules, an irreversible polymer network is produced; thus, the synthesis and shaping of thermosetting polymers is performed in the same process [35]. Another characteristic feature of thermosetting polymers is the location of their glass transition temperature in comparison to the temperature at which the polymer is applied. As, in general, the glass transition temperature of thermosetting polymers is higher than their application temperature, thermosets come with glass-like material properties [36].

Thermosets have a high degree of crosslinking in the polymer network, conferring a high dimensional stability that leads to their excellent mechanical properties [37]. However, the reduced dimensional flexibility of the polymer network causes thermosets to be brittle because plastic deformation of the polymer network is very limited. Due to the high dimensional stiffness, thermosetting polymers are utilized as a matrix material for fiber-reinforced composites [28]. Linear or crosslinked EPs are produced from the polymerization reaction of epoxy monomers and are also referred to as epoxy resins with co-monomers (co-reactive curing agents) and/or initiators (catalytic curing agents). The reaction of epichlorohydrin with bisphenol A (BPA) in the presence of sodium hydroxide produces the most used monomers for epoxy resins, where bisphenol A diglycidyl ether (DBEGA) represents the major product formed [23]. A general reaction scheme can be seen in Figure 2.1 (**A**). The produced linear epoxy monomer DBEGA has two epoxy groups, which are necessary for the crosslinking step in which the epoxy monomer reacts with a co-monomer. Co-monomers can be amines, phenols, mercaptans, isocyanides or acids, but amines are the most used curing agents [38, 39]. In Figure 2.1 (**B**), a primary amine reacts with an epoxy group to from a secondary amine.

In a second step an additional epoxy group reacts with the secondary amine, forming a tertiary amine. These reactions lead to advanced crosslinking of the linear EPs to form a three-dimensional polymer matrix, where the primary amine

was substituted as an amine curing argent. The curing process involving a co-reacting curing agent produces a higher degree of crosslinking compared to catalytic curing agents. If the epoxy monomer possesses more than two epoxy groups, a high degree of crosslinking is achieved without the use of curing agents [40].

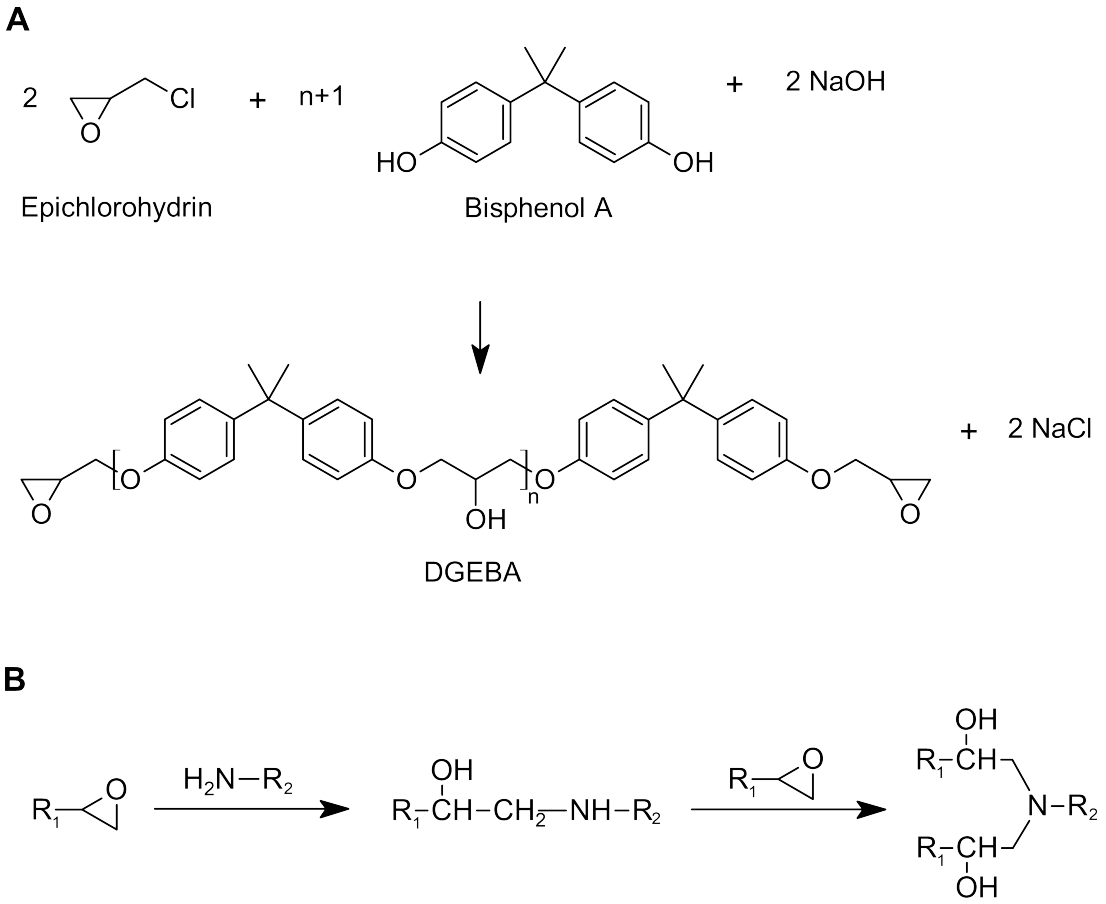

Figure 2.1 Bisphenol A-based synthesis of bisphenol A diglycidyl ether (DGEBA) (**A**) and crosslinking of epoxy monomers with an arbitrary amine curing agent (**B**) (adapted from Klose et al. (2023) [6]).

In contrast to co-reactive curing agents, catalytic curing agents initiate and accelerate the homo-polymerization reaction without becoming part of the polymer matrix after the reaction completes. The homo-polymerization reaction can be initiated by Lewis acids and bases; thus tertiary amines, imidazoles and ammonium salts can start the anionic polymerization, whereas the cationic polymerization can be initiated by boron trifluoride complexes and complex aromatic salts of Lewis acids [23].

The curing reaction of thermosetting EPs is combined with the molding process of the polymer to its desired shape, as the achieved polymerization and crosslinking reaction is irreversible [36, 41]. This process is usually initiated by applying a heating gradient, which is required to start the chemical reaction [42].

2.1.2 Epoxy-based Fiber-Reinforced Composite Materials

Composite materials are created by mixing two or more different components that have complementary synergistic properties. Composites are classified based on their reinforcement and matrix materials. Thus, they can be categorized as fiber-reinforced, particulate or structural composites. The matrix materials are divided into metal, organic and ceramic matrices. Their main purpose is to provide support and protection to the fibers. Epoxy-based thermosetting polymers are the most used matrix material in composites because of their adhesive, physical, chemical and mechanical properties. Strong adhesion between the matrix material and the fiber is required for a good load transfer between the composite components [43]. While the fibers have a low density, they provide reinforcement with their high strength and stiffness. The most used fiber materials are synthetic ones such as carbon, glass, or aramid fibers. However, due to the environmental issues linked to their production, research to develop fibers from natural sources has become more dominant [44]. Natural fibers can be categorized by their origin, which can be from mineral, animal or plant sources [45].

In high-performance applications such as aerospace, automotive, wind turbine blades, compressed gas storage and sports tools, where high strength, stiffness, low weight and fatigue resistance are critical, epoxy-based carbon fiber-reinforced composites are widely used. Out of all commercially available synthetic fiber materials, carbon fibers represent the matrix material with the highest mechanical properties, except for the impact strength, where aramid or glass fibers show better performance [46]. Carbon fibers are produced in a multi-stage process, where the fibers are produced from a precursor material such as poly-acrylonitrile (PAN), pitch, or rayon [47, 48]. Modern carbon fibers are produced from PAN, a long-stranded polymer with a carbon backbone that possesses higher mechanical strength compared to fibers produced from other precursor materials. The precursor material is

converted into carbon fibers via the stabilization, carbonization and graphitization process [49, 50]. During the stabilization process, the precursor is heat-treated at 180 řC to 300 řC in the presence of oxygen. In this step, oxidation, dehydrogenation and cyclization reactions take place. Oxygen is used as an oxidizing agent and is introduced into the PAN structure via ether links, carbonyl groups or via the donation of a lone pair electron from the nitrogen atom to the oxygen atom. In the dehydrogenation reaction, water is formed and removed, leading to the formation of C=C bonds. The most important step of the stabilization process is the cyclization reaction, where nitrile groups react with the neighboring carbon. In this step, the triple-bond structure is converted into a double-bond structure, leading to the formation of a six-membered cyclic pyridine ring structure [10]. The stabilization is followed by the carbonization, which is usually a two-step heating process under an inert atmosphere. The carbonization is schematically shown in Figure 2.2 where the stabilized precursor is slowly heated to 400 řC to 600 řC in the pyrolysis step.

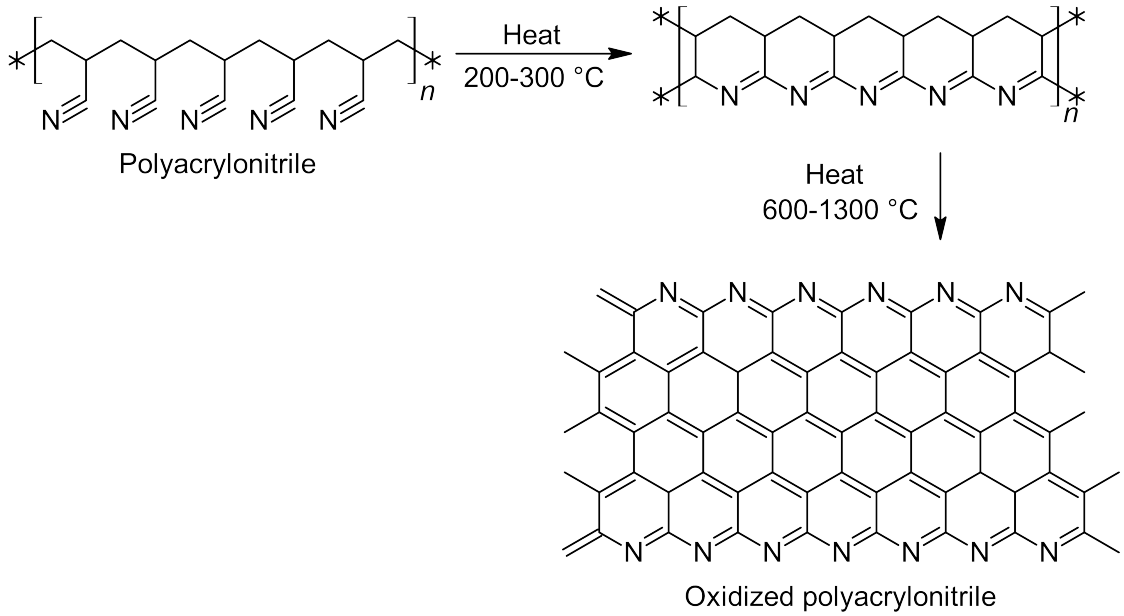

Figure 2.2 Carbonization process of stabilized poly-acrylonitrile (adapted from Rahaman et al. (2007) [49]).

The hydrogen is eliminated and carbon-carbon bonds are formed. In the second heating step, nitrogen is eliminated and a hexagon carbon lattice is produced. The final temperature level of the heat treatment can vary depending on the desired mechanical strength of the produced fibers. Temperatures up to 1300 řC are used

to obtain intermediate modulus type fibers with 96 % carbon content, whereas temperatures under 1000 řC are applied to produce low modulus fibers [26, 6].

To reach carbon contents up to 99 % and a graphite-like crystallinity, the graphitization is carried out. In the graphitization step, temperatures of up to 3000 řC are used under inert gas atmosphere to obtain high modulus type fibers, also referred to as type I carbon fibers [49]. Different surface treatments can be applied to advance the bonding between the fiber and the matrix material. Silane, plasma, acid treatment, and nano-fiber coating are common methods to reach a higher density of active sides on the fiber surface [51].

The carbon fibers are further processed into textiles to allow an even distribution of fiber material in the epoxy resin [52]. Thus, epoxy-based composite materials are categorized into braided, stitched, knitted and woven composites [53]. To produce high-quality and high-strength parts, the composite material is manufactured by pre-impregnating the fiber material with the epoxy resin. In the following step, the mixture is shaped and cured under the application of heat and pressure [54].

In liquid composite molding, the epoxy resin is injected into a closed mold containing the preformed fiber material. Different methods of liquid composite molding exist, with vacuum bagging being a cost-effective method where the resin-impregnated fiber is bagged and placed in a mold. Afterwards, a vacuum is applied to remove the remaining air inside of the fibers and resin, resulting in a low void content [55].

As summarized in Table 2.1, the mechanical properties of carbon-fiber reinforced polymers (CFRPs) significantly exceed those of neat EPs and are in many cases comparable or superior to those of stainless steel. This is primarily attributed to efficient load transfer within the composite structure, enabled by strong interfacial adhesion between the reinforcing fibers and the thermosetting EP matrix [56]. Alongside the up to three-fold lower density of CFRPs compared to steel, the tensile strength and Youngs modulus are markedly enhanced, while the elongation at break remains low, typically in the range of 0.5 % compared to values of up to 12 % observed for ductile metals such as steel [57, 58].

Despite their superior specific strength and stiffness, CFRPs exhibit limitations related to their anisotropic nature, particularly in terms of reduced compressive and inter-laminar shear strength [59]. These mechanical characteristics, coupled with the chemical heterogeneity between matrix and fiber, complicate end-of-life

treatment [60]. The increasing deployment of CFRPs in structural applications thus presents growing challenges for material recovery, as both fiber and matrix must be selectively separated and processed. However, given the high embedded energy and typically non-renewable origin of conventional carbon fibers, the recovery of both the reinforcing phase and the polymeric matrix represents a considerable opportunity for resource conservation [61].

Table 2.1 Mechanical properties of epoxy, carbon-fiber reinforced polymers (epoxy-based), and stainless steel (adapted from Klose et al. (2023) [6]).

Property	**Unit**	**Epoxy**	**CFRP**	**Stainless Steel**
Density	$g \cdot cm^{-3}$	1.11.4	1.52.1	7.85
Tensile Strength	MPa	60	6003920	483690
Youngs Modulus	GPa	2.5	37784	200
Elongation	%	-	0.51.8	612
Coefficient of Linear Expansion	$10^{-6} \cdot$řC^{-1}	-	-90	11.7
Reference		[57]	[58]	[58]

2.2 Recycling of Fiber-Reinforced Composite Materials

Because of their unique properties, fiber-reinforced composite materials are heavily utilized in high-performance applications such as aerospace, automotive, wind turbine blades, compressed gas storage and sports tools. The Boeing 787 Dreamliner and the Airbus A350 XWB have a composite weight share of more than 50 %, where mainly the wings, fuselage and control surfaces are made from composites (Figure 2.3) [62]. Among other applications, this contributed to a global carbon fiber demand of 126.5 Mt in 2024 [9]. In this context, the share of CFRPs is closely linked to emerging sustainable energy sources, where lightweight construction materials are used to increase efficiency [6].

Nowadays, glass fiber-reinforced polymers are used in the wind energy sector as the main structural material of wind turbine blades. Because wind turbine sizes are expected to increase, especially in offshore wind parks, the manufacturers seek a transition towards carbon-fiber composites, supporting a clean energy infrastructure.

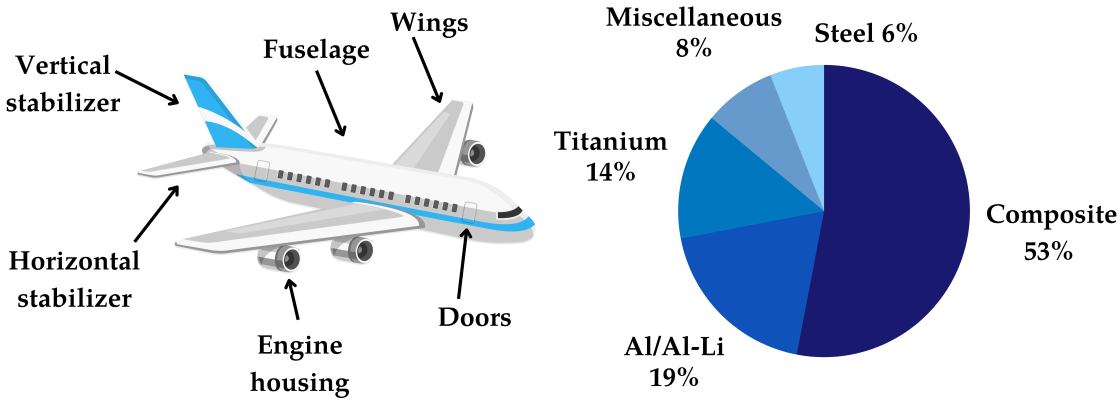

Figure 2.3 Overview of the parts manufactured from composites and percentage composition of the construction materials of the Airbus A350XWB (adapted from Klose et al. (2023) [6]).

Additionally, in the aerospace industry, up to 30% of the aircraft weight can be saved by manufacturing from CFRPs in contrast to aluminum. With an estimated reduction of whole fuel consumption over the lifespan of an aircraft of 0.5-1% per kilogram saved, a significant impact on the carbon footprint of air travel can be achieved [63].

However, the environmental benefits gained by the utilization of composite materials are diminished by the lack of sustainable recycling methods for fiber-reinforced composite materials. As most composite matrix materials are highly crosslinked thermosetting EPs, which underwent an irreversible curing process, recycling of these polymers cannot be achieved via conventional recycling techniques [64]. These would either result in the production of the same initial starting material (primary recycling), a material of lower performance (secondary recycling) or chemical and fuel production (tertiary recycling) (Figure 2.4) [65].

Recycling approaches for CFRPs include mechanical, chemical and thermal treatment. During mechanical treatment, the composite waste is shredded into small particles, which are then used as structural fillers for construction materials like cement. Most of the monetary value of the composite waste is lost during this process because the carbon fiber weaves are destroyed [66]. Chemical recycling approaches involve using strong catalysts like sodium hydroxide, peracetic acid, nitric acid, ionic liquids and metal catalysts to break down the polymer macromolecules into smaller molecules [67, 68, 69]. This process requires high energy input and

produces toxic waste, which makes it limited in terms of sustainability and practicality. Thermal recycling, which is also known as quaternary recycling, comprises the thermal decomposition of the composite waste to produce energy [70]. The thermal decomposition can be carried out in the presence (combustion) or absence of oxygen (pyrolysis). During pyrolysis, the waste is broken down into gas or char, which produces fewer pollutants compared to conventional waste-to-energy methods [71, 72]. Because none of the existing recycling approaches for composite materials are sufficient in terms of sustainability and economic efficiency, research in the field of biocatalytic recycling approaches presents an emerging alternative [73, 74].

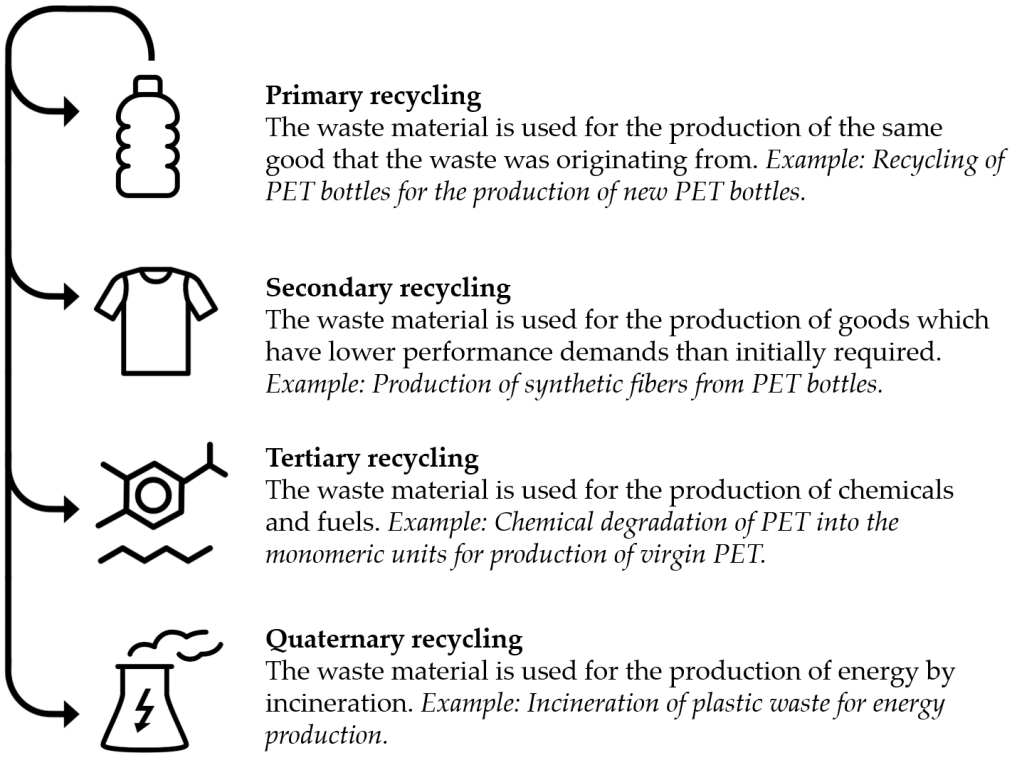

Figure 2.4 Comparison of the four recycling categories (adapted from Klose et al. (2023) [6]).

2.3 Biocatalytic Degradation of Epoxy Resins

Microorganisms have always played a key role in preventing the accumulation of contaminants in the environment (bioaccumulation) by adapting their metabolism toward the degradation of these new compounds [75]. They are incorporated into the metabolic pathway through genome modification, extending the biochemical capabilities of the microorganisms. Different anthropogenic compounds have been added to the metabolic capacity of microorganisms by the natural selection of mutants possessing the required substrate-specific degradative enzymes [76]. Many algae, bacteria and fungi with the ability to biodegrade certain plastic polymers such as polyethylene terephthalate (PET), polyethylene (PE), polyurethanes (PU) and polypropylene (PP) were identified and characterized in recent times [4]. In the case of PET and PU, the degradative enzymes act upon the heteroatomic polymer backbone containing ester bonds, which are vulnerable to enzymatic hydrolysis [77]. But also other synthetic polymers such as polyamide (PA) and polylactic acid (PLA), which both comprise of heteroatomic backbones containing carbon, oxygen and nitrogen, can be hydrolyzed (see Table 2.2).

Table 2.2: Overview of the hetero- and homoatomic backbone classification of selected synthetic polymers [6].

Name	**Structure**
Heteroatomic Backbone	
Polyethylene terephthalate (PET)	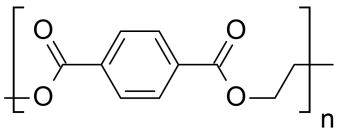
Polyamide (PA)	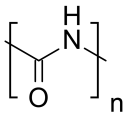
Polylactic acid (PLA)	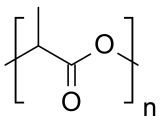

Table 2.2 – Continued from previous page

Epoxy	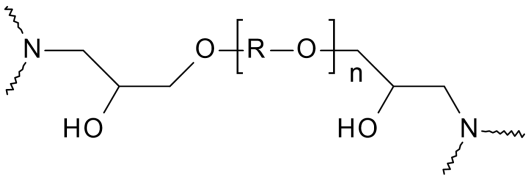
Polyurethanes (PU)	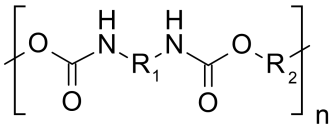
	Homoatomic Backbone
Polyethylene (PE)	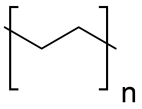
Polypropylene (PP)	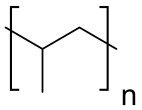
Polyacrylamide (PAM)	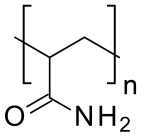
Polyvinyl chloride (PVC)	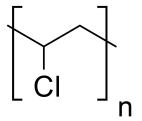
Polystyrene (PS)	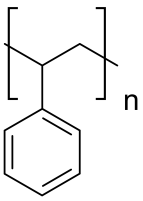

Polymers with homoatomic backbones are more resistant against biodegradation because the carbon-carbon bond is not susceptible to hydrolysis [78]. Additionally, these polymers have not been exposed to natural ecosystems long enough for new enzymatic degradation systems to be developed by nature [79, 80]. Typical examples for polymers

with homoatomic backbones are PE, PP, polyvinylchloride (PVC) and polyacrylamide (PAM).

In the case of EP, the epoxy monomers form a three-dimensional macromolecule with a high degree of crosslinking via ether bonds. If amine curing agents are used, nitrogen atoms are introduced into the backbone of the EPs via amine bonds. However, the heteroatomic backbone does not contain ester or amide bonds, which makes the polymer more recalcitrant against hydrolysis and thus against biodegradation. Nevertheless, biochemical degradation of EPs and epoxy composites was to some extend observed by several authors (see Table 2.3). Especially, marine microorganisms like *Pseudomonas putida* were found to be able to form biofilms on epoxy coatings, reducing their corrosion resistance by oxidizing the hydroxyl groups present on the polymer surface [81]. Additionally, cleavage of ether and carbonyl bonds responsible for crosslinking and surface adhesion was induced by *Pseudomonas aeruginosa* according to Zhang et al. (2023) [82]. Due to the limited metabolic capacity of individual organisms, natural or synthetic compounds like hydrocarbons are often degraded by microbial consortia. This approach was followed by Gu et al. (1997) [83] who studied the biodegradation of an epoxy-based composite by a fungal consortium consisting out of *Aspergillus versicolor*, *Cladosporium chladosporioides* and *Chaetmium sp.* A lower binding strength of the epoxy matrix to the fiber material was observed and an increase in number and pore size was found via electrochemical impedance spectroscopy (EIS). Another biodegradation approach was used by Pardi-Comensoli et al. (2022) [1], which utilized the structural similarity of cured EPs and lignin, which both are composed out of phenolic subunits. The lignin-decaying fungi *Ganoderm adspersum* was used because the authors hypothesized that the two main enzymes, lignin peroxidase and laccase, both involved in lignin biodegradation, would act upon the phenolic units of the EPs. However, only a reduction of surface hydrophobicity was observed via contact angle measurement, indicating a surface oxidation by the fungi. Besides its recalcitrant properties against biochemical degradation, the high hydrophobicity and high molecular weight of EPs hinder the biodegradation by microorganisms, as accessibility of the polymer is hardly given.

While some studies showed that certain microorganisms can oxidize EPs, no clear information about the underlying enzymatic reactions was eluded yet. The first investigation of isolated enzymes for epoxy resin degradation, and the only one so far, was published by Dolz et al. (2022) [84]. They developed a colorimetric highthroughput screening assay to guide the engineering of unspecific peroxygenases (UPOs) toward the depolymerization of Hexflowő RTM-6, a commercial epoxy extensively utilized in the aeronautics industry.

Table 2.3 Reported strains or isolated enzymes in the context of epoxy biodegradation.

Tested Resin	**Applied Biocatalyst(s)**	**Analytics**	**Ref.**
Araldite® LY 5052, Huntsman Corp., The Woodlands, TX, USA & EPON 815C, Hexion, Columbus, OH, USA	*Rhodococcus rhodochrous* *Ochrobactrum anthropi*	Turbidity measurement	[85]
BPA-based epoxy, (not specified)	*Pseudomonas putida*	EIS, SEM, FTIR, Contact angle measurement	[81]
Epoxy varnish, (not specified)	*Bacillus flexus*	EIS, SEM, FTIR	[86]
Epoxy and epoxy-silicone blends, (not specified)	*Bacterium Te68R* *Microbacterium sp.* (strain MK3) *Pseudomonas putida*	FTIR, TGA	[87]
Epoxy resin L + hardener GL21, Suter Kunststoffe, Fraubrunnen, Bern, Switzerland	*Ganoderma adspersum*	Weight loss, Contact angle measurement, Mechanical testing, FTIR	[1]
Epoxy Hercules 3501-6	*Aspergillus versicolor* *Cladosporium cladosporioides*	EIS, SEM, Mechanical testing	[83]
Carbon-fiber-reinforced epoxy and glass- and carbon-fiber-reinforced vinyl ester (not specified)	*Thiobacillus ferroxidans* *Pseudomonas fluorescens* *Lactococcus lactis* *Clostridium acetobutylicum*	SEM, Mechanical testing	[88]
Hexflow® RTM-6 model compound N,N-bis(2-hydroxypropyl)-**p**-toluidine (NNBT)	Unspecific peroxygenases *Agrocybe aegerita*PaDa-I *Psathyrella aberdarensis*GroGu *Marasmius rotula*rMroUPO *Psathyrella aberdarensis*PabUPOII	GC-MS	[84]
PU blend with BPA-based epoxy, amine-hardened (not specified)	*Pseudomonas aeruginosa* (MTCC 7815, MTCC 7814, PN8A1	Weight loss, FTIR, TGA, SEM, Mechanical testing	[89]
BADGE hardened with Jeffamine D230	*Pseudomonas aeruginosa* (1A00099)	Contact angle measurement, Mechanical testing, FTIR, SEM	[82]

UPO variants from both the shortchain family (*Marasmius rotula*) and the longchain families (*Agrocybe aegerita* and *Psathyrella aberdarensis*) were assessed for their *N*-dealkylation activity on *N*,*N*-bis(2-hydroxypropyl)-*p*-toluidine (NNBT), a key structural scaffold of resin transfer mold 6 resin (RTM6). Using a directed evolution platform, the authors generated UPO mutants with increasing activity towards the model compound NNBT. However, experimental validation of backbone cleavage in the intact epoxy resin has not yet been achieved.

2.4 Potential of Oxidative Breakdown of Crosslinked Polymers by Laccases

2.4.1 Laccases

Laccases are blue multi-copper oxidases, classified under EC 1.10.3.2, and belong to the broader enzyme group of oxidoreductases, which catalyze electron transfer reactions leading to substrate oxidation or reduction [90]. The enzymes are secreted by plants, insects, bacteria, and predominantly in fungi as they participate in lignin biosynthesis and degradation by wood-decaying fungi [91, 92, 93]. Apart from lignin as major natural substrate, laccases are capable of oxidizing a wide variety of phenolic and non-phenolic substrates while reducing molecular oxygen to water [94, 95]. Owing to this versatility, laccases are used in pulp and paper processing, wastewater treatment, food and textile industries, biosensor development, and cosmetic applications [91, 96]. The general catalytic reaction is shown in Figure 2.5. One-electron oxidation of a phenolic substrate generates phenoxyl radicals, while O_2 is reduced to H_2O. Depending on the enzyme source, laccase redox potentials range between 400 mV and 800 mV and are therefore categorized into *low redox potential* and *high redox potential* laccases. The redox potential of laccases significantly impacts their potential substrate range, as compounds with high redox potential are less likely to be oxidized by low redox potential laccases [97].

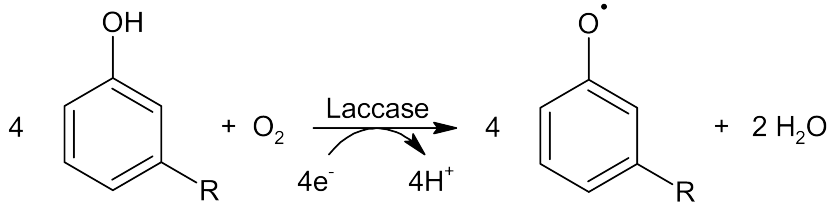

Figure 2.5 General laccase reaction mechanism showing the oxidation of phenolic substrates with concurrent reduction of molecular oxygen to water.

Catalytic activity is facilitated by a conserved arrangement of three copper sites: a mononuclear Type 1 (T1) blue copper center, a mononuclear Type 2 (T2), and a binuclear Type 3 (T3) site [98]. The T2 and T3 centers form a trinuclear copper cluster responsible for oxygen reduction. Substrate oxidation occurs at the T1 site, with electrons transferred via conserved HisCysHis motifs to the cluster [91, 92]. A detailed catalytic cycle is depicted in Figure 2.6.

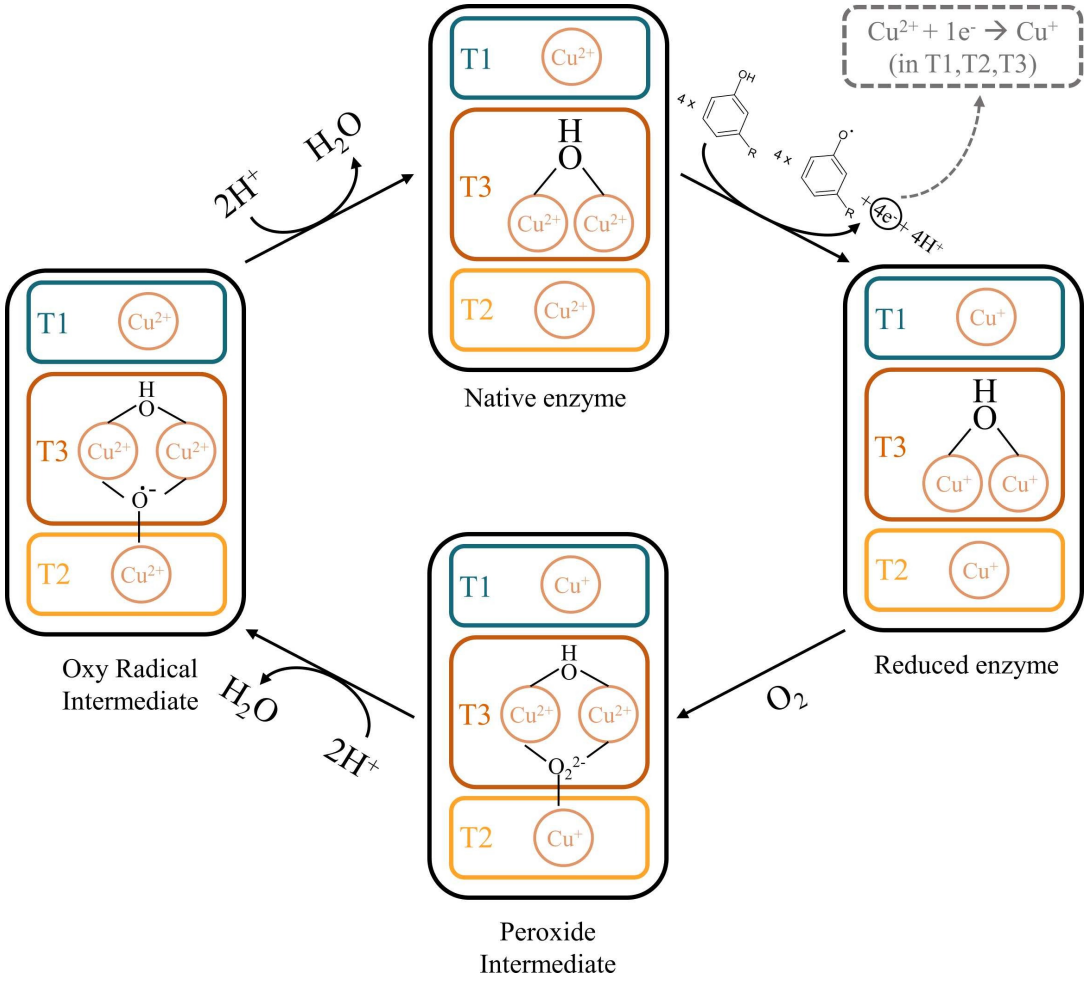

Figure 2.6 Schematic overview of the laccase catalytic cycle. Electrons are transferred from the Type 1 copper site to the trinuclear cluster (T2/T3), enabling oxidation of phenolic substrates and reduction of O_2 to H_2O [97].

In the native state, all copper ions are present as Cu^{2+}. Upon oxidation of a phenolic substrate, one electron is extracted and transferred to the T1 site, then relayed to the trinuclear cluster, where one copper ion is reduced to Cu^{+}. After four substrate oxidations, all copper atoms are reduced, indicating the fully reduced state of the enzyme. Subsequent

binding of molecular oxygen leads to formation of a peroxide intermediate, in which $O_2{}^{2-}$ coordinates with the copper atoms of the cluster. Protonation and further electron transfer result in the formation of an oxy radical intermediate, followed by the generation of two water molecules and regeneration of the oxidized (native) enzyme state [97].

2.4.2 LaccaseMediator Systems

Substrates that are inaccessible due to steric hindrance or possess a redox potential higher than that of the laccase active site can be oxidized using a laccasemediator system (LMS). In this system, a redox mediator is first oxidized by the enzyme, forming a stable radical species capable of oxidizing the target substrate in a subsequent step [99]. A schematic representation of the LMS is shown in Figure 2.7.

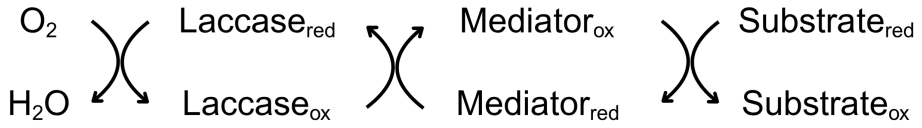

Figure 2.7 General scheme of the laccasemediator system. The mediator transfers redox equivalents from the enzyme to the substrate, thereby enabling the oxidation of sterically hindered or high-redox-potential targets.

In the initial step, the reduced laccase ($\text{Laccase}_{\text{red}}$) transfers electrons from the mediator to the trinuclear copper cluster, reducing molecular oxygen to water and regenerating the oxidized laccase ($\text{Laccase}_{\text{ox}}$). The oxidized mediator ($\text{Mediator}_{\text{ox}}$) then reacts with the substrate, which itself becomes oxidized ($\text{Substrate}_{\text{ox}}$) while the mediator returns to its reduced form ($\text{Mediator}_{\text{red}}$) and re-enters the catalytic cycle [97].

Substrate oxidation via LMS can proceed via two main mechanisms: hydrogen atom transfer (HAT) and electron transfer (ET). In the HAT pathway, the oxidized mediator abstracts a hydrogen atom (proton and electron) from the substrate, generating a substrate radical and restoring the mediator to its reduced form. In the ET mechanism, a single electron is abstracted from the substrate, typically an aromatic compound, forming a resonance-stabilized aryl radical [100]. In both cases, the oxidation process is completed by reducing O_2 to H_2O through the catalytic action of the enzyme. Laccase mediators can be broadly categorized into natural and synthetic types. Natural mediators include small phenolic compounds such as caffeic acid (CA) and ferulic acid (FA), which are structurally similar to lignin-derived degradation products [101]. Synthetic mediators, such as 2,2'-azino-bis(3-ethylbenzothiazoline-6)-sulfonic acid (ABTS) and 2,2,6,6-tetramethylpiperidinyloxyl (TEMPO), often offer higher stability or broader substrate

ranges [102]. LMS have found application in the enzymatic breakdown of lignin within lignocellulosic biomass, where bulky non-phenolic moieties are rendered accessible for oxidation through mediators [103, 104]. Additionally, LMS are used for the transformation of xenobiotic pollutants, such as chlorinated phenols or dyes, in wastewater treatment processes [105]. The mediator acts as a diffusible oxidant that bridges the gap between the enzyme and the otherwise unreactive substrate. The ability to mediate both HAT and ET reactions, in combination with a broad mediator toolbox, significantly expands the substrate scope of laccases and underlines their biotechnological relevance in green chemistry as well as environmental remediation and enables polymer oxidation and subsequent degradation [106].

2.5 Biocatalysis in Deep Eutectic Solvents

2.5.1 Fundamentals of Deep Eutectic Solvents

Deep eutectic solvent (DES) are a class of alternative solvents formed by combining a hydrogen bond donor (HBD) and a hydrogen bond acceptor (HBA), typically in a defined molar ratio. The resulting mixture exhibits a significantly reduced melting point compared to the individual components or an ideal mixture thereof, due to strong hydrogen bonding interactions and entropic effects [107]. This phenomenon is illustrated in Figure 2.8, where the eutectic point defines the composition at which the system remains liquid at the lowest temperature.

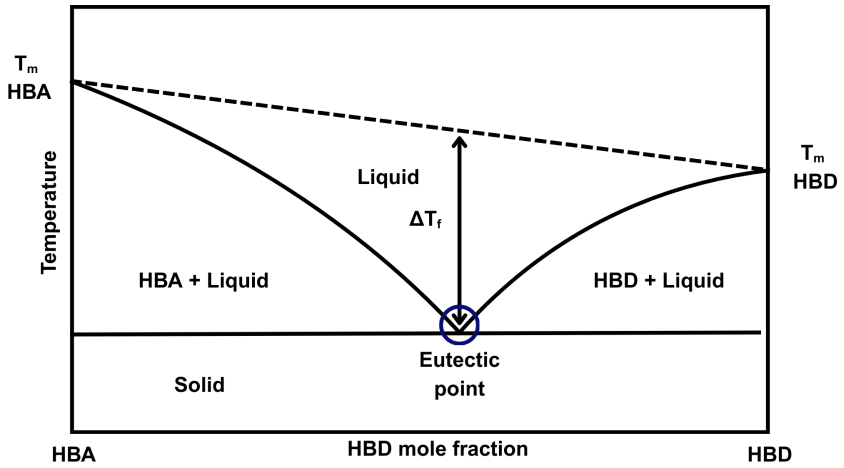

Figure 2.8 Schematic phase diagram of a binary eutectic mixture. The eutectic point indicates the lowest melting temperature of the system (adapted from Marco-Velasco et al. (2024) [107]).

DES are considered promising green solvents due to their low volatility, low toxicity, biodegradability, and facile synthesis from inexpensive and biocompatible precursors. Their dense hydrogen-bonding network provides high solvation capabilities, particularly for phenolic or polar compounds, making them attractive for applications such as lignin extraction, biomass pretreatment, and pharmaceutical formulations [108].

Classification of DESs is generally based on the chemical nature of the hydrogen bond acceptor (HBA) and hydrogen bond donor (HBD). Depending on the combination of ionic or molecular components, four main DES types are commonly distinguished in the literature. An overview of these DES types and their characteristic components is provided in Table 2.4.

Table 2.4 Classification of deep eutectic solvents according to the nature of the hydrogen bond acceptor (HBA) and hydrogen bond donor (HBD).

DES Type	**Hydrogen bond acceptor (HBA)**	**Hydrogen bond donor (HBD)**	**Typical components / examples**
Type I	Quaternary ammonium salts	Metal chlorides	$ZnCl_2$ / tetrabutylammonium bromide
Type II	Quaternary ammonium salts	Metal halide hydrates	Choline chloride / metal halide hydrate
Type III	Quaternary ammonium, sulfonium or phosphonium salts	Carboxylic acids, amines, alcohols, amlides	Choline chloride / urea, organic acids
Type IV	Metal halides	Organic compounds (e.g. diols, carboxylic acids, quaternary ammonium salts)	Metal halide–based systems

Unlike ionic liquids, which are composed of discrete organic and inorganic ions and require multistep syntheses, DES are formed via simple mixing procedures. Typical preparation methods include heating the components from 80 řC to 100 řC until liquefaction occurs, or the use of mechanical grinding at room temperature [109]. The grinding method is considered milder and minimizes undesired sie reactions such as esterification [110]. Due to the modularity of their composition and tunable physicochemical properties such as viscosity, polarity, and solvation capacity DES are increasingly referred to as *designer solvents* [111]. This adaptability makes them suitable candidates for replacing conventional organic solvents in biocatalytic and industrial processes.

2.5.2 Biocatalysis in Deep Eutectic Solvents and Role of Water Activity

Water is the most commonly used solvent in biocatalysis, but its application can be limited due to the poor solubility of non-polar substrates. In contrast, non-aqueous or low-water media such as organic solvents, ionic liquids, supercritical fluids, and DES can offer improved substrate solubility, minimize undesired hydrolytic side reactions, and shift equilibrium positions in favor of product formation [112]. However, their application in biocatalysis requires careful attention to enzyme stability, as the preservation of the hydration shell of the enzyme is essential for catalytic activity [113].

Various enzymes and even whole-cell biocatalysts have been successfully employed in DES-based reaction systems, either as solvent, co-solvent, or even as a reactant component. Esterification and transesterification reactions catalyzed by lipases have been extensively studied due to the hydrophobic nature of the substrates and products involved [112]. Beyond lipases, haloalkane dehalogenases from *Bradyrhizobium japonicum* have been applied in DES-containing systems, where the presence of DES enhanced the solubility of halogenated substrates [114]. In another study, the hydrolysis of (1,2)-trans-methyl styrene oxide by potato epoxide hydrolase was conducted in DES-buffer mixtures. Here, a choline chlorideethylene glycol DES not only improved solubility but also altered the regioselectivity of the enzyme [115].

Furthermore, horseradish peroxidase has been used to catalyze the radical polymerization of acrylamide in nearly water-free DES composed of choline chloride and urea or glycerol. Upon addition of 20 vol % water, a significant increase in thermal stability was observed, especially in the urea-based system. Although catalytic activity decreased compared to aqueous conditions, product formation was still observed at lower temperatures, unlike in DES-free systems [116]. The enantioselective carboligation of aliphatic and aromatic aldehydes using benzaldehyde lyase from *Pseudomonas fluorescens* was also demonstrated in 40 vol % choline chlorideglycerol DES-buffer mixtures, although strong enzyme denaturation occurred under anhydrous conditions [117].

Although DES offer advantages for solubility and selectivity, their high viscosities (often exceeding 100 mPa · s) limit mass transfer in biocatalytic applications at room temperature. While increasing the reaction temperature reduces viscosity, this can come at the cost of reduced enzyme stability, particularly in industrial processes. A widely applied solution is the partial dilution of DES with water. For choline chloride-based systems, adding up to 20 vol % water significantly reduces viscosity while maintaining the eutectic nature and physicochemical properties of the solvent [118, 119].

Spectroscopic techniques such as fourier-transform infrared spectroscopy (FTIR) and ^{1}NMR have shown that water disrupts the hydrogen bonding network of DES by weakening the interactions between HBA and HBD [120]. This has been interpreted as a destructuring effect of water. Ünlü et al. (2023) [121] used conductivity measurements to show that the supramolecular structure of DES begins to disintegrate above 60 vol % water content. A bell-shaped conductivity curve was observed for choline chlorideethylene glycol and betainemannose DES with a maximum at 60 vol %, while salt controls (NaCl, choline chloride) showed a monotonic decrease in conductivity with increasing water content [122].

Beyond total water content, the concept of water activity (a_w) becomes critical in non-aqueous reaction systems. Water activity describes the effective availability of water for hydration and is thus a more relevant parameter than absolute water concentration when assessing enzyme function. In non-aqueous and DES-based systems, water activity can be adjusted independently of the total water content via the addition of inorganic salts that bind free water. As a result, enzyme hydration and catalytic performance can be related to water activity even at identical volumetric water contents. In DES, water molecules distribute between the enzyme surface and the solvent bulk, and this equilibrium is governed by solventwater interactions [118]. Lajtai-Szabó et al. (2020) [123] demonstrated that enzymatic esterification in different solvents showed maximum activity at the same water activity, even though the required water concentrations varied by solvent polarity.

Molecular dynamics simulations by Bittner et al. (2022) [118] revealed how water activity influences enzyme solvation in DESwater mixtures. Using horse liver alcohol dehydrogenase as a model, the authors showed that at water mole fractions below $0.72\,\mathrm{mol} \cdot \mathrm{mol}^{-1}$, no enzyme activity was detected due to the absence of a stable hydration layer. Beyond this threshold, a sharp increase in enzymatic activity was observed. The simulations further revealed that as water was added, the HBA concentration at the protein surface decreased linearly, while the HBD content remained constant up to $0.5\,\mathrm{mol} \cdot \mathrm{mol}^{-1}$, after which it also decreased. These shifts in solventenzyme interface composition were linked to the observed changes in enzyme half-life and activity [118].

The successful application of DES in biocatalytic systems depends strongly on the fine-tuning of water content and water activity to balance substrate solubility, enzyme stability, and catalytic efficiency. While DES provide a versatile reaction medium with tunable physicochemical properties, their impact on enzyme hydration, conformational flexibility, and solvation dynamics must be carefully considered. Experimental observations, complemented by molecular simulations, have highlighted the importance of maintaining a

sufficient hydration shell and minimizing competitive interactions between solvent components and enzyme surfaces. Continued integration of empirical screening with computational modeling is essential to identify suitable DES formulations for specific enzymatic transformations and to optimize bioprocesses under low-water or solvent-rich conditions.

2.5.3 Laccase-catalyzed Reactions in Deep Eutectic Solvents

The applicability of laccases under industrial operation conditions is limited because of the enzymes low stability and activity. Therefore, solvent engineering approaches have been developed to enhance both catalytic efficiency and robustness. In literature, it has been proposed that, depending on multiple factors, DES can be used to overcome the inherent limitations of laccase reaction systems [124].

Several studies have demonstrated increased laccase activity in aqueous DES formulations, primarily investigated through the oxidation of ABTS, a commonly used model substrate in oxidative enzyme assays. Varriale et al. (2022) [125] evaluated the influence of different betaine-based DES in 25 wt.% aqueous solution on laccase activity. Betaine served as the HBA, while sorbitol, xylitol, glycerol, ethylene glycol, and erythritol were employed as HBDs. In all combinations, a maximum activity enhancement of 20 % was observed. In contrast, another study found that choline chloride-based DES negatively affected laccase activity, with an activity drop of 60 % attributed to enzyme inhibition by chloride ions [126]. When the chloride ion was substituted with dihydrogen citrate or dihydrogen phosphate, a substantial increase in activity was observed. Specifically, 25 wt.% choline dihydrogen citrate:erythritol (ChDHC:ERY) and 50 wt.% choline dihydrogen citrate:xylitol (ChDHC:XYL) aqueous solutions led to activity enhancements exceeding 170 %. Based on these findings, the presence and number of hydroxyl groups in the DES components appear to be crucial, as stronger hydrogen-bond interactions with the enzyme surface are believed to promote catalytic activity.

Further confirmation of this trend was reported by Chan et al. (2021) [127], who showed that lactic acidbetaine DES in aqueous concentrations ranging from 2 wt.% to 8 wt.% were able to increase relative laccase activity by up to 300 %. Among the tested combinations, the lactic acidbetaine system exhibited the highest propensity for hydrogen bonding. The inhibitory effect of choline chloride was again confirmed, and it was identified as a non-competitive inhibitor. Its binding was shown to induce conformational changes in the enzyme, leading to reduced activity.

In addition to activity enhancement, increased thermostability of laccases in aqueous DES has also been reported. Khodaverdian et al. (2018) [94] demonstrated that the half-life of laccase at 90 řC could be doubled using a 20 wt.% aqueous solution of a betaine-sorbitol DES. The enhanced thermostability in such systems has been attributed to increased hydrogen bonding capacity, changes in free volume, and a more structured hydration environment [127]. However, the number of hydroxyl groups in the HBD, the total DES concentration, and the pH of the aqueous solution were also shown to significantly affect thermostability [128].

To date, most studies have focused exclusively on the laccase-catalyzed conversion of ABTS in DES-containing reaction media. While these investigations have yielded critical insights into inhibitory effects (e.g. from choline chloride) and structural requirements (e.g., hydroxyl functionality of HBD components), the chemical diversity of DES formulations remains largely underexplored. Given the wide range of available components, and their influence on both biocatalyst and substrate properties, more targeted studies are needed to evaluate the compatibility of DES with structurally diverse laccase substrates [128]. Computational methods such as the conductor-like screening model for real solvents (COSMO-RS) model provide a valuable predictive framework to complement experimental screening of DES. By estimating thermodynamic properties such as activity coefficients, solubilities, and hydrogen-bonding capacities based on quantum chemical surface interactions, COSMO-RS enables rational selection and optimization of DES formulations for specific enzymatic or substrate systems. In this context, COSMO-RS simulations have been used to predict substrate solubility and enzymesolvent compatibility across a wide range of HBD and HBA combinations, thereby reducing the need for exhaustive empirical testing [129]. Furthermore, COSMO-RS was applied to design task-specific DES for efficient phenolic extraction and delignification, highlighting its potential for sustainable bioprocess development [130, 131].

2.6 Epoxidized Vegetable Oils As Renewable Epoxies

Epoxidized vegetable oils (epoxidized vegetable oils (EVOs)) have emerged as a promising class of biobased alternatives to conventional petroleum-derived epoxy resins. In addition to being sourced from renewable feedstocks, EVOs offer the advantage of partial biodegradability, making them attractive for sustainable material applications where end-of-life considerations are critical [132, 133]. Vegetable oils such as linseed, soybean, or

castor oil are naturally rich in unsaturated fatty acid chains, which provide chemically accessible C=C double bonds for functionalization [134]. Through epoxidation, these double bonds are transformed into oxirane groups, enabling the resulting epoxidized oils to act as cross-linkable monomers in resin formulations [135]. When combined with a suitable curing agent, polyaddition or copolymerisation can be used to achieve a mechanically stable, three-dimensional polymer network. In this context, the use of biobased agents such as dicarboxylic acids (e.g., itaconic acid, citric acid) has been explored to produce a fully bio-derived multi-component resin [136]. EVOs exhibit several advantages over conventional BPA-based epoxy systems. They are derived from renewable feedstocks, biodegradable under certain conditions, and free from toxic aromatic precursors. Moreover, their chemical versatility allows tuning of key properties such as epoxy equivalent weight (EEW), viscosity, and reactivity by controlling the degree of epoxidation and the choice of starting oil. Among these, epoxidized epoxidized linseed oil (ELO) stands out due to its exceptionally high iodine value (IV) (up to $190\,\mathrm{g} \cdot 100\,\mathrm{g}^{-1}$), which corresponds to a high content of reactive double bonds and enables the formation of highly functionalized epoxy networks [17]. However, due to the triglyceride-based structure and aliphatic backbone, EVOs typically exhibit lower glass transition temperatures (T_g) and modulus compared to aromatic epoxy resins, which limits their application in high-performance sectors unless modified or blended [20, 137]. Consequently, the development of efficient and selective epoxidation methods, including enzymatic and chemoenzymatic strategies, is critical to maximize epoxy functionality while preserving the integrity of the oil matrix. These approaches not only improve the performance of EVO-based resins but also enhance their environmental profile by reducing hazardous reagents and waste streams.

2.6.1 Epoxidized Linseed Oil (Bio-)Synthesis

The conventional epoxidation of linseed oil (LO) relies on the *Prileshajev* reaction, in which C=C double bonds are oxidized to oxirane rings using peroxycarboxylic acids formed *in situ* from H_2O_2 and carboxylic acids [16]. While industrially employed for decades, this method often depends on stoichiometric use of strong acids or halogenated reagents and generates aqueous and chlorinated waste [138]. Additionally, side reactions such as oxirane ring-opening are promoted under acidic conditions and elevated water activity, reducing epoxy yield and quality [18]. Due to its high degree of unsaturation, owing to contents of up to 53 % α-linolenic and 17 % linoleic acid, LO provides a large amount of double bonds, enabling high levels of epoxidation and network functionality [139]. Chemoenzymatic epoxidation (CEE) presents a more selective and environmentally favorable alternative

by integrating biocatalytic oxidant generation with mild peracid-based oxygen transfer. The process is catalyzed almost exclusively by Novozyme® 435, an immobilized form of lipase from *Candida antarctica* (CALB), typically applied at 15 wt. % relative to the oil substrate [16, 140]. In the first step, CALB catalyzes the perhydrolysis of a short-chain free fatty acid (FFA) (e.g., butyric or caprylic acid) with H_2O_2,

$$\mathrm{R{-}COOH} + \mathrm{H_2O_2} \xrightarrow{\text{Lipase}} \mathrm{R{-}COOOH} + \mathrm{H_2O},$$

followed by a non-enzymatic epoxidation of the C=C double bond with the generated peracid,

$$\mathrm{R^1{-}CH{=}CH{-}R^2} + \mathrm{R{-}COOOH} \longrightarrow \mathrm{R^1{-}CH(O){-}CH(O){-}R^2} + \mathrm{R{-}COOH},$$

which regenerates the FFA and allows the process to operate with catalytic FFA loadings of $0.1\,\mathrm{mol} \cdot \mathrm{mol}^{-1}$ to $1\,\mathrm{mol} \cdot \mathrm{mol}^{-1}$ C=C [16]. The process proceeds under mild conditions (typically around 50 řC) and in bi-phasic media to maintain low water activity, which reduces ring-opening side reactions and improves EEW [141, 142]. CALB shows limited tolerance to oxidative stress, with irreversible inactivation occurring from the reaction with H_2O_2 due to methionine and tryptophan oxidation [143]. Therefore, controlled dosing of H_2O_2 is essential. Several studies have demonstrated the applicability of CEE in epoxidizing LO and other vegetable oils. Hilker et al. (2001) [144] observed complete epoxidation of linseed oil within 6 h at 40 řC using 14 wt. % Novozyme® 435, 20 wt. % H_2O_2, and a fed-batch reactor with enzyme recycling. Orellana-Coca et al. (2007) [145] used stoichiometric amounts H_2O_2 for epoxidation of methyl linoleate and emphasized the importance of peroxide control to avoid enzyme inactivation. They also stated an optimal amount of Novozyme® 435 of $6.7\,\mathrm{mg} \cdot \mathrm{mmol}^{-1}$. Schneider et al. (2009) [146] achieved >99 % conversion of sunflower oil methyl esters within 16 h at 30 řC, using octanoic acid ($10\,\mathrm{mmol} \cdot \mathrm{g}_{\mathrm{oil}}^{-1}$), $100\,\mathrm{mg} \cdot \mathrm{g}_{\mathrm{oil}}^{-1}$ Novozyme® 435, and a 30 wt. % H_2O_2 feed in a biphasic CH_2Cl_2/H_2O system. Beyond its environmental advantages, CEE offers a technically versatile and industrially relevant platform for the synthesis of biobased epoxy monomers. Its compatibility with mild temperatures, renewable co-substrates, and *in-situ* oxidant generation aligns well with principles of green chemistry and process intensification. As a result, chemoenzymatic approaches are increasingly recognized not only for their ecological merits, but also for enabling selective, high-yield epoxidation under conditions that preserve the structural integrity of unsaturated oils [147].

2.6.2 *Inline* ATR-FTIR Monitoring and Indirect Hard Modeling

Real-time monitoring plays a crucial role in the intensification and digitalization of chemical processes, offering enhanced control, reduced waste, and improved product quality [148]. Traditional quality control in batch and semi-batch processes often relies on *offline* analytics, where samples are withdrawn and measured externally, sometimes hours after collection (see Figure 2.9).

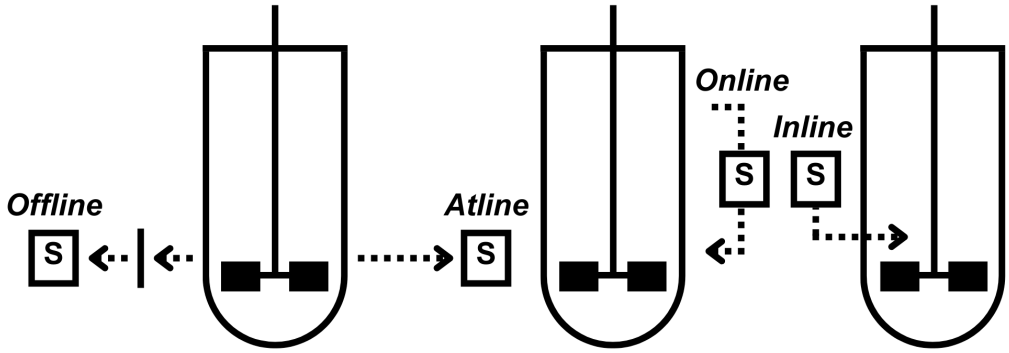

Figure 2.9 Process-monitoring concepts in chemical engineering. S - Sampling site

This time lag prevents direct feedback and introduces significant risks for product consistency and process stability. *Atline* analytics, where samples are manually measured in a nearby laboratory, improve speed but still require operator intervention. *Online* methods, in contrast, use a continuous stream of process fluid through an external analyzer, reducing the delay to seconds or minutes. The most direct approach is *inline* process analytics, where e.g., a spectroscopic probe is immersed directly into the reaction vessel, enabling uninterrupted, real-time data acquisition [149].

Among available analytical technologies for *inline* and *online* applications, vibrational spectroscopy has become especially relevant. Raman, near-infrared spectroscopy (NIR), mid-infrared spectroscopy (MIR), and nuclear magnetic resonance spectroscopy (NMR) each offer unique advantages, but also come with practical limitations in the context of multiphase, enzyme-catalyzed systems. Raman spectroscopy is less sensitive to water and provides detailed structural information, but it often suffers from weak signal intensity and fluorescence interference in complex matrices [150]. NMR delivers molecular-level insights and direct quantification without the need for calibration but requires expensive instrumentation and strong magnetic shielding. Furthermore, bench-top devices have not yet achieved the resolution of high-field devices with cryogenic cooling [151]. NIR has been widely applied in agricultural and food processing but exhibits poor specificity for functional groups and suffers from extensive baseline drift [152].

In contrast, MIR spectroscopy offers a practical and chemically informative approach. FTIR spectroscopy provides access to fundamental vibrational bands in the range of $4000\,\mathrm{cm}^{-1}$ to $600\,\mathrm{cm}^{-1}$, where C–H, C=C, C–O, and O–H stretching (ν) and bending (δ) modes occur. The attenuated total reflection (ATR) configuration is especially suitable for liquid-phase monitoring. By measuring the evanescent field that penetrates only a few micro meter into the sample, it circumvents issues related to turbidity, bubbles, or strong scattering which are common problems in biphasic systems such as in chemoenzymatic epoxidation [153, 154]. Several studies have demonstrated the potential of attenuated total reflection fourier-transform infrared spectroscopy (ATR-FTIR) for monitoring epoxidation reactions. Vlek and Petrovi (2006) [155] characterized the FTIR spectra of soybean oil during CEE, highlighting oxirane ring vibrations near $840\,\mathrm{cm}^{-1}$ and the disappearance of C=C signals at $3010\,\mathrm{cm}^{-1}$. Tavassoli-Kafrani et al. (2017) [156] applied ATR-FTIR to develop a chemometric model to track the chemical epoxidation of LO with H_2O_2 and acetic acid, confirming epoxide formation via the increase of the oxirane band at $822\,\mathrm{cm}^{-1}$ and the decrease in C=C absorbance at $3008\,\mathrm{cm}^{-1}$ and $1654\,\mathrm{cm}^{-1}$, respectively. Similarly, Bhalerao et al. (2018) [157] demonstrated that the carbonyl band near $1743\,\mathrm{cm}^{-1}$ and the fingerprint region between $1161\,\mathrm{cm}^{-1}$ to $822\,\mathrm{cm}^{-1}$ show characteristic changes upon epoxidation.

In the context of *inline* or *online* measurements, indirect hard modeling (IHM) provides a transparent and physically grounded approach for quantifying reaction progress from FTIR spectra. According to Alsmeyer et al. (2004) [158] and Beumers (2019) [159], IHM relies on the principle of spectral additivity, wherein the measured spectrum $\mathbf{s}$ is modeled as a linear combination of pure-component reference spectra $\mathbf{A} = [\mathbf{a}_1, \ldots, \mathbf{a}_k]$ with concentration-dependent coefficients $\mathbf{c}$:

$$\mathbf{s} = \mathbf{A} \cdot \mathbf{c} + \boldsymbol{\varepsilon} \tag{1}$$

where $\boldsymbol{\varepsilon}$ denotes the residual error. Unlike soft models such as partial least squares regression (PLS), IHM retains interpretability as each coefficient in $\mathbf{c}$ corresponds to a physically defined concentration, and the matrix $\mathbf{A}$ consists of real, experimentally recorded spectra [160, 161]. As a result, the model can be constrained using known process chemistry (e.g., constant solvent fraction, non-negativity) and extended across different scales without re-training, in the case that probe geometry and optical conditions remain constant [162].

In practice, IHM-driven *inline* FTIR enables the real-time, quantitative tracking of key species with measurement latencies, mostly only constrained by the acquisition times of the analytical device employed. This makes it compatible with advanced process control strategies, such as adaptive dosing or automated endpoint detection. Studies in flow chemistry and bioreactor systems demonstrate that IHM maintains high accuracy with minimal calibration, even when scaled up or when the reaction environment is slightly altered [163]. Coupled with its transparent, constraint-ready framework, this approach supports robust, scalable control architectures in intensification and manufacturing settings.

3 Aim of the Thesis

The overarching aim of this dissertation is to address sustainability challenges associated with epoxy polymers (EPs) by developing biocatalytic strategies that target both the beginning and the end of the material life cycle. By integrating enzymatic catalysis into the synthesis of renewable epoxy monomers and the degradation of persistent thermoset polymers, this work contributes to the realization of a circular bioeconomy for high-performance composite materials. To achieve this goal, the thesis pursues two complementary main objectives:

Biocatalytic Degradation Strategies for Aerospace-Grade Epoxies

The first objective is to investigate an enzymatic route for the oxidative degradation of amine-cured aromatic EPs, with a focus on the aerospace-grade thermoset system resin transfer mold 6 resin (RTM6), which is currently regarded as non-biodegradable. This part aims to:

- Identify suitable oxidative enzymes, particularly fungal laccases (e.g. laccase from *Funalia trogii* (LacF), laccase from *Trametes versicolor* (LacTV), and Novozym 51003 from *Myceliophthora thermophila* (LacMT)), capable of inducing chemical modifications within the polymer network.
- Overcome steric limitations of direct enzymatic attack by implementing laccase-mediator systems (LMSs), enabling long-range electron transfer mechanisms such as electron transfer (ET) and hydrogen atom transfer (HAT).
- Enhance substrate accessibility and polymer wetting by evaluating deep eutectic solvents (DESs) as biocompatible reaction media.
- Characterize structural changes and degradation products using attenuated total reflection fourier-transform infrared spectroscopy (ATR-FTIR), gas chromatography coupled mass spectrometry (GC-MS), and thermogravimetric analysis (TGA) to propose a mechanistic pathway for biocatalytic polymer breakdown.

Sustainable Chemoenzymatic Synthesis for Biobased Epoxies

The second objective is to develop a mild, scalable, and fully bio-based synthesis route for epoxy monomers using linseed oil (LO) as a renewable feedstock. This approach aims to replace petrochemical precursors such as bisphenol A diglycidyl ether (DBEGA) with epoxidized linseed oil (ELO) while maintaining suitable processing and material performance. This includes:

- Optimization of a chemoenzymatic epoxidation (CEE) process employing immobilized lipase from *Candida antarctica* (CALB) (Novozyme® 435), enabling *in situ* peracid formation while avoiding harsh mineral acids and toxic oxidants.
- Implementation of real-time process monitoring via *inline* ATR-FTIR monitoring combined with chemometric modeling using indirect hard modeling (IHM).
- Demonstration of scalability and improved mass transfer through the use of a rotating bed reactor (RBR) (SpinChem®).
- Evaluation of curing behavior and thermal properties using differential scanning calorimetry (DSC) and modulated differential scanning calorimetry (MDSC) to verify suitability as a sustainable alternative to conventional thermoset systems.

By addressing these objectives, this dissertation aims to evaluate whether high-performance thermoset epoxy materials can be produced and managed in a more environmentally responsible manner. The proposed strategies are intended to explore viable pathways for renewable epoxy production and the biological recycling of persistent polymer waste.

4 Materials and Methods

4.1 Chemicals

Table 4.1: Used Chemicals.

Chemical (Purity/Content)	**Information**
0.1 M KOH in ethanol (99.6 %)	Carl Roth®, Carl Roth GmbH + Co. KG, Karlsruhe, Germany
0.1 N perchloric acid in ethanol (99.5 %)	Carl Roth®, Carl Roth GmbH + Co. KG, Karlsruhe, Germany
1,10-decandiol (98 %)	Sigma-Aldrich®, Merck KGaA, Darmstadt, Germany
2-2'-azino-di(3-ethylbenythazolin-6-sulfonic acid) ($\geq$ 98 %)	TCI®, TCI Deutschland GmbH, Eschborn, Germany
2-propanol ($\geq$ 99.8 %)	Carl Roth®, Carl Roth GmbH + Co. KG, Karlsruhe, Germany
4,4'-methylenebis(*N*,*N*-dimethylaniline) (Michlers Base) ($\geq$ 98 %)	Sigma-Aldrich®, Merck KGaA, Darmstadt, Germany
4,4'-methylen-bis(*N*,*N*-diglycidylanilin) ($\geq$ 98 %)	Carl Roth®, Carl Roth GmbH + Co. KG, Karlsruhe, Germany
4,4'-methylenebis(2,6-diethylaniline) ($\geq$ 98 %)	Carl Roth®, Carl Roth GmbH + Co. KG, Karlsruhe, Germany
4,4'-methyylenebis(2-isopropyl-6-methylaniline) ($>$ 95 %)	Lonza Group AG, Basel, Switzerland
Ammonium thiocyanate ($\geq$ 99 %)	Sigma-Aldrich®, Merck KGaA, Darmstadt, Germany
Betaine ($\geq$ 98 %)	Sigma-Aldrich®, Merck KGaA, Darmstadt, Germany
Butyric acid ($\geq$ 99 %)	TCI®, TCI Deutschland GmbH, Eschborn, Germany

Table 4.1 – Continued from previous page.

Chemical	Information
Caffeic acid (≥ 98 %)	Carl Roth®, Carl Roth GmbH + Co. KG, Karlsruhe, Germany
Chloroform (≥ 99 %)	Carl Roth®, Carl Roth GmbH + Co. KG, Karlsruhe, Germany
Choline chloride (98 %)	Sigma-Aldrich®, Merck KGaA, Darmstadt, Germany
Choline dihydrogen citrate (≥ 99 %)	TCI®, TCI Deutschland GmbH, Eschborn, Germany
Citric acid (≥ 99 %)	Carl Roth®, Carl Roth GmbH + Co. KG, Karlsruhe, Germany
Crystal violet (97.5–100.5 %)	Sigma-Aldrich®, Merck KGaA, Darmstadt, Germany
Dichloromethane (≥ 99.5 %)	Carl Roth®, Carl Roth GmbH + Co. KG, Karlsruhe, Germany
Dimethyl sulfoxide (≥ 99.9 %)	Carl Roth®, Carl Roth GmbH + Co. KG, Karlsruhe, Germany
Dimethylformamide (≥ 99 %)	Carl Roth®, Carl Roth GmbH + Co. KG, Karlsruhe, Germany
Disodium phosphate (≥ 99 %)	Carl Roth®, Carl Roth GmbH + Co. KG, Karlsruhe, Germany
Epoxidized linseed oil (-)	HOBUM Oleochemicals GmbH, Hamburg, Germany
Ethanol (≥ 99.8 %)	Carl Roth®, Carl Roth GmbH + Co. KG, Karlsruhe, Germany
Ethyl acetate (≥ 99.8 %)	Carl Roth®, Carl Roth GmbH + Co. KG, Karlsruhe, Germany
Ethylene glycol (≥ 99.9 %)	Thermo Fisher Scientific Inc., Walthamn, U.S.

Table 4.1 – Continued from previous page.

Chemical	**Information**
Formic acid (99.9 %)	Carl Roth®, Carl Roth GmbH + Co. KG, Karlsruhe, Germany
Glacial acetic acid (99.8 %)	Carl Roth®, Carl Roth GmbH + Co. KG, Karlsruhe, Germany
Glycerol (≥ 99.5 %)	Carl Roth®, Carl Roth GmbH + Co. KG, Karlsruhe, Germany
Hydrochloric acid (36 %)	Carl Roth®, Carl Roth GmbH + Co. KG, Karlsruhe, Germany
Hydrogen peroxide (35 %)	Sigma-Aldrich®, Merck KGaA, Darmstadt, Germany
L-(-)-Malic acid (≥ 99 %)	MERCK®, Merck Schuchardt oHG, Hohenbrunn, Germany
Lactic acid (90 %)	Carl Roth®, Carl Roth GmbH + Co. KG, Karlsruhe, Germany
Linseed oil (99 %)	Carl Roth®, Carl Roth GmbH + Co. KG, Karlsruhe, Germany
m-Erythritol (99 %)	TCI®, TCI Deutschland GmbH, Eschborn, Germany
N,*N*-bis(2-hydroypropyl)-*p*-toluidine (≥ 98 %)	LGC Standards, LGC Limited, Teddington, U.K.
Oxalic acid (≥ 99.5 %)	Carl Roth®, Carl Roth GmbH + Co. KG, Karlsruhe, Germany
Potassium dihydrogen phosphate (≥ 99.5 %)	Carl Roth®, Carl Roth GmbH + Co. KG, Karlsruhe, Germany
Pyridine (≥ 99 %)	Carl Roth®, Carl Roth GmbH + Co. KG, Karlsruhe, Germany
L-(-)-Proline (≥ 99 %)	Sigma-Aldrich®, Merck KGaA, Darmstadt, Germany

Table 4.1 – Continued from previous page.

Chemical	Information
Sodium azide (99 %)	Sigma-Aldrich®, Merck KGaA, Darmstadt, Germany
Sodium bicarbonate (99 %)	Carl Roth®, Carl Roth GmbH + Co. KG, Karlsruhe, Germany
Sodium hydroxide (≥ 99 %)	Carl Roth®, Carl Roth GmbH + Co. KG, Karlsruhe, Germany
Sodium sulfate (≥ 99 %)	Carl Roth®, Carl Roth GmbH + Co. KG, Karlsruhe, Germany
Sorbitol (≥ 99 %)	Carl Roth®, Carl Roth GmbH + Co. KG, Karlsruhe, Germany
Tetraethylammonium bromide (≥ 98 %)	Sigma-Aldrich®, Merck KGaA, Darmstadt, Germany
Tetramethylammonium bromide (98 %)	Carl Roth®, Carl Roth GmbH + Co. KG, Karlsruhe, Germany
Toluene (≥ 99.5 %)	Carl Roth®, Carl Roth GmbH + Co. KG, Karlsruhe, Germany
Tween 20 (≥ 99 %)	Sigma-Aldrich®, Merck KGaA, Darmstadt, Germany
Violuric acid (≥ 98 %)	Alfa Chemicals, Zhengzhou, China
Xylitol (≥ 99 %)	TCI®, TCI Deutschland GmbH, Eschborn, Germany
Zinc chloride (≥ 98 %)	Carl Roth®, Carl Roth GmbH + Co. KG, Karlsruhe, Germany

4.2 Enzymes

For epoxy degradation studies, three different fungal laccases with varying redox potentials were obtained from ASA Spezialenzyme (Wolfenbüttel, Germany). These were the following: Laccase from *Trametes versicolor* (LacTV), laccase from *Funalia trogii* (LacF), and

a laccase of undisclosed origin (LacU). Novozym 51003 from *Myceliophthora thermophila* (LacMT) (recombinantly expressed in *Aspergillus sp.*) was purchased from Sigma-Aldrich® (Merck KGaA, Darmstadt, Germany). Chemoenzymatic epoxidation of linseed oil was conducted using Novozyme® 435 with an activity of 5000 U · g^{-1} (Novozymes, Bagsværd, Denmark).

4.2.1 Handling and Storage Conditions

All laccases apart from Novozym 51003 from *Myceliophthora thermophila* (LacMT) were obtained as powdered solid. Stock solutions were prepared by dissolving 0.02 g in 2 mL phosphate-citrate buffer at pH 7 and kept at 4 řC until use.

4.3 Preparation of Polymeric Materials

4.3.1 Hexflow® Resin Transfer Mold 6 Synthesis

Hexflow® (Hexcel, Stamford, US) resin transfer mold 6 resin (RTM6) is a commercially available epoxy resin that is extensively used in the aerospace sector as a matrix material for carbon-fiber reinforced polymers (CFRPs). RTM6 utilizes *N*,*N*,*N*',*N*'-tetraglycidyl-4,4'-methylenebisbenzenamine (TGMDA) as an epoxy monomer, while 4,4'-methylenebis(2,6-diethylaniline) (MDEA) and 4,4'-methylenebis(2-isopropyl-6-methylaniline) (M-MIPA) are used as hardeners. TGMDA was heated to 100 řC in an oil bath to reduce its viscosity. Then, TGMDA was mixed with MDEA and M-MIPA in a mass ratio of 10:7:3. The mixture was stirred at 100 řC until all components were melted and fully homogenized. The epoxy resin was poured into a Teflon®-coated, disc-shaped mold and placed in an UN30 oven (Memmert GmbH + Co. KG., Schwabach, Germany). For the first curing step, the oven was heated from room temperature to 120 řC at a heating rate of 20 řC · min^{-1} (see Table 4.2). The temperature was maintained for 1 h. The second curing step was conducted at 180 řC for 2 h, following a ramp of 20 řC · min^{-1}.

Table 4.2 Curing profile for Hexflow® RTM6.

Temperature [řC]	**Rate [řC·min^{-1}]**	**Hold [min]**
20		
120	20	60
180	20	120

4.3.2 Milling methods for Hexflow® RTM6

To obtain fine particulate material for degradation studies, Hexflow® RTM6 was milled using three different techniques. Initial coarse fragmentation was performed using a Retsch ZM200 centrifugal mill (Retsch GmbH, Haan, Germany) equipped with a 250 ţm or 500 ţm sieve. RTM6 particles were pre-cooled in liquid nitrogen to improve brittleness and milling efficiency. For further particle size reduction, samples from the centrifugal mill (from 250 ţm sieve fraction) were subjected to a Retsch S1 planetary ball milling (Retsch GmbH, Haan, Germany) using an agate milling bucket loaded with three agate balls. In the standard ball mill protocol, 0.2 g of material was milled in three intervals of 10 min at 100% motor speed. To maintain cryogenic conditions the milling bucket was pre-cooled and filled with dry ice up to the brim before each interval. Prior to analysis and application of the material in degradation experiments, the particles were dried in a vacuum oven (VTR 5022, Heraeus, Hanau, Germany) at $1{\cdot}10^{-3}$ mbar and 40 řC for 48 h. The particles were kept in a sealed tube and in the absence of sunlight.

4.4 Solids Analysis and Characterization

4.4.1 Particle Size Distribution Determination

Particle size distributions of all milled fractions were measured in suspension using a Mastersizer 3000 (Malvern Panalytical, Malvern, UK) at the Institute of Solids Process Engineering and Particle Technology at Hamburg University of Technology. Each measurement consisted of six cycles of 20 s and a drop of Tween 20 was used to improve suspendability of the particles. Due to the irregular and amorphous nature of the particles, the Fraunhofer approximation was used for particle size calculation.

4.4.2 Thermal Analysis

The characterization of the in-house produced epoxy was done by Airbus Defence and Space GmbH (Taufkirchen, Germany). Thermogravimetric analysis (TGA) was performed using a TGA Q5000 (TA Instruments, New Castle, US) under nitrogen atmosphere. The temperature program ranged from room temperature to 1000 řC with a constant heating rate of $10\,\mathrm{K} \cdot \mathrm{min}^{-1}$. Weight loss was recorded as a function of temperature and the corresponding first derivative of weight ($\% \cdot \mathrm{řC}^{-1}$) was calculated using Origin 2024b (OriginLab Corporation, Northampton, US). Modulated differential scanning calorimetry (MDSC) was performed using a DSC Q2000 (TA Instruments, New

Castle, US) with hermetically sealed aluminum pans. The measurements were conducted under nitrogen atmosphere. The temperature program ranged from 0 řC to 320 řC with an underlying heating rate of 5 K · min^{-1}. A temperature modulation of 0.5 K amplitude and 60 s period was applied. Reversing and non-reversing heat flow signals were evaluated separately.

Thermogravimetric analysis of incubated epoxy samples was carried out by the Institute of Polymer Composites at the Hamburg University of Technology using a TGA/DSC 1 STARe system (Mettler Toledo, Columbus, US). The measurement parameters were identical to the acquisitions carried out by Airbus as described above.

The reactivity of biobased epoxidized linseed oil (ELO) toward citric acid as a biobased curing agent was investigated using differential scanning calorimetry (DSC). Measurements were performed by the Institute of Polymer Composites at the Hamburg University of Technology on a DSC 204 F1 Phoenix (NETZSCH, Selb, Germany) using open aluminum crucibles. The temperature program ranged from 20 řC to 280 řC with a constant heating rate of 10 K · min^{-1}. Analyses were conducted under nitrogen atmosphere, and data were recorded in exothermic-up mode. For sample preparation, citric acid was ground and mixed with ELO in the appropriate ratio using a SpeedMixer DAC 150.1 FVZ (Hauschild SpeedMixer Inc, Hamm, Germany) at 3500 rpm for 3 min. For ELO from Hobum (Epoxy equivalent weight (EEW): 177 g · mol^{-1}), a mass ratio of 100:27.1 (ELO:citric acid) was used. For internally synthesized ELO (EEW: 224 g · mol^{-1}), the mass ratio was 100:21.41.

4.4.3 Elemental Analysis

The elemental analysis of carbon, hydrogen, nitrogen and oxygen in RTM6 samples was conducted by the central laboratory of the Hamburg University of Technology using a Vario Macro Cube by Elementar (Langenselbold, Germany) in duplicate.

4.4.4 *Offline* Attenuated Total Reflection Fourier-Transform Infrared Spectroscopy

Spectra were recorded using attenuated total reflection fourier-transform infrared spectroscopy (ATR-FTIR) (Vertex 70, Bruker, Billerica, USA). Dried samples were scanned 50 times in the range of 650 cm^{-1} to 4000 cm^{-1} at a resolution of 2 cm^{-1}. Spectral data

were processed using OPUS 8.5 software (Bruker), including baseline correction and normalization. Unless otherwise stated, all samples were pre-dried at 40 řC and 1×10^{-3} mbar for 48 h in a vacuum oven (VTR 5022, Heraeus, Hanau, Germany) to eliminate residual moisture prior to analysis. To evaluate the oxidative modification of the epoxy material, the carbonyl index (CI) was calculated from the fourier-transform infrared spectroscopy (FTIR) spectra [164]. For this purpose, the area under the carbonyl band (integration range: 1530 cm^{-1} to 1800 cm^{-1}) was divided by the area under the methylene reference band (integration range: 1485 cm^{-1} to 1530 cm^{-1}) according to Equation 2. Spectra were recorded in triplicate, baseline-corrected and normalized (min-max), then averaged prior to integration.

$$\mathrm{CI}\,[-] = \frac{\text{Peak area}_{\text{Carbonyl}}}{\text{Peak area}_{\text{Methylene}}} = \frac{\text{Peak area}_{1530-1800}}{\text{Peak area}_{1485-1530}} \tag{2}$$

4.5 ABTS Activity Assay

The 2,2'-azino-bis(3-ethylbenzothiazoline-6)-sulfonic acid (ABTS) assay is one of the most commonly used enzyme activity assays in high-throughput screening of oxidative enzymes such as peroxidases, oxidases and laccases. ABTS is used as a substrate and acts as a redox indicator. When oxidized, ABTS forms a blue-green radical ion which is spectroscopically detectable at 420 nm. The activity assay can be performed within a large temperature and pH range, as the radical ion shows high stability. The ABTS assay is applicable to aqueous surrounding as well as organic solvents, due to the high solubility of the substrate in polar and non-polar media. In the present work, a microplate ultraviolet-visible light (UV/VIS) spectrometer was used for measuring the laccase activity. For aqueous solutions, the assay was performed - unless otherwise stated - at 30 řC, pH 4 and at an ABTS concentration of 1 mmol $\cdot$ L^{-1} over a time course of 3 min. For investigating the effect of deep eutectic solvent (DES) on the ABTS activity, the enzyme was pre-incubated in the respective DES to allow the enzyme to adjust to the DES environment according to Toledo et al. (2019) [126] (see Table 4.3).

In the present work the laccase stock was pre-incubated 10 min at room temperature in the DES prior to the start of the measurement. For reference measurements the DES was replaced by a 0.1 mol $\cdot$ L^{-1} citrate-phosphate buffer at pH 4.

After incubation, the assay was performed by pipetting 5 ţL of the sample into a 96-well plate and adding 195 ţL of 1 mmol $\cdot$ L^{-1} ABTS solution. The change in absorption at 420 nm was measured at 30 řC for 3 min.

Table 4.3 Sample preparation for the ABTS assay.

Parameter	**Value**
DES Volume	45 ţL
Incubation temperature	25 řC
Incubation time	10 min
Sample Volume	50 ţL
Volume LacF Stock Solution	5 ţL

The measurements were performed at large substrate excess so that the change in substrate concentration does not influence the reaction rate.

For the calculation of the volumetric activity from the spectral data, the change in absorption was transferred into a concentration change using the LambertBeer law and the extinction coefficient ε_λ of ABTS at 420 nm [165].

$$\mathrm{E} = \mathrm{c} \cdot \varepsilon_\lambda \cdot \mathrm{d} \tag{3}$$

With E being the measured absorption, c the concentration of ABTS and d the distance of the light path through the sample. When a change over time is measured the measured absorption and the concentration can be expressed dependent on time:

$$\Delta\mathrm{E}\left[\frac{1}{\mathrm{min}}\right] = \mathrm{v}\left[\frac{\text{ţmol}}{\mathrm{mL}\cdot\mathrm{min}}\right] \cdot \varepsilon_\lambda\left[\frac{1}{\mathrm{M}\cdot\mathrm{cm}}\right] \cdot \mathrm{d}\,[\mathrm{cm}] \tag{4}$$

Equation 4 can be rearranged and simplified to determine the change in concentration which equals the reaction rate:

$$\mathrm{v}\left[\frac{\text{ţmol}}{\mathrm{mL}\cdot\mathrm{min}}\right] = \frac{\Delta\mathrm{E}\left[\frac{1}{\mathrm{min}}\right]}{\varepsilon_\lambda\left[\frac{1}{\mathrm{M}\cdot\mathrm{cm}}\right]\cdot\mathrm{d}\,[\mathrm{cm}]} = \frac{\Delta\mathrm{E}\left[\frac{1}{\mathrm{min}}\right]}{\varepsilon_\lambda\left[\frac{1000\ \mathrm{cm}^3}{\mathrm{mol}\cdot\mathrm{cm}}\right]\cdot\mathrm{d}\,[\mathrm{cm}]} = \frac{\Delta\mathrm{E}\left[\frac{1}{\mathrm{min}}\right]}{\varepsilon_\lambda\left[\frac{\mathrm{cm}^2}{1000\ \mathrm{mol}}\right]\cdot\mathrm{d}\,[\mathrm{cm}]} \tag{5}$$

The extinction coefficient of ABTS at 420 nm equals to 36 000 L · mol^{-1} · cm^{-1} and when the plate well is filled with 200 ţL the light path has a distance of 0.7065 cm. Additionally, the LacF stock solution was diluted by a factor 10 for the sample incubation and then by a factor of 40 due to the mixing with the ABTS substrate solution. Inserting the extinction coefficient, the distance and the dilution factor in Equation 5 leads to the final equation used for determining the change in substrate concentration which now equals the reaction rate of the undiluted stock solution:

$$v\left[\frac{\text{ţmol}}{\text{mL}\cdot\text{min}}\right] = \frac{40\cdot 10\cdot \Delta E\left[\frac{1}{\text{min}}\right]}{36000\left[\frac{\text{cm}^2}{1000\,\text{mol}}\right]\cdot 0.7065\ [\text{cm}]} = \frac{400\cdot\Delta E}{36\cdot 0.7065}\left[\frac{\text{ţmol}}{\text{mL}\cdot\text{min}}\right] \quad (6)$$

In the present work the volumetric enzymatic activity is defined as the production of $1\,\text{ţmol}\ \cdot\ \text{mL}^{-1}\ \cdot\ \text{min}^{-1}$ of oxidation product.

4.6 Oxidation of Surrogate Substrates *N,N*-Bis(2-hydroxypropyl)-*p*-toluidine and Michlers base

High throughput screening methods require water-soluble substrates, thus cured resin cannot be used as substrate due to its insolubility. *N*,*N*-bis(2-hydroxypropyl)-*p*-toluidine (NNBT) and Michlers base (MB) were selected as model substrates for Hexflow® RTM6 to study their oxidation via fungal laccases. NNBT was selected because it exhibits both amide and hydroxyl functionalities, which are frequently present in epoxy resin curing agents and can undergo laccase-mediated oxidation. MB, on the other hand, contains aromatic amino functionalities, is highly conjugated, and known as a dye precursor and model substrate for studies on electron-rich aromatic amines. Enzymatic reactions with the surrogate compounds were conducted at a maximum concentration of 5 mmol NNBT or 4 mmol MB in 5% (v/v) dimethyl sulfoxide (DMSO) in buffer or DES, respectively.
The reaction conditions and quantification methods for buffered reactions are given in Section 4.7 and for reactions in DES in Section 4.10.

4.7 Investigation of Laccases for Surrogate Oxidation in Aqueous Buffer

4.7.1 Quantification of Surrogate Compounds via Gas Chromatography

Surrogate compound quantification was done using gas chromatography coupled flame ionization detector (GC-FID) measurements on a HP5 column installed in a GC5975 system (Agilent Technologies, Santa Clara, US). Preceding the gas chromatography (GC) analysis, samples were prepared as follows: 200 ţL of reaction supernatant were inhibited by addition of 5 ţL of 0.05% NaN_3. For adjustment of the pH value of the NNBT samples, 5 ţL of 5 M NaOH were added. An equivolumetric amount of GC-grade ethyl acetate (EtOAc) was used to extract the model compounds from the aqueous into the organic phase by vigorously vortexing the tube for 30 s. The phases were left to separate and the

upper, organic phase was withdrawn using a micropipette. The sample was transferred to a GC vial an subjected to GC-FID measurement according to Table 4.4.

Table 4.4 Parameters of the GC-FID methods for determination of surrogate concentrations.

Parameter	**Value for NNBT**	**Value for MB**
Injection Volume [ţL]	1	1
Column Type	HP-5, Agilent Technologies	HP-5, Agilent Technologies
Initial Column Temperature [řC]	120	200
Heating Profile [-]	10 řC · min^{-1} to 170 řC	10 řC · min^{-1} to 280 řC
	5 min hold	1 min hold
	5 řC · min^{-1} to 190 řC	40 řC · min^{-1} to 325 řC
	40 řC · min^{-1} to 280 řC	
	0.5 min hold	
Total Flow [mL · min^{-1}]	34	33
Septum Purge Flow [mL · min^{-1}]	3	2
Mode [-]	Split	Split
Split Ratio [-]	30:1 (1-5 mmol · L^{-1})	30:1
	10:1 (0.1-1mmol · L^{-1})	
Flow [mL · min^{-1}]	1	1
Average Velocity [cm · s^{-1}]	35.67	40.51

Quantification of NNBT was accomplished through external calibration over a concentration range of 0.1 mmol · L^{-1} to 1 mmol · L^{-1} (10:1 split) and 1 mmol · L^{-1} to 5 mmol · L^{-1} (30:1) split with standards prepared in EtOAc. The calibration for MB was prepared over a range from 0.1 mmol · L^{-1} to 4 mmol · L^{-1}. Typical retention times for NNBT and MB were 14.6 min and 6.1 min, conversely. The corresponding calibration plots are depicted in Figure A.2.

4.7.2 Laccase Activity Screening

To evaluate the suitability of different laccases for oxidative degradation of the epoxy model compound NNBT according to Dolz et al. (2022) [84], the conversion of the surrogate was assessed in buffered aqueous solution [166]. Reactions were carried out in 10 mL volume in 25 mL double-jacketed thermovessels containing 5 mmol · L^{-1} NNBT,

prepared from a 100 mmol · L^{-1} stock solution in DMSO due to its limited aqueous solubility. Each reaction was adjusted to a final laccase activity of 0.1 U · mL^{-1}, with volumes adapted according to the specific activity of the respective enzyme preparation. The remaining volume was filled with 0.1 mol · L^{-1} citrate-phosphate buffer at pH 4.5. Reactions were performed in duplicate at 30 řC with continuous stirring at 750 rpm using magnetic stir bars. The reaction was initiated by addition of the laccase solution, and aliquots were withdrawn after 0, 5, 10, 20, 40, 60, 80, 100, 120, 150, and 180 min for subsequent analysis according to Section 4.7.1. Kinetic modeling was performed using the `scipy.optimize.curve_fit` function from the NumPy library (v2.0, Python v3.11.2, Listing 1) to determine apparent first-order rate constants according to Equation 7:

$$c_{\mathrm{NNBT}} = c_{\mathrm{NNBT,0}} \cdot e^{-kt} \tag{7}$$

4.7.3 Redox Mediator Screening

Following identification of a suitable laccase, the influence of various redox mediators on the oxidation of NNBT was investigated. The experimental setup was analogous to the conditions described in Section 4.7, with the additional inclusion of 1.5 mmol · L^{-1} mediator as proposed by Obleser et al. (2022) [166]. The following mediators were tested: ferulic acid (FA), caffeic acid (CA), violuric acid (VA), ABTS, and 2,2,6,6-tetramethylpiperidinyloxyl (TEMPO). All other parameters, including temperature, buffer conditions, enzyme loading, and sampling intervals, were kept identical to the non-mediated reactions (Section 4.7.2).

4.7.4 Electrochemical Characterization of Mediators

Cyclic voltammetry (CV) was employed to investigate the redox behavior of selected mediators under near-reaction conditions. All measurements were performed in 0.1 mol · L^{-1} citrate-phosphate buffer (pH 4) using a Gamry Interface 1010 potentiostat (Gamry Instruments, Warminster, US) operated in potentiostatic mode. The electrochemical cell (Figure 4.1) consisted of a 99.95 % platinum plate (1 mm thickness, 9 mm^2 surface area) as working electrode, a platinum wire counter electrode, and a Ag/AgCl reference electrode (RE-1B, ALS Japan, Tokyo, Japan) [167].

Prior to each measurement, the system was sparged with nitrogen gas for 5 min to remove dissolved oxygen. Mediator solutions were prepared at a concentration of

10 mmol · L^{-1}. Voltammograms were recorded over a scan range of −0.3 V to 1.3 V vs. Ag/AgCl at a scan rate of 100 mV · s^{-1} and step size of 2 mV.

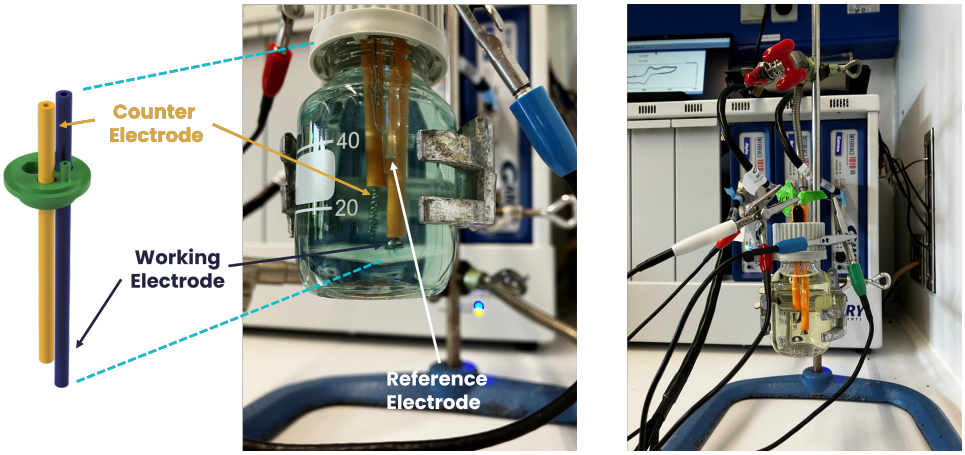

Figure 4.1 Custom 3D-printed electrochemical cell setup for circular voltammetry measurements.

The electrode area was fixed at 0.09 cm^2, and each measurement consisted of 150 cycles. For the evaluation of redox potentials, the first three recorded voltammograms were averaged, and the half-wave potential $E_{1/2}$ was calculated as the arithmetic mean of the anodic and cathodic peak potentials according to Equation 8:

$$E_{1/2} = \frac{E_{P,anode} + E_{P,cathode}}{2} \tag{8}$$

To enable comparison with literature data, the measured potentials were converted to the normal hydrogen electrode (NHE) scale using the following relationship:

$$E_{vs.\,NHE} = E_{measured} + E_{Ag/AgCl\,vs.\,NHE}, \quad E_{Ag/AgCl\,vs.\,NHE} = 0.197\,V \tag{9}$$

4.7.5 Investigation of Reaction Conditions: pH, Temperature, Mediator Ratio

Systematic variation of reaction parameters was performed to evaluate the influence of pH, temperature, and mediator-to-substrate ratio on the oxidation of NNBT by laccase from *Funalia trogii* (LacF). All reactions were carried out in sealed 2 mL glass vials with a liquid volume of 1 mL. The enzyme activity was kept constant at 0.1 U · mL^{-1} for all reactions. Reaction mixtures were shaken at 750 rpm using a thermomixer, and endpoint samples were taken after 30 min for GC analysis (Section 4.7.1). Optimization was conducted sequentially: first, the pH was varied from 2.2 to 8 in 0.1 mol · L^{-1} citrate-phosphate buffer, identifying pH 4 as optimal. This pH was then used to evaluate temperature effects

between 20 řC and 80 řC, yielding an optimum at 50 řC. Finally, the effect of the mediator-to-substrate ratio was assessed by varying TEMPO concentration from 0.1 mmol · L^{-1} to 20 mmol · L^{-1}, with 10 mmol · L^{-1} determined as the optimal concentration under the previously identified conditions.

4.7.6 Investigation of Temperature Stability of Laccase

The thermal stability of LacF was investigated by incubating the enzyme in the presence of 10 mmol · L^{-1} TEMPO in 0.1 mol · L^{-1} citrate-phosphate buffer at pH 4. The solutions were set up in sealed 2 mL glass vials containing a volume of 1 mL with an initial laccase activity of 0.6 U · mL^{-1} to increase the measurable range of activity loss. Incubations were carried out at defined temperatures between 25 řC and 80 řC with orbital shaking at 750 rpm. At defined time points over a total period of 24 h, aliquots were withdrawn and stored at 4 řC until analysis. Residual enzymatic activity was determined using the ABTS activity assay as described in Section 4.5. Activity data were transformed to a logarithmic scale, and the deactivation kinetics were modeled assuming first-order decay. The apparent half-life time $t_{1/2}$ of the enzyme under the respective incubation conditions was calculated using the following relationship:

$$t_{1/2} = \frac{\ln(2)}{k} \tag{10}$$

where k is the first-order deactivation rate constant obtained by exponential regression of the residual activity over time.

4.7.7 Aeration of Surrogate Oxidation Reactions with Laccase

To assess potential oxygen limitation in surrogate oxidation reactions catalyzed by LacF, selected model reactions were carried out with and without aeration using pressurized air. The overall experimental setup and reaction conditions followed the procedure described in Section 4.7.2. Dissolved oxygen concentrations were monitored in real time using a PSt3-DP dipping probe connected to a Fibox 4 fiber-optic oxygen meter (PreSens Precision Sensing GmbH, Regensburg, Germany). A two-point calibration was carried out under the corresponding process conditions of the experiment at 0 % [a.s.] and 100 % [a.s.] by sparging with nitrogen and compressed air, respectively. For aerated conditions, the membrane of the screw-cap lid of the glass reactor was pierced with two stainless steel needles. One served as a gas outlet, and the second was used for sparging with pressurized air (Sterican 21G, 0.8 × 120 mm; B. Braun Melsungen AG, Melsungen, Germany). The

required gas flow rate was set prior to each experiment using a flowmeter (Wagner Mess- und Regeltechnik GmbH, Offenbach am Main, Germany). Reactions were performed at room temperature with continuous stirring at 750 rpm. Samples were taken at defined intervals and analyzed according to Section 4.7.1 to quantify substrate conversion.

4.8 GC-MS Analysis of Surrogate Oxidation Products

For gas chromatography coupled mass spectrometry (GC-MS) (GC7890A-MS5975C, Agilent Technologies, Santa Clara, US) analysis, sample preparation followed a protocol consistent with the NNBT quantification, with the exception of supersaturating the aqueous phase with Na_2SO_4 prior to extraction. The inlet temperature was set at 300 řC and a 1 ţL sample volume was injected in splittless mode. The carrier gas helium was set to a rate of 1 ţL $\cdot$ min^{-1}. The temperature ramp protocol involved a gradual increase from 50 to 325 řC at a rate of 5 řC $\cdot$ min^{-1}, with a hold at 325 řC for 5 min. The transfer line maintained a temperature of 250 řC while the electron ionization (EI) source was configured at 230 řC with an ionization voltage of 70 eV. The quadrupole temperature was set to 150 řC throughout the measurement. Mass spectra were acquired in the range of 50-800 $m{\cdot}z^{-1}$ after a solvent delay of 3 min. Data interpretation was conducted using the NIST 23, MassBank, and MoNa libraries through the NIST Search Program V2.3. Validation of oxidation product fragmentation patterns was carried out using CFM-ID 4.0, ensuring the accuracy of compound identification. Additionally, manual mass spec scission was performed using ChemSketch (ACD/Labs, Toronto, CA), providing further insights into the molecular structures present in the samples.

4.9 Molecular Docking Simulations with Laccase from *Funalia trogii*

Molecular docking was performed using AutoDockTools 1.5.7 and AutoDock4 [168]. The crystal structure of LacF was retrieved from the Protein Data Bank (PDB ID: 2HRH [169]), and the binding site was defined based on the coordinates reported by Pardo and Camarero (2015) [170]. The grid box was placed around the active site of the enzyme, covering residues V162, T164, D205, S264, F331, F336, and P390. Receptor preparation was performed using AutoDockTools 1.5.6 by removing all crystallographic water molecules, adding polar hydrogens, and assigning Kollman charges. Atomic force field parameters for the four copper centers in the laccase were added manually. Ligands were drawn

in ChemSketch and processed by assigning Gasteiger charges and defining all rotatable bonds. A grid box was centered on the active site using AutoGrid 4.0. Docking was executed in AutoDock 4.0 using the Lamarckian Genetic Algorithm, performing 20 runs per ligand with default settings and the maximum number of evaluations enabled.

4.10 Characterization of Deep Eutectic Solvents for Laccase-driven Oxidation of RTM6 Surrogates

4.10.1 COSMO-RS Simulation for Deep Eutectic Solvent Screening

To identify DES systems with enhanced affinity towards epoxy resin substructures, the conductor-like screening model for real solvents (COSMO-RS) was employed. All COSMO-RS calculations were carried out by Dr. Filipe H. B. Sosa (University of Aveiro, Portugal) using a two-step quantum-chemical procedure.

In the first step, molecular geometries of all hydrogen bond acceptor (HBA) and hydrogen bond donor (HBD) as well as the epoxy query molecule were optimized with Turbomole (TmoleX19, Version 4.5) applying the COSMO-BP-TZVP level of theory, which includes a def-TZVP basis set and density-functional treatment with the B-P86 functional and the COSMO solvation model. The resulting COSMO files provided surface polarization charge densities (σ) for subsequent thermodynamic evaluation.

In the second step, COSMOtherm (Version 21.0) with the BP_TZVP_21.ctd parameterization was used to calculate the activity coefficients at infinite dilution ($\ln \gamma_\infty$) of the epoxy model compound in each equimolar HBA-HBD combination at 25 řC. The epoxy query molecule (Figure 4.2) represented the repeating-unit substructure of the RTM6 epoxy resin and served as a simplified molecular proxy for the cured network.

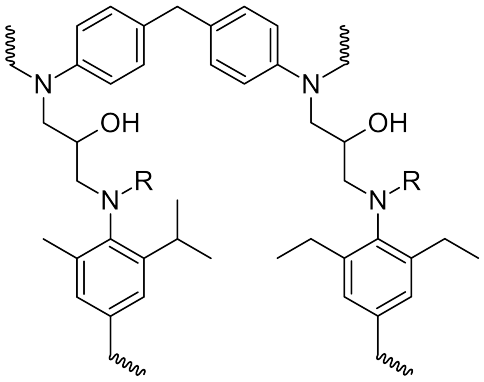

Figure 4.2 Model compound based on RTM6 epoxy resin repeating unit used in COSMO-RS solubility simulation.

A comprehensive library comprising 162 HBA and 187 HBD was screened, yielding 30 284 possible equimolar mixtures. Lower $\ln \gamma_\infty$ values correspond to stronger solute–solvent interactions and thus higher predicted solubility of the epoxy substructure in the respective DES.

4.10.2 Surrogate Quantification in DES and their Aqueous Mixtures

To enable the activity screening of LacF towards epoxy model compounds in different DES, a microplate UV/VIS spectrometer had to be employed as the formerly used liquid-liquid extraction for GC-FID yielded non-reproducible data when DES and aqueous mixtures thereof were extracted. For spectroscopic measurement, the extinction coefficients of either the model substrates or their oxidized products must be known in order to correlate absorbance rates with reaction rates. Previous investigations in purely aqueous buffers had shown that LacF oxidizes NNBT and MB, leading to a color change, whereas the substrate solutions exhibit no visible color. Therefore, the extinction coefficients of the oxidation products were determined in the present study. LacF was employed to oxidize the model substrates, yielding the respective products. The experimental parameters are summarized in Table 4.5. At the end of the reaction, the enzyme was deactivated by adding 5 ţL of a 0.05 % (v/v) NaN_3 solution.

Table 4.5 Experimental parameters of the first batch reaction with model substrates.

Parameter	**NNBT**	**MB**
pH [–]	4	4
Reaction time [min]	30	30
Reaction volume [mL]	0.2	0.2
Substrate concentration [mmol·L^{-1}]	5	2
Temperature [řC]	50	20
Enzyme activity in test [U · L^{-1}]	1.50	1.50

To determine the absorption wavelengths of the oxidation products, UV/VIS spectra of the unreacted model substrates and their oxidized counterparts were recorded in a range from 240 nm to 940 nm. Additionally, spectra of LacF and the applied DES were obtained to identify potential overlapping absorbance maxima. Absorbance peaks attributable to product formation were identified by subtracting the spectra of the unreacted substrates, which were used as blanks. Subsequently, an additional batch experiment was conducted

in which LacF catalyzed the oxidation of the model substrates. Samples were taken at defined time points and analyzed in duplicates.

To stop the reaction, 10 µL of a 0.05 % (v/v) NaN_3 solution was added to every 100 µL of sample. Quantification of the model substrates was carried out via GC-FID (Section 4.7.1), while absorbance at the previously identified wavelength was measured in parallel. Absorbance was recorded immediately after sampling for 1 min, whereas samples for GC-FID analysis were collected until the end of the experiment. It was assumed that all depleted substrate was quantitatively converted into a single product. Thus, the product concentration was calculated as the difference between the initial substrate concentration and the concentration measured at each time point. Both concentration and absorbance were plotted against time to derive reaction and absorbance rates. The extinction coefficients of the model substrates were determined by rearranging Equation 4:

$$\varepsilon_\lambda \left[\frac{1}{\mathrm{M}\cdot\mathrm{cm}}\right] = \frac{\Delta \mathrm{E}\left[\frac{1}{\mathrm{min}}\right]}{\mathrm{v}\left[\frac{\mu\mathrm{mol}}{\mathrm{mL}\cdot\mathrm{min}}\right]\cdot 10^{-3}\cdot \mathrm{d}\,[\mathrm{cm}]} \tag{11}$$

From Equation 11 it can be seen that the extinction coefficient is determined by dividing the rate in absorption by the reaction rate and the distance of the light path. The corresponding results from the calibration are depicted in Table 4.6.

Table 4.6 Results from the determination of the extinction coefficients of oxidation products of NNBT and MB.

Parameter	**NNBT**	**MB**
E [min^{-1}]	0.023	0.039
v [$\mu\mathrm{mol}\cdot\mathrm{mL}^{-1}\cdot\mathrm{min}^{-1}$]	0.034	0.015
ε_λ [$\mathrm{M}^{-1}\cdot\mathrm{cm}^{-1}$]	0.96	3.68

4.10.3 Conductivity Measurements

The electric conductivity is an intrinsic property of a charge-carrying material to accommodate the movement of an electrical charge which is measured in $\mathrm{S}\cdot\mathrm{m}^{-1}$. In liquids, charges move via ions carrying an electrical charge. Thus, the conductivity of electrolytes depends on the concentration of the ions in the solution and the temperature. According to Ünlü et al. (2023) [121], conductivity measurements can be used as a tool to gather information about the integrity of the eutectic structure of DESs when water is used as

a co-solvent. Therefore, electrical conductivity measurements of DESs were monitored in dependence of the water concentration in the present work.

4.10.4 Contact Angle Measurements

To evaluate the wettability of the RTM6 surface, contact angle measurements were performed. The goniometer experimental setup at the Institute of Solids Process Engineering and Particle Technology at Hamburg University of Technology consisted of an epoxy disc, placed on an adjustable table, with a water level ensuring a perfectly level measuring surface. An electronic pipette (Multipette E3, Eppendorf SE, Hamburg, Germany) was used as a drop dispenser to maintain high precision and repeatability of drop deposition. The pipette tip was fixed 1 cm above the epoxy surface using a rack. A lamp provided illumination to enhance droplet visibility, and a high-speed camera positioned opposite to the light source recorded the droplet deposition process. The experimental parameters for contact angle measurements are summarized in Table 4.7.

Table 4.7 Experimental parameters for contact angle measurements.

Parameter	**Value**
Dispense Speed	$0.125\,\mathrm{mL} \cdot \mathrm{s}^{-1}$
Dispense Volume	5 ţL
Drop Height	1 cm
Recording Time	120 s to 280 s

To measure the contact angle, a video recording was started while a sample drop was dispensed onto the epoxy disc using the electronic pipette. An image analysis tool automatically determined the contact angle in each recorded frame. All contact angles were measured in triplicates to ensure accuracy and reproducibility.

4.10.5 Maximum Dissolved Oxygen Measurement

The dissolved oxygen (DO) refers to the concentration of unbound oxygen in water, which is usually measured in $\mathrm{mg} \cdot \mathrm{L}^{-1}$ or $\mathrm{mmol} \cdot \mathrm{L}^{-1}$. The maximum DO depends on the atmospheric pressure, temperature and salinity of the water. In general, the maximum DO decreases with increasing temperature and salt concentrations. At 20 řC and atmospheric pressure, water has a maximum DO of $9.1\,\mathrm{mg} \cdot \mathrm{L}^{-1}$, which equals approximately $0.28\,\mathrm{mmol} \cdot \mathrm{L}^{-1}$. Most DES consist of different salts, so it can be expected that the high ion concentration affects the maximum DO of the solvent. As the laccase-catalyzed

oxidation reaction is oxygen-dependent, the maximum DO represents a crucial reaction parameter. Therefore, the maximum DO of DESs with different water concentrations was determined in the present work using a fiber optic oxygen meter. The maximum DO was determined using a pH 4 0.1 mol $\cdot$ L^{-1} citrate-phosphate buffer as a reference. The oxygen meter was calibrated using this reference buffer. A two-point calibration was performed by sparging the buffer with nitrogen to degas all solubilized oxygen and subsequently with pressurized air to reach full absolute saturation. To determine the maximum DO in DESs, the solvents were sparged with pressurized air prior to measurement.

4.10.6 Determination of Kinetic Parameters

In the present work, initial rate measurements at varying substrate concentrations were used as a tool to determine the kinetic parameters of the laccase-catalysed reaction in buffer and DES. To determine the kinetic parameters, initial rate measurements were performed by varying the ABTS concentration in the range 0.005 mmol to 0.5 mmol while ensuring that the substrate conversion remained below 10 %. The enzymatic activity was measured using the ABTS assay (Section 4.5). The kinetic parameters K_M and V_{max} were determined by employing numerical fitting of the Michaelis–Menten model (Equation 12) to the initial reaction rates in Origin 2024b (OriginLab Corporation, Northampton, US).

$$v = \frac{V_{max}\,[S]}{K_M + [S]} \tag{12}$$

4.10.7 Enzyme Activity at Elevated Temperatures

To investigate the effect of elevated temperature on the activity of LacF in DES, the ABTS assay was performed at 40 řC, 50 řC, 60 řC, 70 řC, and 80 řC. For these measurements, a heated UV/VIS spectrometer was used and the assays were carried out in 1 mL cuvettes. The experimental parameters of the ABTS assay (Section 4.5) were modified to suit the cuvette-based setup (see Table 4.8 and Table 4.9).

Table 4.8 Sample preparation for ABTS assay at different temperatures.

Parameter	**Value**
DES volume	180 ţL
Incubation time	10 min
Sample volume	200 ţL
Volume LacF stock solution	20 ţL

Table 4.9 Experimental parameters of the ABTS assay at different temperatures.

Parameter	Value
ABTS concentration	3 mmol · mL^{-1}
Enzyme activity in test	0.03 U · mL^{-1}
Sample volume	10 µL
Substrate volume	990 µL
Time	1 min
Wavelength	420 nm

Both the pre-incubation of the enzyme and the subsequent absorption measurement were conducted at the respective assay temperature. The change in absorption was recorded over 1 min. To maximize the effect of the DES, the experiments were conducted using 80% (w/v) DES solutions.

The sample preparation and experimental setup resulted in a 1000-fold dilution of the LacF stock solution. The cuvettes had a light path of 1 cm. Considering this, the rate equation used was:

$$v\ [\mu mol \cdot mL^{-1} \cdot min^{-1}] = \frac{1000 \cdot \Delta E\ [\cdot min^{-1}]}{36\ [L \cdot cm^{-1} \cdot mmol^{-1}] \cdot 1\ [cm]} \tag{13}$$

where ΔE is the change in absorption per minute and 36 is the extinction coefficient of oxidized ABTS at 420 nm in L · cm^{-1} · $mmol^{-1}$.

4.11 Enzymatic Incubation with RTM6 Epoxy

4.11.1 Biotransformation in Aqueous Buffer

Enzymatic oxidation of cured RTM6 powder was conducted in a fixed-bed reactor setup to assess oxidative surface modification under continuous flow conditions. The reactor circuit consisted of a 25 mL double-jacketed thermovessel (working volume: 10 mL), which served as the enzyme reservoir and was continuously aerated with pressurized air at 5 vvm using a canula. The reservoir was thermostated to 50 řC. The fluid was circulated through a self-constructed fixed-bed column (4.5 (inner diameter (ID)) × 10 (height) mm packed with 200 mg of RTM6 resin (produced as described in Section 4.3.1). The column was assembled from male and female 1/4 inch to 1/16 inch high-performance liquid chromatography (HPLC) fittings and suspended within a repurposed XK16 column body (Cytiva Europe GmbH, Freiburg im Breisgau, Germany) connected to a separate

external thermostat, also maintained at 50 řC. Circulation was realized using a Knauer Pump 64 (Knauer Wissenschaftliche Geräte GmbH, Berlin, Germany) and PTFE tubing (0.8 (ID) × 1.6 mm (outer diameter (OD))) with a flow rate of 10 mL · min^{-1}. Reactions were carried out over a period of 120 h using 0.1 mol · L^{-1} citrate-phosphate buffer (pH 4) as the reaction medium. The enzyme loading was 1 U · mL^{-1} and 10 mmol · L^{-1} TEMPO was initially added. Enzyme was replenished every 24 h. The negative control was carried out in the absence of enzyme.

4.11.2 Incubation in Deep Eutectic Solvent

For comparison, additional incubations were carried out in DES suspensions under batch conditions. Here, ground RTM6 powder (50 mg) was suspended in 1 mL of a 20 % (w/w) DES solution prepared in 0.1 mol · L^{-1} citrate-phosphate buffer (pH 4), using either choline dihydrogen citrate:xylitol (ChDHC:XYL) or choline dihydrogen citrate:erythritol (ChDHC:ERY) as DES formulations. The suspensions were placed in 2 mL glass vials and incubated at room temperature for 48 h with constant stirring (750 rpm). The enzyme was dosed to a final concentration of 1 U · mL^{-1}. Control reactions without enzyme were performed analogously.

After incubation, the resin was recovered by filtration on cellulose filter paper and washed three times with 50 mL ultrapure water. Samples were dried in a desiccator and subsequently processed according to Section 4.4.4. Analytical characterization of the treated material included ATR-FTIR spectroscopy, TGA (Section 4.4.2), and elemental analysis (Section 4.4.3).

4.12 Chemoenzymatic Epoxidation of Linseed Oil

4.12.1 Biphasic Reaction Setup with Suspended Novozyme® 435 & Acid Selection

To investigate the chemoenzymatic epoxidation of linseed oil (LO) using Novozyme® 435 and an acid co-reactant, the molar content of unsaturated bonds per g_{LO} had to be calculated as reference for the amounts of reactants needed. For this, a representative composition of the free fatty acids (FFAs) in LO from Popa et al. (2012) [139] (Table 4.10) was used to calculate the number of unsaturated bonds per $mmol_{FFA}$.

Table 4.10 Fatty acid composition of linseed oil and corresponding amount of unsaturated bonds according to Popa et al. (2012) [139].

Fatty acid	**Molecular weight [g·mol^{-1}]**	**Content [%]**	**Unsaturated bonds per molecule [-]**	**FFA:Oil [g·g$_{oil}^{-1}$]**	**Unsat. bonds per mmol FFA [mmol^{-1}]**
C16:0	256.42	6.58	0	0.07	0
C18:0	284.50	4.43	0	0.04	0
C18:1	282.50	18.51	1	0.19	0.67
C18:2	280.40	17.25	2	0.17	1.22
C18:3	278.40	53.21	3	0.53	5.70

Following this, the average molecular weight of FFAs was calculated according to Equation 14, utilizing the compositional profile from Table 4.10:

$$\text{Avg. MW}_{\text{FFA, LO}} = \sum \text{MW}_{\text{FFA, i}} \cdot \text{w}_\text{i} \left[\text{g} \cdot \text{mol}^{-1}\right] \tag{14}$$

Using this approach, the molar amount of unsaturated bonds per g_{lo} was calculated as a basis for stoichiometric planning of the epoxidation reaction. The term $MW_{FFA,\,i}$ denotes the molecular weight of each fatty acid, and w_i its mass fraction in the oil. To estimate the molecular weight of a representative triglyceride, Equation 15 was applied. It assumes one glycerol backbone ($92\,\text{g} \cdot \text{mol}^{-1}$) esterified with three fatty acid residues, each losing one molecule of water ($18\,\text{g} \cdot \text{mol}^{-1}$) during esterification.

$$\text{Avg. MW}_{\text{triglyceride}} = 92 + 3 \cdot (\text{Avg. MW}_{\text{FFA, LO}} - 18) \left[\text{g} \cdot \text{mol}^{-1}\right] \tag{15}$$

The average number of unsaturated bonds per triglyceride molecule, $\text{Avg. Nr.}_{\text{unsat. bonds, triglyceride}}$, was then determined from the weighted sum of double bonds in each FFA multiplied by three, as shown in Equation 16:

$$\text{Avg. Nr.}_{\text{unsat. bonds, triglyceride}} = 3 \cdot \sum \text{w}_\text{i} \cdot \text{Nr.}_{\text{unsat. bonds,i}} \left[-\right] \tag{16}$$

Finally, the number of unsaturated double bonds per g_{lo} was calculated using Equation 17, which normalizes the value to a gravimetric basis and converts to $\text{mmol} \cdot \text{g}^{-1}$:

$$\text{Nr.}_{\text{unsat. bonds per g LO}} = \frac{\text{Avg. Nr.}_{\text{unsat. bonds, triglyceride}}}{\text{Avg. MW}_{\text{triglyceride}}} \cdot \frac{1000\ \text{mmol}}{\text{mol}} \left[\text{mmol} \cdot \text{g}_{\text{LO}}^{-1}\right] \tag{17}$$

This value was used to determine the required equivalents of hydrogen peroxide and acid for epoxidation reactions under biphasic conditions with suspended Novozyme® 435. All stoichiometric calculations were based on the assumption that each double bond could be epoxidized.
Reactions were carried out in a 250 mL double-jacketed reaction vessel utilizing an overhead magnetic stirrer at 750 rpm. For initial experiments, an enzyme loading of 6.7 mg:C=C was used as proposed by Orellana-Coca et al. (2007) [145]. Furthermore, the acid:C=C and H_2O_2:C=C ratios were set to 0.5 and 1, respectively [140, 171].

For small scale reactions in the thermovessel, 10 g of LO were used and diluted with 50 mL synthesis-grade toluene prior to transferring it into the pre-heated reactor at 50 řC. Afterwards, the acid (stearic acid (SA) or butyric acid (BA)) and Novozyme® 435 were added to the vessel. The reactions were started by addition of the corresponding amount of H_2O_2 from a 35% (v/v) aqueous solution through a dropping funnel. Throughout the progress of the reaction, samples were taken and analyzed for EEW and acid number (AN) according to Section 4.13.1 and 4.13.2, respectively.

Inline FTIR measurements were conducted as described in Section 4.12.4. After the reaction, the catalyst particles were separated using a 125 ţm mesh filter and the biphasic supernatant was kept at 4 řC for phase separation and further processing.

4.12.2 DoE-based Optimization of Chemoenzymatic Epoxidation of Linseed Oil

Design of experiments (DoE) was employed to optimize the chemoenzymatic epoxidation of LO with respect to equivalent ratios of hydrogen peroxide and acid, as well as enzyme loading. A Box-Behnken design was constructed using DesignExpert 12® software (Stat-Ease, Minneapolis, US), covering three numeric factors: H_2O_2:C=C (0.53), BA:C=C (0.53), and enzyme loading (1-6 % ($w \cdot w_{oil}^{-1}$)). Experimental conditions were randomized to avoid systematic bias and are summarized in Table 4.11. The reactions were carried out as described in Section 4.12.1, but with a halved amount of LO and toluene of 5 g and 25 mL, respectively, to allow for parallelization in smaller reaction vessels and to decrease the amount of required catalyst. The reactions were stopped after 300 min reaction time and analyzed for EEW and AN according to Section 4.13.1 and 4.13.2, respectively. Data analysis was performed by fitting a quadratic model and evaluating significance using analysis of variance (ANOVA).

Table 4.11 Box-Behnken design matrix for the DoE-based optimization of chemoenzymatic epoxidation.

Std[a]	Run	Enzyme loading [% ($w \cdot w_{oil}^{-1}$)]	H_2O_2:C=C [-]	BA:C=C [-]
10	1	3.5	3.00	0.50
5	2	1.0	1.75	0.50
3	3	1.0	3.00	1.75
2	4	6.0	0.50	1.75
11	5	3.5	0.50	3.00
17	6	3.5	1.75	1.75
8	7	6.0	1.75	3.00
15	8	3.5	1.75	1.75
9	9	3.5	0.50	0.50
7	10	1.0	1.75	3.00
12	11	3.5	3.00	3.00
6	12	6.0	1.75	0.50
1	13	1.0	0.50	1.75
16	14	3.5	1.75	1.75
14	15	3.5	1.75	1.75
13	16	3.5	1.75	1.75
4	17	6.0	3.00	1.75

[a] Standard order of the design matrix as defined in the Box-Behnken design; independent of the actual experimental run sequence.

4.12.3 Scale-up in Rotating Bed Reactor (SpinChem®) & Mixing Time Determinations

Scale-up of the chemoenzymatic epoxidation was conducted in a 300 mL double-jacketed glass vessel (SpinChem® V2) equipped with a rotating bed reactor basket (S2, SpinChem AB, Umeå, Sweden). The immobilized catalyst Novozyme® 435 was confined within the rotating bed and retained by a 104 µm stainless steel mesh to prevent particle leakage during operation. Temperature control was achieved via the double jacket connected to a thermostatic circulator. Reactions were conducted at a rotation speed of 1000 rpm; in comparison, small-scale reactions in the 150 mL thermovessel were carried out at 750 rpm. For spectroscopic process monitoring during scale-up, two configurations were employed: a direct *inline* ATR-FTIR setup and an *online* bypass configuration. In the direct configuration, the ATR-FTIR probe was immersed directly into the main reactor volume.

Due to scale-dependent emulsification effects observed under these conditions, an alternative *online* monitoring strategy was implemented using a bypass loop. The bypass setup consisted of a continuously operated recirculation line connecting the main rotating bed reactor to a separate 250 mL thermovessel. The reaction mixture was withdrawn from the main reactor using chemically resistant tubing at a rate of 50 mL · min^{-1} and circulated through the bypass vessel by means of a peristaltic pump, adjusting the level to approx. 10 mL. The dimensions, probe immersion depth, and agitation conditions of the bypass vessel (750 rpm) were chosen to match those used during small-scale calibration experiments (Section 5.2.4). Mixing times were determined by submerging a handheld pH meter (FiveGo, Mettler Toledo, Columbus, US) approximately 1 cm into water inside the respective reactor. A droplet of 1 mol · L^{-1} hydrochloric acid was added at the opposite side of the vessel, and the time was measured until the pH reading reached a stable value. Mixing time experiments were conducted for both reactor scales and rotation speeds.

4.12.4 *Inline* ATR-FTIR Monitoring and Chemometric Modeling

Inline monitoring of the epoxidation reaction was performed using a Matrix-MF multichannel FTIR spectrometer equipped with an IN350 ATR fiber optic probe (Bruker, Billerica, US). Spectra were acquired every 2 min over a range of 850 cm^{-1} to 4000 cm^{-1} with a resolution of 4 cm^{-1}, averaging 128 scans per measurement. Chemometric modeling was carried out using the Peaxact software suite (S-PACT GmbH, Aachen, Germany). Spectral data were restricted to the range of 1000 cm^{-1} to 1550 cm^{-1} and preprocessed by offset-based baseline correction followed by minmax normalization. An indirect hard modeling (IHM) was developed based on calibration spectra of artificial reaction mixtures containing varying volumetric ratios of LO, ELO, BA, and toluene, covering the full conversion range ($\chi = 01$, Table 4.12).

Calibration measurements were recorded under identical instrumental settings as the actual *inline* measurements. Pure component spectra were recorded for LO, ELO, BA, and toluene. Model performance was validated by comparing predicted conversions to reference values derived from EEW titration. The inferred conversion values were back-calculated from EEW according to the method described in Section 4.13.1.

Table 4.12 Calibration samples for indirect hard modeling using *inline* FTIR spectroscopy. LO - linseed oil, ELO - epoxidized linseed oil, BA - butyric acid, TOL - toluene.

χ [mol·mol^{-1}]	LO [vol·vol^{-1}]	ELO [vol·vol^{-1}]	BA [vol·vol^{-1}]	TOL [vol·vol^{-1}]
0	0.168	0	0.0506	0.7814
0.05	0.1596	0.0084	0.0506	0.7814
0.1	0.1512	0.0168	0.0506	0.7814
0.15	0.1428	0.0252	0.0506	0.7814
0.2	0.1344	0.0336	0.0506	0.7814
0.3	0.1176	0.0504	0.0506	0.7814
0.4	0.1008	0.0672	0.0506	0.7814
0.5	0.084	0.084	0.0506	0.7814
0.6	0.0672	0.1008	0.0506	0.7814
0.7	0.0504	0.1176	0.0506	0.7814
0.75	0.042	0.126	0.0506	0.7814
0.8	0.0336	0.1344	0.0506	0.7814
0.85	0.0252	0.1428	0.0506	0.7814
0.9	0.0168	0.1512	0.0506	0.7814
0.95	0.0084	0.1596	0.0506	0.7814
1	0	0.168	0.0506	0.7814

4.12.5 Bio-ELO Purification via Liquid-Liquid Extraction

Purification of the biobased ELO was achieved via liquidliquid extraction to remove residual BA from the organic product phase. The feed material was the organic upper phase of the biphasic supernatant obtained from the chemoenzymatic epoxidation reaction, preclarified by filtration through a 125 ţm mesh to remove suspended Novozyme® 435. Extraction was performed in 50 mL plastic reaction tubes using a 1:1 volume ratio of organic phase to aqueous washing solution, with typical volumes of 25 mL per phase. Depending on the experimental condition, the aqueous phase consisted either of ultrapure water preheated to 70 řC following the procedure described by Liu et al. (2016) [172], or of a 0.1 mol $\cdot$ L^{-1} sodium bicarbonate solution at room temperature. The extraction protocol involved up to three consecutive washing steps, with sampling after each stage for AN determination as a quality control measure. The phases were mixed for 30 s using a Vortex Genie 2 (Faust Lab Science, Klettgau, Germany) and separated by centrifugation (Universal 320R, Andreas Hettich GmbH, Tuttlingen, Germany) at 3500 g. The aqueous extract (containing the majority of BA) was discarded, and the organic raffinate (toluene phase containing the ELO) was subjected to rotary evaporation (Rotavapor R-200, Büchi Labortechnik AG, Flawil, Switzerland) to remove residual toluene. The remaining viscous

product was stored at 4 řC until further analysis via DSC. The partitioning efficiency of BA between the organic and aqueous phases was quantified via the apparent partition coefficient $P_{org/aq}$, calculated according to Equation 18:

$$P_{org/aq} = \frac{c_{org}}{c_{aq}} \tag{18}$$

where c_{org} and c_{aq} denote the concentrations of BA in the organic and aqueous phases, respectively, as determined via titration of the AN.

4.13 Wet Chemical Titration Methods

4.13.1 Titration of Epoxy Groups

The EEW is defined as the mass of substance in grams containing one mole of epoxy groups. It is a key parameter for characterizing epoxy-functionalized materials, particularly in the context of stoichiometric calculations for curing reactions. The EEW is expressed in units of $g \cdot mol^{-1}$ and provides insight into the functionality per unit mass of the epoxidized sample. The epoxy number (EN) describes the number of epoxy groups per 100 grams of substance and is often used as an alternative representation of epoxy functionality in industry. It is calculated from the inverse of the EEW and expressed in units of $mol \cdot 100\,g^{-1}$. The EEW and EN of the samples were determined by titration following a modified protocol based on the peracetic acid method described in ASTM D1652-11 [173]. Approximately 0.5 g of the sample was weighed into a baffled shake flask. To the sample, 10 mL of dichloromethane and 10 mL of a $250\,g \cdot L^{-1}$ solution of tetraethylammonium bromide (TEAB) in glacial acetic acid were added. The mixture was thoroughly homogenized, and 5 drops of a 1% (w/v) solution of crystal violet in ethanol were added as an indicator. The resulting solution was titrated against a standardized 0.1 N peracetic acid solution in ethanol using a Titrette® digital burette (Brand GmbH & Co. KG, Wertheim, Germany), until a stable color change from violet to green was observed. All determinations were performed in duplicate, and blank titrations were carried out in parallel using the same solvent and reagent volumes without sample addition. The EEW was calculated according to Equation 19:

$$EEW = \frac{m_{sample} \cdot 1000}{(V_{sample} - V_{blank}) \cdot c} \quad \left[g \cdot mol^{-1}\right] \tag{19}$$

where

- m_{sample} = sample mass [g],
- V_{sample} = sample titrant volume [mL],
- V_{blank} = blank titrant volume [mL],
- c = concentration of peracetic acid solution [mol $\cdot$ L^{-1}].

The EN was calculated from the EEW using Equation 20:

$$EN = \frac{43 \cdot 100}{EEW} \quad \left[\text{mol} \cdot 100\,\text{g}^{-1}\right] \tag{20}$$

where:

- EN is the epoxy number [mol $\cdot$ 100 g^{-1}],
- EEW is the epoxy equivalent weight [g $\cdot$ mol^{-1}],
- 43 is the molar mass of the oxirane group [g $\cdot$ mol^{-1}].

This method allows reliable quantification of epoxy functionality in epoxidized linseed oil samples and was used to validate *inline* FTIR model predictions throughout the epoxidation study.

4.13.2 Acid Number Titration

The AN was determined using a Metrohm autotitrator 848 Titrino plus (Herisau, Switzerland) equipped with a Solvotrode easyClean. Approximately 0.5 g of the sample was weighed into a 100 mL to 200 mL plastic beaker using a fine balance under a fume hood. The exact weight was recorded. The sample was dissolved in 50 mL of ethanol (>99.5 %, synthesis grade), and a small magnetic stir bar was added. Before the measurement, the pH electrode, temperature sensor, and dosing tip were cleaned with deionized water and ethanol. The beaker was placed on the magnetic stirrer of the autotitrator, and the sensors were immersed into the solution with the dosing tip positioned approximately 3 mm below the liquid surface. The sample weight was entered into the autotitrator interface, and the titration was initiated using a 0.1 mol $\cdot$ L^{-1} KOH solution in ethanol as titrant. The acid number was automatically calculated by the instrument using the following Equation 21:

$$AN = \frac{1000 \cdot V_{KOH} \cdot c_{KOH} \cdot M_{KOH}}{m_{sample}} \quad \left[\text{mg} \cdot\ \text{g}^{-1}\right] \tag{21}$$

where, by convention, AN is the acid number in mg $\cdot$ g^{-1}, V_{KOH} is the volume of KOH titrant in L, c_{KOH} is the concentration of KOH in mol $\cdot$ L^{-1}, M_{KOH} is the molar mass of KOH in g $\cdot$ mol^{-1}, and m_{sample} is the sample mass in g. The result was documented along with the volume of titrant used.

5 Results and Discussion

5.1 Biocatalytic Approaches to the Oxidative Breakdown of Thermoset Epoxy Networks

The enzymatic degradation of high-performance thermoset epoxy resins represents a largely unexplored approach for the recovery of carbon fibers and the chemical valorization of polymer matrices. Due to the aromatic content, high cross-link density, and elevated glass transition temperatures of aerospace-qualified systems such as resin transfer mold 6 resin (RTM6), biocatalytic cleavage is presumed to be limited by both chemical inertness and steric inaccessibility. As, according to Buchholz et al. (2022) [174], little to no enzyme was previously characterized for epoxy degradation, a rational screening approach was adopted. The chemical structure of the RTM6 matrix was analyzed and compared to lignin, a naturally occurring aromatic polymer known to be susceptible to oxidative attack. On the basis of this structural analogy, fungal laccases were selected for investigation, owing to their known capability of generating diffusible radical species via redox mediators and their established role in lignin depolymerization (see Section 2.4) [175, 176].

To facilitate degradation studies under controlled conditions, the RTM6 resin was synthesized in-house, cured, and subsequently milled to defined particle sizes (Section 5.1.1). The resulting material was characterized by attenuated total reflection fourier-transform infrared spectroscopy (ATR-FTIR), thermogravimetric analysis (TGA), and particle size distribution. In parallel, model compounds structurally resembling Sections of the epoxy network were employed as low-molecular-weight surrogates for enzymatic screening, reaction condition optimization, and product identification. The oxidative degradation of the primary model compound *N*,*N*-bis(2-hydroxypropyl)-*p*-toluidine (NNBT) was monitored in the presence of various commercial laccases and correlated with their redox potentials (Section 5.1.2). Molecular docking studies were carried out to evaluate steric constraints within the enzyme active sites and to estimate the structural limits of direct substrate binding (Section 5.1.2).

Subsequently, a selection of redox mediators was screened and characterized by cyclic voltammetry (CV) to identify stable mediators under the relevant process conditions. Reaction parameters including pH, temperature, mediator concentration, and aeration were systematically optimized to enhance activity (Section 5.1.2). The most promising reaction system was applied to the degradation of the polymeric resin in a fixed-bed reactor, following preliminary tests in stirred-tank configurations. Chemical changes in

the epoxy matrix were evaluated by ATR-FTIR spectroscopy and elemental analysis and were consistent with partial oxidation of the polymer backbone (Section 5.1.5). To address the limited wettability of the hydrophobic polymer surface, deep eutectic solvent (DES) and aqueous DES mixtures were screened as alternative reaction media (Section 5.1.6). The results presented in this section describe a stepwise methodology for identifying and applying oxidative enzyme systems to aerospace-grade epoxy resins and provide a basis for further biocatalytic strategies in thermoset recycling.

5.1.1 Resin Production, Characterization, and Model Compound Evaluation

Due to the lack of commercially available, fully cured, and structurally defined aerospace-grade epoxy materials, the thermoset system RTM6 was prepared in-house to provide a reproducible and representative substrate for enzymatic degradation studies. RTM6 is a widely applied thermosetting matrix resin in the aerospace sector and is used particularly in resin transfer molding processes for high-performance carbon-fiber reinforced polymers (CFRPs). The resin consists of multifunctional aromatic epoxy monomers and aliphatic or aromatic amine-based curing agents that form a densely crosslinked, highly thermostable polymer network upon curing. The principal monomers and curing agents used in the formulation were *N*,*N*,*N*',*N*'-tetraglycidyl-4,4'-methylenebisbenzenamine (TGMDA), 4,4'-methylenebis(2,6-diethylaniline) (MDEA), and 4,4'-methylenebis(2-isopropyl-6-methylaniline) (M-MIPA) and are depicted in Figure 5.1. The resin was produced according to Section 4.3.1. After curing, the resin was subjected to mechanical milling to enable further analytical characterization and to prepare samples for degradation experiments. Milling was necessary to increase the accessible surface area for enzymatic attack and to ensure homogeneous solidliquid interaction in both batch and packed-bed reactor formats.

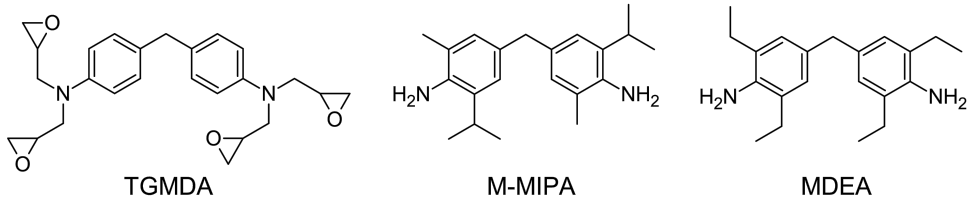

Figure 5.1 Chemical structures of the monomers used in the RTM6 epoxy resin system.

Different milling approaches were evaluated, including cryogenic ball milling and centrifugal milling using sieve inserts of 250 µm and 500 µm mesh size (see Section 4.3.2). The resulting volume-based particle size distributions and percentile values of size fractions

are presented in Figure 5.2. Cryogenic milling produced the finest and broadest distribution, with a median particle size $d_{x50} = 86.2 \pm 0.32$ µm, compared to 157.0 ± 0.84 µm and 233.0 ± 4.52 µm for centrifugal milling with 250 µm and 500 µm sieves, respectively.

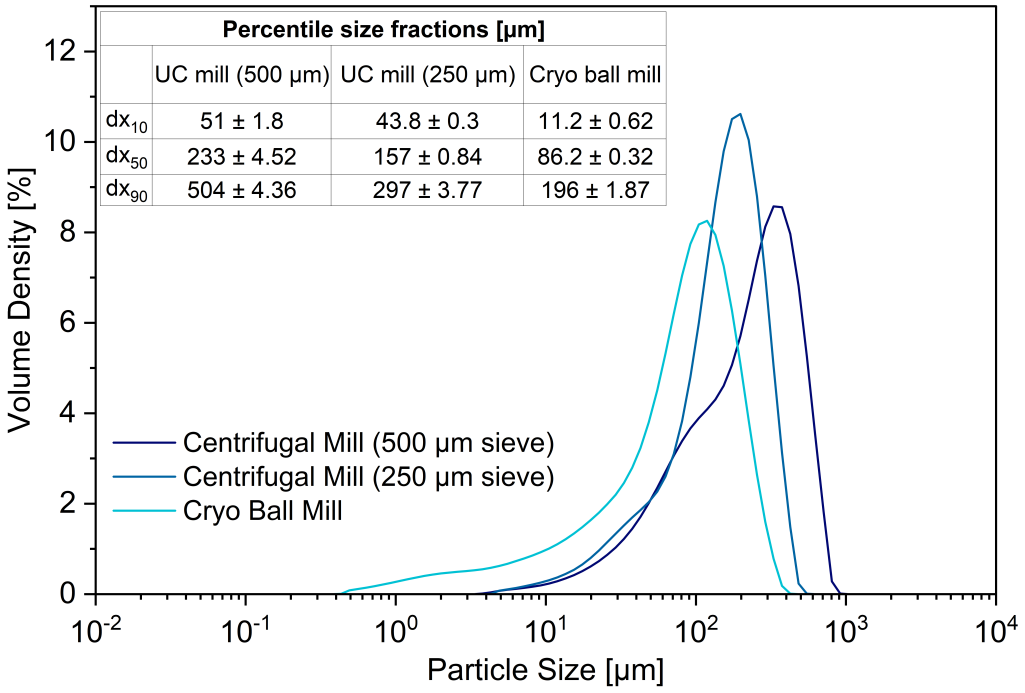

Figure 5.2 Volume-based particle size distributions and percentile values of size fractions of RTM6 particles after milling in a ultracentrifugal mill (Retsch ZM200, 250 µm or 500 µm sieve, 100 %, pre-cooled with liquid N_2) and a planetary ball mill (Retsch S1, three balls, 100 %, 5 min or 3×10 min with repeated addition of dry ice); particle size distributions were recorded using a Mastersizer 3000 at the Institute of Solids Process Engineering and Particle Technology at Hamburg University of Technology according to 4.4.1.

The smallest size fraction d_{x10} was 11.2 ± 0.62 µm for cryo-milled samples, markedly smaller than 43.8 ± 0.3 µm and 51.0 ± 1.8 µm for the centrifugal methods. Similarly, the coarse fraction d_{x90} reached 196.0 ± 1.87 µm for cryo milling and up to 504.0 ± 4.36 µm for the 500 µm centrifugal fraction. Among the tested conditions, the 250 µm centrifugal milling fraction was selected as the standard particle preparation for subsequent studies, as it represents a compromise between narrow distribution, sufficient surface area, and practical handling. This particle fraction was considered the most representative and was used consistently throughout enzymatic degradation experiments.

To confirm successful curing and validate the chemical structure of the in-house-produced RTM6, the material was analyzed by ATR-FTIR. As shown in Figure 5.3, the

cured resin exhibited characteristic bands associated with aromatic and aliphatic components. Aromatic C=C stretching vibrations were detected at 1610 cm^{-1}, 1510 cm^{-1}, and 1460 cm^{-1}, and substitution patterndependent C–H out-of-plane bending modes appeared at 800 cm^{-1} and 750 cm^{-1}.

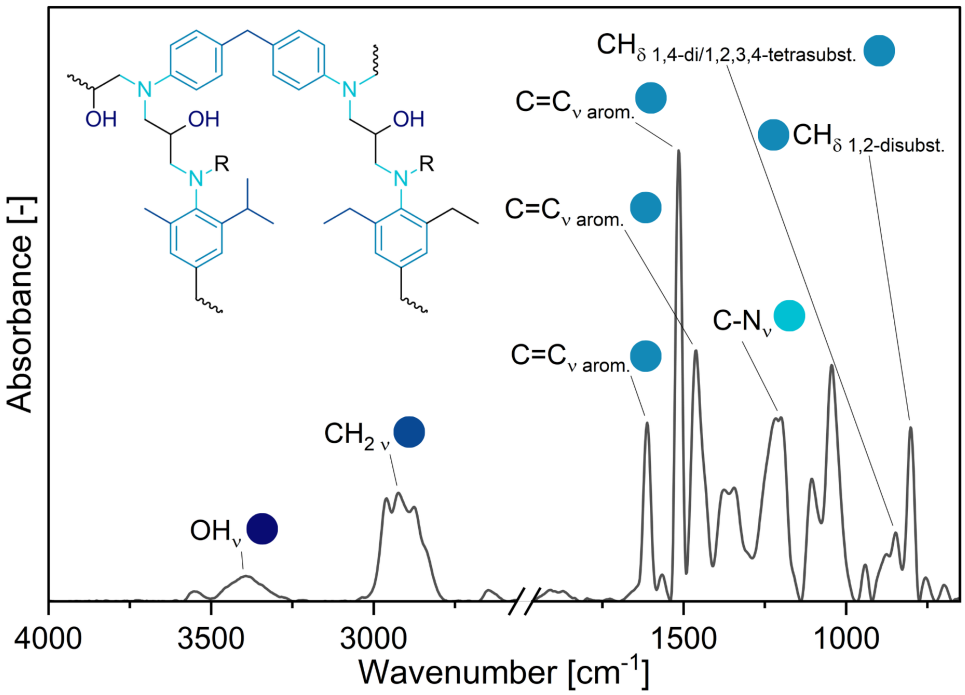

Figure 5.3 ATR-FTIR spectrum of cured RTM6 epoxy resin; spectra was recorded on a Bruker Vertex 70 according to 4.4.4.

A broad band at 3380 cm^{-1} confirmed the presence of hydroxyl groups generated during epoxide ring opening, while C–H stretching of methyl and isopropyl groups occurred below 3000 cm^{-1}. Additionally, a distinct band at 1215 cm^{-1} was attributed to C–N stretching in tertiary amines formed during the crosslinking reaction. The spectrum is consistent with literature reports for RTM6 and validates the presence of epoxy-derived and amine-derived linkages [177].

As the resin was produced and cured manually, it was essential to verify that complete network formation had occurred. Therefore, thermal analysis techniques were employed to evaluate the degree of curing, thermal stability, and transition behavior. TGA was conducted under nitrogen atmosphere up to 1000 řC. The thermogram shown in Figure 5.4 (A) exhibits a single major decomposition event with the temperature at maximum mass loss rate (T_{max}) determined to be 373.5 řC.

The inflection point of the mass loss curve, indicating the midpoint of decomposition, was located at 402.8 řC. These values are in agreement with literature values for neat RTM6 resin and are indicative of a sufficiently crosslinked and thermally stable network. For instance, Greiner et al. (2019) [178] reported a T_{max} of approximately 379 řC for fully cured RTM6 resin under comparable conditions, validating the quality of the manually cured material.

To further assess the curing state and quantify residual reactivity, modulated differential scanning calorimetry (MDSC) was performed. The thermogram presented in Figure 5.4 (B) displays a well-defined glass transition temperature (T_g) at 168.8 řC, which closely matches the reference value of 170 řC provided by Airbus Defence and Space GmbH.

The absence of post-curing exotherms confirmed that no significant residual curing potential remained in the material. The reverse heat flow signal of 0.81 mW was used to calculate the enthalpy of curing, ΔH, according to Equation 22, taking into account heating rate and sample mass. A final enthalpy value of 398.7 J $\cdot$ g^{-1} was obtained (Equation 23), which lies well within the expected range of 391 ś 12 J $\cdot$ g^{-1} and further supports the conclusion that the resin was fully cured [179].

This provided a high degree of confidence that subsequent degradation experiments were performed on a representative and chemically uniform substrate.

$$\Delta H = \frac{\left(\frac{\text{peak temperature } [^\circ\text{C}]}{\text{heating rate } [^\circ\text{C}\cdot\text{s}^{-1}]}\right) \cdot \text{rev. heat flow } [\text{J}\cdot\text{s}^{-1}]}{\text{sample mass [g]}} \tag{22}$$

$$\Delta H = \frac{\left(\frac{168.55}{5\cdot 60}\right) \cdot 0.8082 \cdot 10^{-3}}{0.0041} = 398.7\,\text{J}\cdot\text{g}^{-1} \tag{23}$$

To facilitate mechanistic studies of enzymatic oxidation under defined and reproducible conditions, a series of low-molecular-weight model compounds was initially considered based on structural similarity to representative moieties within the cured RTM6 epoxy network. These included NNBT, 1,3-bis(*N*-methylanilino)propan-2-ol, and *N*,*N*,*N*',*N*'-tetramethyl-4,4'methylenedianiline, commonly refered to as Michlers base (MB). All candidates contained either electron-rich aromatic amines, hydroxylated aromatic structures, or tertiary amines with alkyl substituents, reflecting key motifs of the crosslinked thermoset resin as depicted in Figure 5.5, according to color coding. Among the tested compounds, NNBT and MB were selected as primary surrogates for the subsequent screening and kinetic experiments.

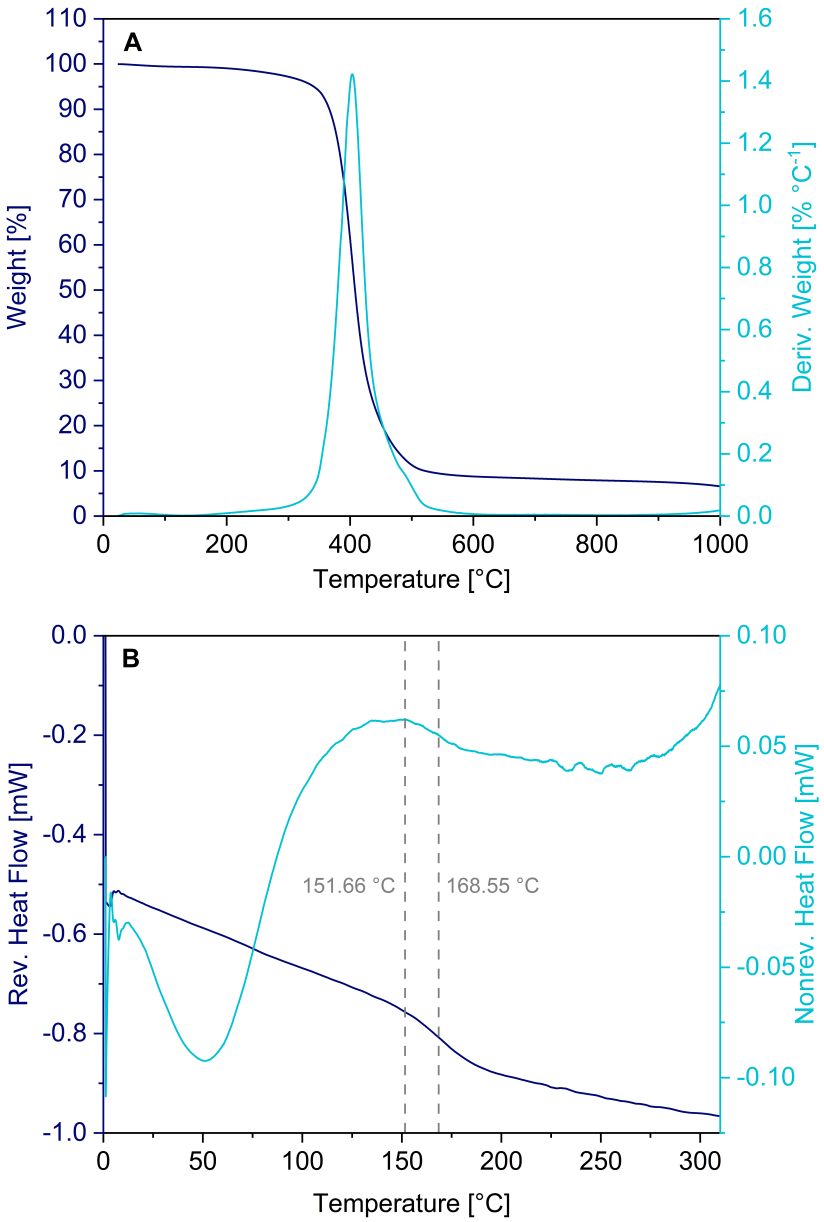

Figure 5.4 (A) TGA of cured RTM6 resin under nitrogen atmosphere. **(B)** Modulated differential scanning calorimetry (DSC) thermogram of cured RTM6 epoxy showing glass transition temperature and curing enthalpy; measurements were conducted by Airbus Defence and Space GmbH according to 4.4.2.

NNBT, a hydroxylated toluidine derivative, exhibited a solubility of approximately 5 mmol · L^{-1} in 5% DMSO-containing buffer and could be reliably quantified via gas chromatography (GC) following extraction.

Moreover, NNBT had previously been proposed by Dolz et al. (2022) [84] as a surrogate substrate in high-throughput screening assays for the identification of putative epoxy-degrading unspecific peroxygenases (UPOs) targeting RTM6-type thermosets. Similarly, MB showed adequate aqueous solubility (4 mmol · L^{-1}) and was quantifiable by GC as well. In contrast, 1,3-bis(*N*-methylanilino)propan-2-ol exhibited limited solubility ($\leq$ 0.5 mmol · L^{-1}), required multistep synthesis, and displayed poor extraction efficiency for GC analysis. Furthermore, 1,3-bis(*N*-methylanilino)propan-2-ol was classified as highly toxic and was excluded from further experimentation due to safety and analytical concerns. NNBT and MB were therefore retained as model substrates for all subsequent studies, owing to their structural relevance, reliable quantification by gas chromatography coupled flame ionization detector (GC-FID), and compatibility with the enzymatic reaction.

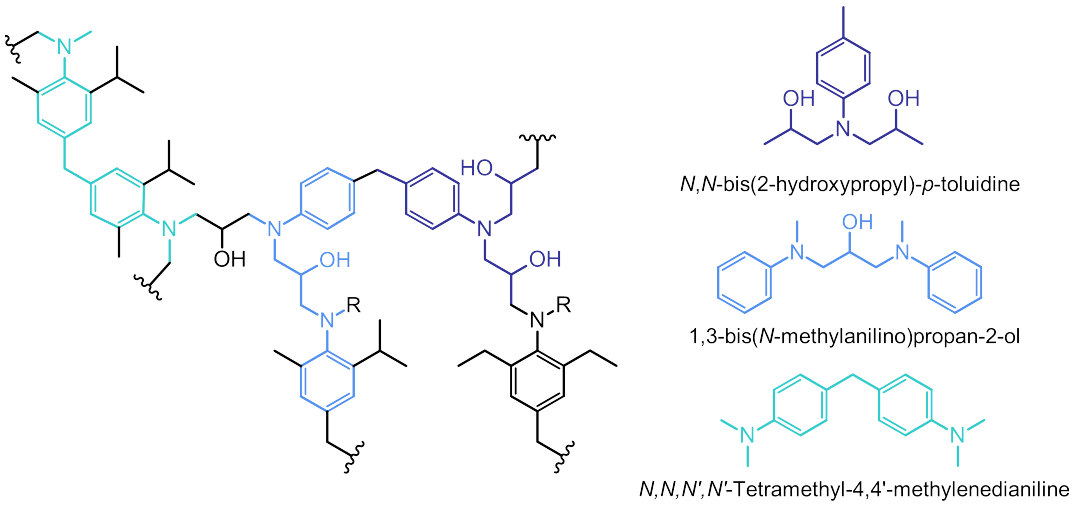

Figure 5.5 Selected surrogate compounds for RTM6 structure motifs and their experimental evaluation.

5.1.2 Screening for Oxidoreductases With Epoxylytic Activity via Model Compound Reaction Systems

Laccase Activity Screening using RTM6 Model Compound NNBT

To identify suitable biocatalysts for the oxidative degradation of epoxy-derived model substrates, a panel of four fungal laccases (Novozym 51003 from *Myceliophthora thermophila*

(LacMT), laccase from *Trametes versicolor* (LacTV), laccase of undisclosed origin (LacU), and laccase from *Funalia trogii* (LacF)) was screened for their activity toward NNBT in buffered aqueous solution. These enzymes were chosen to cover a range of redox potentials and phylogenetic origins, including low-redox laccases (LacMT), high-redox laccases from white-rot fungi (LacTV and LacF), and a commercial high-potential laccase of undisclosed origin (LacU). The main characteristics of the selected laccases, including their biological source, supplier, and reported redox potential, are summarized in Table 5.1.

Enzyme activity was normalized to $0.1\,\mathrm{U}\cdot\mathrm{mL}^{-1}$ using 2,2'-azino-bis(3-ethylbenzothiazoline-6)-sulfonic acid (ABTS) as the standard substrate. A reaction pH of 4.5 was selected, as it represents the typical activity optimum for fungal laccases and has been used in comparable screening assays for aromatic substrates [166].

Table 5.1 Screened laccases, their commercial source, biological origin, and reported redox potential.

Name	**Supplier**	**Organism**	**Redox Potential $\mathbf{E_0}$ [V]**
LacMT	Novozymes	*Myceliophthora thermophila*	0.46 **[4]**
LacTV	ASA Spezialenzyme	*Trametes versicolor*	0.78 **[5]**
LacU	ASA Spezialenzyme	non-disclosed	≥ 0.5
LacF	ASA Spezialenzyme	*Funalia trogii*	0.79 **[6]**

The oxidation of NNBT was monitored over 3 h in a 10 mL reaction system under mediator-free conditions. Substrate concentrations were quantified by GC-FID, and non-linear least-squares fitting was performed using a first-order kinetic model. All laccases were able to catalyze NNBT oxidation without the addition of mediators, despite NNBT not being a phenolic compound, indicating that its hydroxylated arylamine structure is susceptible to direct one-electron oxidation. The time-resolved depletion curves are shown in Figure 5.6.

Substantial differences in reaction rates were observed. LacMT, a known low-redox potential laccase ($E^0 \approx 0.46\,\mathrm{V}$), exhibited the slowest conversion with a rate constant of $0.0043\,\mathrm{min}^{-1}$ [180]. LacU, which is marketed as a high-redox laccase but lacks publicly disclosed sequence or origin data, showed intermediate activity ($0.0094\,\mathrm{min}^{-1}$). The highest rates were recorded for LacTV and LacF, both associated with redox potentials in the range of 0.78 V to 0.79 V and derived from basidiomycete fungi. These findings are in agreement with prior observations by Obleser et al. (2022) [166], who described a positive correlation between laccase redox potential and oxidation rate for non-phenolic substrates.

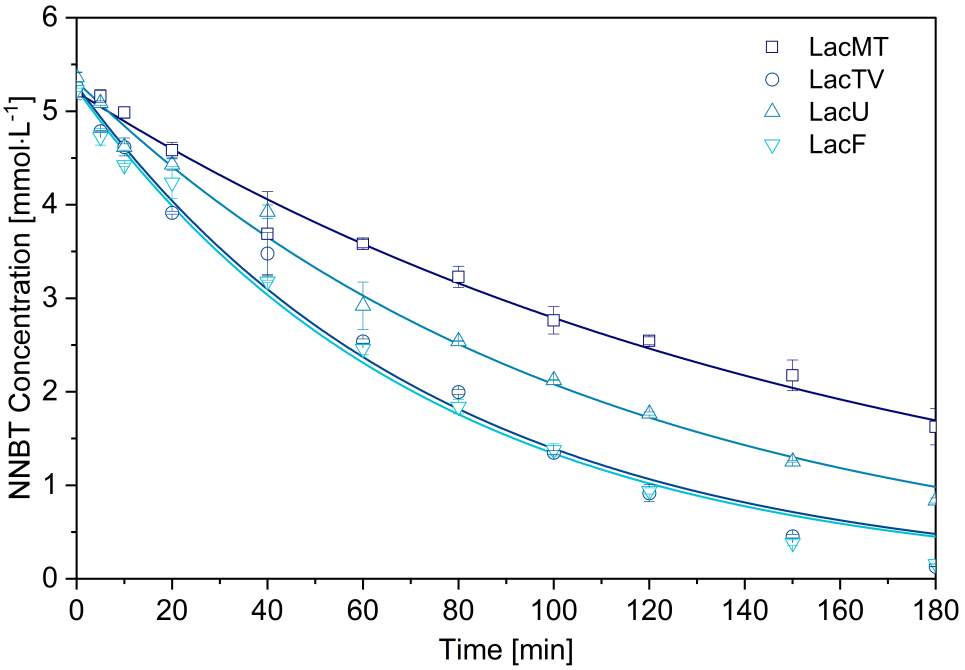

Figure 5.6 Time-resolved oxidation of NNBT by different fungal laccases; 10 mL reaction volume, 5 mmol · L^{-1} NNBT, 0.1 U · mL^{-1} laccase, 0.1 mol · L^{-1} citrate-phosphate buffer (pH 4.5), 30 řC, 750 rpm, $t_{reaction}$ = 3 h, 200 ţL sample was inhibited by 5 ţL 0.05 % NaN_3, remaining NNBT concentration was determined after pH adjustment to 7 and 1:1 extraction with EtOAc via GC-FID, first-order kinetic fitting was done with the `scipy.optimize.curve_fit` (NumPy library) function (all $R^2 > 0.98$).

The trend in oxidation rate constants, LacMT < LacU < LacTV ≈ LacF, thus reflects the expected order of oxidative capability based on redox potential. These results suggest that high-potential laccases are more effective at oxidizing electron-rich arylamines such as NNBT, which lack the classical phenolic hydroxyl group typically associated with native laccase substrates. Given its superior activity towards NNBT and availability in consistent quality, LacF was selected as the most promising candidate for further optimization and application studies.

To evaluate whether the reactivity of the enzymes could be further enhanced by redox mediation, a preliminary test was conducted using two representative mediators: 2,2,6,6-tetramethylpiperidinyloxyl (TEMPO) and ABTS. This experiment was not designed as a comprehensive mediator screening but rather as an initial comparison of mediator responsiveness among the four laccases. A fixed mediator-to-substrate ratio of 0.3 was used, and oxidation yields were determined at 0.5 h and 2 h. The results are summarized in Figure 5.7.

For all enzymes, the addition of TEMPO resulted in increased or similar substrate conversion compared to the mediator-free controls, confirming the viability of mediated oxidation for NNBT. The magnitude of this effect, however, varied depending on the enzyme. LacTV and LacF showed the largest relative increases, reaching nearly complete NNBT conversion within 2 h in the presence of TEMPO. LacU and LacMT also benefited from TEMPO addition, though their overall performance remained lower.

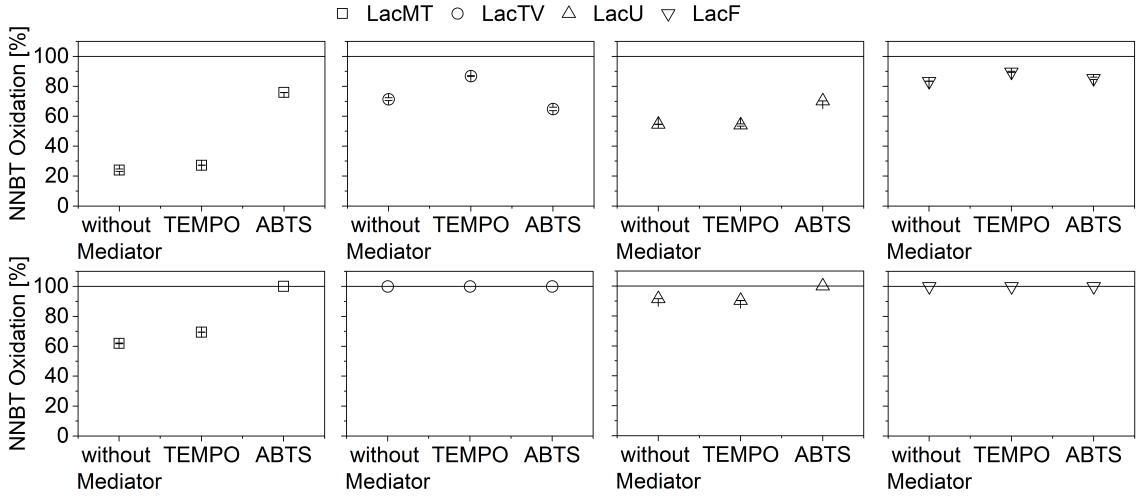

Figure 5.7 NNBT oxidation by four fungal laccases after 0.5 (top row) and 2 hours (bottom row) with and without redox mediators; 1 mL reaction volume, 5 mmol · L^{-1} NNBT, 1.5 mmol · L^{-1} mediator, 0.1 U · mL^{-1} laccase, 0.1 mol · L^{-1} citrate-phosphate buffer (pH 4.5), 30 řC, 750 rpm, n=2, 200 ţL sample was inhibited by 5 ţL 0.05 % NaN_3, remaining NNBT concentration was determined after pH adjustment to 7 and 1:1 extraction with EtOAc via GC-FID. 100 % refer to full depletion of NNBT.

ABTS, in contrast, produced more modest or negligible enhancements and in some cases appeared to slow the reaction, possibly due to its limited reactivity with non-phenolic substrates or side reactions with NNBT, when combined with LacTV and LacF. The strongest effect of ABTS was observed with LacMT, where an increase in NNBT oxidation by 30-40% was observed at both sampling time points. As LacMT is considered a low-redox potential laccase with an E_0 of 460 mV, the observed effect is consistent with a reported extension of the substrate spectrum and reaction kinetics when a redox mediator is employed [181, 182]. Overall, these findings support earlier studies in which TEMPO was identified as a highly efficient mediator for electron-rich amine oxidation, including in the context of laccasemediated C–N bond activation [183, 184]. Taken together, the data show that redox mediation enhances NNBT oxidation, particularly for high-potential laccases, and that TEMPO is a more suitable mediator than ABTS for this class of substrates.

Based on its consistently high activity across all tested conditions, LacF was selected for a dedicated mediator screening and further optimization studies, which are presented in Section 5.1.2.

Molecular Docking Simulation

To first gain theoretical insights into steric constraints during enzymesubstrate interactions, molecular docking simulations were conducted with the high-performing laccase LacF. These *in silico* studies aimed to evaluate the binding behavior of redox mediators and epoxy-derived model compounds in the active site of the enzyme. Due to the poor solubility of large, polymer-like structures in aqueous systems, this approach served as a valuable alternative to wet-lab experimentation. In particular, the simulations were designed to estimate the maximum molecular size and complexity compatible with binding to the catalytic site and to justify the use of small, diffusible redox mediators that circumvent steric hindrance.

As demonstrated in the preceding section, laccases can catalyze model compound oxidation irrespective of the presence of a mediator. Consequently, elucidating the impact of larger epoxy structures on putative active site binding is vital for determining the continued utilization of mediators.

The ligand panel comprised the redox mediators ABTS and TEMPO, the substrate surrogate NNBT, and five epoxy-related model compounds representing increasing structural complexity within the RTM6 network (Figure 5.8).

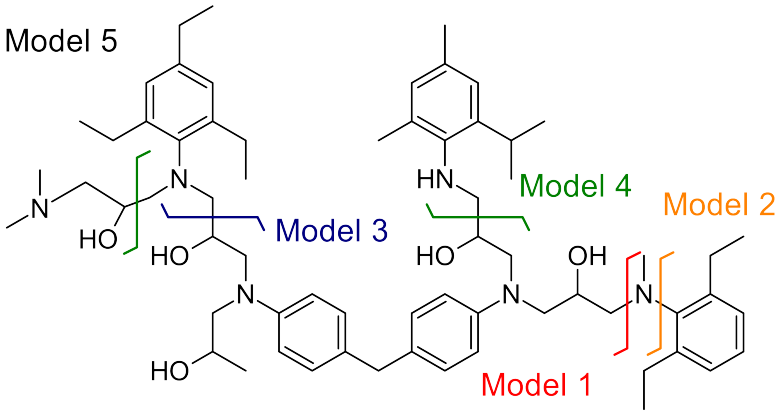

Figure 5.8 Epoxy model structures used for molecular docking simulations (Models 15).

After docking, the most energetically favorable configurations for each ligand were identified, and their respective binding poses were analyzed using AutoDockTools and visualized in ChimeraX (Figure 5.9). As summarized in Table 5.2, a gradual increase in

calculated free binding energy (ΔG_{bind}) was observed as the molecular size and branching of the epoxy-like structures increased. While smaller structures such as Models 1 and 2 yielded moderately favorable binding energies (3.6 to 3.8 kcal·mol^1), Models 3 and 4 were already associated with weaker binding.

Notably, Model 5, the largest and most sterically demanding compound, exhibited a slightly positive free energy of binding (+0.14 kcal·mol^1), indicating that its interaction with the enzyme was no longer thermodynamically favorable. Visual inspection of the binding poses revealed that Models 14 were still able to insert into the binding pocket of LacF with varying degrees of fit and interaction. Key active-site residues, such as Phe331, Phe336, Val162, and the catalytic copper center (T1 Cu), remained within proximity to the ligand [185, 175].

Table 5.2 Free binding energies of selected ligands in their most favorable docking conformations with LacF.

Ligand	**Free Binding Energy (kcal·mol^1)**
NNBT	4.87
ABTS	7.68
TEMPO	3.88
RTM6 Model 1	3.61
RTM6 Model 2	3.81
RTM6 Model 3	2.72
RTM6 Model 4	2.47
RTM6 Model 5	+0.14

However, Model 5, due to its extended and branched structure, adopted a more peripheral orientation with limited contact to the copper center and surrounding residues, consistent with the calculated unfavorable binding energy. These results illustrate a size-dependent steric exclusion effect and demonstrate that direct binding of large RTM6-like fragments is sterically and energetically disfavored. Furthermore, the decline in chain flexibility and degrees of freedom associated with increasing molecular weight reduces the likelihood of favorable interaction. The docking results for NNBT and TEMPO further support their role as effective small-molecule substrates and mediators. NNBT displayed a moderately favorable binding energy and showed a reasonable proximity to the catalytic center, rationalizing the observed reactivity in wet-lab assays. TEMPO, despite its low molecular weight and lack of aromatic groups, also exhibited favorable docking, highlighting its accessibility to the active site.

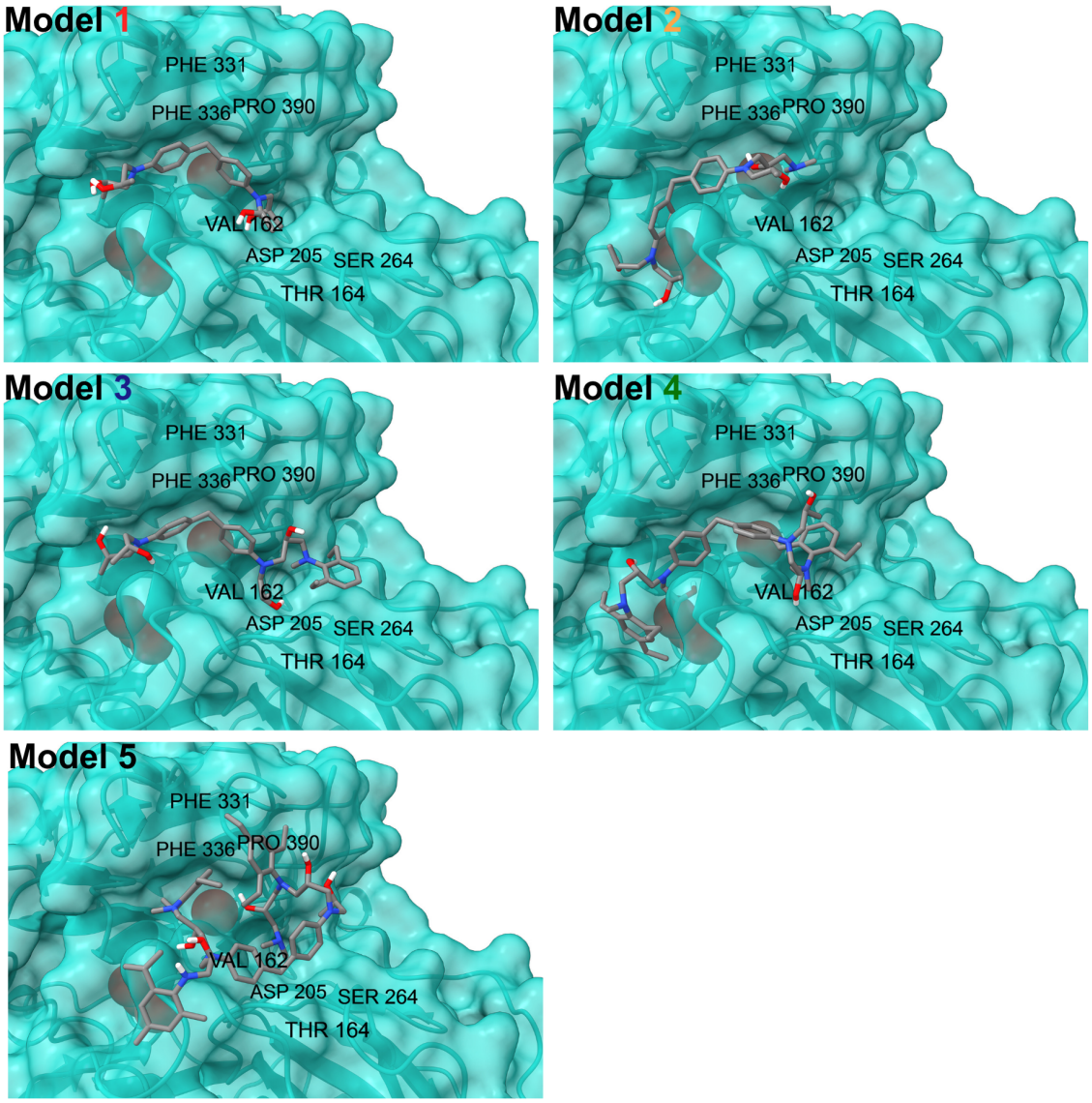

Figure 5.9 Most energetically favorable conformations of RTM6 models 15 docked into the active site of LacF (PDB: 2HRH). Red spheres indicate copper ions. Structural preparation and docking performed with AutoDockTools and AutoDock 4.0; visualization with ChimeraX.

This provides theoretical justification for the use of mediators in the degradation of epoxy-based materials. While polymeric structures exceed the spatial capacity of the active site, smaller diffusible redox mediators can access and shuttle electrons to the catalytic center without steric limitation.

Taken together, these molecular docking simulations provide mechanistic support for the observed reactivity trends and demonstrate the steric limitations of laccase-substrate interactions. The results confirm that mediator-assisted oxidation is likely essential for the enzymatic degradation of bulky epoxy thermosets and reinforce the rationale for combining high-redox potential laccases with small, reactive mediators in composite recycling strategies.

Mediator Screening and Electrochemical Characterization

Following the initial observation that LacF exhibited only limited responsiveness to mediator supplementation during NNBT oxidation, a dedicated mediator screening was conducted to re-evaluate the effect of various natural and synthetic mediators under controlled conditions. The screening panel included ABTS, violuric acid (VA), ferulic acid (FA), caffeic acid (CA), and TEMPO. NNBT conversion was tracked over time, and rate constants were extracted by non-linear regression using a first-order kinetic model according to 4.7.3.

As depicted in Figure 5.10, compared to the mediator-free reaction, where LacF already catalyzed NNBT oxidation with high efficiency ($k = 0.0134\,min^{-1}$), the addition of most mediators resulted in only modest rate enhancements. ABTS and CA slightly decreased the reaction rate, while VA produced a nearly identical rate constant (Table 5.3). A small increase in activity was observed with FA and most notably with TEMPO, which delivered the highest rate among the tested mediators. Although the improvements were less pronounced than anticipated, these findings are consistent with the molecular docking simulations presented in Section 5.1.2, where it was demonstrated that larger epoxy-like structures are sterically hindered from binding to LacF. Therefore, the true benefit of the mediator is expected to emerge more clearly when polymeric substrates are used, rather than the small and highly accessible NNBT molecule. As such, mediator-assisted oxidation remains a relevant strategy in the context of epoxy resin degradation.

To further assess mediator suitability beyond kinetic enhancement, the redox properties and electrochemical stability of selected compounds were characterized by CV. Measurements were carried out in a custom 3D-printed three-electrode cell comprising a platinum wire counter electrode, an Ag/AgCl reference electrode, and a $9\,mm^2$ platinum working electrode (Section 4.7.4, Figure 4.1). All scans were conducted at $50\,mV \cdot s^{-1}$ in

0.1 mol · L^{-1} phosphate-citrate buffer (pH 4.5) according to 4.7.4. The resulting voltammograms revealed distinct differences in both redox potential and cycling behavior between the tested mediators.

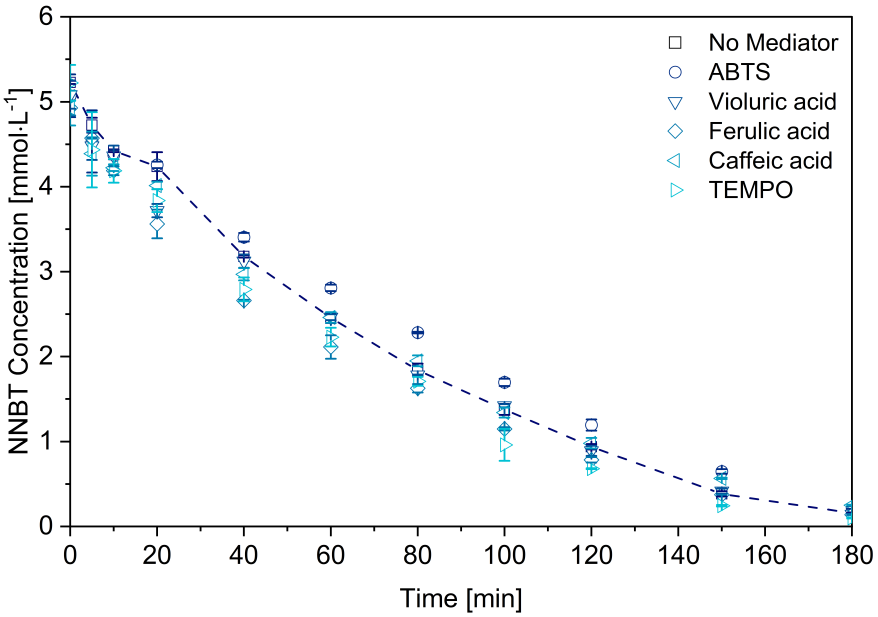

Figure 5.10 NNBT oxidation over time in the presence of various redox mediators. Dotted line inserted to enhance readability. 10 mL reaction volume, 5 mmol · L^{-1} NNBT, 1.5 mmol · L^{-1} mediator, 0.1 U · mL^{-1} laccase, 0.1 mol · L^{-1} citrate-phosphate buffer (pH 4.5), 30 řC, 750 rpm, 200 ţL sample was inhibited by 5 ţL 0.05 % NaN_3, remaining NNBT concentration was determined after pH adjustment to 7 and 1:1 extraction with EtOAc via GC-FID.

As summarized in Table 5.4, TEMPO exhibited a half-wave potential of 526 mV vs. Ag/AgCl, in good agreement with literature values reported by Obleser et al. (2022) [166]. Its voltammetric profile, depicted in Figure 5.11, was mostly symmetric with minimal peak separation, suggesting a quasi-reversible electron transfer and negligible degradation over the time scale of the repeated measurement.

In contrast, ABTS displayed the highest redox potential in the series at 765 mV, but its broad and asymmetric peaks indicated low reversibility and possible side reactions [186]. The natural phenolic mediators CA and FA yielded lower redox potentials in the range of 350 mV to 600 mV, yet their peak definitions were poor, which may reflect rapid follow-up oxidation steps, adsorption, or chemical instability in the electrochemical environment [187]. For the investigation of the long-term electrochemical behavior, repeated CV scans were recorded over 150 cycles (Figure 5.11).

Table 5.3 First-order rate constants k for NNBT oxidation by LacF in the presence of different mediators; 10 mL reaction volume, 5 mmol · L^{-1} NNBT, 1.5 mmol · L^{-1} mediator, 0.1 U · mL^{-1} laccase, 0.1 mol · L^{-1} phosphate-citrate buffer (pH 4.5), 30 řCC, 750 rpm, 200 ţL sample was inhibited by 5 ţL 0.05 % NaN_3, remaining NNBT concentration was determined after pH adjustment to 7 and 1:1 extraction with EtOAc via GC-FID.

Mediator	**Rate Constant k** [min^1]
No Mediator	0.0136
2,2'-Azino-bis(3-ethylbenzothiazoline-6-sulfonic acid)	0.0113
Violuric acid	0.0134
Ferulic acid	0.0150
Caffeic acid	0.0127
(2,2,6,6-Tetramethylpiperidin-1-yl)oxyl	0.0154

Among all tested compounds, TEMPO stood out by retaining sharp and consistent redox peaks with negligible loss in current or increase in peak separation, demonstrating a high electrochemical stability under oxidative conditions. In contrast, ABTS showed substantial signal fading, peak broadening, and increasing overpotential over time, consistent with oxidative degradation. Similarly, FA exhibited a marked decline in peak intensity, confirming its limited durability despite a redox potential similar to that of LacF. While CA and VA showed slightly more stable profiles, they nonetheless experienced gradual current decay, suggesting partial degradation and insufficient reversibility. These results highlight that electrochemical reversibility, not just redox potential, plays a decisive role in the suitability of a mediator for application in laccasemediator system (LMS). The combination of moderate redox potential and high electrochemical stability renders TEMPO particularly well-suited for use in redox-based electron shuttling [188].

While its redox potential is lower than that of ABTS, it is sufficient to accept electrons from LacF and transfer them to moderately reactive substrates, as confirmed by the kinetic data and molecular docking results presented earlier. Moreover, the reversible nature of the TEMPO redox couple allows for sustained mediator turnover without loss of activity over extended reaction times. In contrast, mediators with very high redox potentials, such as ABTS, may offer greater thermodynamic driving force but often suffer from rapid chemical or electrochemical degradation, thereby limiting their long-term applicability. This trade-off is well documented in scientific literature, where the most efficient LMS are consistently based on redox mediators that exhibit both sufficient oxidizing power and stable redox cycling [190, 192].

Table 5.4 Redox potentials of selected mediators determined by CV.

Molecule	**Redox Potential $E_{1/2}$ [mV]**			**Reference conditions**	**Ref.**
	vs Ag/AgCl	vs NHE	vs NHE_{Ref}		
TEMPO	526	723	696	Acetate buffer, pH 4.5	[166]
VA	693	891	871	Sodium phosphate buffer, pH 7	[189]
CA	359	556			
FA	599	796	790	Tartrate buffer, pH 5	[190]
ABTS	765	962	1090		
LacF	562	759	790	Citrate-phosphate buffer, pH 5	[191]

Overall, the results of the electrochemical analysis underline the performance of TEMPO observed during kinetic screening and support its continued use in LMS targeting sterically hindered, epoxy-based substrates. The data further emphasize that the practical efficacy of a mediator in laccase-catalyzed systems cannot be predicted from its redox potential alone. Instead, the interplay of redox potential, reversibility, structural compatibility, and long-term stability must be considered to design mediator systems that are both efficient and robust.

In this context, TEMPO combines key advantages of synthetic accessibility, oxidative stability, and redox compatibility with fungal laccases, making it the rational choice for future optimization of biocatalytic degradation strategies as described in the following Sections.

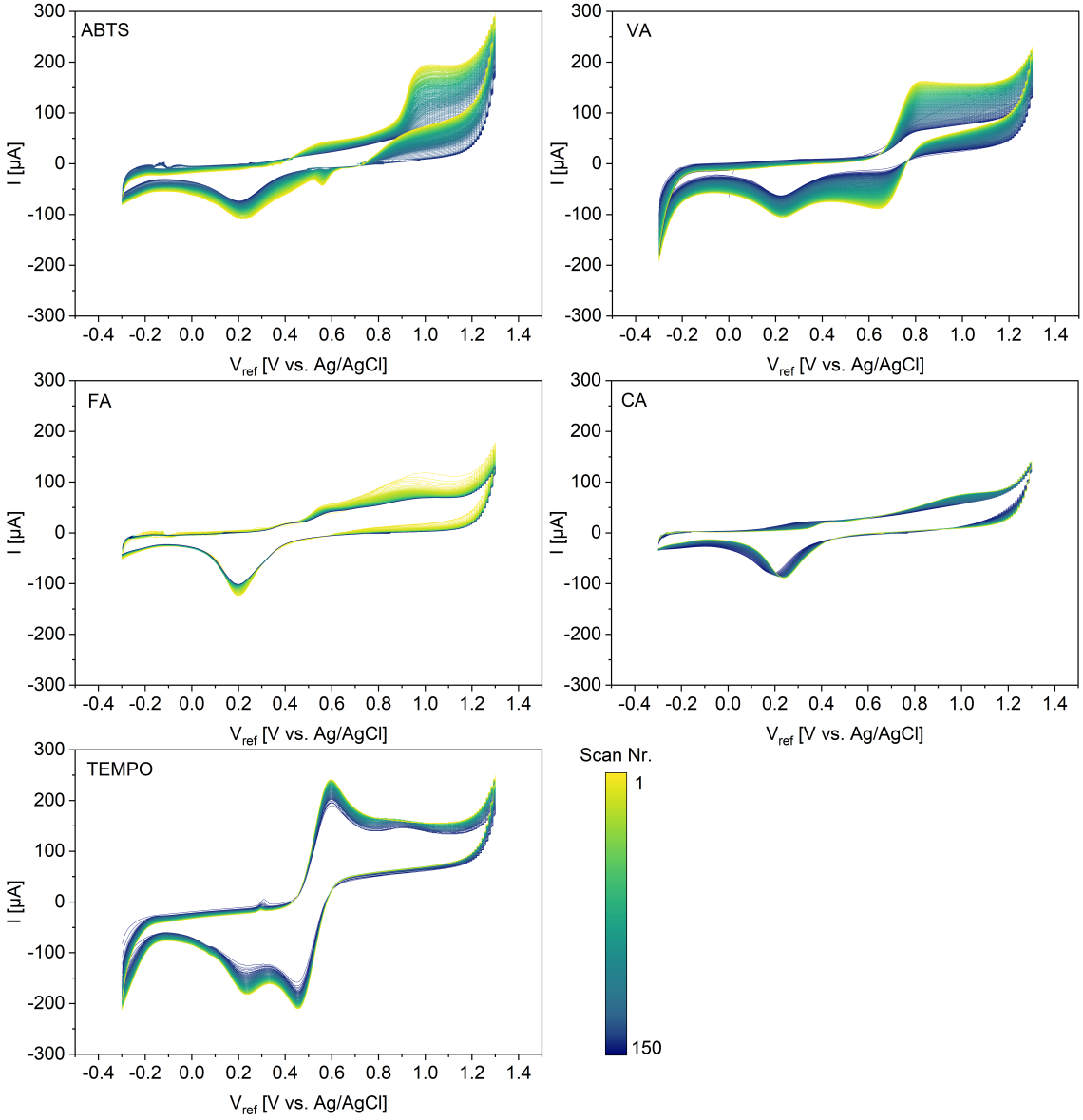

Figure 5.11 Electrochemical stability of redox mediators over 150 consecutive CV cycles. Analyte concentration: 10 mmol · L^{-1}, −0.3 V to 1.3 V, working electrode: 99.95 % platinum plate (1 mm thickness, 9 mm^2 surface area), reference electrode: Ag/AgCl, solution was sparged with N_2. Color progression from yellow (1st scan) to blue (150th scan).

5.1.3 Investigation and Optimization of Reaction Conditions of Laccase-mediated Oxidation of Epoxy Model Compounds

After identifying TEMPO as the most promising mediator for the laccase-mediated oxidation of NNBT, the influence of key reaction parameters on the extent of oxidation was systematically investigated. Optimization experiments focused on the effects of pH, temperature, mediator concentration, and enzyme stability as described by Obleser et al. (2022) [166]. All assays were conducted at a down-scaled volume of 1 mL in glass vials and stopped after 30 min to facilitate comparative analysis. As shown in Figure 5.12, the pH screening revealed a sharp optimum at pH 4, resulting in an NNBT oxidation of approximately 80%.

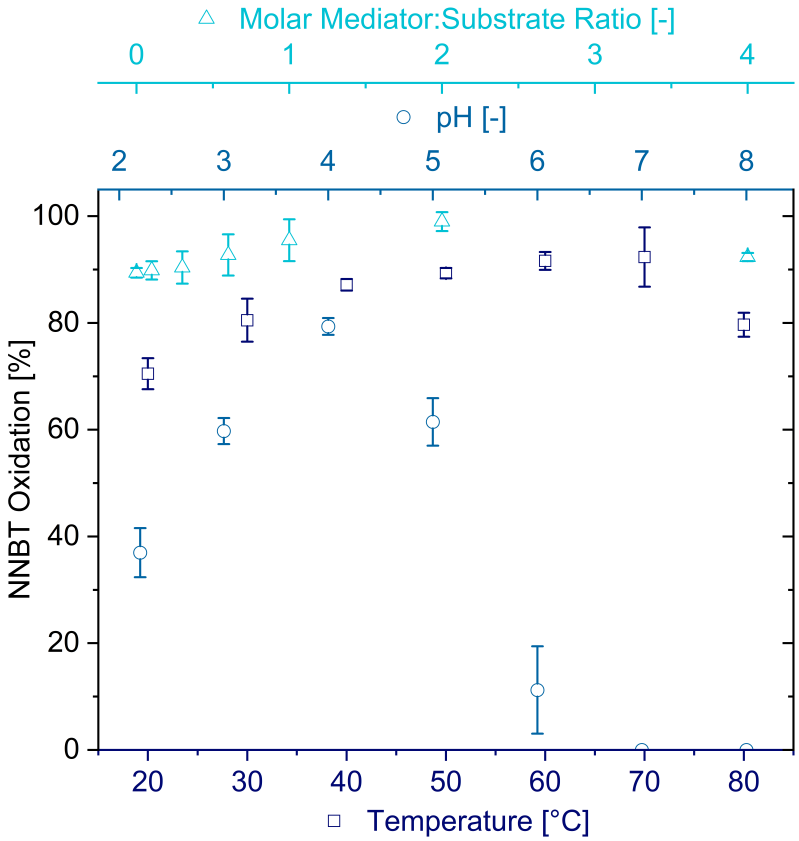

Figure 5.12 Parameter optimization of LacF-TEMPO mediated oxidation of NNBT. Influence of pH (circles), temperature (squares), and TEMPO:NNBT molar ratio (triangles) was evaluated by determining residual substrate after 30 min; 1 mL reaction volume, 0.1 mol · L^{-1} citrate-phosphate buffer pH 2.2 to 8, 5 mmol · L^{-1} NNBT, 0.1 mmol · L^{-1} to 20 mmol · L^{-1} TEMPO, 20 řC to 80 řC, 0.1 U · mL^{-1} LacF, 200 ţL sample was inhibited by 5 ţL 0.05 % NaN_3, remaining NNBT concentration was determined after pH adjustment to 7 and 1:1 extraction with EtOAc via GC-FID.

At higher pH values, especially beyond pH 6, the oxidation efficiency declined drastically and was negligible at pH 7 and 8. This pH-dependence is in line with the known activity profiles of fungal laccases, which typically exhibit maximum activity under acidic conditions due to the protonation state of the active site residues and the redox potential alignment between enzyme and substrate [193, 194]. Temperature profiling between 20 řC to 80 řC under constant pH 4 and mediator concentration (1.5 mmol · L^{-1} TEMPO) indicated an increase in oxidation from 71% to 90% between 20 řC to 60 řC, followed by a significant decline at 80 řC. The increase at moderate temperatures reflects enhanced substrate diffusion and enzyme kinetics, a common feature in *Trametes*-derived laccases such as LacF from *Funalia trogii* [195]. However, the thermal inactivation of LacF became apparent at higher temperatures, necessitating a compromise between activity and stability.

To assess the influence of temperature on enzyme stability, LacF was incubated at pH 4 for 24 h at temperatures ranging from 20 řC to 70 řC. The specific ABTS activity was monitored over time and fitted to first-order deactivation kinetics using a semi-logarithmic plot of residual activity (Figure 5.13). This allowed for the determination of the decay constant λ and the corresponding half-life $t_{1/2}$ for each condition according to Equation 10.

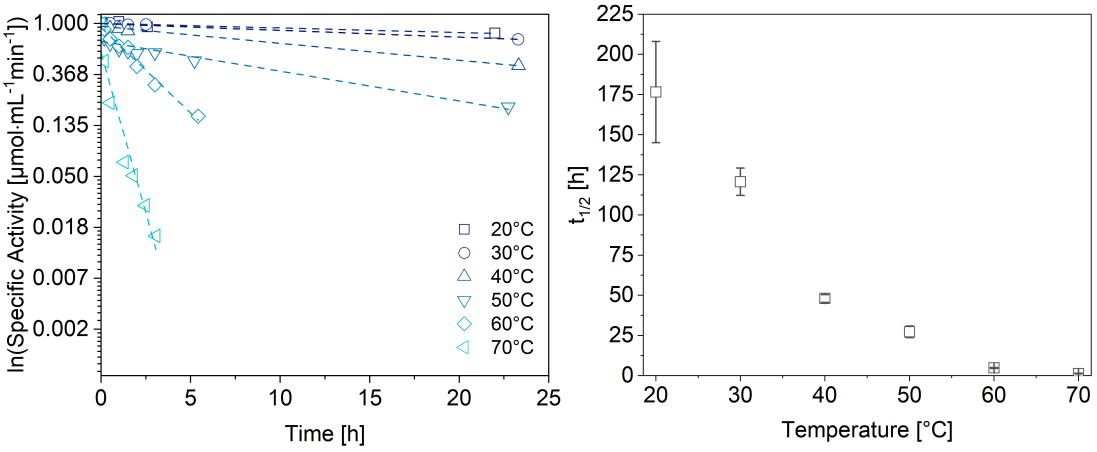

Figure 5.13 Thermal stability of LacF under process conditions. **Left**: Specific ABTS activity during 24 h incubation at different temperatures as semi-logarithmic plot with first-order deactivation kinetics **Right**: Temperature-dependent half-live times of LacF; pH = 4, 10 mmol·L^{-1} TEMPO.

The results revealed a strong dependence of enzyme stability on temperature. At 20 řC, LacF showed exceptional stability with a calculated half-life of 176.51 h. Increasing the temperature to 30 řC reduced the half-life to 120.64 h. Further elevation to 40 řC decreased

stability significantly, yielding a half-life of 47.99 h. At 50 řC, which had previously been identified as an optimal trade-off between activity and stability, the half-life dropped to 27.25 h. At 60 řC and 70 řC, the enzyme rapidly lost activity, with half-lives of 4.75 h and 1.27 h respectively.

These results confirm that the thermal stability of LacF is compromised at elevated temperatures. Consequently, 50 řC was selected as the preferred reaction temperature, as it enables enhanced catalytic performance while maintaining sufficient stability for practical use in prolonged oxidation experiments.

After identifying the most suitable operating temperature, the effect of mediator concentration was investigated in the range of 0 mmol · L^{-1} to 20 mmol · L^{-1} TEMPO (Figure 5.12). A steep increase in oxidation rate up to 10 mmol · L^{-1} was observed, with values approaching quantitative oxidation. Further increase to 20 mmol · L^{-1}, however, led to a decrease in substrate turnover. This decline is likely due to substrate inhibition or destabilizing effects at higher mediator concentrations, as previously observed for similar LMS systems [166]. Overall, combining all optimized parameters (pH 4, 50 řC, and 10 mmol · L^{-1} TEMPO) resulted in a relative NNBT oxidation of approximately 100% within 30 min at the small scale. When these conditions were transferred to a 10 mL reaction volume, the apparent rate constant increased by 50% compared to the initial parameter setup. However, the overall conversion remained lower than in the small-scale experiments. This discrepancy was attributed to a high likelihood of limited oxygen availability in the stirred batch reactor as previously reported by other authors [166, 196]. To investigate whether the reduced reaction rates in the 10 mL setup were due to insufficient oxygen availability, oxygen saturation was monitored using a PreSens (Regensburg, Germany) dipping probe according to Section 4.7.7.

In the absence of active aeration, a rapid decline in dissolved oxygen was observed within the first few minutes of the reaction (Figure 5.14 (Left)). Oxygen saturation dropped to around 6 % and remained below 30 % for the majority of the reaction time. This trend coincided with a plateau in the oxidation of NNBT, as shown in the left-hand graph. This observation aligns with findings that oxygen can be a limiting factor in laccase-mediated oxidation processes, resulting in reduced turnover frequencies when dissolved oxygen is rapidly consumed [197]. Mechanistically, this phenomenon is rooted in the catalytic cycle of laccases, in which molecular oxygen acts as the terminal electron acceptor at the T2/T3 copper cluster as highlighted in Section 2.4. Once oxygen becomes depleted, the oxidation of the reduced trinuclear center is stalled, preventing the regeneration of the catalytically active oxidized form of the enzyme.

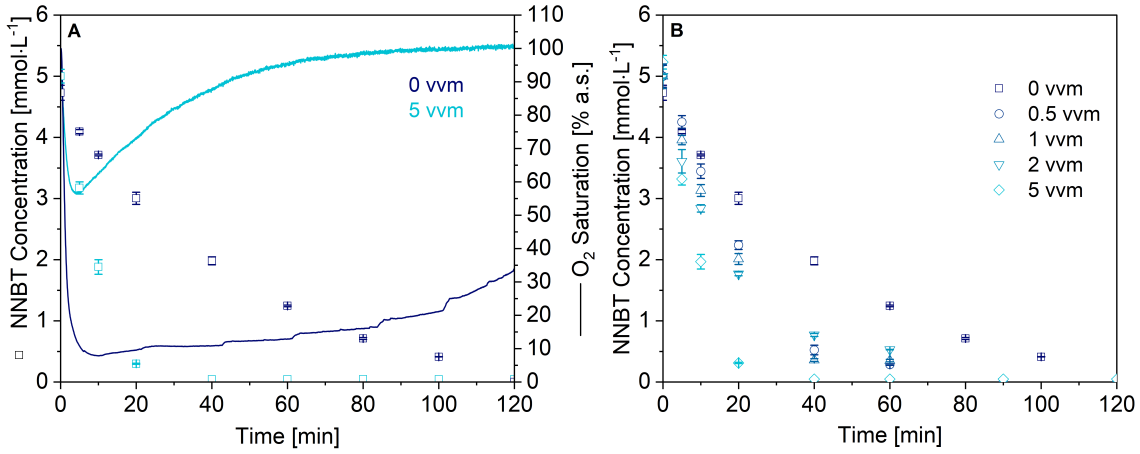

Figure 5.14 Left: Monitoring of NNBT concentration and oxygen saturation in 10 mL batch reactions with and without aeration. **Right**: Time-dependent NNBT concentration in batch reactions with varying aeration rates from 0 to 5 vvm. 5 mmol · L^{-1} NNBT, 10 mmol · L^{-1} TEMPO, 0.1 U · mL^{-1} LacF, pH 4, 50 řC, 750 rpm. Oxygen concentration was measured using a PreSens (Regensburg, Germany) DP-PSt3 probe.

Applying an air flow of 5 vvm (equivalent to 200 mL · min^{-1}) significantly increased oxygen availability and restored saturation levels to nearly 100 % after around 1 h. This enhancement in oxygen supply translated into markedly improved reaction performance, with NNBT being completely oxidized within 60 min under otherwise identical conditions. Similar improvements in substrate conversion under aerated conditions have been reported for other laccase-catalyzed reactions [198]. Matijosyte (2008) [199] has shown that aeration can accelerate laccase-mediated TEMPO oxidations of alcohols by up to one order of magnitude, particularly when using *Trametes sp.*-derived laccases, which display a high k_{cat} for molecular oxygen. These findings underline that the apparent reaction rate is not solely determined by substrate or mediator concentration but strongly depends on oxygen transfer from the gas phase to the liquid phase.

The extent of this dependency is further supported by the experiments conducted at varying specific aeration rates ranging from 0 to 5 vvm. As shown in Figure 5.14 (Right), incremental increases in aeration led to a progressive acceleration of the reaction, with complete substrate conversion only achieved at the highest tested flow rate. While moderate effects were observed at 0.5 to 2 vvm, a flow rate of 5 vvm was sufficient to fully counteract oxygen limitation. As oxygen solubility in aqueous buffers is intrinsically low (typically 0.25 mmol · L^{-1} at 25 řC and 1 atm), making oxygen diffusion into the reaction phase a critical bottleneck when laccases are operating at high turnover [200, 201].

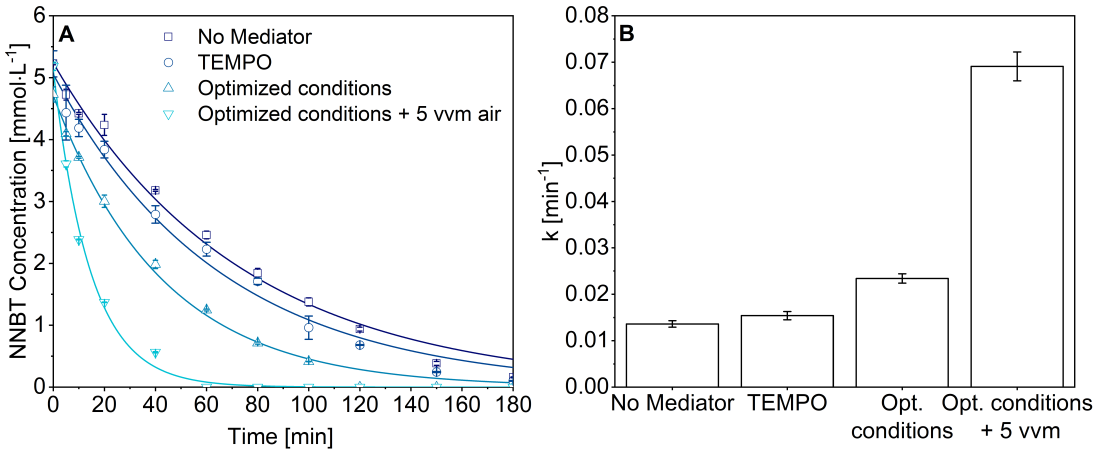

Figure 5.15 Comparison of NNBT oxidation by LacF under different conditions. **Left:** Monitoring of NNBT concentration over time. **Right:** First order reaction constants derived from non-linear fitting of reaction progression. 10 mL reaction volume, 5 mmol · L^{-1} NNBT, 0.1 U · mL^{-1} enzyme, 0.1 mol · L^{-1} citrate-phosphate buffer pH 4.5, 750 rpm; Without Mediator: 30 řC, TEMPO: 1.5 mmol · L^{-1} TEMPO, 30 řC, pH 4.5, Optimized Conditions: 10 mmol · L^{-1} TEMPO, 50 řC, pH 4, Aeration: 5 vvm air; 200 ţL sample was inhibited by 5 ţL 0.05 % NaN_3, remaining NNBT concentration was determined after pH adjustment to 7 and 1:1 extraction with EtOAc via GC-FID; first-order kinetic fitting was done with the `scipy.optimize.curve_fit` (NumPy library) function (all $R^2 > 0.98$).

Given these considerations, 5 vvm was selected as the standard condition for all subsequent reactions. The cumulative impact of the individual optimization steps is summarized in Figure 5.15. A stepwise improvement in reaction rate was observed as each key parameter was adjusted. The starting point, using LacF without a mediator at pH 4.5 and 30 řC, resulted in the slowest conversion of NNBT, with less than 50 % oxidation after 90 min. Supplementing the system with TEMPO as a redox mediator increased the rate constant modestly, confirming its role in accelerating the oxidation cycle via radical-mediated electron transfer from the substrate to the enzyme's active site [166]. Further improvement was achieved by implementing the optimized reaction conditions (pH 4, 50 řC, 10 mmol · L^{-1} TEMPO), which maximized substrate oxidation within a significantly shorter time frame. This enhancement can be attributed to the improved ratios of enzyme, mediator, and substrate under acidic and thermally activated conditions. The final step, applying 5 vvm compressed air as an additional oxygen source, yielded the highest rate of NNBT depletion. The resulting apparent first-order rate constant (0.0691 min^{-1}) was more than fivefold higher than in the non-aerated reference system without a mediator (0.0136 min^{-1}). This underlines the synergistic effect of combining optimized mediator concentration, temperature, pH, and sufficient oxygen supply. The integrated approach addresses both kinetic and

thermodynamic limitations of the laccase-mediator system, facilitating rapid and complete oxidation of the model substrate.

5.1.4 Degradation Pathways of Model Compounds

To investigate the degradation of the model compound NNBT upon oxidation with the LMS, gas chromatography coupled mass spectrometry (GC-MS) analysis was performed on reaction supernatants after incubation under optimized conditions. The sample preparation involved liquidliquid extraction using ethyl acetate (EtOAc) while employing Na_2SO_4 in the aqueous phase to promote a salting-out effect and thereby enhance the extraction efficiency of polar degradation products (Section 4.8). The resulting total ion chromatogram (TIC) chromatograms (Figure 5.16) revealed substantial differences between the control and the laccase-treated samples.

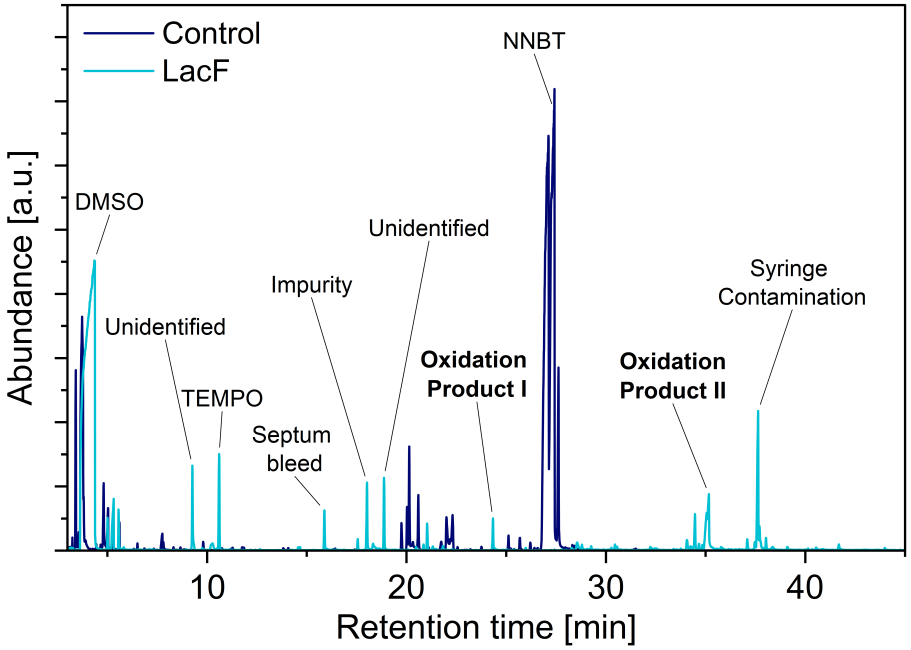

Figure 5.16 GC-MS chromatogram of NNBT oxidation reactions with and without LacF/TEMPO. Extraction was performed with EtOAc using Na_2SO_4 in the aqueous phase according to Section 4.8.

While the control primarily contained the unreacted NNBT along with known impurities and solvent traces, the treated samples exhibited two additional, well-defined peaks at retention times of 24.3 min and 35.2 min. These peaks were not present in the control and were therefore assigned to oxidation products of NNBT. The mass spectra (Figure 5.17) of these oxidation products were interpreted based on fragment ion patterns, elemental

composition, and comparison with database entries. One of the major fragments ($m \cdot z^{-1}$ = 120.1) in oxidation product I corresponds to a C_8H_9N moiety, suggesting that cleavage occurred adjacent to the nitrogen atom. A second fragment of 29.0 $m \cdot z^{-1}$ (CHO) indicates an aldehyde functional group, consistent with a C–C bond scission in the side chain. In contrast, oxidation product II retains the entire side chain but shows a prominent fragment of 192.1 $m \cdot z^{-1}$, indicating hydroxylation followed by oxidation of a secondary alcohol to a ketone. These findings suggest a sequential oxidation mechanism (Figure 5.18), in which initial hydroxylation of the propyl side chain is followed by either direct ketone formation or C–C bond cleavage.

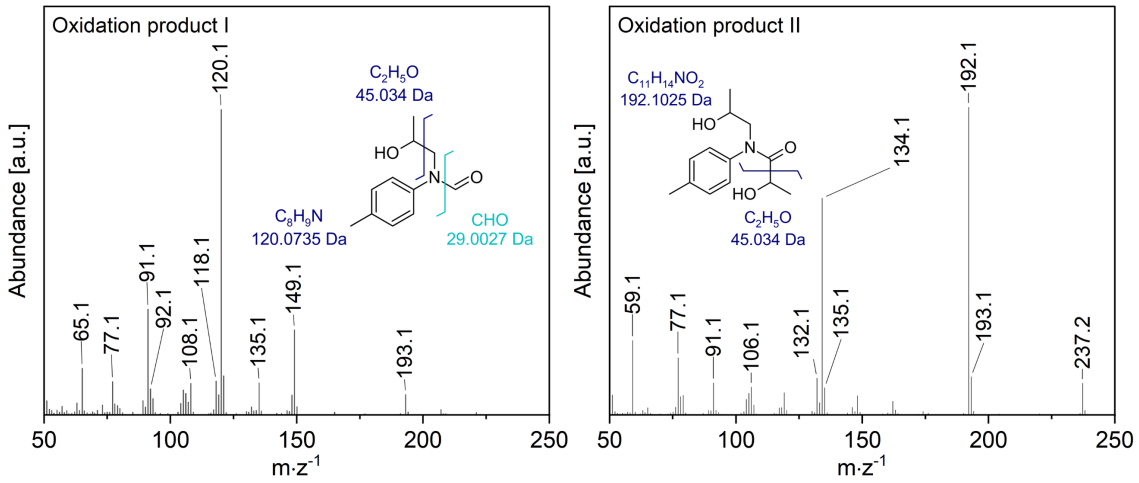

Figure 5.17 Fragmentation pattern of oxidation products I and II from NNBT as identified in the TIC. Assignments are based on elemental composition and structure-supported fragmentation. Proposed fragments are color-coded.

Both routes are likely initiated by the redox mediator in its oxidized form (Med_{ox}) or the laccase itself, which abstracts an electron from the substrate to form a substrate radical. The radical intermediate can then undergo oxygen insertion and further oxidative cleavage through interaction with the oxidized laccasemediator couple. Similar fragmentation patterns and pathways have been reported for other *N*-substituted aromatic amines under oxidative conditions [182, 202, 203]. A related oxidative degradation mechanism has been described by Dolz et al. (2022) [84], who investigated the transformation of NNBT using UPOs.

In their study, the authors demonstrated that UPOs can catalyze selective hydroxylations and *N*-dealkylations of the amine-containing structure via substrate radical formation. While the catalytic mechanism differs fundamentally from that of the LacF/TEMPO system, the observed reaction outcomes show notable similarities of the (per)oxidases.

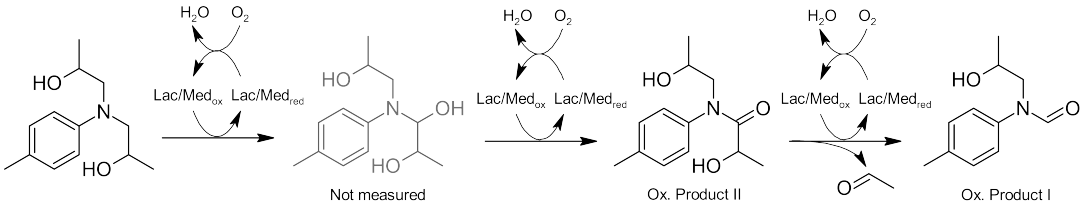

Figure 5.18 Reaction scheme illustrating the proposed oxidative degradation pathway of NNBT via hydroxylation and subsequent ketone formation or CC bond cleavage, catalyzed by the LacF/TEMPO LMS.

For instance, the cleavage of C–N and adjacent C–C bonds, as observed in the formation of oxidation product I from NNBT, resembles the fragmentation of aliphatic substituents reported for UPO-treated substrates. These parallels support the hypothesis that substrate-derived radicals, once formed, can follow comparable degradation trajectories regardless of whether the initiating oxidant is a high-valent ironoxo species or an organic radical derived from a redox mediator.

To complement the investigation of NNBT as epoxy surrogate, the degradation of a structurally distinct second model compound MB was evaluated under the same oxidative conditions. MB contains a central methylene bridge flanked by two electron-rich aromatic amines, making it representative of the highly conjugated amine-functionalized polymer structure of RTM6. Due to its extended conjugation and polarizability, MB is expected to be more prone to oxidation at the benzylic position than NNBT.

The reaction mixtures were subjected to GC-MS analysis following liquidliquid extraction with EtOAc and phase saturation using Na_2SO_4, as described before. Compared to the untreated control, the LMS-treated samples showed the formation of two distinct new peaks in the TIC (Figure 5.19), eluting at approximately 19 min and 21 min. These peaks were absent in the control and consistently observed in replicate reactions, strongly suggesting that they represent MB-derived oxidation products. The time-resolved TIC overlay further demonstrated a steady increase in peak intensity over the reaction course from 0 min to 60 min, indicating continuous and progressive formation of both oxidation products. Analysis of the corresponding mass spectra revealed fragmentation patterns consistent with benzylic hydroxylation and C–C bond cleavage, as shown in Figure 5.20. In oxidation product I, major fragments were detected at 134.1 and 151.2 $m \cdot z^{-1}$, which can be attributed to hydroxylated benzylamine derivatives. Product II displayed prominent fragments at 105.1, 120.1, and 148.1 $m \cdot z^{-1}$, consistent with cleavage of the central methylene group and formation of a carbonyl-containing aromatic compound.

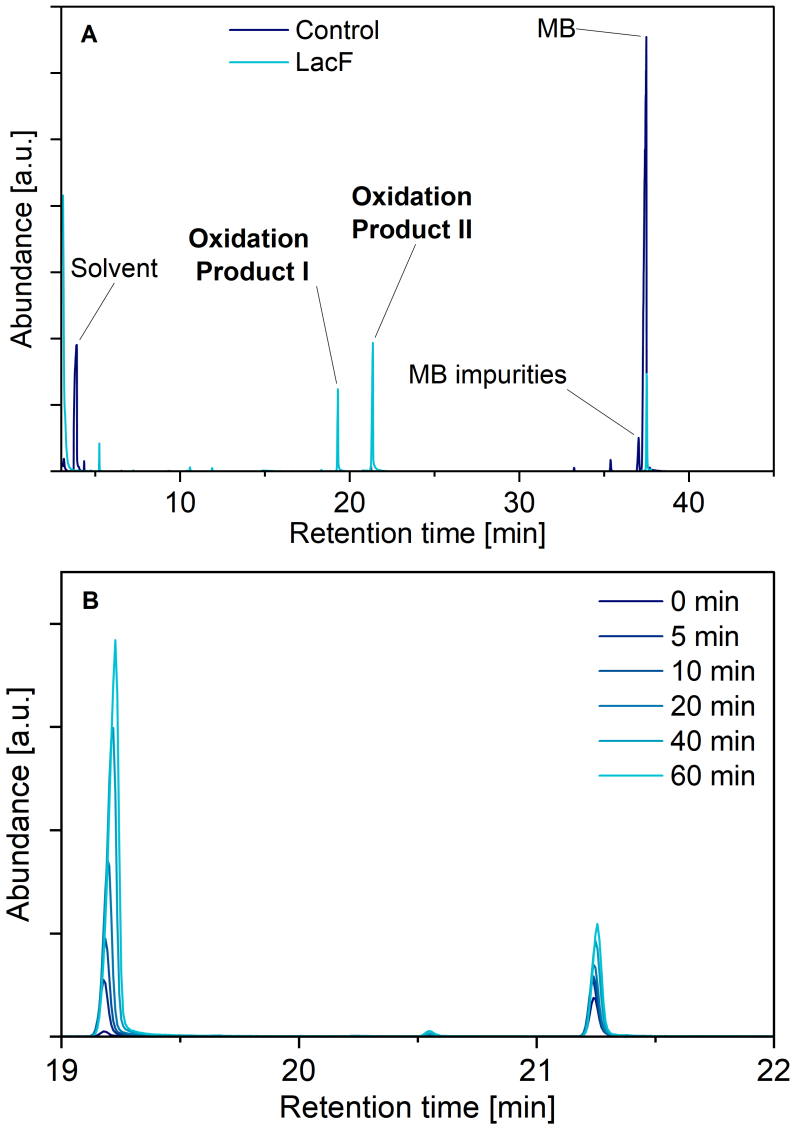

Figure 5.19 A: GC-MS chromatogram comparing LMS-treated and control MB reactions. Oxidation products I and II are observed only after enzymatic treatment. **B**: Time-resolved TIC overlay illustrating the progressive accumulation of both products over a time course of 60 min. Extraction was performed with EtOAc using Na_2SO_4 in the aqueous phase according to Section 4.8.

These fragmentation patterns align with proposed structures based on electron-rich aromatic substitution and resonance stabilization of radical intermediates. A mechanistic rationale for the formation of the two observed products is presented in Figure 5.21. The initial step likely involves hydrogen abstraction at the benzylic carbon, forming a stabilized benzyl radical intermediate. This radical can undergo oxygen insertion to form a hydroxylated derivative (oxidation product I), or it may react further to induce cleavage of the central methylene group. The latter route would generate two mononuclear aromatic fragments, one of which carries a newly introduced aldehyde or ketone group (oxidation product II). Both transformations are consistent with radical-driven oxidations previously described for other methylene-bridged aromatic amines [204, 205].

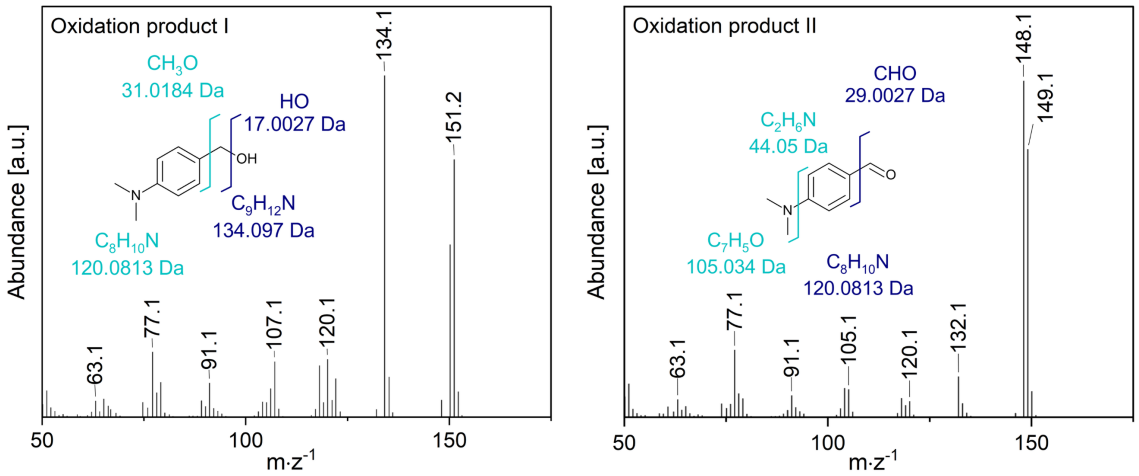

Figure 5.20 Fragmentation pattern of oxidation products I and II from MB as identified in the TIC. Assignments are based on elemental composition and structure-supported fragmentation. Proposed fragments are color-coded.

Overall, these findings are in agreement with literature describing similar transformations. For instance, laccase-catalyzed degradation of diarylamines and triarylmethanes has been shown to proceed via comparable benzylic and arylamine oxidation pathways [206]. Furthermore, the observed stepwise formation and accumulation of oxidation products mirrors the LMS-mediated degradation of hydroxycinnamic acids and aromatic pollutants in environmental applications, where progressive oxygen incorporation and radical rearrangement guide substrate breakdown [207, 208].

NNBT and MB prove to be structurally informative substrates for monitoring LMS-mediated oxidation of RTM6-related structures. For both molecules, relevant oxidative degradation patterns could be derived from the GC-MS data, translating to backbone scission when extrapolated to the actual crosslinked polymer structure. These findings

emphasize the applicability of LMS for epoxy polymer oxidation and potential degradation, as discussed in the subsequent section.

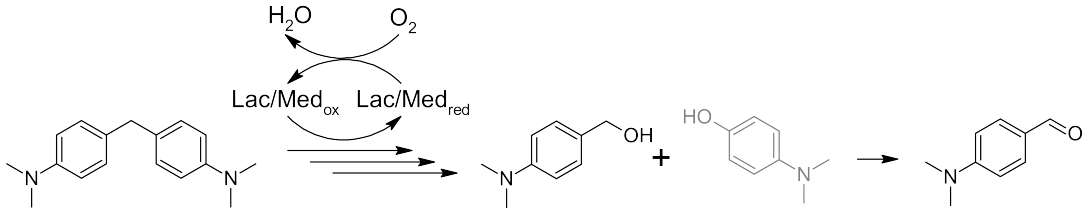

Figure 5.21 Proposed degradation mechanism of MB catalyzed by the LacF/TEMPO LMS. The reaction proceeds via benzylic radical formation and either hydroxylation or bond cleavage to yield the observed products.

5.1.5 Resin Treatment with Laccase-Mediator System

To evaluate the applicability of the LMS to real polymeric substrates, the epoxy resin particles prepared as described in Section 5.1.1, were subjected to enzymatic oxidation using the previously optimized LacF/TEMPO system. However, preliminary batch experiments in stirred-tank reactors revealed that, instead of being suspended in the reactor, the particles tended to float persistently on the surface of the aqueous phase, practically eliminating proper contact to the enzymatic reaction system. This behavior was attributed to their relatively low specific density of $1.14\,\mathrm{g}\cdot\mathrm{cm}^{-3}$ in combination with the high hydrophobicity of the cured epoxy network (Figure A.5). Consequently, an alternative reactor concept was required to ensure adequate contact between solid and liquid phases. A packed-bed configuration was chosen, in which resin particles were immobilized within a vertical flow cell and continuously perfused with aerated LMS solution. The corresponding process and instrumentation diagram is shown in Figure 5.22. This setup allowed for extended contact times, minimized phase separation, and enabled reuse of enzyme solution by recirculation.

Following a 24 h reaction period under optimized LMS conditions according to Section 4.11, multiple analytical techniques were employed to assess resin modification by the LMS. ATR-FTIR provided molecular-level insight into chemical changes of the epoxy resin surface upon LMS treatment. As shown in Figure 5.23, the fourier-transform infrared spectroscopy (FTIR) spectra of control and LMS-incubated samples differ notably in key absorption regions. A clear increase in C=O stretching intensity near $1700\,\mathrm{cm}^{-1}$ and a broadening of the OH stretching band between $3200\,\mathrm{cm}^{-1}$ to $3500\,\mathrm{cm}^{-1}$ indicate the formation of carbonyl- and hydroxyl-groups. These are consistent with oxidation of the polymer backbone as seen before in the early reaction steps of the proposed oxidation mechanisms of the RTM6 model compounds in Section 5.1.4.

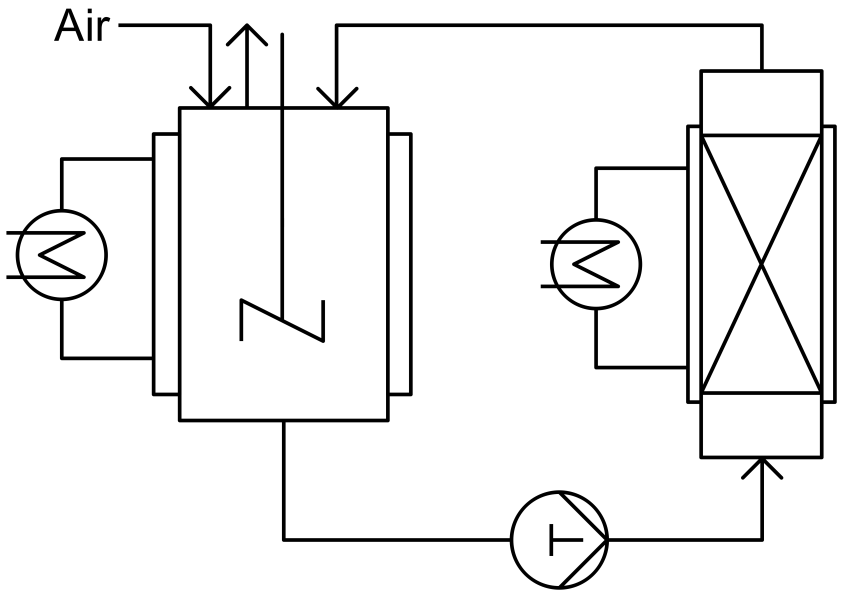

Figure 5.22 Process and instrumentation diagram of the fixed-bed reactor used for resin oxidation with the LMS. A HPLC pump enabled continuous circulation of LMS solution over a packed bed of epoxy resin particles under oxygenated conditions.

Slight alterations in intensity of amine- and aromatic-associated vibrations (1350 cm^{-1} to 1200 cm^{-1} and > 900 cm^{-1}) further indicate the oxidation of electron-rich sites. The inset photograph illustrates the accompanying visual change of the polymeric material. The initially pale-yellow particles became distinctly green after incubation, likely due to oxidized derivatives of aromatic structures formed during oxidation [209]. Furthermore, the observed alterations in the FTIR spectra can be interpreted to imply a physical degradation of the polymer backbone. As can be seen in Figure 5.3, RTM6 is a nitrogen-rich macromolecule whose bond cleavage would have caused an increase in the frequencies of secondary and primary amines in the FTIR spectrum. As these are, among others, located within the hydroxyl band and result in a shift towards lower wavenumbers, it can be deduced that a low degree of degradation has occurred. The increase and broadening of the peak just above 1600 cm^{-1} can also be interpreted in terms of C–N bond cleavage, in addition to the oxidation of the molecule [210, 211].

Additionally, TGA was performed to evaluate the thermal integrity of epoxy resin before and after oxidative modification as an indicator for potential backbone breakage and decrease in molecular weight. Figure 5.24, shows the TGA profiles of the untreated reference and the LacF/TEMPO-treated sample under a nitrogen atmosphere. Both samples

exhibit thermal stability up to approximately 300 řC, with negligible mass loss in this range, indicating the absence of significant volatile impurities or moisture.

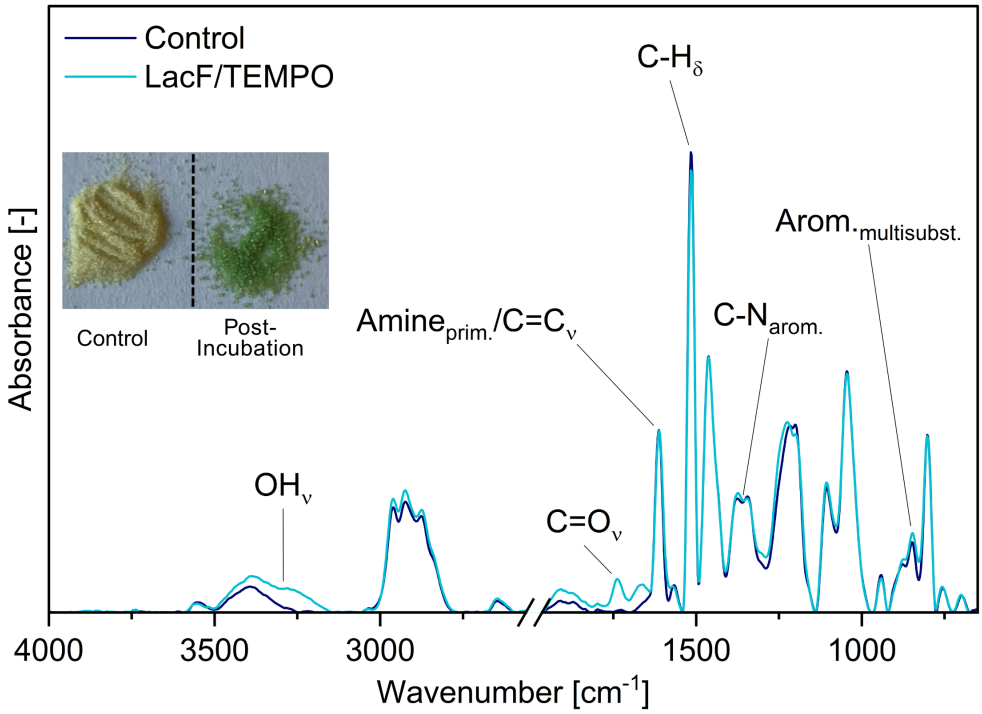

Figure 5.23 ATR-FTIR spectra of untreated (control) and LMS-treated epoxy resin recovered from the packed-bed reactor. **Inset:** visual comparison of resin particle color before and after LMS treatment. Incubation according to Section 4.11 and FTIR acquisition as described Section 4.4.4.

The primary degradation event for both materials occurs between approximately 300 řC to 450 řC. The LMS-treated sample shows an earlier onset of thermal degradation at around 342 řC, compared to the reference with 362 řC, as well as a slightly more gradual mass loss. This behavior indicates that the oxidation process introduces thermally labile functionalities, such as hydroxyl and carbonyl groups, into the polymer network [212]. Similar observations were made by Aracri et al. (2012) [213], who investigated the effect of a *Trametes villosa*-TEMPO LMS treatment of cellulose fibers by TGA. They detected an earlier thermal degradation of the fibers due to oxidative damage of the reaction system, similar to the observed effect in Figure 5.24. A notable difference between the two samples is the residual mass at 600 řC. The reference sample retains 12.88% of its initial mass, whereas the LacF/TEMPO-treated sample retains 30.88%. The increased char yield in the oxidized sample suggests reduced crosslinking or the formation of aromatic or polyaromatic structures during decomposition, resulting in a more thermally stable residue [214].

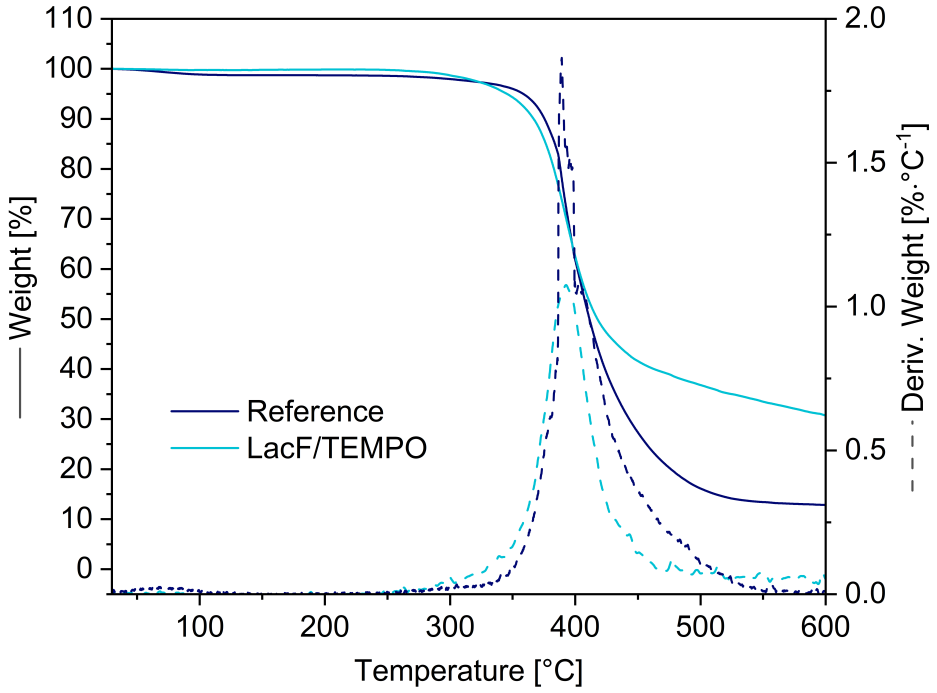

Figure 5.24 Thermogravimetric curves of epoxy resin before and after LMS treatment. Incubation according to Section 4.11 and TGA acquisition as described Section 4.4.2.

These findings are consistent with the FTIR results and indicate that enzymatic oxidation not only alters surface chemistry but also impacts thermal degradation behavior. In addition to spectral and thermal analysis, elemental composition of the resin was evaluated via CHNS analysis. The detailed results are summarized in Table 5.5. Compared to the untreated control, the LMS-incubated sample showed a negligible decrease in nitrogen (from 76 g · kg^{-1} to 73 g · kg^{-1}) and carbon content (from 760 g · kg^{-1} to 750 g · kg^{-1}), while the oxygen content increased markedly from 84 g · kg^{-1} to 110 g · kg^{-1}. Sulfur and hydrogen remained essentially unchanged. These compositional shifts are reflected in the calculated elemental ratios: the C/O ratio decreased from 9.05 to 6.82, while the C/H and C/N ratios increased slightly. The increase in oxygen content confirms the incorporation of oxidized functionalities (e.g., hydroxyls and carbonyls) into the polymer matrix. The slight nitrogen depletion suggests partial *N*-dealkylation, which is in agreement with the proposed LMS-mediated degradation mechanism. These changes are consistent with the formation of polar groups and support the oxidative modification pathway inferred from ATR-FTIR and TGA results. However, it should be noted that the CHNS analysis of the small resin samples is subject to relatively high analytical uncertainty. According to the standard errors reported by the Central Laboratory of the Hamburg University of

Technology, the reproducibility, particularly for nitrogen and carbon contents, can vary significantly at low sample masses. Therefore, the observed elemental differences should be interpreted as indicative trends rather than absolute quantitative changes.

Table 5.5 Elemental composition and atomic ratios of untreated and LMS-treated epoxy resin particles. Elemental analysis was carried out by the Central laboratory of the Hamburg University of Technology as described in Section 4.4.3.

	Concentration [$\mathbf{g \cdot kg^{-1}}$]					**Elemental Ratios** [–]		
Sample	N	C	H	S	O	C/O	C/H	C/N
Control	76	760	86	2	84	**9.05**	10.00	8.84
LMS-incubated	73	750	86	5	110	**6.82**	10.27	8.72

To rationalize the observed chemical and thermal changes in the LMS-treated epoxy resin, a set of plausible oxidative degradation pathways is proposed. These are based on the known chemistry of benzylic alcohol oxidation and *N*-dealkylation, and are visualized in Figure 5.25, using RTM6-derived monomer structures as representative epoxy building blocks. The hypothesized reaction cascade is initiated by the oxidation of benzylic alcohols present in the epoxy network (structure I). In the presence of laccase-generated $TEMPO^+$, a hydride transfer from the alcohol to the oxoammonium species yields the corresponding ketone (structure III or V). In aqueous and mildly acidic environments, species II or IV can undergo nucleophilic attack by water, leading to formation of a hydroxy group.

While these intermediates may not be stable in isolation, their formation can be plausible under continuous oxidizing conditions. This mechanism is consistent with well-characterized TEMPO-mediated oxidations of primary and secondary alcohols [166]. Compound III can further oxidize to the ketone species IV. Oxidized forms such as IV are expected to exhibit the pronounced C=O bands observed in the ATR-FTIR spectra near $1700\,cm^{-1}$, as well as thermal destabilization due to the cleavage of nearby ether linkages.

Parallel to these benzylic pathways, $TEMPO^+$ may also attack *N*-substituted aromatic sites. Starting from precursor I, hydride abstraction yields a reactive iminium ion (species VII) that reacts to hydroxylated intermediate VIII. The hydroxylated species can further oxidize to ketone IX, and subsequently lead to backbone scission near the tertiary amine. Similar oxidative *N*-dealkylation and ring-oxidation patterns have been described in LMS-catalyzed breakdown of lignin model compounds and polyaromatic amines [104, 215].

These conjugated structures can be considered to contribute to coloration (e.g., green-brown discoloration of the treated resin), as well as to the increased char formation during thermal degradation due to their aromatic stabilization and lower volatility [216, 217].

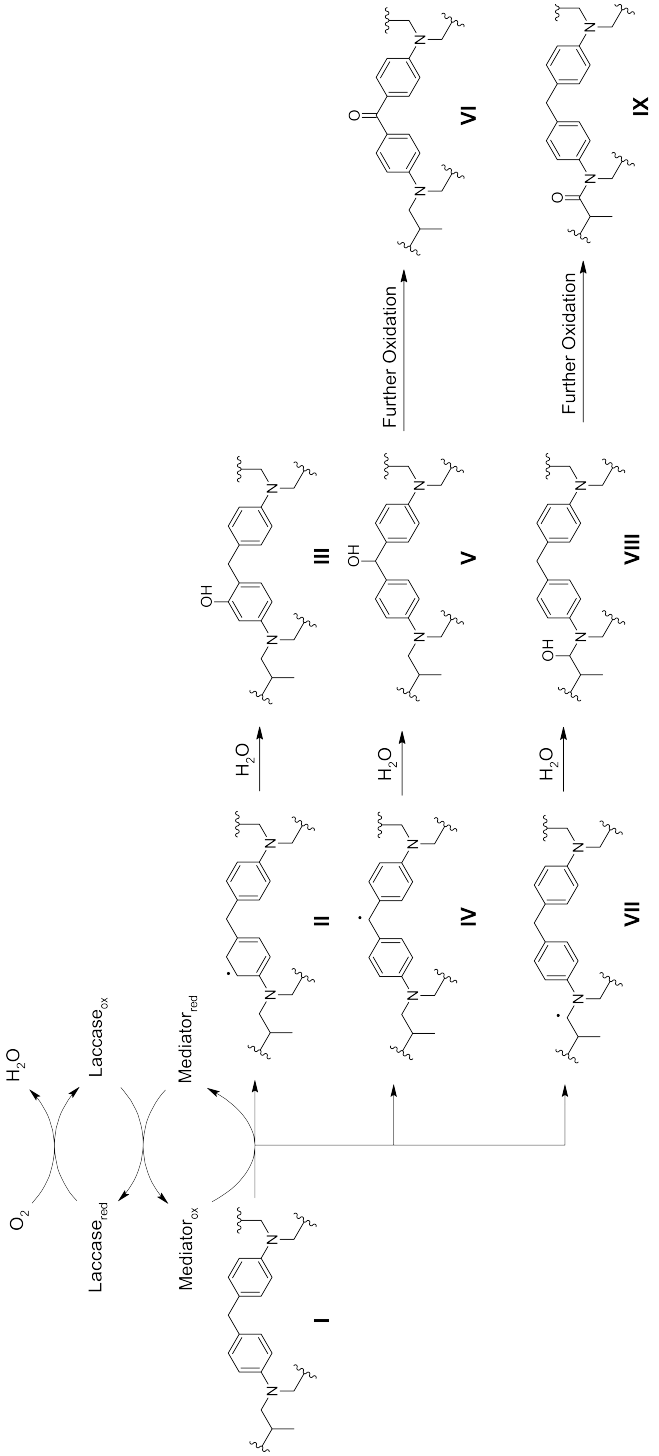

Figure 5.25 Proposed degradation mechanism of epoxy resin network motifs based on RTM6 structure. Products IIX denote possible intermediates and oxidized structures.

In summary, the LMS-induced oxidation of RTM6-based resin segments likely proceeds via multiple converging pathways involving benzylic alcohol oxidation (I → II → III), amine oxidation and (I → VII → VIII), and eventual formation of highly oxidized fragments (IX). These mechanisms are consistent with the combined results from ATR-FTIR, TGA, and elemental analysis, and are in line with mechanistic studies on LMS-mediated transformations of aromatic polymers [195]. Importantly, these mechanistic considerations are also in agreement with the results obtained for the model compounds NNBT and MB, discussed in Section 5.1.4. In both cases, GC-MS analysis revealed oxidation adjacent to aromatic and tertiary amine motifs, producing structurally related carbonyl-rich degradation products. The spectral and structural changes observed in the RTM6 resin, particularly the formation of carbonyl and hydroxyl functionalities, thermal destabilization and increased char yield, and a decreased C/O ratio, can thus be interpreted as analogues to the model compound reactions. The agreement across scales and substrates validates the conceptual use of NNBT and MB as mechanistically relevant surrogates for epoxy resin degradation and confirms the broad applicability of the LMS for targeting benzylic and aromatic amine motifs in crosslinked thermoset networks. Overall, the observed physicochemical changes support the assumption that the applied LMS treatment initiated oxidative modifications in the cured epoxy network. Nevertheless, the fixed-bed reactor setup used in this study was primarily intended to demonstrate the general feasibility of enzymatic oxidation of solid epoxy materials rather than to provide optimized process conditions. Future experiments could focus on improving mass transfer and enzymesubstrate interaction by adjusting the particle size distribution, modifying the surface hydrophobicity of the resin particles through pretreatment, or implementing alternative reactor designs with enhanced contact efficiency.

5.1.6 Investigation of DES as Alternative Reaction Medium for Biocatalytic Epoxy Degradation

To improve the solubility and wettability of the hydrophobic epoxy matrix, deep eutectic solvents (DES) were explored as alternative media for biocatalytic treatment. DES, as introduced in Section 2.5.1, are designer solvents typically formed by mixing a hydrogen bond acceptor (HBA) with a hydrogen bond donor (HBD), which form a eutectic mixture characterized by a lower melting point than each component. Their tunable physicochemical properties make DES promising candidates for enzymatic biotransformations and polymer dissolution.

Selection and Synthesis of DES for Epoxy Degradation

A conductor-like screening model for real solvents (COSMO-RS) simulation was employed to identify promising HBA/HBD combinations for enhanced interaction with the epoxy resin substructure. Based on quantum chemical descriptors and statistical thermodynamics, COSMO-RS predicts solutesolvent affinities by estimating activity coefficients ($\ln \gamma$) at infinite dilution. A representative epoxy model compound derived from RTM6 was used as the query molecule (Figure 4.2). The simulation yielded over 30,000 equimolar HBAHBD combinations. A visual matrix of activity coefficients (Figure 5.26) revealed that alkane diols and carboxylic acids as HBD paired with phenolics and tertiary ammonium salts as HBAs showed the highest predicted solubility for the epoxy model. From the ranked output, three combinations were selected for experimental synthesis based on predicted affinity and commercial availability (Table 5.6). These were synthesized by combining HBA and HBD in equimolar ratio and incubating the mixture at 80 řC to 100 řC under constant stirring until a homogeneous liquid formed.

In addition to the COSMO-RS-predicted systems, several DES were selected based on literature reports for their relevance in biocatalysis or lignocellulosic biomass processing [126, 108, 111, 218]. These included common quaternary ammonium-based systems such as choline chloride:ethylene glycol (ChCl:EG), choline chloride:lactic acid (ChCl:LA), and choline chloride:formic acid (ChCl:FA), all of which have previously been shown to enhance the solubility of hydrophobic substrates or act as compatible media for laccases and other oxidoreductases. Furthermore, polyol-based DES such as betaine:glycerol (BET:GLY), betaine:sorbitol (BET:SOR), and formulations with sugar alcohols like choline dihydrogen citrate:xylitol (ChDHC:XYL) and choline dihydrogen citrate:erythritol (ChDHC:ERY) were included to assess the effect of high hydrogen-bond donor density and hydroxyl-rich environments on DES polarity and enzyme compatibility.

These literature-based mixtures served as important reference systems, allowing for comparison between novel COSMO-RS-generated candidates and DES already validated in biocatalytic or lignin extraction contexts. Notably, while many of these systems did not exhibit the lowest COSMO-RS-predicted activity coefficients, their physical properties and proven enzyme tolerance made them attractive options for testing of LMS performance and epoxy resin wetting. Most of the synthesized DES exhibited moderate viscosity at room temperature, comparable to that of glycerol.

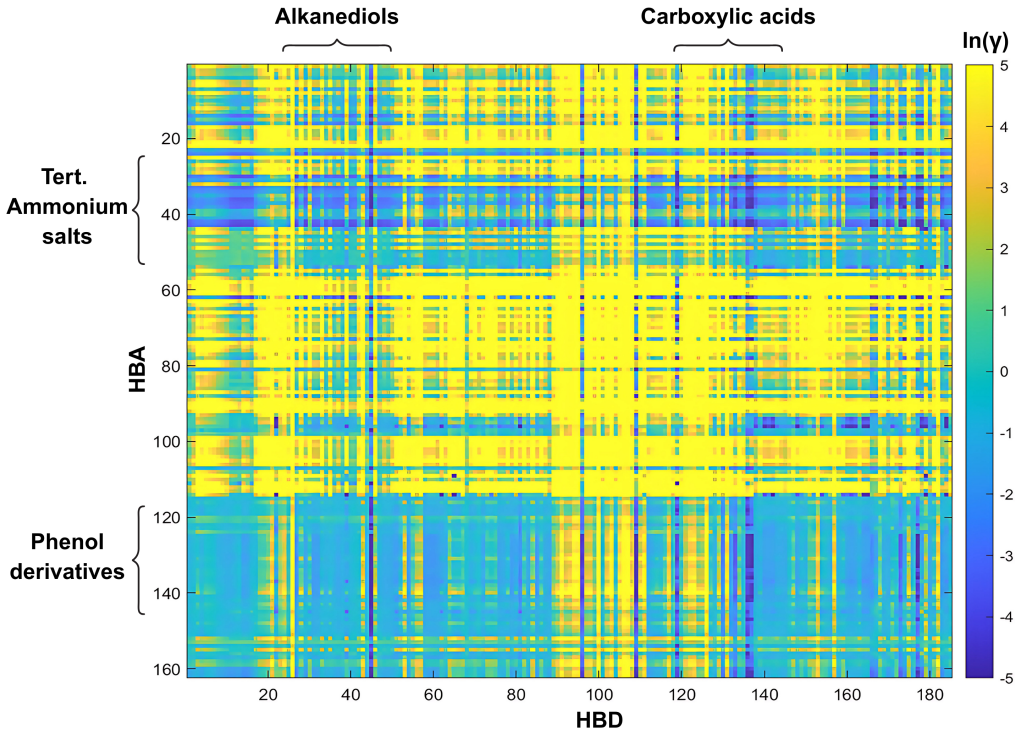

Figure 5.26 Heatmap of predicted activity coefficients (ln γ) from COSMO-RS simulation for equimolar HBAHBD combinations, screened against an RTM6 epoxy model substructure. Lower values (blue) indicate higher solubility. The simulation was performed by Dr. Filipe H. B. Sosa from University of Aveiro.

However, certain systems including proline:malic acid (PRO:MA), ChDHC:ERY, and ChDHC:XYL were highly viscous and required preheating in a water bath to facilitate handling and pipetting. Notably, choline chloride:dimethylformamide (ChCl:DMF), ChCl:EG, ChCl:LA, and ChCl:FA were each based on at least one liquid component under ambient conditions.

Specifically, lactic acid and formic acid have melting points of 16.8 řC and 8.3 řC, while ethylene glycol and dimethylformamide (DMF) melt at −12.9 řC and −61 řC, respectively [219, 220, 221, 222]. In contrast, choline chloride and betaine are solid at room temperature, with melting points near 300 řC [223, 224]. The formation of a homogeneous liquid phase from a solid component with such a high melting point and a room-temperature liquid strongly suggests the establishment of a robust hydrogen-bonding network.

Table 5.6 Successfully synthesized DES with component classes, COSMO-RS activity coefficients, and origin.

Rank	HBA	HBA Type	HBD	HBD Type	Abbreviation	Origin
3	Choline chloride	Quaternary ammonium salt	Betaine	Zwitterion: ammonium + carboxylic acid	ChCl:BET	Simulation
6	$ZnCl_2$	Metal halide	Formic acid	Carboxylic acid	ZCl:FA	Simulation
8	Choline chloride	Quaternary ammonium salt	DMF	Amide	ChCl:DMF	Simulation
8451	Choline chloride	Quaternary ammonium salt	Ethylene glycol	Polyol	ChCl:EG	[225]
12925	Choline chloride	Quaternary ammonium salt	Lactic acid	Carboxylic acid	ChCl:LA	[111]
13932	Choline chloride	Quaternary ammonium salt	Formic acid	Carboxylic acid	ChCl:FA	[108]
19684	Proline	Proteinogenic amino acid	Malic acid	Carboxylic acid	PRO:MA	[111]
19924	Betaine	Zwitterion: ammonium + acid	Glycerol	Polyol	BET:GLY	[94]
26461	Betaine	Zwitterion: ammonium + acid	Sorbitol	Polyol	BET:SOR	[128]
28126	Choline dihydrogen citrate	Quaternary ammonium salt	Xylitol	Polyol	ChDHC:XYL	[126]
28746	Choline dihydrogen citrate	Quaternary ammonium salt	Erythritol	Polyol	ChDHC:ERY	[126]

This behavior is characteristic of eutectic mixtures, where intermolecular interactions lead to significant melting point depression and the emergence of new physicochemical properties distinct from those of the individual components as discussed in Section 2.5.1.

To evaluate water compatibility and extend the range of application conditions, all synthesized DES were mixed with deionized water to form 20, 40, 60, and 80 % (w/w) solutions (DES:water). The respective DES was weighed into centrifuge tubes, and the calculated amount of water was added using a pipette. Samples were incubated in an orbital shaker at room temperature for 24 h to ensure complete mixing.

All systems successfully formed monophasic aqueous mixtures, confirming the general water miscibility of the produced DES, which is crucial for downstream enzymatic and wetting studies involving LMS. As the dilution of the DES with water results in the cancellation of its deep eutectic properties at a certain water content, the electrical conductivity was utilized as a benchmark for characterization according to Ünlü et al. (2017) [122]. These measurements are described in Section 5.1.9.

5.1.7 Contact Angle Analysis of DESWater Mixtures on RTM6 Epoxy

To evaluate the wettability of the RTM6 epoxy surface with the synthesized DES formulations, static contact angle measurements were performed using sessile drop analysis as described in Section 4.10.4. All DESwater mixtures were tested at concentrations of 20 to 80 % (w/w), and ultrapure water served as a reference. The droplets were applied with a defined volume of 3 µL and imaged using a goniometer at the Institute of Solids Process Engineering and Particle Technology at TUHH within the first 10 s of deposition. The left and right contact angles were averaged per droplet, and three replicates were measured per condition.

As illustrated in Figure 5.27, the majority of synthesized DES led to an improved wettability of the RTM6 surface, as indicated by a reduction in static contact angle compared to the water reference. The choline chloride:betaine (ChCl:BET) system showed an atypical trend: while a small decrease in contact angle was observed at 20 % (w/w), the value at 40 % (w/w) approached that of pure water, and further increase in DES content led to a continuous rise in contact angle, suggesting a deterioration in surface wettability. In contrast, the ChCl:DMF system exhibited the most significant enhancement, with a sharp decline in contact angle beyond 40 % (w/w), reaching a maximum reduction of $-45.73 \pm 1.49°$ relative to the water control. No consistent monotonic trend was observed for most other DES systems. For instance, zinc chloride:formic acid (ZCl:FA) yielded the

strongest wetting effect at 60 % (w/w), but higher concentrations reversed this trend. Similarly, ChCl:FA and ChCl:LA showed improvements from 20 to 40 % (w/w), after which the contact angle plateaued or increased.

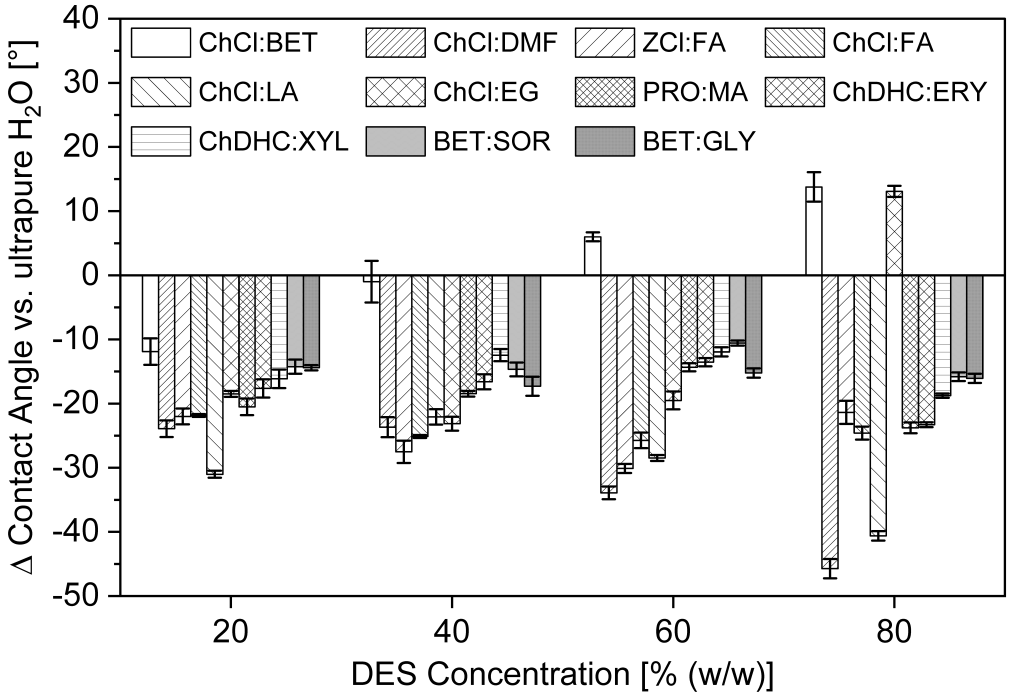

Figure 5.27 Change in contact angle on RTM6 epoxy surfaces relative to water, across varying DES concentrations. Lower values indicate improved wettability.

The ChCl:EG mixture reached its lowest contact angle at 40 % (w/w), while at 80 % (w/w) it unexpectedly surpassed the value of deionized water, indicating reduced surface affinity. The polyol-based systems PRO:MA, ChDHC:ERY and ChDHC:XYL showed only moderate wetting improvements at lower concentrations, but their maximum effect was achieved at 80 % (w/w). Conversely, the BET:SOR and BET:GLY systems displayed only marginal concentration-dependent changes across the tested range, suggesting a limited influence of their composition on spreading behavior. Based on the predicted activity coefficients derived from the COSMO-RS model, a different ranking of wettability would have been expected. Specifically, the model forecasted the following order of interaction strength with the epoxy surface: ChCl:BET > ZCl:FA > ChCl:DMF ≫ ChCl:EG ≫ ChCl:LA ≫ ChCl:FA ≫ PRO:MA ≫ BET:GLY ≫ BET:SOR ≫ ChDHC:XYL ≫ ChDHC:ERY. However, the experimental findings contradict this prediction. While ChCl:BET was ranked highly by COSMO-RS, it caused the most pronounced loss in wettability. ChCl:DMF, ranked eighth, achieved the strongest enhancement. Likewise,

ChCl:LA and ChCl:FA, although ranked very low (12925 and 13932, respectively), provided better wetting performance than ZCl:FA, which held rank six. This discrepancy highlights the limitations of COSMO-RS descriptors for modeling surface interactions of crosslinked polymers. A likely explanation is that the simulation assumed pure DES, whereas all experiments were conducted with water-diluted mixtures. Since water can disrupt the hydrogen-bonding network and significantly influence viscosity and surface tension, its presence is expected to affect interfacial behavior. It must also be considered that the complex topology of the RTM6 matrix deviates from the simplified molecular surfaces assumed in COSMO-RS calculations. The densely crosslinked structure and the size limitations of the query molecules may impair the predictive capacity of the model. Interestingly, literature-derived DES such as ChDHC:ERY and ChDHC:XYL, selected for their known LMS activation potential, displayed contact angle reductions comparable to those of ChCl:FA and PRO:MA, which had been identified for their lignin extraction efficiency. This dual performance makes them promising candidates for further surface treatment studies. Finally, the unpredictable influence of water content, which resulted in divergent trends across different systems, emphasizes the need for experimental validation when evaluating DES wettability on epoxy polymer (EP) surfaces.

5.1.8 Biochemical Characterization of DES-Water Mixtures for Laccase Reactions

To identify promising DES candidates for biocatalytic application with LacF, a preliminary screening of enzymatic activity was conducted using the oxidation of ABTS as a model reaction as described in Section 4.5. LacF was incubated in various DESwater mixtures (2080 % (w/w)) and the initial oxidation rates of ABTS were compared to those in 0.1 mol $\cdot$ L^{-1} citrate-phosphate buffer (pH 4) as reference. Figure 5.28, shows the relative ABTS activity of LacF after pre-incubation in various DES. No enzyme activity was observable when ZCl:FA, ChCl:FA, BET:GLY and BET:SOR were used as pre-incubation solvents, independent on their water content. In addition, no DES mixture was able to oxidize ABTS in absence of enzyme, making any observed oxidation directly related to the enzyme itself. A pronounced decrease in relative activity was observed for choline chloride-based systems, particularly at elevated DES concentrations. For ChCl:BET, enzymatic activity remained at approximately 75 % at 20 and 40 % (w/w) DES but decreased to 56 % at 60 and 80 % (w/w). Similarly, ChCl:DMF induced a stepwise reduction from 83 % (2060 % (w/w)) to 45 % activity at 80 % (w/w). The ChCl:LA and ChCl:EG systems also

reduced LacF activity in a concentration-dependent manner. Notably, ChCl:LA caused a strong deactivation, with relative activity declining from 63 % at 20 % (w/w) to 3.41 % at 80 % (w/w). This trend is consistent with the observation that no activity was detected in ChCl:FA, supporting the negative effect of organic acids.

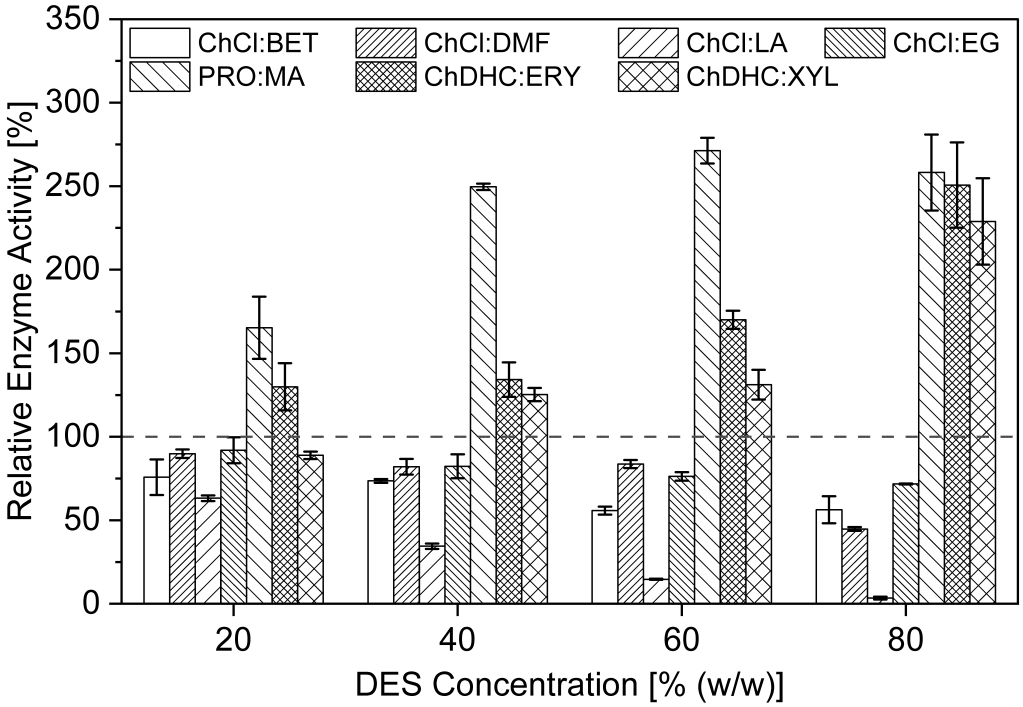

Figure 5.28 Relative activity of LacF toward ABTS in different DESwater mixtures (2080 % (w/w)) compared to 100 % 0.1 mol · L^{-1} citrate-phosphate buffer (pH 4).

Unexpectedly, no ABTS activity was measurable after pre-incubation in BET:GLY and BET:SOR, despite literature reports describing thermostabilizing effects of these polyol-based DES at 25 % (w/w) and 2:1 molar ratio [125]. A possible explanation for the lack of activity in the present study is the consistent application of a 1:1 molar ratio across all systems. The lower polyol content may have altered the hydration shell and destabilized the enzyme by disrupting waterenzyme and HBDenzyme interactions. Among the tested choline chloride systems, ChCl:EG resulted in the mildest inhibition (91.9 % to 71.7 % activity from 20 to 80 % (w/w)), followed by ChCl:DMF and ChCl:BET. This ranking aligns with the hypothesis that stronger HBDwater interactions withdraw water molecules from the enzyme surface, thereby disrupting hydration-dependent stability. Therefore, it can be concluded that ChCl:BET retains the hydration shell to the lowest degree, followed by ChCl:DMF and ChCl:EG. The observed inhibitory effect of choline chloride is in agreement with reports from Bittner et al. (2022) [118], who reported that

Cl^- ions compete with polar interaction side on the enzyme surface leading to a reduced hydration of the enzyme. Furthermore, at higher water content, differential adsorption behavior of HBA and HBD to the protein surface was observed, resulting in a destabilizing imbalance. In contrast to these inhibitory systems, an activation of LacF was observed upon pre-incubation in PRO:MA, ChDHC:ERY, and ChDHC:XYL. For the choline dihydrogen citrate-based DES, the relative activity steadily increased from 129.9 % to 250.6 % (ChDHC:ERY) and from 88.9 % to 228.9 % (ChDHC:XYL) over the tested concentration range. The PRO:MA system yielded the strongest activation, peaking at 271.3 % at 60 % (w/w) and slightly decreasing to 258.2 % at 80 wt.,%. Notably, the high viscosity of these DES at elevated concentrations posed experimental challenges, such as substrate mixing, which contributed to the increased standard deviation in the measurements. In previous studies, PRO:MA was investigated for lignin extraction but its effect on LacF activity remained unexplored [111].

The present results suggest that, unlike formic or lactic acid, malic acid does not cause enzyme deactivation and may instead support stabilization. The activation observed with ChDHC:XYL is consistent with literature reports of up to 170 % activity enhancement at 50 % (w/w) [126], which was previously linked to hydrogen bonding between the polyol and the enzyme surface. However, in the present work, ChDHC:ERY showed stronger activation than ChDHC:XYL, despite the latter containing a higher nominal number of hydroxyl functionalities. This observation indicates that laccase activation in DES cannot be rationalized solely based on the absolute number of hydrogen-bond-donating groups. Importantly, the hydroxyl groups in erythritol and xylitol differ fundamentally from dissociable acidic functionalities, as they do not contribute to proton activity or buffering capacity but primarily act as neutral hydrogen-bond donors. Moreover, the highest activation was observed for PRO:MA, although malic acid contains only two hydroxyl groups and one dissociable carboxylic acid moiety. This further challenges the assumption of a direct correlation between hydroxyl group density and enzymatic activation. Instead, the results suggest that the nature, accessibility, and spatial organization of functional groups, as well as their impact on local hydration structure and enzyme–solvent interactions, play a more decisive role than functional group count alone. In this context, malic acid-based systems appear to provide a favorable balance between hydrogen-bonding capability and controlled acidity without inducing enzyme deactivation, in contrast to formic or lactic acid-based DES. The observed concentration-dependent increase in relative activity across all three activating systems (PRO:MA, ChDHC:ERY, and ChDHC:XYL) therefore supports the conclusion that the strength and quality of DES-enzyme interactions, rather than

individual donor or acceptor characteristics, dominate the modulation of laccase catalytic performance.

In summary, organic acids such as formic and lactic acid proved detrimental to LacF activity, while chloride-based DES exerted a concentration-dependent inhibitory effect. In contrast, pre-incubation in PRO:MA, ChDHC:ERY, and ChDHC:XYL led to significant enzyme activation, underscoring their potential as enabling solvents for subsequent epoxy resin degradation. These DES also improved wettability on RTM6 surfaces via reduced contact angles, making them the candidates of choice for further evaluation in degradation studies.

Based on the ABTS screening results, the three most promising DES (PRO:MA, ChDHC:ERY, and ChDHC:XYL) were selected for further kinetic, thermal, and stability investigations.

Although laccase-catalyzed ABTS oxidation formally represents a bi-substrate reaction involving molecular oxygen, kinetic analysis was performed under pseudo-single-substrate conditions. All experiments were conducted under air-saturated conditions with identical shaking times and intensity immediately before measurements, ensuring that dissolved oxygen was present in large excess relative to ABTS. As shown in Section 5.1.9, oxygen saturation levels in the investigated DES-water mixtures were comparable to those in aqueous buffer, excluding oxygen limitation under the applied conditions. To mechanistically evaluate the observed activity enhancements, kinetic parameters of LacF were determined for the three most promising DES identified in the ABTS screening. Initial reaction rates were recorded using varying concentrations of ABTS and fitted to the MichaelisMenten model by non-linear regression (Figure 5.29). Accordingly, the derived kinetic constants represent apparent Michaelis-Menten parameters with respect to ABTS concentration. Explicit variation of oxygen concentration would require complex gas-phase control and was therefore not pursued. The resulting kinetic parameters are summarized in Table 5.7.

All tested DES systems exhibited substantially higher V_{max} values compared to the $0.1\,mol \cdot L^{-1}$ citrate-phosphate buffer (pH 4) reference, suggesting a pronounced increase in catalytic turnover. PRO:MA showed the highest V_{max} of $2.74\,\mu mol \cdot min^{-1}$, corresponding to a 3-fold improvement relative to buffer, while ChDHC:ERY and ChDHC:XYL also resulted in strongly elevated turnover rates. Interestingly, all DES systems showed slightly higher K_m values compared to the $0.1\,mol \cdot L^{-1}$ citrate-phosphate buffer (pH 4).

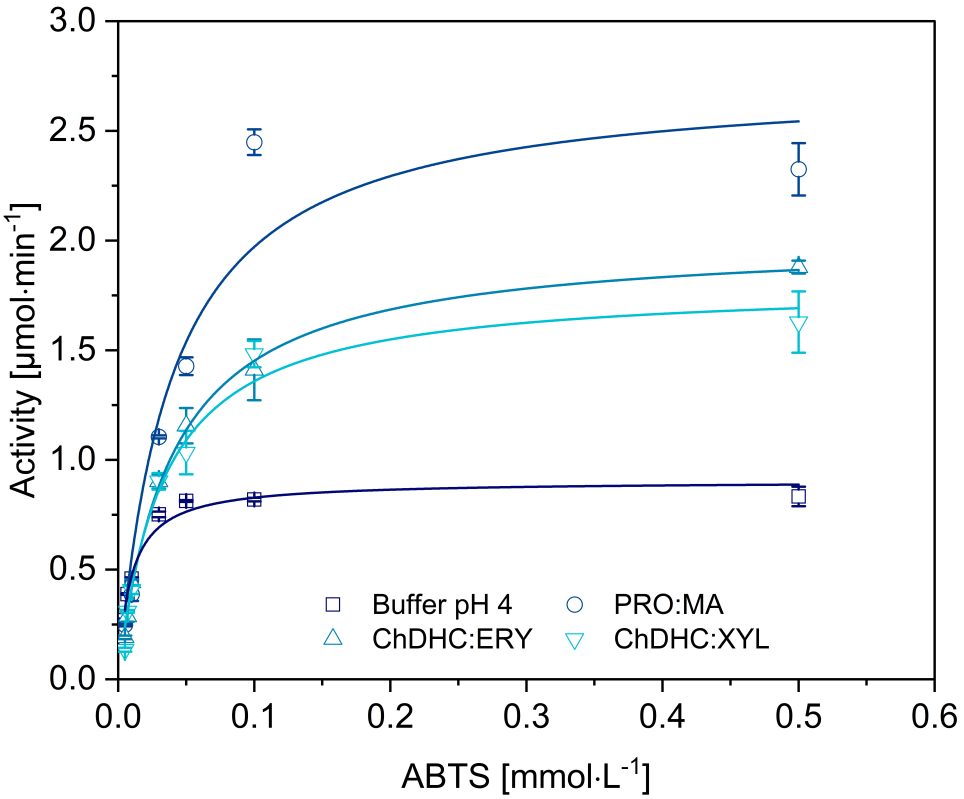

Figure 5.29 MichaelisMenten kinetics of LacF for ABTS oxidation in 0.1 mol · L^{-1} citrate-phosphate buffer (pH 4) and selected DESwater mixtures. Curves represent nonlinear fits.

However, the K_m values determined for the different DES-water mixtures were of the same order of magnitude and largely overlapping within their respective standard deviations, indicating that no statistically significant differences in apparent substrate affinity can be resolved under the applied conditions. Consequently, the observed enhancement in catalytic performance is primarily attributed to the pronounced increase in V_{max} rather than changes in substrate binding. These findings are in line with reports demonstrating that moderately polar DES can reduce activation energy barriers by stabilizing enzyme-substrate transition states and maintaining the protein's active conformation through water-mediated hydrogen bonding networks [226]. Specifically, Chan (2020) [227] conducted kinetic analyses of *Myceliophthora thermophila* laccase in various DES and reported enhanced turnover coupled with mild substrate affinity shifts in lactic acidbetaine systems, whereas glycerolcholine chloride DES displayed inhibitory behavior consistent with increased K_m and decreased V_{max}.

Table 5.7 Kinetic parameters of LacF in different DESwater mixtures (60 % (w/w)) obtained by non-linear Michaelis-Menten fit using Origin 2024b (OriginLab Corporation, Northampton, US).

Medium	K_m **[mmol·L^{-1}]**	V_{max} **[ţmol·min^{-1}]**	R^2
0.1 mol · L^{-1} citrate-phosphate buffer	9.17 Œ 10^{-3} ś 1.40 Œ 10^{-3}	0.904 ś 0.036	0.959
PRO:MA	3.92 Œ 10^{-2} ś 1.49 Œ 10^{-2}	2.74 ś 0.338	0.906
ChDHC:ERY	3.84 Œ 10^{-2} ś 2.20 Œ 10^{-3}	2.01 ś 0.0384	0.997
ChDHC:XYL	3.27 Œ 10^{-2} ś 5.10 Œ 10^{-3}	1.80 ś 0.0918	0.979

Taken together, the kinetic data confirm that DESwater mixtures not only maintain enzymatic function but can also enhance laccase catalytic capabilities. The increased V_{max} values highlight the potential of such systems for applications requiring high turnover, such as polymer oxidation or dye decolorization.

To further assess the functional performance of LacF in DESwater environments, temperature-dependent activity profiles were generated. Enzymatic ABTS oxidation was measured after pre-incubation in the selected DES formulations (PRO:MA, ChDHC:ERY, and ChDHC:XYL) and compared to aqueous 0.1 mol · L^{-1} citrate-phosphate buffer (100 %, 0.1 mol · L^{-1}, pH 4) over a temperature range of 40 řC to 80 řC.

As shown in Figure 5.30, all DES systems led to increased activity across the temperature range, with no signs of thermal denaturation or inactivation. While the buffer control exhibited a peak activity of approximately 16 ţmol · min^{-1} · mL^{-1} at 70 řC, all DES samples maintained or surpassed this level even at 80 řC. The most pronounced effect was observed in ChDHC:ERY, where activity reached 18.5 ţmol · min^{-1} · mL^{-1}, indicating a distinct thermal activation of the enzyme in this medium.

These findings suggest that the DES environment stabilizes the tertiary structure of the enzyme or shifts the optimal catalytic temperature, an effect that has been linked to lower dielectric constant, enhanced hydration shell preservation, and reduced conformational entropy in non-aqueous matrices [228, 229]. The improved thermal robustness in DES may be particularly advantageous for oxidation reactions at elevated temperatures or in the context of polymer degradation, where an increased reaction temperatures usually favors the interaction with the enzyme due to higher chain mobility [230].

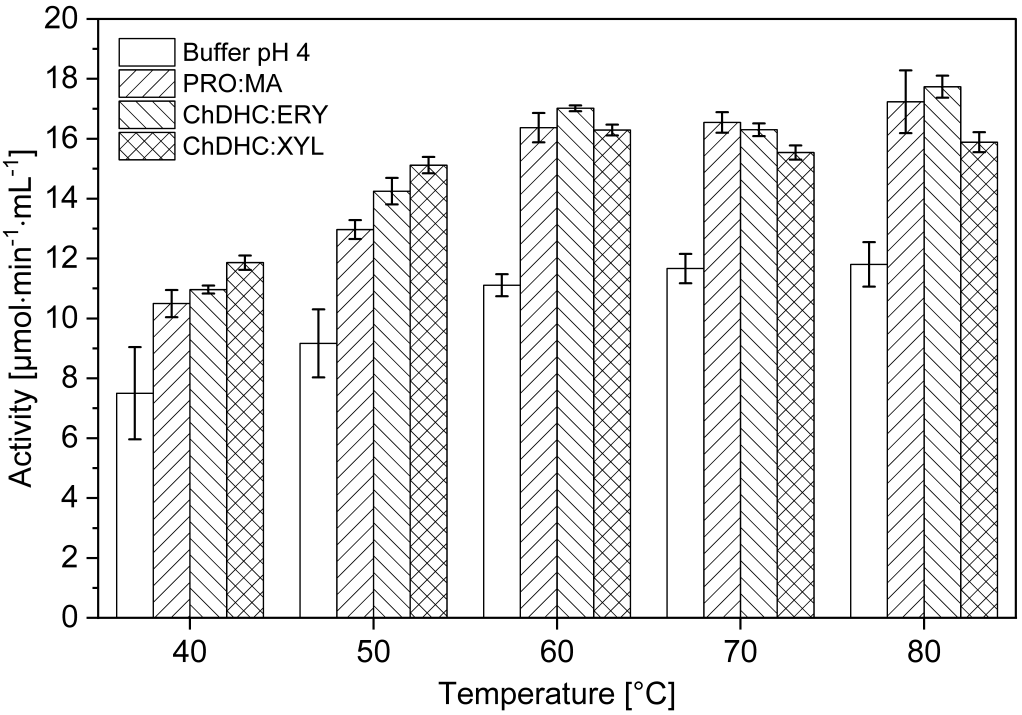

Figure 5.30 Temperature-dependent ABTS oxidation by LacF in buffer and selected DESwater mixtures (60 % (w/w)) compared to 0.1 mol · L^{-1} citrate-phosphate buffer.

To evaluate the long-term compatibility of DES with LacF, the residual enzymatic activity was monitored at room temperature over a storage period of 200 h. Samples were incubated at 60 % (w/w) DES content, and ABTS oxidation was measured at defined intervals. For comparison, a buffer-stored reference was included.

As shown in Figure 5.31, LacF retained nearly full activity in 0.1 mol · L^{-1} citrate-phosphate buffer over the tested timeframe, with only minor fluctuations between 100 %-120 % relative activity. This increase in activity is most likely due to steric alterations in the enzyme caused by the temperature change from 4 řC to 30 řC when the cooled enzyme solution was added to the buffer solution. In contrast, DES formulations showed varying deactivation kinetics. While PRO:MA led to rapid inactivation within the first 30 h (half-life $\tau_{1/2} \approx 1.2$ h), both polyol-based systems, ChDHC:ERY and ChDHC:XYL, showed markedly improved performance with calculated half-lives of 30.1 h and 25.7 h, respectively. These results indicate a trade-off between initial activity enhancement and long-term stability in DES systems.

The rapid deactivation observed in PRO:MA may result from the acidity of the solution or local dehydration effects that destabilize active site residues. In contrast, the better

performance in sugar alcohol-based DES (ChDHC:ERY and ChDHC:XYL) is likely due to a higher degree of hydrogen bonding and reduced oxidative stress [231, 232].

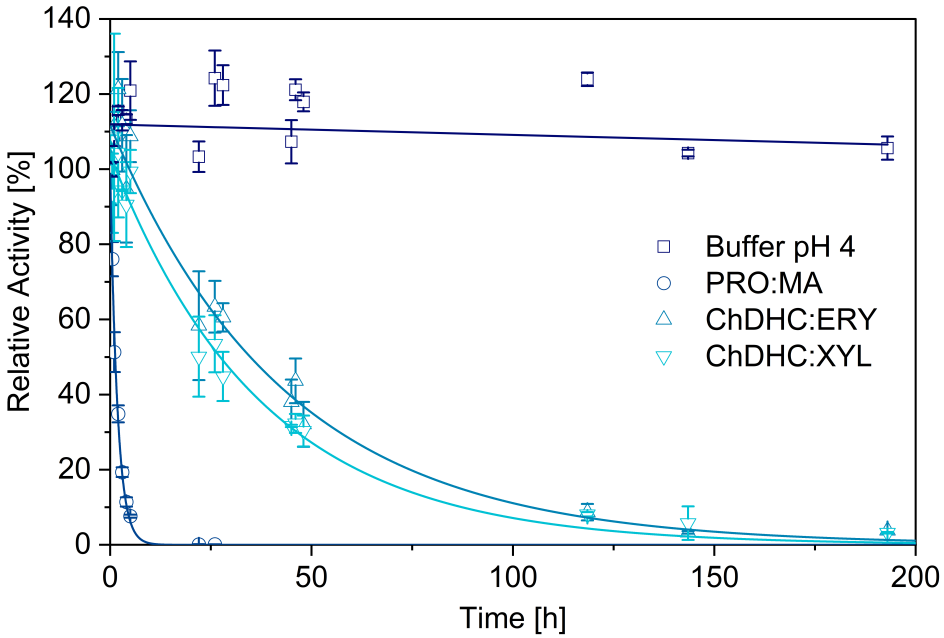

Figure 5.31 Stability of LacF in 80 % DES during storage at room temperature over 200 h. 30 řC, 5 mmol · L^{-1} ABTS, 0.075 U · mL^{-1} LacF, 750 rpm. Non-linear first order deactivation fits were performed with Origin 2024b (OriginLab Corporation, Northampton, US) ($R^2 \geq 0.97$).

Comparable findings were reported for other oxidoreductases in polyol-rich DES, supporting their use in short-term biocatalysis under mild aqueous conditions [129, 233].

5.1.9 Physicochemical Characterization of DES-Water Mixtures

To further characterize the synthesized DES, key physicochemical parameters, namely electric conductivity, pH, and maximum dissolved oxygen (DO) were assessed in aqueous mixtures containing 080 % (w/w) DES. The conductivity measurements, in particular, were performed to draw conclusions about the preservation or breakdown of the eutectic network upon dilution with water according to Ünlü et al. (2017) [122].

As expected, the conductivity profiles of PRO:MA, ChDHC:ERY, and ChDHC:XYL exhibited bell-shaped trends with increasing DES content, as shown in Figure 5.32. Such profiles are characteristic of aqueous DES systems and are commonly interpreted as an indicator of the presence and progressive disruption of the eutectic hydrogen-bond network upon water addition. At low to intermediate DES contents, increasing conductivity reflects

enhanced ionic dissociation within an intact or partially preserved eutectic structure. The occurrence of a distinct conductivity maximum at 3040 % (w/w) DES therefore marks the transition region in which the eutectic properties are still present but increasingly disturbed by water. Beyond this point, further dilution leads to a breakdown of the eutectic network, and the systems can be more appropriately described as aqueous solutions of the individual DES components rather than fully developed DES.

Maximum conductivity values were observed at 3040 % (w/w) DES, reaching 6.90 mS · cm^{-1} for PRO:MA, 14.34 mS · cm^{-1} for ChDHC:ERY, and 16.17 mS · cm^{-1} for ChDHC:XYL. This concentration range can thus be considered representative of DES-dominated regimes, whereas mixtures containing higher water fractions predominantly exhibit solution-like behavior [121].

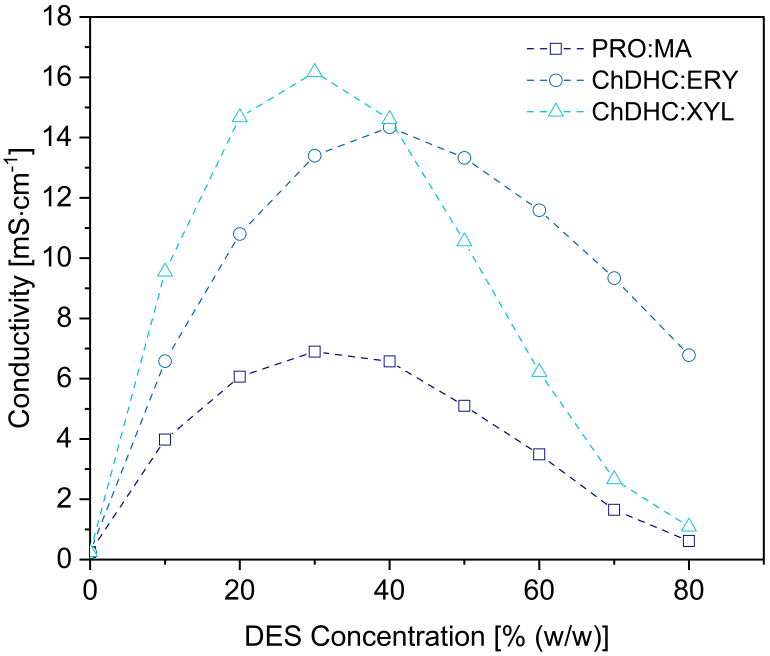

Figure 5.32 Electric conductivity of PRO:MA, ChDHC:ERY, and ChDHC:XYL in aqueous mixtures.

Notably, ChDHC:ERY retained relatively high conductivity at 80 % (w/w), suggesting high ion mobility beyond the eutectic composition. In contrast, the lower conductivity of PRO:MA and ChDHC:XYL at high concentrations suggests a stronger supramolecular network with limited water interaction. This interpretation is supported by the high viscosity and poor miscibility of PRO:MA, and by the greater number of hydroxyl groups in xylitol, which likely enhance hydrogen bonding and reduce water accessibility in ChDHC:XYL.

Additionally, DO measurements (Figure 5.33) revealed that all systems maintained high DO saturation levels close to or slightly above 100 % a.s. compared to aqueous buffer at pH 4 across the tested concentration range, indicating sufficient oxygen solubility even in low-water formulations.

The pH of the PRO:MA system remained constant around 2.6, independent of dilution, while both choline-based systems showed moderate increases from acidic values at low DES content (~pH 3.8) to pH 4.24.6 at 80 % (w/w) DES. These differences may significantly affect enzyme stability as observed before in Section 5.1.8. Ai et al. (2015) [234] reported a complete loss of LacF activity after 24 h at pH 2, whereas maximum stability was observed between pH 69. Accordingly, the reduced stability of LacF in PRO:MA can be attributed primarily to its low pH.

Interestingly, contact angle and activity assays further revealed that a fully formed eutectic network was not a prerequisite for improving surface wettability or enhancing enzymatic activity.

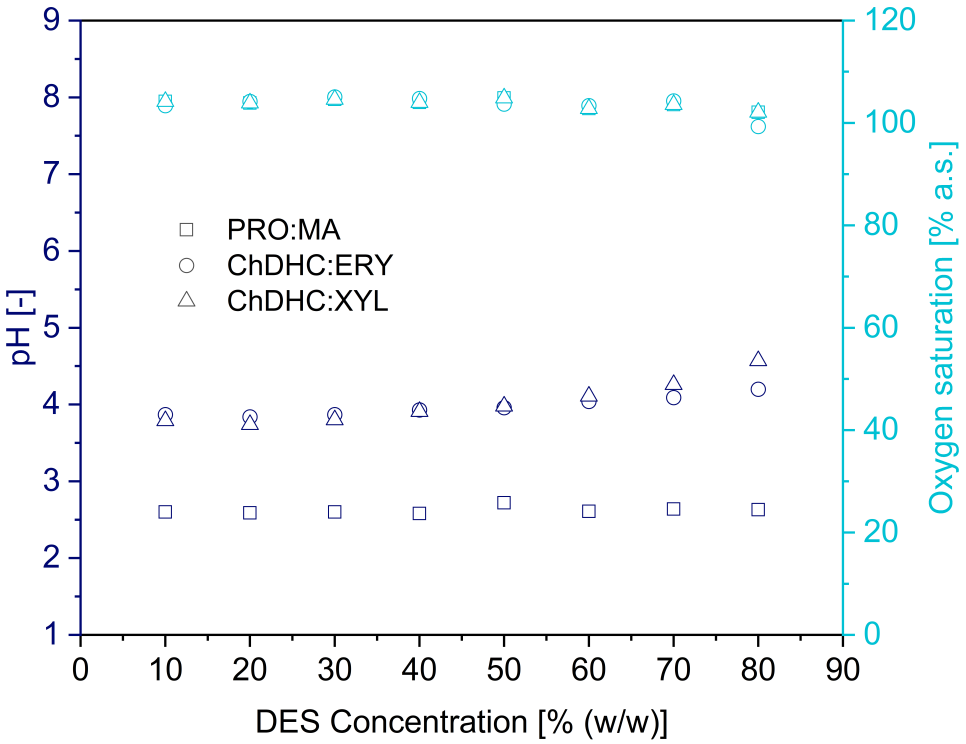

Figure 5.33 Measured pH values (top) and oxygen saturation compared to 0.1 mol · L^{-1} citrate-phosphate buffer pH 4 (bottom) of DESwater systems.

In fact, for all systems, the most favorable surface wetting was observed at 80 % (w/w) DES (Section 5.1.7), where the eutectic structure is largely disrupted. Similarly, laccase

activity increased with DES addition even before full network formation, indicating that beneficial effects arise from direct interactions with DES components rather than the supramolecular structure alone. For ChDHC:ERY and PRO:MA, 40 % (w/w) DES was sufficient to boost LacF activity, while ChDHC:XYL required 80 % (w/w) to reach comparable effects. Despite its higher pH, ChDHC:XYL resulted in a shorter enzyme half-life compared to ChDHC:ERY, likely due to intensified interactions between the enzyme and the polyhydroxylated xylitol donor.

5.1.10 Enzymatic Oxidation of Model Compounds and Epoxy Resin in Deep Eutectic Solvents

The enzyme activity of LacF in dependence on the water content of the PRO:MA, ChDHC:ERY, and ChDHC:XYL DES was determined according to Section 4.10.2. The resulting enzyme activities were calculated using the previously determined extinction coefficients and the LambertBeer law. To analyze the obtained values, the relative enzyme activity was calculated by comparison to the reference activity measured in 0.1 mol $\cdot$ L^{-1} citrate-phosphate buffer at pH 4. Figure 5.34 (left), shows the results of the activity assay using NNBT as a substrate.

The use of PRO:MA led to a loss of approximately 94 % relative enzyme activity compared to the reference. In contrast, the choline dihydrogen citrate (ChDHC)-based DES enabled enzyme activation, with relative activity surplus of 93.65±7.70 % and 101.33±8.45 % at 20 % (w/w) ChDHC:ERY and ChDHC:XYL, respectively. These values decreased to 58.48±4.70 % and 59.72±5.69 % at 40 % (w/w). At higher concentrations, a further decline in enzyme activity was observed. A continuous downward trend in relative activity was found in both ChDHC-based systems. In the case of ChDHC:XYL, the activity decreased at a nearly constant rate, whereas for ChDHC:ERY, a sharp drop from 158.48 ± 4.70 % at 40 % (w/w) to 33.74 ± 3.61 % at 60 % (w/w) was measured.

The right-hand graph of Figure 5.34 displays the results obtained with MB as a substrate. Contrary to the use of NNBT, with which at least a low but detectable activity was measured, no activity was obtained at all for MB in the PRO:MA system. The use of MB resulted in similar activities for ChDHC:ERY and ChDHC:XYL, both of which were lower than the reference. Activity decreased from around 62.50 % at 20 % (w/w) to 37.60 % at 60 % (w/w). No enzyme activity was detectable at 80 % (w/w). This observed

loss in enzyme activity cannot be attributed to enzyme deactivation within the measurement period, since stability tests showed that LacF retained sufficient stability under the conditions used (Section 5.1.8).

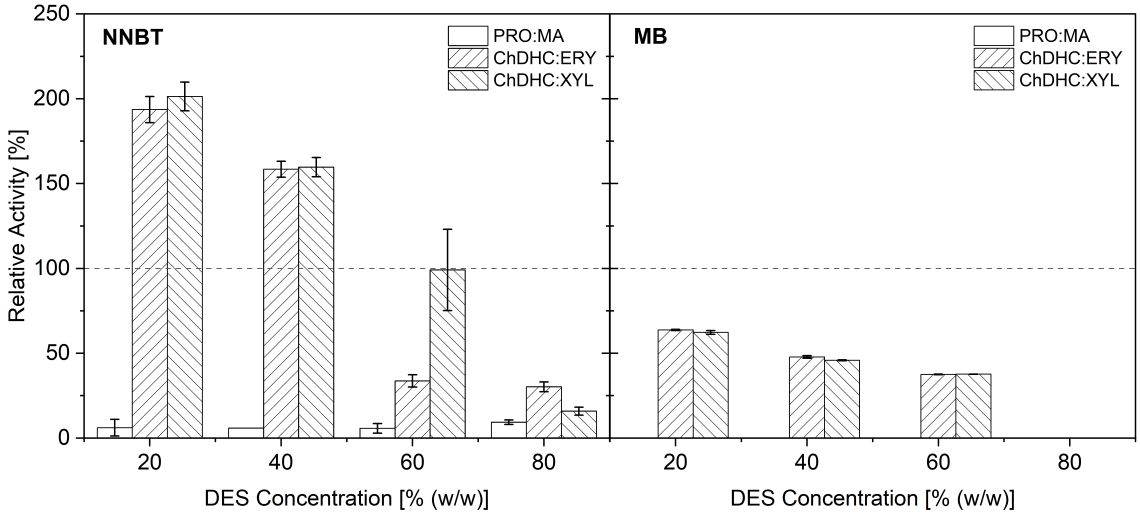

Figure 5.34 Relative enzyme activity of LacF in different DES compositions containing PRO:MA, ChDHC:ERY, or ChDHC:XYL, measured using either NNBT (left) or MB (right) as model substrate. Conditions for NNBT: 5 mmol · L^{-1} NNBT, 0.3 U · mL^{-1} LacF, 450 nm, 30 řC, 10 min assay time. Conditions for MB: 2 mmol · L^{-1} MB, 1.5 U · mL^{-1} LacF, 730 nm, 30 řC, 10 min assay time. Activities were normalized to the 0.1 mol · L^{-1} citrate-phosphate buffer control (pH 4).

Furthermore, preliminary experiments have shown that incubation in up to 5 % (v/v) dimethyl sulfoxide (DMSO) does not significantly inhibit laccase activity (Figure A.1). Unlike the ABTS assay, the activity assays with NNBT and MB were not performed in aqueous solution. Therefore, the observed effects are likely caused by the specific reaction conditions in the DES environment. As the use of PRO:MA led to minimal laccase activity with NNBT and complete inhibition with MB, it can be assumed that direct interaction between the enzyme and the PRO:MA solvent resulted in biocatalyst inactivation, even at 20 % (w/w). However, since LacF retained high ABTS activity even after incubation in 80 % (w/w) PRO:MA, irreversible damage to the enzyme structure can be ruled out. Instead, the low pH value of PRO:MA (2.6) is a likely explanation. Ai et al. (2015) [234] reported that the pH value at which laccases lose catalytic activity depends on the substrate and ranges from 1.5 for ABTS to 3.5 for syringaldazine. The ChDHC-based DES exhibited more favorable pH values in the range of 3.9 to 4.6. Since water content had only a minor effect on pH, changes in activity can be attributed to other factors. For NNBT, enzyme activation was observed at 20 % (w/w) and 40 % (w/w), followed by a decline. The

activation could be explained by hydrogen bonding interactions between the DES and the enzyme that enhance catalytic turnover. NNBT contains two hydroxyl groups and one tertiary amide group, which may allow for strong hydrogen bonding with the DES, facilitating oxidation. However, as DES content increased, the relative activity dropped, reaching $33.74 \pm 3.61\,\%$ for ChDHC:ERY at $60\,\%$ (w/w), and continuously decreasing for ChDHC:XYL. This decrease may be caused by displacement of water from the enzyme surface or by reduced oxygen availability due to higher DES viscosity. The latter would lower the diffusion coefficient of oxygen, potentially making oxygen transfer from bulk to enzyme surface the rate-limiting step, even though the absolute saturation was shown to be comparable to that of buffer (Figure 5.33).

A similar phenomenon has been described by Zhang et al. (2021) [235], who investigated the oxygen transfer rates for different DES. They showed, that regardless of a potentially high oxygen solubility in the medium, an up to 11-fold reduction in the volumetric mass transfer coefficient for choline chloride:ethylene glycol DES is measured as a result of the high viscosity and chemical nature of certain DES.

In the case of MB, no enzyme activation was observed in either ChDHC-based solvent. Instead, enzyme activity was consistently lower than in the reference and declined with increasing DES concentration. Since MB possesses only two tertiary amide groups, weaker hydrogen bonding interactions with the DES are expected compared to NNBT. Additionally, low oxygen diffusion in more viscous media may have contributed to the observed inhibition, as described before. Furthermore, as seen in Figure A.7, MB oxidation may produce multiple products, as indicated by several formed peaks in the ultraviolet-visible light (UV/VIS) spectra and as discussed before for purely buffer-based reaction systems (Section 5.1.4). Since the photometric assays were based on the absorption at one wavelength, only the formation of one putative oxidation product was monitored. It is conceivable that the DES environment promoted formation of alternative products that remained undetected while the measured product was formed more slowly. Consequently, the findings must be interpreted with caution, as a more precise analytical resolution of the reaction steps in the DES was not feasible due to analytical limitations.

From the experiments carried out in a DES environment it can be concluded that the reaction conditions such as the pH and the oxygen availability to the enzyme, which is highly affected by the DES viscosity (and hence, concentration in dilutions with water), were outlined as key factors influencing the enzyme activity. Additionally, substratesolvent interaction and hydration shell stability of the enzyme play an important role in the catalytic activity towards different substrates. For experiments using the polymeric resin,

the PRO:MA system was excluded from further investigation, as the results showed that LacF could not maintain catalytic activity under the conditions of this solvent.

To evaluate oxidative degradation of solid material, RTM6 epoxy resin powder was incubated with LacF in 20 % (w/w) ChDHC:ERY and ChDHC:XYL suspensions according to Section 4.11. The experiment was conducted using the same setup as described for the model substrates, with a reduced reaction volume of 2.5 mL and an extended reaction time of 48 hours. The reaction vessels were aerated using pressurized air to maintain sufficient oxygen supply. The dried residues were analyzed by ATR-FTIR spectroscopy, and the resulting spectra are shown in Figure 5.35.

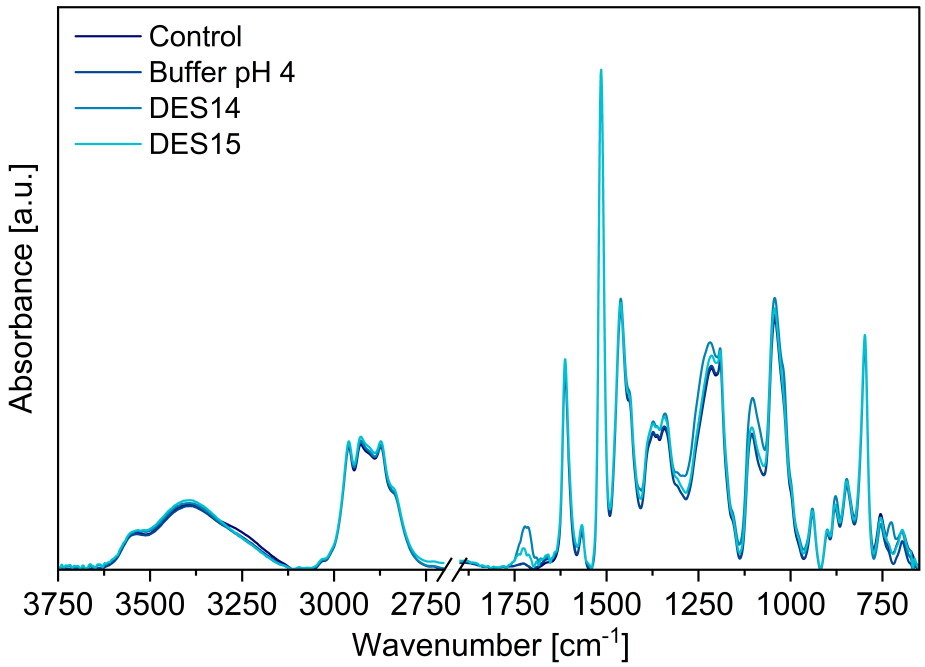

Figure 5.35 ATR-FTIR spectra (resolution 2 cm^{-1}, range 4000 cm^{-1} to 650 cm^{-1}, 50 scans) of dried RTM6 powder incubated in 0.1 mol · L^{-1} citrate-phosphate buffer pH 4, 20 % (w/w) ChDHC:ERY and ChDHC:XYL, aerated with 3 vvm pressurized air, 2.5 U · mL^{-1} LacF, 0.1 g · mL^{-1} RTM6 loading, 2.5 mL reaction volume, and 48 h reaction time.

Similar to the results obtained in pure buffer in the packed-bed reactor (Section 5.1.5) subtle changes in the FTIR spectra were observed in regions associated with C=O and tertiary amines. In particular, increased carbonyl vibrations appeared in the region of 1800 cm^{-1} to 1530 cm^{-1} for both DES compared to the untreated and buffer-incubated samples. The highest absorbance at 1700 cm^{-1} was found in the ChDHC:ERY sample, followed by ChDHC:XYL. This clear indicator of the oxidation level was quantified by

using carbonyl index calculations based on the ratio of carbonyl and methylene peak areas. The results are summarized in Table 5.8. Compared to the untreated RTM6 powder, a moderate increase of 6.45 % was observed in buffer, while a substantial increase of 37.10 % and 27.42 % was found in the presence of ChDHC:ERY and ChDHC:XYL, respectively. Amine-associated absorbances between 1450 cm^{-1} to 1250 cm^{-1} were also more intense in the DES-treated samples compared to the control and buffer, suggesting possible overlap with newly formed primary or secondary amides.

The results demonstrate that both DES enhanced oxidation of the solid epoxy matrix, likely due to improved wettability and higher accessibility of the LacF to the resin surface. These findings are consistent with earlier observations on contact angle changes (Section 5.1.7) and further support the hypothesis that DES can promote oxidative polymer degradation by increasing local enzyme activity and substrate exposure. Additionally, it must be highlighted, that the oxidation effect was achieved after incubation in suspension, contrasting the instrumentally more extensive setup used in Section 5.1.5.

Table 5.8 Carbonyl indices determined for the untreated and enzymatically treated RTM6 powder in DES from FTIR spectra according to Equation 2.

Sample	**Carbonyl Index** [-]
Reference	0.62
Buffer pH 4	0.66
20 % (w/w) ChDHC:ERY	0.85
20 % (w/w) ChDHC:XYL	0.79

The resin's ability to suspend properly, as opposed to its behavior in pure buffer, where it floated on top of the liquid during incubation in DES, suggests the potential for DES and aqueous solutions thereof to serve as a promising alternative. This approach offers the advantage of simplification in reactor configuration and the achievement of a comparable degree of oxidation in a reduced time-frame, as compared to the fixed-bed reactor. It is noteworthy that no mediator was utilized during the incubation process with the resin in the DES solutions, yet measurable oxidation still occurred. This observation underlines the altered interaction of the enzyme with the solid substrate, thereby opening opportunities for further experimentation with the use of mediators, which could even be components of the DES. However, the alterations in the resin observed in this study, as previously seen in purely aqueous systems, do not yet indicate extensive degradation. Further systematic investigations are necessary to comprehend the biochemical processes involved and to advance the degradation of the resin. Nevertheless, the findings obtained in this section

have laid the foundation for a fundamental understanding of the interaction of laccases with thermosetting resins in different reaction media.

5.2 Chemoenzymatic Epoxidation of Linseed Oil for Renewable Epoxies

While a large portion of current research concentrates on the biochemical depolymerization and recycling of polymers, an equally significant challenge lies in establishing renewable and reactive building blocks for future material systems. Especially in the context of epoxy-based fiber reinforced polymers, no breakthroughs on bio-degradation of conventional materials hav yet been achieved [6]. Furthermore, as discussed in Section 5.1 of the present work, even highly efficient, commercial oxidoreductases and mediator systems, only manage to slightly oxidize the polymer with an insignificant degree of degradation. Thus, as many of the current biochemical recycling approaches for synthetic polymers are still in the early research stages and far from industrial implementation, owing to the strong recalcitrance of the polymers, novel materials with inherent biodegradability need to be developed.

One such approach is the chemoenzymatic epoxidation (CEE) of unsaturated plant oils, which provides access to epoxidized biobased monomers under mild, environmentally benign conditions. By coupling enzyme-catalyzed peracid formation with selective olefin oxidation, this method enables the conversion of natural triglycerides into reactive epoxy-functionalized compounds suitable for thermoset and coating applications [141]. These epoxidized vegetable oils (EVOs) play a vital role in development of inherently biobased and -degradable resins and novel vitrimer materials, as curing them with compounds such as citric acid, itaconic acid, or even certain amino acids retains an ester-containing polymer backbone that is susceptible to biological attack [19, 236]. Hence, this section explores the chemoenzymatic synthesis of epoxidized linseed oil (ELO) and its *inline* analytical monitoring as a complementary line of investigation within the overarching goal of circular polymer technologies.

5.2.1 Establishment of Chemoenzymatic Epoxidation Route for Linseed Oil Epoxidation

The CEE of unsaturated fatty acids and triglycerides combines the selectivity of enzymatic catalysis with the reactivity of chemical oxygen donors and has several environmental benefits over the conventional *Prileshajev* reaction as outlined in Section 2.6.1. As illustrated in Figure 5.36, the reaction proceeds via an *in-situ* formation of peracids from carboxylic acids and hydrogen peroxide, usually catalyzed by an immobilized lipase (e.g., *Candida antarctica* lipase B, commercially available as Novozyme® 435).

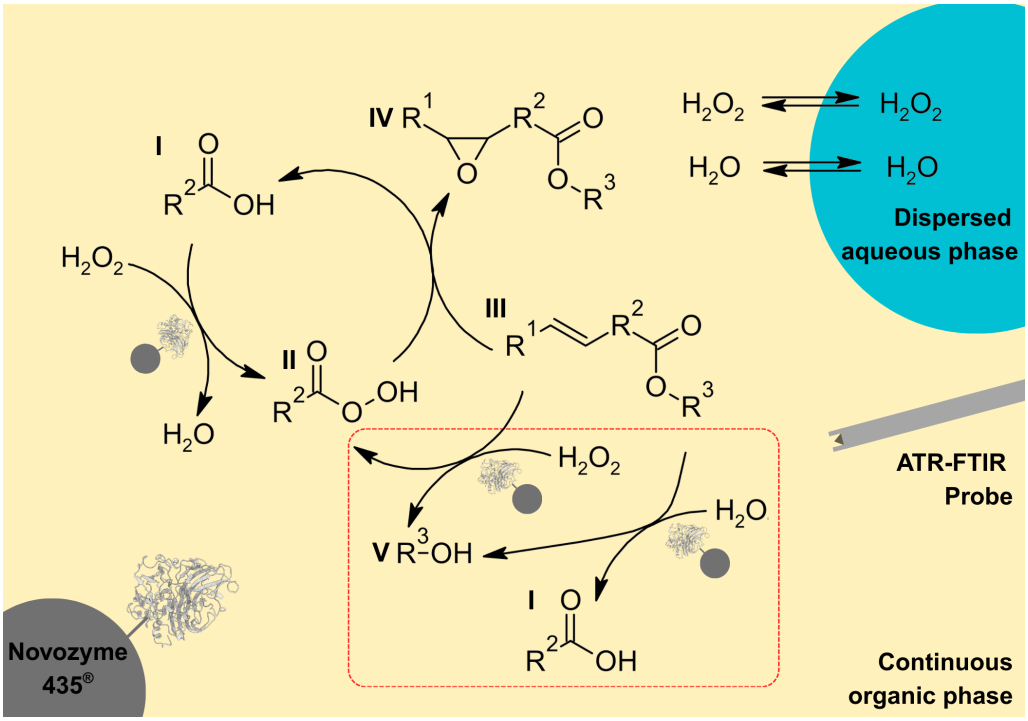

Figure 5.36 Reaction scheme for the chemoenzymatic epoxidation of an arbitrary unsaturated fatty acid on a triglyceride backbone (III) in a liquid two-phase system with Novozyme® 435 as heterogenous catalyst. Undesirable side reactions are indicated within the red box. Illustrations are schematic and not to true to scale. I - free fatty acid, II - peroxy acid, III - unsaturated fatty acid on trigylceride, IV - epoxidized fatty acid, V - hydrolyzed triglyceride; R_1 & R_2 - fatty acid chain, R_3 - triglyceride backbone.

In the presence of a suitable free fatty acid (FFA), the enzyme catalyzes the perhydrolysis step, forming peracids that act as electrophilic oxygen donors in the subsequent epoxidation of the olefinic substrate. The reaction takes place in a bi-phasic medium, consisting of a continuous organic phase (e.g., toluene or hexane containing the triglyceride substrate) and a dispersed aqueous phase supplying hydrogen peroxide [237]. Diffusion of H_2O_2 into the organic phase is critical for maintaining the presence of the oxygen donor. Once in the organic phase, H_2O_2 reacts with the FFA to form a peracid intermediate, which subsequently transfers an oxygen atom to the alkene moiety of the unsaturated triglyceride, yielding the corresponding epoxide (oxirane) and regenerating the acid catalyst. In parallel, side reactions such as hydrolysis of ester bonds can occur, particularly under high water activity. The hydrolysis of triglycerides into FFA and alcohols (or mono-/diacylglycerides) can contribute to a reduction in epoxide yields and decreases the degree of crosslinking when curing the product with a hardener. Therefore, controlling the amount

of water and H_2O_2 is essential for maintaining enzyme activity and optimizing selectivity, as H_2O_2 additional poses the risk of deactivating the enzyme by bleaching.

5.2.2 Selection of Acid Co-Reactant for Chemoenzymatic Epoxidation of Linseed Oil

The reaction depicted in Figure 5.37, represents the initial epoxidation attempt carried out with stearic acid (SA), employing Novozyme® 435 as catalyst and linseed oil (LO) dissolved in toluene as detailed in Section 4.12. SA was initially chosen as it is frequently discussed as a suitable reactant for the CEE of vegetable oils [140]. The aim was to verify whether the reaction proceeds as expected and allows reaching the theoretical maximum epoxy number (EN). This value can be estimated based on the iodine value (IV) of the starting material, which was $179\,\mathrm{g}\cdot 100\,\mathrm{g}^{-1}$ for the specific LO used (Figure A.4). Assuming complete conversion of all carboncarbon double bonds, the theoretical EN can be calculated according to Equation 24:

$$\mathrm{EN_{theo}} = \frac{\mathrm{IV}\cdot \mathrm{M_{ox}}}{2\cdot \mathrm{M_{I_2}}} \quad (\mathrm{g}\cdot 100\ \mathrm{g}^{-1}) \tag{24}$$

Here, M_{ox} is the molar mass of the oxirane oxygen ($16\,\mathrm{g}\cdot\mathrm{mol}^{-1}$) and M_{I_2} is the molar mass of iodine ($253.8\,\mathrm{g}\cdot\mathrm{mol}^{-1}$). Inserting the given IV leads to a theoretical EN of approximately $26\,\mathrm{g}\cdot 100\,\mathrm{g}^{-1}$.

The results of the non-aqueous titration show that this theoretical value is nearly reached after 16 h to 18 h of reaction time, indicating high conversion under the chosen conditions. Simultaneously, the epoxy equivalent weight (EEW) decreases significantly over time, reflecting the increasing functionality of the ELO. The dashed line in the plot represents the calculated target EN value derived from the IV, as discussed above.

The primary objective of this initial experiment was to investigate whether the maximum theoretical conversion could be achieved using SA under standard conditions. As shown in Figure 5.37, the EN increased steeply within the first 3 h to around $20\,\mathrm{g}\cdot 100\,\mathrm{g}^{-1}$ and approached the expected upper limit of $25\,\mathrm{g}\cdot 100\,\mathrm{g}^{-1}$ after leaving the reaction over night, indicating that full conversion was, in principle, attainable with the applied protocol.

However, upon cooling the reaction mixture to ambient temperature, the entire supernatant phase was observed to solidify into a wax-like mass (Figure 5.38 (B)). This effect, which was reproducibly observed across multiple runs, is likely attributed to a co-crystallization behavior between SA and components of the epoxidized product mixture.

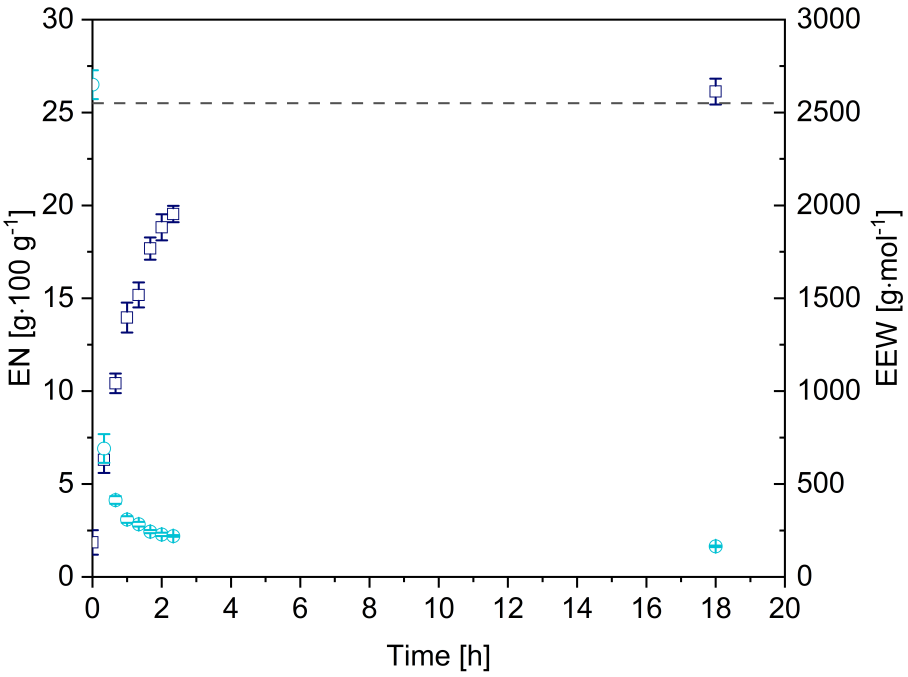

Figure 5.37 Chemoenzymatic epoxidation of LO to ELO in toluene with Novozyme® 435 and SA, 10 g LO in 50 mL toluene, 50 řC, 6.7 mg:C=C Novozyme® 435, 0.5 mol_{SA}:C=C, 1.0 $mol_{H_2O_2}$:C=C, 750 rpm overhead stirring. EEW and EN determined via non-aqueous titration according to Section 4.13.

Especially, the surfactant properties of ELO can contribute to a rapid crystallization of the FFA [238, 239]. The solidification process gave rise to a number of issues with regard to the purification of the final product. The straightforward removal of the solid catalyst and acid, as initially intended, was not a viable option, as the product-containing liquid phase was no longer accessible. The resulting solid matrix hindered both phase separation and downstream purification and rendered SA unsuitable for the intended workflow.

To address this limitation and ensure a readily separable liquid supernatant, the reaction was repeated using butyric acid (BA) as described by Liu et al. (2016) [172]. Short-chain carboxylic acids such as BA have been reported to exhibit favorable solubility in the organic phase and separation behavior, particularly when coupled with liquidliquid extraction from nonpolar organic solvents such as toluene using alkaline washing. Under otherwise identical reaction conditions, the use of BA led to a slightly reduced epoxidation rate, as seen by the flatter EN progression in Figure 5.38 (A). In contrast to the SA-based reaction, which approached an EN of $20\,g \cdot 100\,g^{-1}$ after 2.5 h, the BA-catalyzed system started to plateau earlier, reaching a comparable EN only after 4 h. This observation is consistent with prior literature reports and can be explained by the decreased nucleophilicity and

shorter chain length of BA, which likely result in a slower formation and turnover of the peracid intermediate [240, 241, 242]. Nevertheless, the use of BA provided a clear advantage in terms of processability. Cooling the reaction with BA yielded a homogeneous liquid organic phase, consisting solely of toluene, LO, and remaining BA. This stands in strong contrast to the wax-like solidification of the whole bi-phasic reaction system as seen with SA (Figure 5.38 (B)). This clean separation opens straightforward pathways for downstream purification via liquidliquid extraction of BA and solvent evaporation of toluene, as detailed in Section 5.2.6.

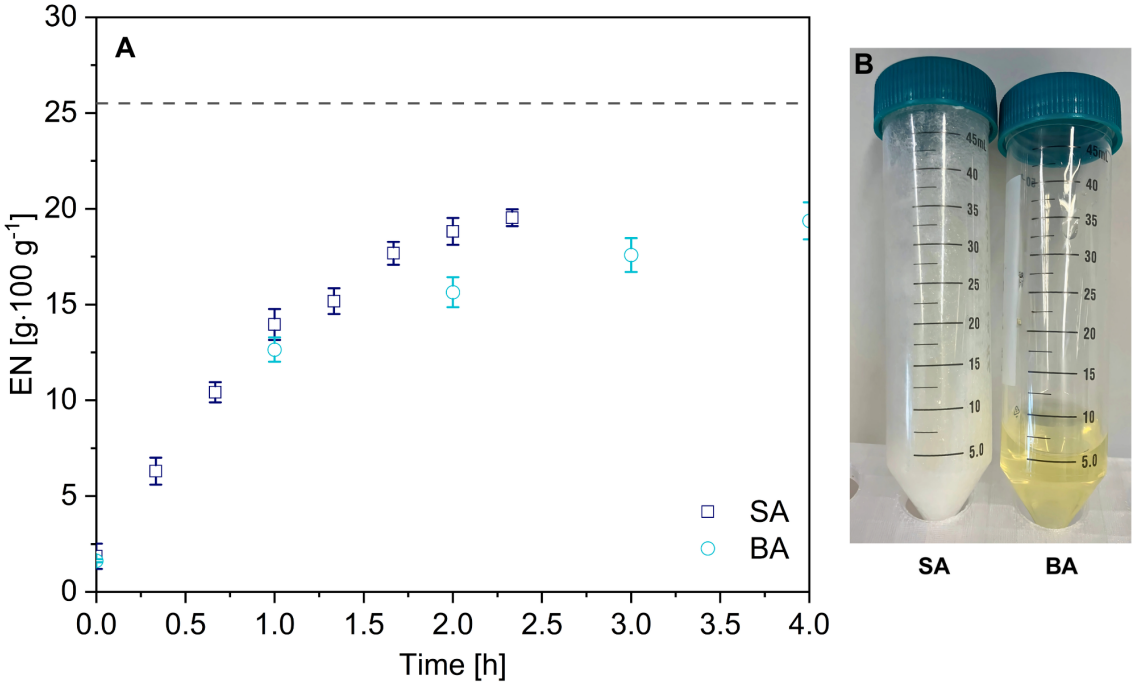

Figure 5.38 (A) Chemoenzymatic epoxidation of LO to ELO in toluene with Novozyme® 435 and SA or BA, 10 g LO in 50 mL toluene, 50 řC, 6.7 mg:C=C Novozyme® 435, 0.5 $mol_{SA/BA}$:C=C, 1.0 $mol_{H_2O_2}$:C=C, 750 rpm overhead stirring. EN determined via non-aqueous titration according to Section 4.13. **(B)** Physical state of the organic phase of the reaction mixture at room temperature after chemoenzymatic epoxidation of linseed oil with Novozyme® 435 utilizing **(left)** SA and **(right)** BA as free fatty acid co-reactant.

From a process-engineering standpoint, the trade-off of a slightly lower epoxidation efficiency in exchange for significantly improved phase behavior strongly favored the use of BA for the CEE of LO and was the subject of the subsequent optimization of the reaction parameters (Section 5.2.4) following the establishment of FTIR-based *inline* analysis of the reaction progress presented in the following section.

5.2.3 Set up of a Chemometric Model for *inline* Measurement of Epoxidized Linseed Oil

To monitor the structural transformation of LO during its CEE, FTIR spectra were recorded over a range of defined, artificial conversion levels, realized by mixing unreacted LO with chemically epoxidized ELO with full epoxide yield (Figure 5.39). The spectral data provide insight into the molecular changes occurring in the reaction mixture and serve as a foundation for mechanistic interpretation and quantification via indirect hard modeling (IHM). A prominent feature in the low-conversion spectra is the strong absorption band at approximately $1653\,\mathrm{cm}^{-1}$, attributed to the $\mathrm{C{=}C_{conjugated}}$ stretching vibration of alkene moieties in the unsaturated fatty acid chains of LO. As the reaction progresses, the intensity of this band decreases systematically, indicating the progressive consumption of C=C double bonds through electrophilic addition of the *in situ* formed peracid (perbutyric acid). This transformation is in line with the expected mechanism of Novozyme® 435-catalyzed perhydrolysis and subsequent oxygen transfer. The bending vibrations in the region around $1465\,\mathrm{cm}^{-1}$ to $1375\,\mathrm{cm}^{-1}$ correspond to CH_2 and CH_3 deformation modes. These bands show increases in intensity throughout the reaction due to changes in local polarity or molecular conformation upon epoxide formation. A key indicator of product formation is the spectral evolution in the region between $1250\,\mathrm{cm}^{-1}$ to $1100\,\mathrm{cm}^{-1}$, where C–O stretching vibrations of newly formed oxirane (epoxy) rings appear. The increase in absorbance within this window directly correlates with the formation of the epoxidized product (ELO) and represents the primary spectral range for product quantification. Furthermore, in the area below $1050\,\mathrm{cm}^{-1}$, strong epoxide bending modes are observed that increase with increasing conversion. However, the superposition and overlap of multiple vibrational modes in this region necessitate chemometric decomposition to resolve individual contributions.

Taken together, the evolution of these key spectral bands provides a robust basis for monitoring the CEE reaction in real time. The depletion of olefinic bands and the concurrent emergence of epoxy-specific signals confirm the mechanistic pathway and validate the use of FTIR spectroscopy in combination with IHM as a quantitative analytical strategy. However, as the actual spectral acquisition would proceed in the continuous organic phase, the other components apart from the substrate and product had to be taken into account for model development.

To establish a quantitative model for *inline* FTIR-based monitoring of epoxidation, a defined set of calibration mixtures was prepared with known molar conversion (χ), ranging from 0 to 1.

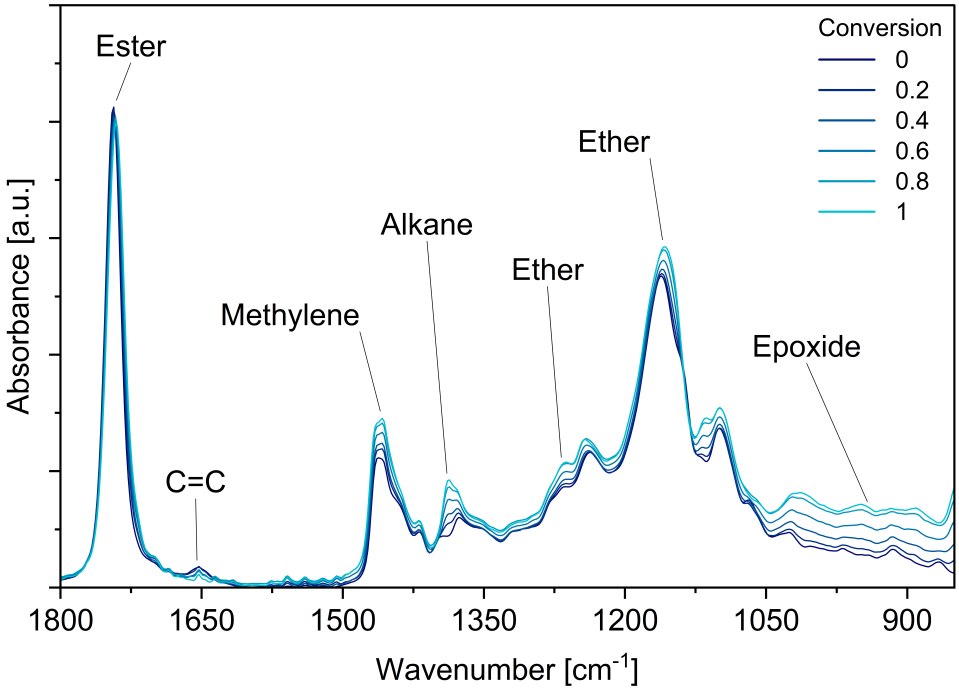

Figure 5.39 Overlay of mixture ATR-FTIR spectra of LO and ELO at different conversion. Scan resolution: $2\,cm^{-1}$, Scan number: 50, rubberband baseline correction (64 nodes, 10 iterations), min-max normalization.

The exact volumetric composition of each mixture with respect to LO, ELO, BA, and toluene (TOL) is provided in Table 4.12. The LO/ELO ratio was systematically varied while the concentrations of BA and TOL were kept constant in all mixtures to isolate the spectral contributions of substrate and product. This design enabled robust modeling of the conversion-dependent spectral features while minimizing effects from solvent or co-substrate. The aqueous phase containing H_2O_2 was not considered in the IHM because the ATR-FTIR measurements were only acquiring the continuous organic phase. As all components, including LO, ELO, BA, and the reaction solvent TOL were present in the mixtures at defined and constant concentrations, the system was modeled using a IHM approach. This strategy builds on the principle that all spectroscopically active species in the mixture are directly measured natively, thereby enabling decomposition of overlapping absorption bands into physically meaningful contributions of the actual spectrum. No assumptions about background subtraction or independent spectral behavior are required,

as the model is constructed using representative mixture and pure component spectra. The resulting overlay of ATR-FTIR spectra from the calibration mixtures is shown in Figure 5.40. The spectra display interpretable changes across the full conversion range, but also reveal the effect of the presence of BA and TOL, whereby some of the key regions identified before appear as overlap of underlying vibrations. An example of this is the methylene band just below 1500 cm^{-1}, which now represents the base peak of the spectrum due to the presence of TOL and BA and therefore no longer allows interpretation about product formation due to the normalization carried out. However, as the LO fraction decreases and the ELO fraction increases, bands associated with ether-type C–O stretching vibrations (in the region from 1250 cm^{-1} to 1100 cm^{-1}) show increasing intensity with rising conversion, reflecting the formation of epoxy rings in the product. Smaller but noticeable variations are also visible in the CH_2/CH_3 deformation region (1470 cm^{-1} to 1370 cm^{-1}) and in the fingerprint region below 1100 cm^{-1}, where C–H and additional C–O vibrations overlap.

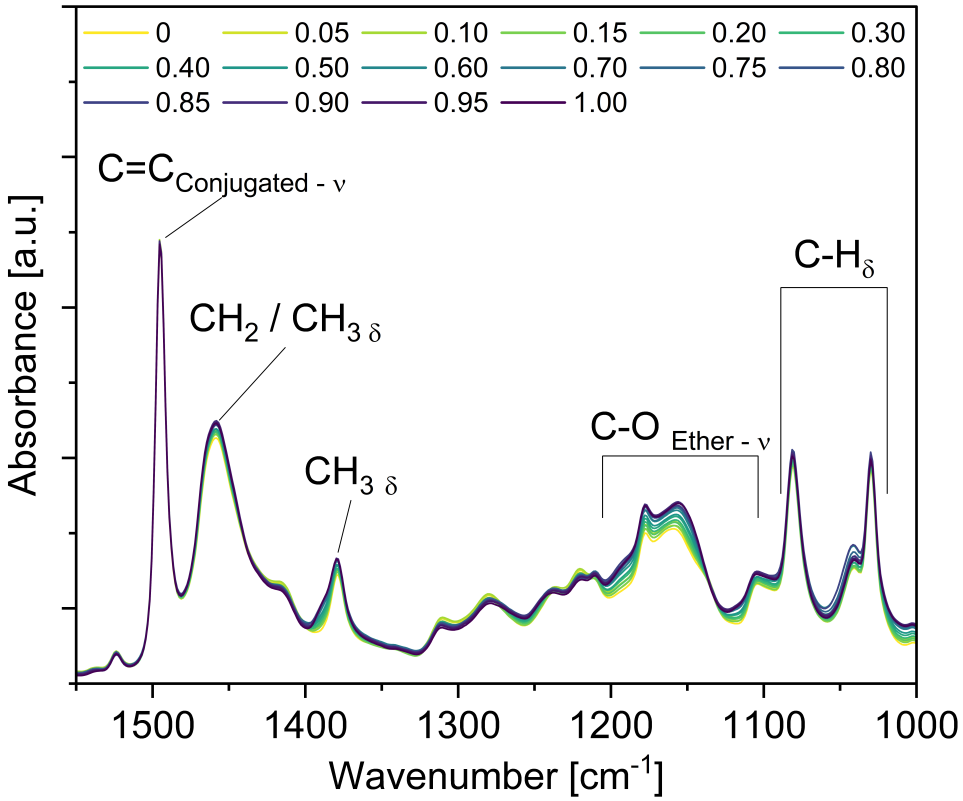

Figure 5.40 ATR-FTIR mixture spectra of LO and ELO in TOL and BA at different artificial conversion. Acquisition parameters: Scan resolution: 2 cm^{-1}, Scan number: 200, rubber-band baseline correction, area normalization.

The superposition of signals from all matrix components, including BA and TOL, results in broad baseline features that are accounted for explicitly within the model calibration. These spectra constitute the analytical foundation for the hard modeling approach described in the subsequent sections. The development of the IHM was based on the superposition of reference FTIR spectra of individual reaction components and their mixtures. Figure 5.41, shows the input spectra of pure TOL and BA, as well as of LO and ELO in toluene. These spectra were used to generate the additive spectral model representing the complete CEE system using the software Peaxact 5 (S-Pact GmbH, Aachen, Germany) according to Section 4.12.4. The bold line in Figure 5.41, represents the resulting complemental hard model, derived by linear combination of the reference spectra.

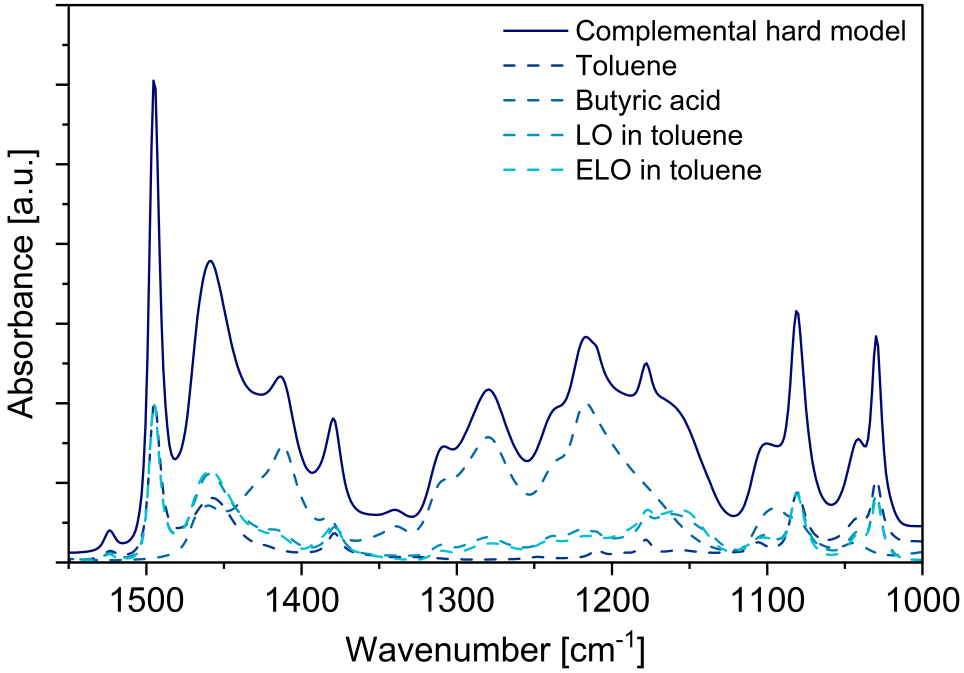

Figure 5.41 Complemental hard model derived from mixture spectra of LO and ELO in TOL and BA. Modeling was done in Peaxact 5.1 (S-Pact, Aachen, Germany) using pure component and mixture spectra. Acquisition parameters: Scan resolution: $2\,cm^{-1}$, Scan number: 200, rubber-band baseline correction, area normalization.

As seen in the figure, each component exhibits characteristic absorbance bands across the mid-infrared region. TOL contributes distinct signals in the region between $1500\,cm^{-1}$ to $1350\,cm^{-1}$, overlapping with CH_2/CH_3 deformation modes of the triglyceride components. BA, while present at a lower concentration, shows pronounced C–O stretching contributions between $1250\,cm^{-1}$ to $1100\,cm^{-1}$, partially overlapping with the oxirane-associated ether bands of the epoxidized product. The spectra of LO and ELO, measured

in TOL to match the reaction matrix, contribute the conversion-dependent features used for quantification. These are namely rising absorption intensity in the epoxy-sensitive regions (1250 cm^{-1} to 1050 cm^{-1}). The final complemental hard model spectrum demonstrates how the summed contributions of the individual species combine to form the expected spectral profile of a reaction mixture at intermediate conversion. This model served as the basis for interpreting *inline* FTIR data by multivariate regression, enabling accurate, component-specific quantification during the epoxidation reaction. The complemental hard model was calibrated against the known concentrations of LO and ELO in the prepared calibration mixtures. Linear regression was applied to correlate the FTIR-predicted signal intensities with the theoretical conversion-based concentrations of LO and ELO, respectively. The resulting calibration curves are presented in Figure 5.42. For LO, a robust linear calibration model was developed based on artificial conversion spectra, capturing the direct spectral response of the substrate with high fidelity across the entire conversion range. The regression line derived from the model (Figure 5.42 (A)) exhibited a slope of 0.184 and passed through the origin, in agreement with the physical expectation that the LO concentration reaches zero at full conversion ($\chi = 1$). The statistical evaluation confirmed this visual trend: the coefficient of determination was $R^2 = 0.991$, indicating strong linearity, while the root mean square error of calibration (RMSEC) and cross-validation (root mean square error of cross-validation (RMSECV)) were low at $5.4 \cdot 10^{-3}$ and $5.06 \cdot 10^{-3}$, respectively (Table 5.9).

Table 5.9 Calibration performance metrics of the FTIR-based IHM models for LO and ELO quantification.

Parameter	**LO**	**ELO**
R^2	0.991	0.998
RMSEC	$5.40 \cdot 10^{-3}$	$2.62 \cdot 10^{-3}$
RMSECV	$5.06 \cdot 10^{-3}$	$3.02 \cdot 10^{-3}$
Bias (Calibration)	$-1.91 \cdot 10^{-3}$	$-1.17 \cdot 10^{-17}$
Bias (Cross-validation)	$-1.83 \cdot 10^{-3}$	$-2.42 \cdot 10^{-4}$

The bias terms for both calibration (BiasC $= -1.91 \cdot 10^{-3}$) and cross-validation (BiasCV $= -1.83 \cdot 10^{-3}$) remained small, suggesting a slight but systematic underestimation that does not impair the reliability of the model. A separate but methodologically consistent calibration model was constructed for ELO.

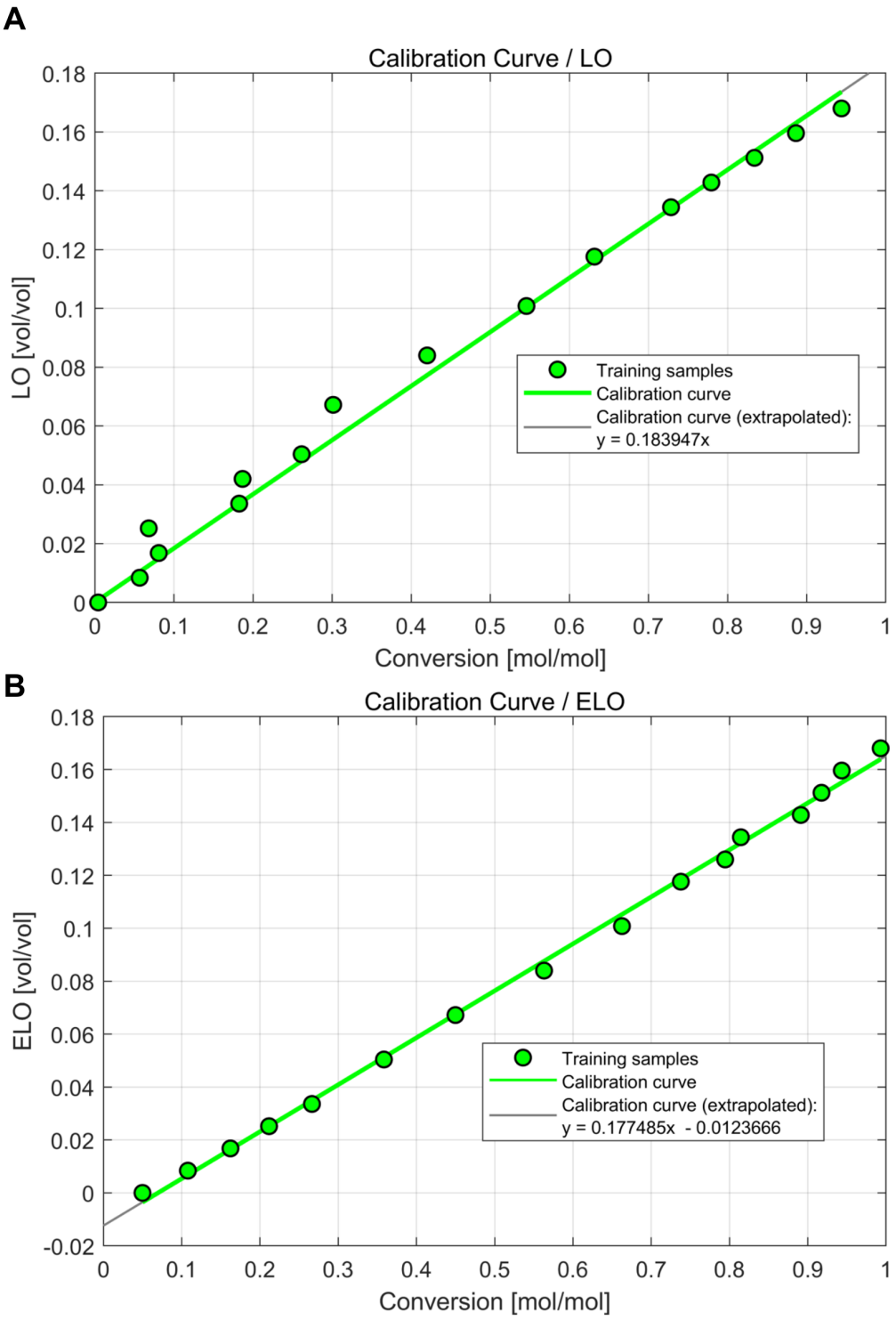

Figure 5.42 IHM calibration curves for the conversion of LO (**A**) to ELO (**B**) in TOL and BA using mixture ATR-FTIR spectra with different artificial conversion.

The resulting calibration curve Figure 5.42 (B)) showed a slope of 0.178 and a small negative intercept of −0.013, pointing to a minor underestimation of ELO concentration in the low-conversion regime. This was possibly due to matrix interactions or residual overlap with substrate or solvent bands. Nevertheless, the regression displayed near-perfect linearity with $R^2 = 0.998$ and very low errors (RMSEC = $2.62 \cdot 10^{-3}$, RMSECV = $3.02 \cdot 10^{-3}$). The bias terms were negligible in both calibration (BiasC ≈ 0) and cross-validation (BiasCV = $-2.42 \cdot 10^{-4}$), confirming the absence of any meaningful prediction offset.

This confirms that the FTIR signal of ELO increases proportionally with the degree of conversion and is accurately captured by the hard model throughout the reaction. As with LO, this enables reliable real-time tracking of product formation.

Overall, both models exhibited a strong signal-to-concentration correlation and minimal systematic error across the conversion range, confirming that the IHM approach using simulated reaction spectra effectively captures the key spectral contributions of substrate and product. To assess the predictive performance of the complemental hard models based on *inline* FTIR data, parity plots were generated for both LO and ELO. Figure 5.43 compares the predicted concentrations against the true values for both the calibration and validation samples. The dashed recovery line ($y = x$) represents the ideal case of perfect agreement.

For LO (left), the model predictions show a strong correlation with the true values across the entire concentration range. Both the training samples (blue squares) and the validation samples (cyan circles) cluster closely around the recovery line, with only minor deviations observed at intermediate values. This confirms the model's capacity to robustly quantify the depletion of LO during the CEE process. For ELO (right), the predictions are even more accurate. All data points follow the recovery line with minimal deviation, underscoring the models high predictive precision. These results are fully consistent with the statistical performance metrics (e.g., higher R^2, lower RMSEC and bias) and validate the suitability of the IHM for monitoring product formation and substrate depletion simultaneously.

To investigate the actual applicability of the model for the CEE of LO catalyzed by Novozyme® 435 in the presence of BA and to perform an *offline* validation of the predicted yields, a model validation reaction was carried out with the ATR-FTIR probe submerged in the bi-phasic system. Figure 5.44, illustrates the temporal evolution of LO and ELO concentrations over the course of a 4 h reaction.

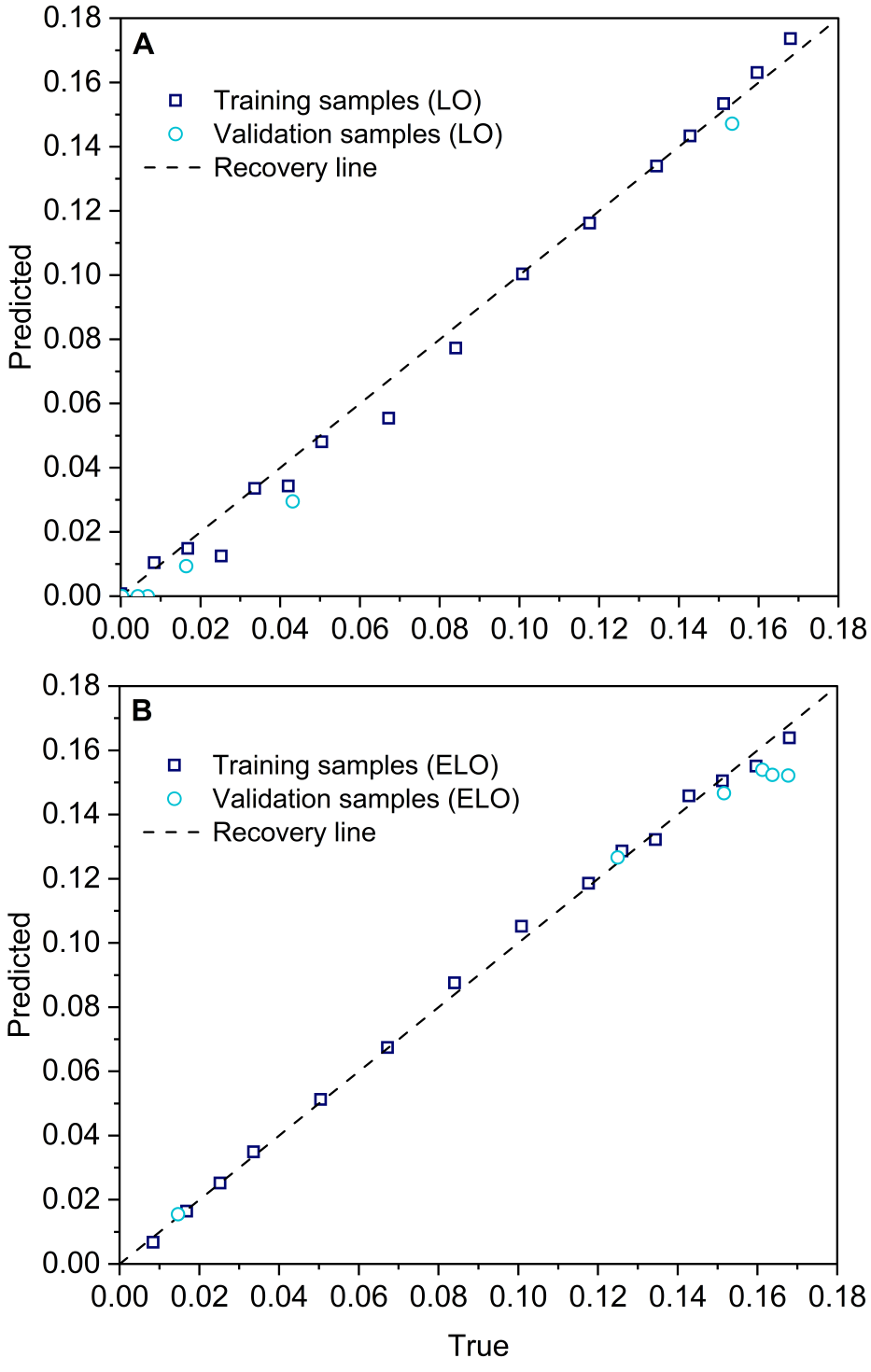

Figure 5.43 Parity plots comparing predicted and true concentrations for LO (**A**) and ELO (**B**) using FTIR-based IHM models. Training samples (blue squares) and validation samples (cyan circles) are shown relative to the ideal recovery line (dashed).

The cyan circles represent the volumetric concentration of LO, which decreases rapidly during the first 90 min of reaction, followed by a more gradual decline. This behavior suggests a high initial epoxidation rate likely driven by the rapid formation and availability of peracid. As the reaction progresses, the conversion slows down, possibly due to local depletion of hydrogen peroxide, enzyme deactivation, or increasing viscosity of the medium. In contrast, the formation of ELO, indicated by dark blue triangles, follows a hyperbolic progression, reaching a plateau after approximately 3 h, closely matching a final conversion observed in the acid screening before (Section 5.2.2).

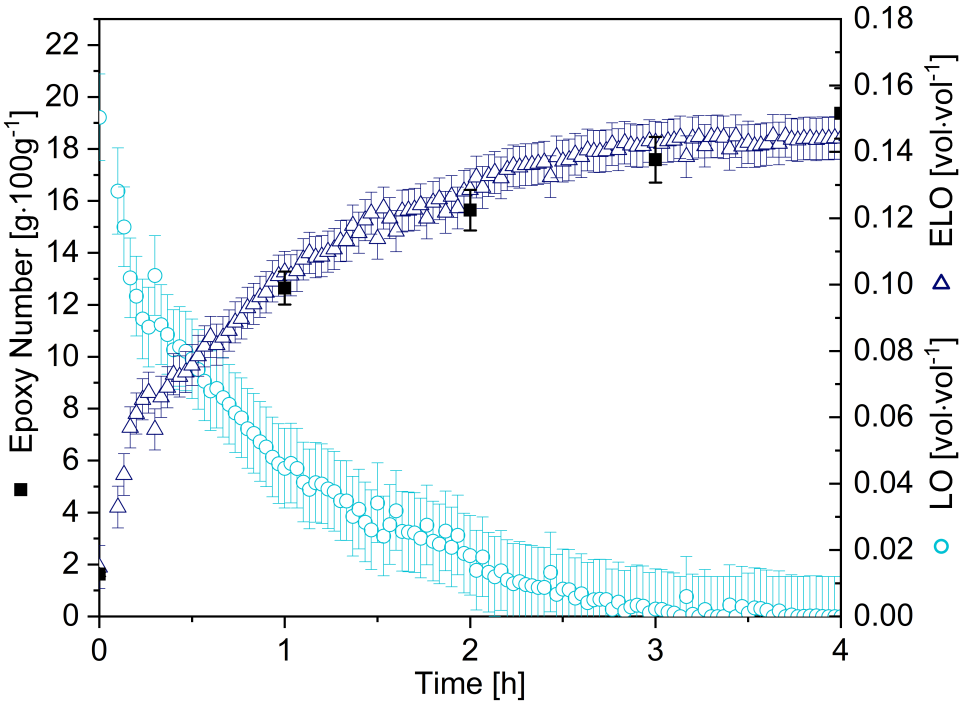

Figure 5.44 Chemoenzymatic epoxidation of LO to ELO in TOL with Novozyme® 435 and BA. 10 g LO in 50 mL toluene, 50 řC, 6.7 mg:C=C Novozyme® 435, 0.5 mol_{SA}:C=C, 1.0 $mol_{H_2O_2}$:C=C, 750 rpm overhead stirring. EN determined via non-aqueous titration according to Section 4.13. *Inline* ATR-FTIR acquisition in 2 min intervals.

The concurrent decline of LO and rise of ELO demonstrates the successful transformation of unsaturated bonds to epoxy groups. The *inline* FTIR model predictions for ELO closely match the values obtained from *offline* EN titration (black squares), confirming the accuracy of the indirect hard model in tracking product formation. This *inline* profile

highlights the suitability of the complemental hard model for real-time reaction monitoring and supports its application for scale-up and process optimization efforts in biobased epoxy resin production, as is part of the following sections.

5.2.4 Optimization of the Chemoenzymatic Epoxidation of Linseed Oil

To systematically investigate the influence of key process parameters on the efficiency and conversion kinetics of the CEE of LO, a design of experiments (DoE) approach was employed. A BoxBehnken design was selected due to physical limitations of the design space, while still enabling the construction of a second-order response surface model [243]. This design allows for efficient estimation of linear, quadratic, and two-factor interaction effects without requiring experiments at extreme highlow combinations of all factors, which may be infeasible or undesirable under certain reaction conditions. The following three factors were identified as critical parameters based on prior mechanistic understanding, preliminary experiments and literature suggestions:

- the enzyme loading (Novozyme® 435) relative to oil mass,
- the molar ratio of hydrogen peroxide to unsaturated double bonds (C=C),
- the molar ratio of BA to C=C.

Each factor was varied across five levels, including center points and factorial points, according to standard Box-Behnken methodology. The coded levels and corresponding real values are summarized in Table 5.10 and the DoE was carried out as described in Section 4.12.2.

Table 5.10 Factor coding and levels for DoE-based optimization of chemoenzymatic linseed oil epoxidation.

Factor	Name	Unit	Coding
A	Enzyme amount	% ($w \cdot w_{oil}^{-1}$)	$-1 \Leftrightarrow 1.00$, $+1 \Leftrightarrow 6.00$
B	H_2O_2/C=C	$mol \cdot mol^{-1}$	$-1 \Leftrightarrow 0.50$, $+1 \Leftrightarrow 3.00$
C	BA/C=C	$mol \cdot mol^{-1}$	$-1 \Leftrightarrow 0.50$, $+1 \Leftrightarrow 3.00$

The statistical evaluation of the design of experiments revealed distinct behavior for the two key responses: EN, used as an indicator for epoxidation yield, and acid number (AN), representing the accumulation of unreacted BA and reaction by-products from potential ester hydrolysis. For the response AN, the reduced two-factor interaction (2FI) model was

found to be statistically significant with a model p-value below 0.0001 and an R^2 of 0.8397 (Table 5.11). The adjusted and predicted R^2 values (0.8053 and 0.6872, respectively) were in acceptable agreement, indicating moderate predictive capability.

Table 5.11 Model statistics and significant model terms for epoxy number and acid number.

Statistic / Term	**EN Model**	**AN Model**
R^2	0.8397	0.9918
Adjusted R^2	0.8053	0.99
Predicted R^2	0.6872	0.9839
Adeq Precision	16.87	62.99
p-value (Model)	< 0.0001	< 0.0001
Lack of Fit (p)	0.0449	0.0459
Significant factors	A, C, AC	C

Among the tested factors, enzyme amount (factor A), the BA:C=C ratio (factor C), and their interaction (AC) were all statistically significant ($p < 0.05$). As shown in the left-hand contour plot in Figure 5.45, increasing the enzyme concentration had a positive effect on EN, particularly at lower BA:C=C ratios. However, a strong negative coefficient for factor C (5.92) indicates that higher amounts of BA substantially decreased epoxy yield.

The negative interaction between A and C further suggests that high levels of both enzyme and BA diminish the beneficial catalytic effect of the lipase, possibly due to local substrate inhibition as described by Nordblad and Adlercreutz (2008) [244] for high concentration of polar carboxylic acids, which could further explain the observed profile. For AN, a quadratic model provided the best fit and was statistically significant with a high R^2 and predicted R^2 values of 0.9918 and 0.9839, respectively. The adeq. precision of 62.99 further confirmed high model reliability. Here, only the BA:C=C ratio (factor C) was statistically significant, while enzyme amount (A) and the AC interaction term were not. The corresponding contour plot (Figure 5.45 right) illustrates a steep increase in AN with rising BA concentrations, while variation in enzyme loading had negligible impact. This confirms that excess BA remains unconverted under the tested conditions and accumulates in the organic phase, thereby increasing the acid number. The minor effect of enzyme concentration on AN also suggests that the reaction is limited by peroxide availability or equilibrium constraints rather than by catalyst turnover.

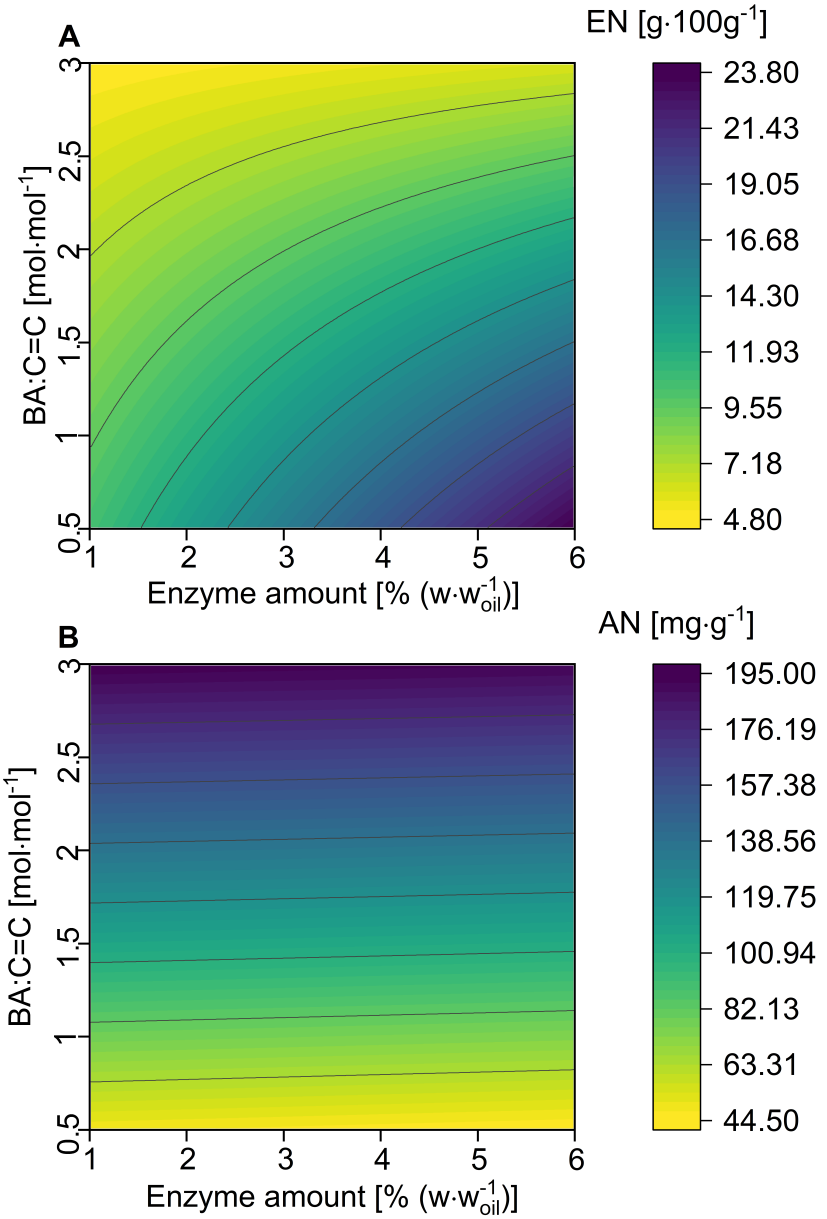

Figure 5.45 Contour plots showing the effect of enzyme concentration and BA:C=C ratio on epoxy number (**A**) and acid number (**B**) at fixed H_2O_2/C=C ratio. A high EN and low AN indicate favorable process conditions.

Furthermore, since no increase in AN was detected with increasing enzyme amounts, triglyceride hydrolysis was likely not present. Overall, the model results support the conclusion that high enzyme loading combined with a low BA:C=C ratio maximizes epoxidation yield while minimizing acid residues. These findings dictate the subsequent selection of optimal process conditions for scale-up and *inline*-monitored epoxidation.

To verify the predictive accuracy of the statistical model and assess its practical utility, a validation batch was conducted under the optimal conditions identified via the BoxBehnken design. The selected parameter set (enzyme amount: 6% ($w \cdot w_{oil}^{-1}$), H_2O_2:C=C molar ratio: 1.75 mol · mol^{-1}, BA:C=C molar ratio: 0.5 mol · mol^{-1}) was applied in a batch reaction monitored by *inline* FTIR and validated through *offline* epoxy number titration. The time-resolved reaction data are shown in Figure 5.46.

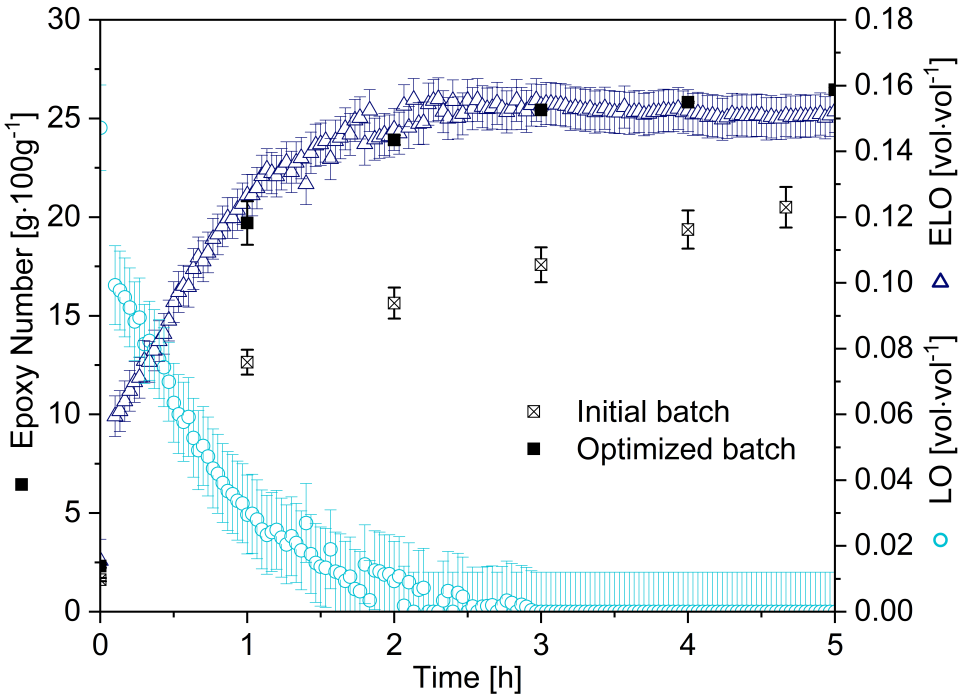

Figure 5.46 *Inline* measurement validation batch of chemoenzymatic epoxidation of LO to ELO in TOL with Novozyme® 435 and BA. EN determined via non-aqueous titration. *Inline* ATR-FTIR acquisition in 2 min intervals. 40 mL-scale: 10 g LO in 50 mL toluene, 50 řC, 6% ($w \cdot w_{oil}^{-1}$ Novozyme® 435, 0.5 $mol_{SA/BA}$:C=C, 1.75 $mol_{H_2O_2}$:C=C, 750 rpm overhead stirring. EN determined via non-aqueous titration according to Section 4.13.

Compared to the initial batch, the optimized process exhibited a significantly accelerated reaction rate, achieving full conversion within less than 3 h. The EN reached its theoretical maximum of 25 g · $100\,g^{-1}$, consistent with the modeled prediction. The *inline* FTIR measurements for both LO depletion and ELO formation closely matched the

offline titration values (black squares), confirming the accuracy and robustness of the indirect hard model under process-relevant and changing conditions. The initial batch, conducted under baseline conditions, showed markedly slower epoxidation rates and incomplete conversion over the same time period, only reaching approximately $19\,\mathrm{g} \cdot 100\,\mathrm{g}^{-1}$. The improvement achieved with the optimized conditions underscores the benefit of model-guided process design and illustrates the successful integration of chemometric and statistical modeling strategies in the development of a robust CEE protocol employing Novozyme® 435.

5.2.5 Scale Up of Chemoenzymatic Epoxidation of Linseed Oil using a SpinChem® Rotating Bed Reactor

To evaluate the transferability of the optimized chemoenzymatic epoxidation process to a larger scale, the reaction was conducted in a 200 mL batch using a SpinChem® rotating bed reactor (RBR). This reactor configuration offers efficient mixing and catalyst containment in a confined, exchange-optimized volume, making it particularly suitable for immobilized enzymes such as Novozyme® 435 and enabling straightforward catalyst recovery. A photograph of the experimental setup is provided in Figure 5.47. The baffled glass reactor was equipped with a heated double jacket for temperature control and fitted with the ATR-FTIR probe for *inline* analysis. Enzyme beads were confined within the rotating cylindrical mesh of the RBR, ensuring mechanical integrity and high surface area exposure while preventing bead dispersion into the bulk medium. The RBR continuous stirring motion and radial flow characteristics enhance substrate diffusion to the enzyme surface and promote uniform reaction conditions throughout the vessel. This configuration is especially beneficial in viscous multiphase systems, where conventional stirring may lead to inhomogeneities and enzyme bead damage.

To ensure proper scalability of the reaction, mixing times were experimentally determined at 750 and 1000 rpm for both 40 mL and 200 mL reaction volumes, respectively, as described in Section 4.12.3. The results showed highly comparable mixing behavior with mean values of 2.32 ± 0.19 s for the small scale and 2.37 ± 0.09 s for the large scale. As the Reynolds and Newton number could not be determined for the given reaction setups, the mixing time was used as a substitute approximation for hydrodynamic characterization in the scale-up. Maintaining such similarity of mixing times is critical in multiphase systems, where mass transfer limitations can significantly influence reaction kinetics and conversion

efficiency. The scaled-up reaction was carried out under the previously validated optimal conditions.

Offline epoxy number determinations were performed at defined intervals to track the conversion over time. As shown in Figure 5.48, the reaction proceeded with comparable kinetics and final conversion as in the small-scale validation experiment, confirming the robustness of the developed protocol under increased volume.

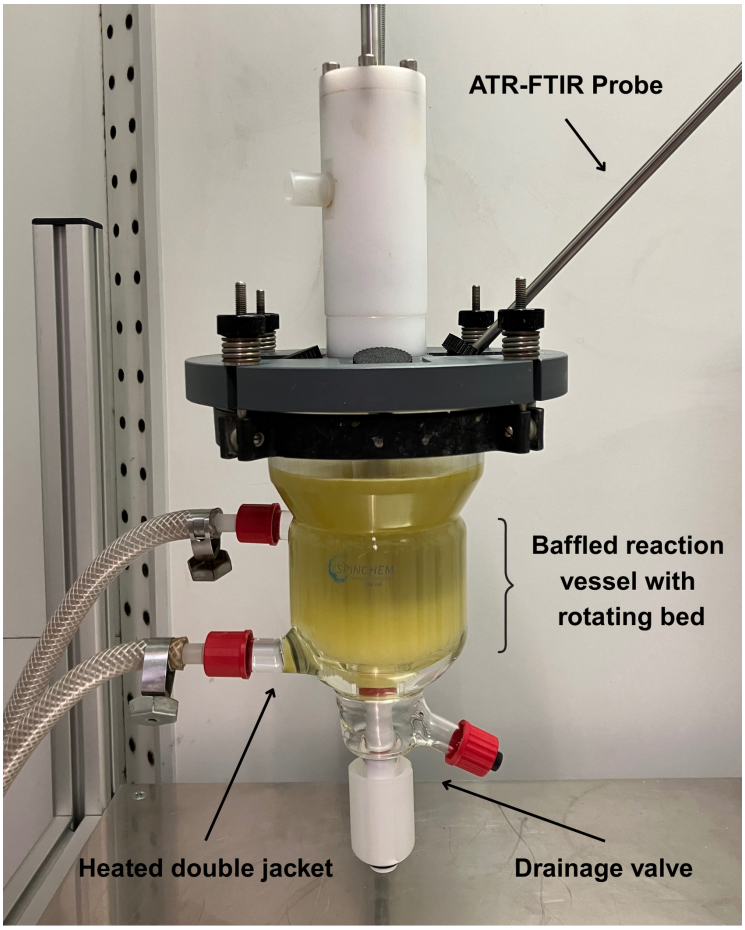

Figure 5.47 Photograph of reaction setup employing the SpinChem® V2 RBR (SpinChem®, Umeå, Sweden) system with *inline* ATR-FTIR acquisition.

Notably, the system reached the theoretical epoxy number maximum of approximately $25\,\mathrm{g} \cdot 100\,\mathrm{g}^{-1}$ within a similar reaction time, and with equivalent reproducibility, demonstrating the resilience of the enzyme under intensified mixing regimes. However, during *inline* FTIR measurements in the scaled system, unexpected broad absorption bands associated with water appeared, which were absent under small-scale conditions.

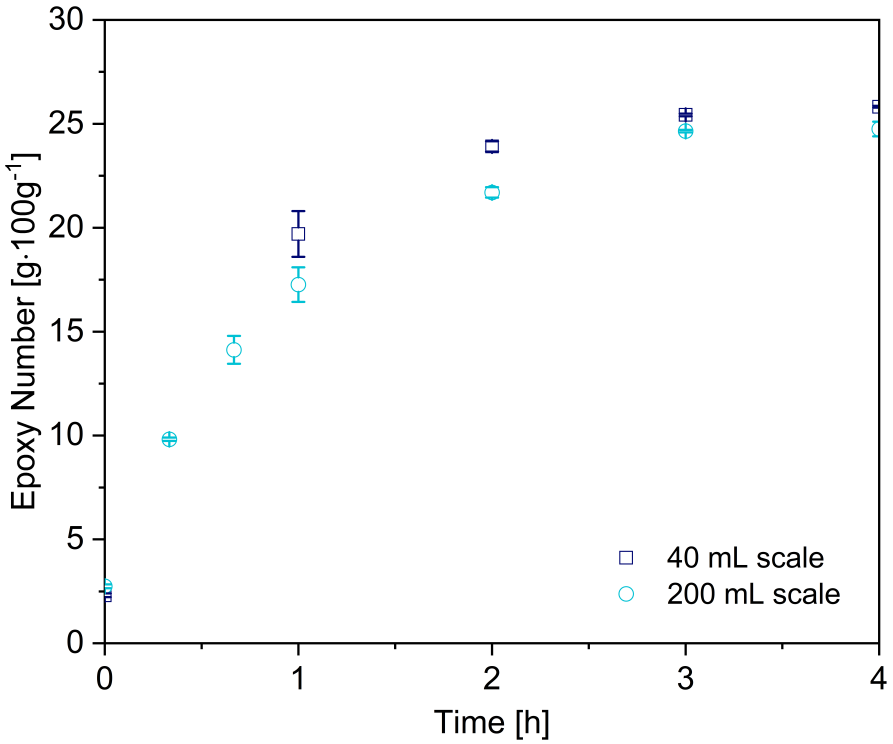

Figure 5.48 Chemoenzymatic epoxidation of LO to ELO in toluene with Novozyme® 435 and BA in SpinChem® V2 rotating bed reactor, 26.8 g LO in 200 mL toluene, 50 řC, 6% ($w \cdot w_{oil}^{-1}$ Novozyme® 435, 0.5 mol_{BA}:C=C, 1.75 $mol_{H_2O_2}$:C=C, 1000 rpm overhead stirring. EN determined via non-aqueous titration according to Section 4.13.

These bands obscured key regions used in the spectral quantification model, as depicted in Figure 5.49 (left). The formation of a fine emulsion, caused by the strong shear and dispersion induced by the RBRs 104 ţm metal mesh, is the most likely explanation. The intensified droplet formation increased the effective water surface area and led to water being suspended in the organic phase, thereby affecting the FTIR baseline and contributing additional, broad absorbance bands in the OH stretching regions near 1650 cm^{-1} and 1350 cm^{-1}.

To quantify the influence of mechanical agitation on this effect, the FTIR signal intensity in the 1250 cm^{-1} region was measured as a function of the RBR stirring speed. The results, presented in Figure 5.49 (right), show a clear dependence of water band intensity on rpm, with a maximum observed between 800 min^{-1} to 1000 min^{-1}. Beyond this range, a slight decrease was noted, likely due to droplet coalescence or detachment from the probe surface caused by high fluid velocities.

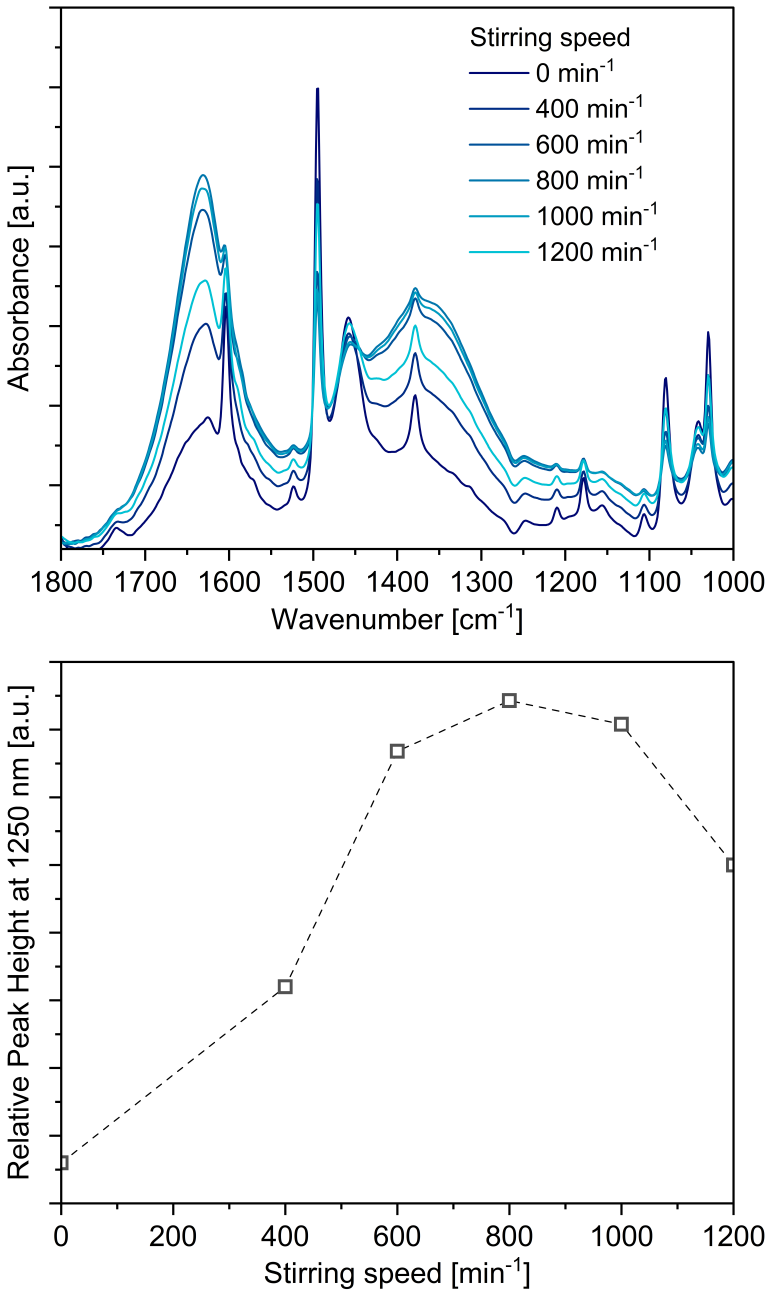

Figure 5.49 Spectral effect of water in liquid two-phase system for chemoenzymatic epoxidation of LO to ELO in TOL with Novozyme® 435 and BA.

These results also imply that the physical nature of the water emulsion is dynamic and shear-sensitive and might therefore undergo changes during the progress of the reaction as the viscosity of the organic phase increases. These findings highlight the importance of understanding interfacial and emulsification phenomena during the scale-up of chemoenzymatic systems and underscore the need to adapt *inline* spectroscopic monitoring strategies accordingly. The shift in signal baseline and band interference renders simple extrapolation of small-scale models impractical unless adjustments are made to match the optical conditions used during model development. Nevertheless, attempts to replicate the flow conditions and emulsion characteristics in relation to the aqueous phase droplet size proved unsuccessful. This was primarily due to the inherent scale effects that prevented precise reproduction. Moreover, the requirement for extensive quantities of reactants to ensure precise calibration within the reactor itself was deemed unfeasible and ultimately rejected.

To still overcome the limitations caused by emulsion-induced signal distortion, a modified monitoring strategy was implemented. The approach involved transitioning from a direct *inline* setup to an *online* configuration using a bypass stream. This design allowed for controlled sampling of the reaction mixture under more representative and spectroscopically favorable optical conditions, thereby mitigating spectral interference from aqueous micro-droplets.

A process and instrumentation (P&I) diagram of the bypass loop is shown in Figure 5.50. The ATR-FTIR probe was repositioned into a dedicated analysis vessel equipped with its own agitation, flow regulation, and thermal control.

The vessel dimensions and configuration matched those used during small scale experiments (Section 5.2.4), ensuring consistency in the emulsion regime and spectral fingerprint. Continuous circulation between the main reactor and the bypass vessel allowed for representative real-time sampling. Flow velocity and agitation intensity within the bypass reactor were tuned such that emulsification matched previously established reference conditions, effectively preventing the influence of water in the FTIR spectra while keeping the residence time reasonably low at approx. 12 s. As ATR-FTIR spectra were acquired at 2 min intervals with an individual acquisition time of approximately 40 s, the additional residence time introduced by the bypass configuration can be considered negligible with respect to the temporal resolution of the measurement.

Using this bypass configuration, *online* ATR-FTIR measurements were successfully reinitiated. As shown in Figure 5.51, the signal profiles for LO and ELO showed a strong agreement with *offline* titration values, closely mirroring the temporal conversion trends observed in the 40 mL scale.

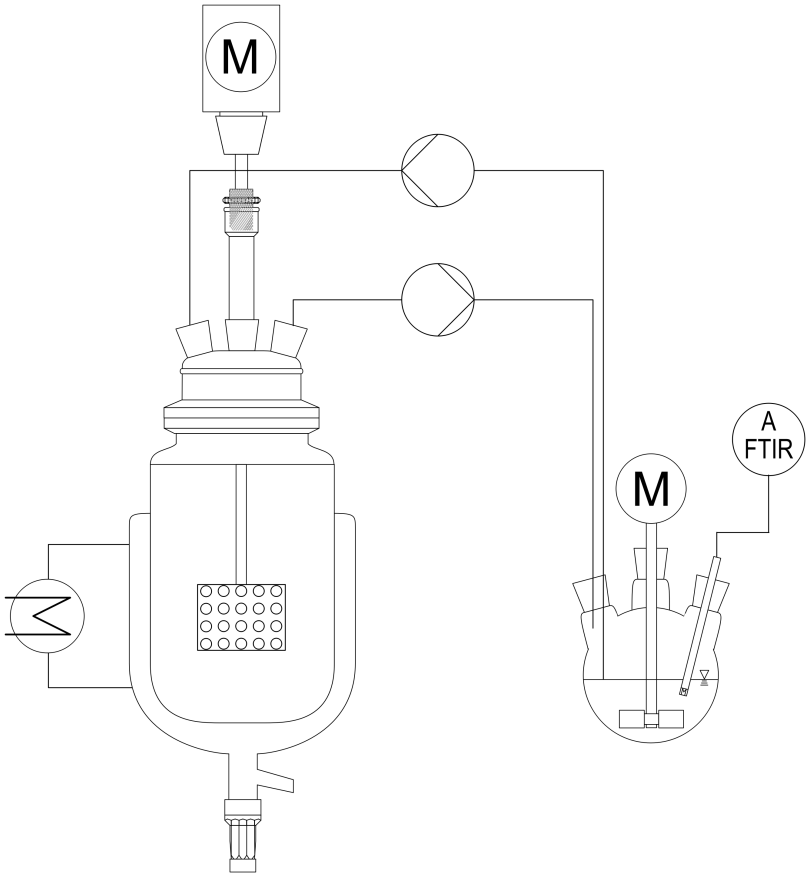

Figure 5.50 Flow scheme of SpinChem® V2 rotating bed reactor with *online* ATR-FTIR measurement using a bypass vessel for chemoenzymatic epoxidation of LO to ELO in TOL with Novozyme® 435 and BA.

This confirms that the revised *online* monitoring configuration preserved the calibration validity of the indirect hard model, even in the presence of intensified emulsification dynamics. The ability to adapt model-based FTIR monitoring to scale-dependent physical phenomena significantly enhances the practical utility of chemometric process control.

The successful implementation of the bypass strategy and accurate *online* monitoring in the 200 mL rotating bed reactor establishes a robust and transferable methodology for larger-scale epoxidation processes. The RBR-based setup provides a modular and scalable platform that combines efficient catalyst handling with real-time process control. As the role of hydrogen peroxide dosing was not thoroughly investigated in this study, the established system can make a valuable contribution in this area, for instance, by monitoring the deactivation of the catalyst in real-time or investigating recyclability using the packed bed reactor.

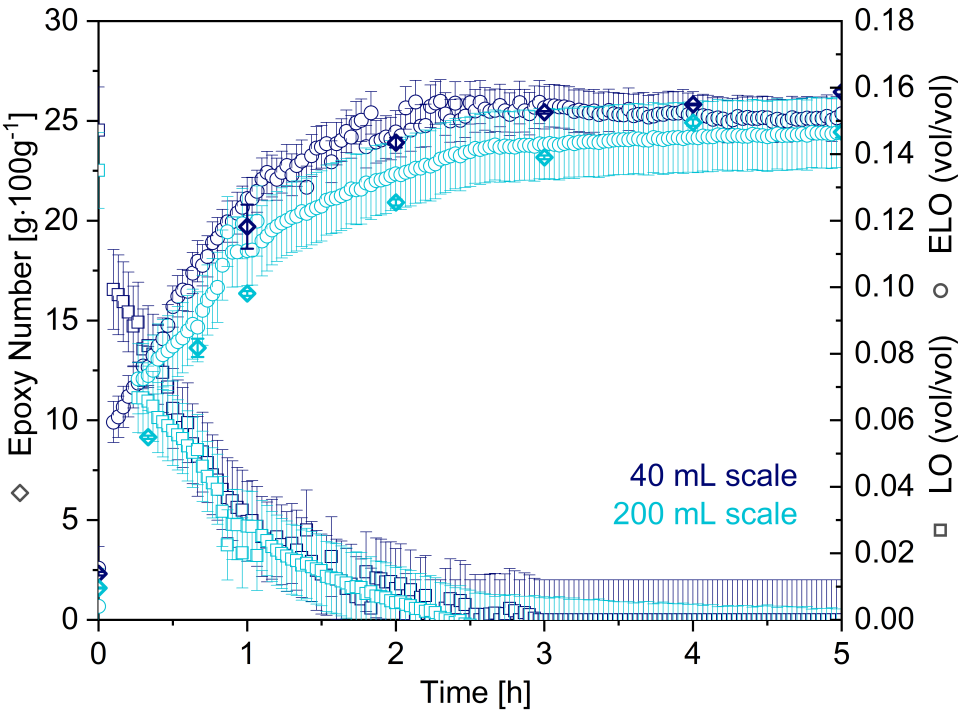

Figure 5.51 *Online* ATR-FTIR monitoring of chemoenzymatic epoxidation of LO to ELO in toluene with Novozyme® 435 and BA in Spinchem® rotating bed reactor under bypass configuration. 40 mL-scale: 10 g LO in 50 mL toluene, 50 řC, 6% (w·w_{oil}^{-1} Novozyme® 435, 0.5 $mol_{SA/BA}$:C=C, 1.75 $mol_{H_2O_2}$:C=C, 750 rpm overhead stirring, 200 mL-scale: 26.8 g LO in 200 mL toluene, 50 řC, 6% (w·w_{oil}^{-1} Novozyme® 435, 0.5 mol_{BA}:C=C, 1.75 $mol_{H_2O_2}$:C=C, 1000 rpm overhead stirring. EN determined via non-aqueous titration according to Section 4.13.

Importantly, the confined rotating bed design simplifies catalyst recovery and reuse, supporting green chemistry objectives in biocatalytic process development. With process monitoring restored through bypass adaptation, the platform is well-suited for further scale-up to pilot or technical-scale bioreactor systems. This positions the method as a promising candidate for industrial application in sustainable epoxy resin synthesis. Moreover, the insights gained regarding the interplay between reactor configuration, emulsion dynamics, and spectral accuracy can serve as guiding principles for scaling additional chemoenzymatic transformations beyond the current system.

5.2.6 ELO Purification and Production of Biobased Epoxy

Following successful scale-up of the CEE of LO, downstream purification was investigated to ensure a proper processability as thermoset formulation. A critical requirement for successful curing with anhydride or multifunctional carboxylic acid hardeners is the absence of free carboxylic acids, particularly the co-reactant BA used during the epoxidation. If not removed, residual BA can react with epoxide groups via ring-opening esterification, effectively terminating the reactive sites and thereby suppressing the intended crosslinking reaction [133]. Initial purification trials employed alkaline extraction using 0.1 mol · L^{-1} NaOH solution in a 1:1 volume ratio with the organic reaction phase as mentioned by Rüsch gen. Klaas and Warwel (1999) [171]. However, this approach led to visible hydrolysis of the triglyceride backbone, evidenced by pronounced thickening of the organic layer and the formation of a persistent, viscous emulsion. These effects were attributed to partial saponification and ester bond cleavage under the strongly basic conditions, effectively destroying the product.

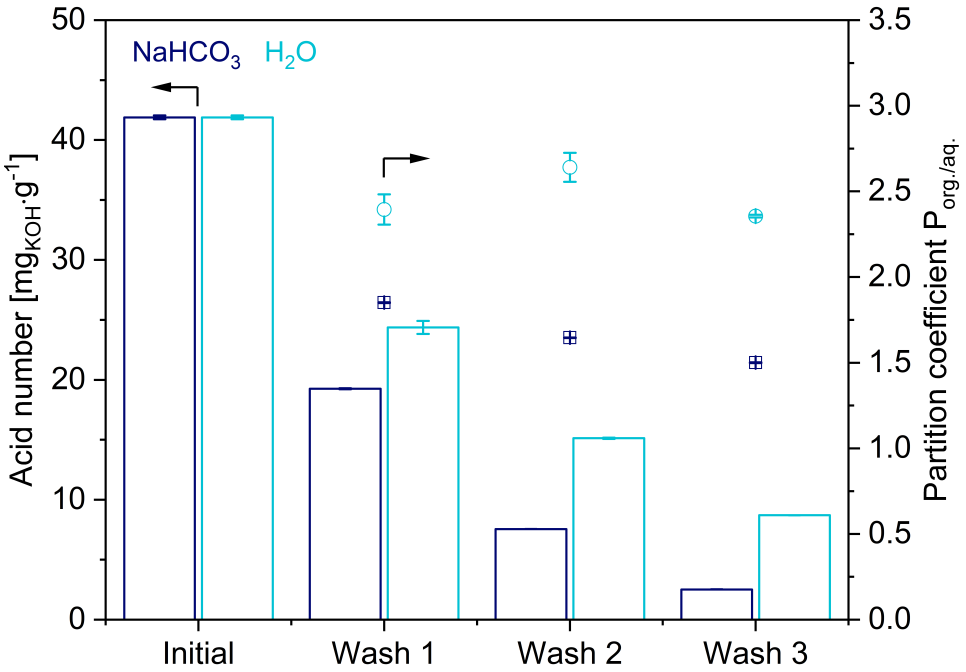

Figure 5.52 Acid number and distribution coefficient $P_{org./aq.}$ of butyric acid enriched in extract phase during three washing steps of organic supernatant of chemoenzymatic linseed oil epoxidation using either hot ultrapure water (70 řC) or 0.1 mol · L^{-1} $NaHCO_3$ solution.

As a result, alternative milder extraction strategies were explored to preserve product integrity while effectively removing the acid.

To this end, extractions using either hot ultrapure water at 70 řC or 0.1 mol · L^{-1} $NaHCO_3$ solution were evaluated [172, 245]. Each approach was carried out over three consecutive liquid-liquid extraction cycles in a separatory funnel, maintaining a 1:1 organic-to-aqueous phase ratio for each wash. After each step, the AN of the organic phase was measured according to standard titration procedures as described in Section 4.12.5. Additionally, the distribution coefficient $P_{org./aq.}$ of BA was calculated to compare extraction efficiencies across the two methods. The results, illustrated in Figure 5.52, demonstrate that $NaHCO_3$ was significantly more effective than hot water at reducing the AN of the ELO phase. After three washing steps, the $NaHCO_3$-treated samples achieved final acid numbers of 2.52 ± 0.01 $mg_{KOH} \cdot g^{-1}$, thereby being in a a well acceptable range for most crosslinking applications [246]. This amounted to an overall removal of BA of approx. 94% using bicarbonate washing, while hot water extraction only decreased the amount of acid by 79.2%, amounting to a final AN of 8.71 ± 0.005 $mg_{KOH} \cdot g^{-1}$. Moreover, the consistently lower partition coefficients in the range of 1.5-1.75 observed for $NaHCO_3$ suggest a more favorable phase distribution of BA into the aqueous phase, promoting an almost complete extraction and enhanced selectivity without inducing hydrolysis or promoting formation of an emulsion. This is the result of the dissociation of the $NaHCO_3$ in aqueous media which leads to the formation of the watersoluble carboxylate of BA according to the following equation:

$$CH_3CH_2CH_2CO_2H + NaHCO_3 \longrightarrow CH_3CH_2CH_2CO_2^- \, Na^+ + H_2CO_3$$

Mild alkaline washing with $NaHCO_3$ thus offers a practical and scalable purification approach for chemoenzymatically epoxidized vegetable oils. By maintaining the structural integrity of the triglyceride backbone while efficiently reducing residual acidity, this method ensures compatibility of the resulting ELO with curing agents. After purification, the organic phase was concentrated under reduced pressure to remove toluene, yielding a viscous, clear product with high epoxy content and minimal residual odor from BA. To validate the curing performance of the purified biobased ELO, DSC analysis was performed using citric acid as a biobased crosslinking agent. The resulting thermograms were benchmarked against a chemically epoxidized commercial reference resin from HOBUM Oleochemicals GmbH (Hamburg, Germany) cured under identical conditions according to Section 4.4.2.

As shown in Figure 5.53, the Bio-ELO and the chemical reference exhibited nearly identical exothermic curing behavior, with peak maxima centered at 133.4 řC and 136 řC, respectively. The total curing enthalpy was also comparable (35.06 and 37.08 J · g^{-1}), indicating equivalent reactivity and crosslinking density. A minor endothermic event was observed at 59.2 řC in the biobased sample, which was absent in the reference material. This deviation is attributed to residual toluene that was not fully removed during the concentration step. Nevertheless, the overall thermal conversion profile of the Bio-ELO was considered equivalent to that of the industrial benchmark. Overall, these findings are also consistent with DSC results described by Fuste-Dmoc et al. (2023) [247], who reported a T_{peak} of 131 řC.

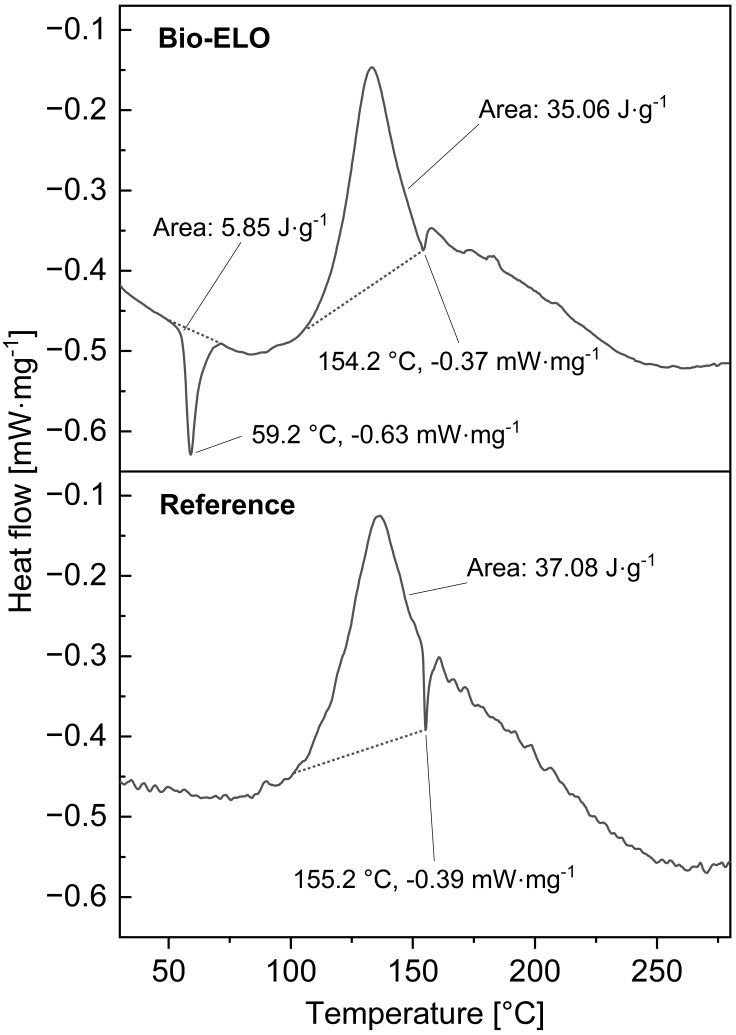

Figure 5.53 DSC curves of biobased ELO and chemically epoxidized reference cured with citric acid.

These results confirm that ELO produced via the chemoenzymatic route can be processed into thermoset networks with performance comparable to that of conventional petrochemical analogs. The compatibility with biobased hardeners such as citric acid further supports the sustainability of this approach and its potential for future use in greener coating, adhesive, and composite formulations.

6 Overall Discussion & Outlook

In this final section, the dual achievements of the present study are examined in a broader context and suggestions towards future work in this field are presented. The work has advanced two complementary fronts in sustainable epoxy resin technology:

1. advancing biocatalytic pathways to degrade conventional thermoset epoxies, and
2. developing biobased epoxy monomers via green chemoenzymatic synthesis.

The following sections discuss how the results contribute to scientific understanding and practical applications in each domain, while seamlessly integrating forward-looking perspectives inspired by the findings.

6.1 High-performance Thermoset Epoxy Resins are Susceptible to Enzymatic Oxidation

This study demonstrated a novel enzymatic strategy to attack highly inert, aerospace-grade epoxy networks, which had previously seen virtually no documented biocatalytic degradation [6, 85]. By drawing an analogy between the synthetic epoxy matrix and lignin, a natural recalcitrant aromatic polymer, the work investigated fungal laccases known from lignin depolymerization literature [1, 183].

Figure 6.1 summarizes the central mechanistic concept underlying the enzymatic activation of highly crosslinked epoxy networks developed in this work. Laccases were chosen for their ability to generate diffusible radical mediators that can penetrate a polymer matrix. The in-house preparation of a cured resin transfer mold 6 resin (RTM6) epoxy resin provided a realistic, high-performance substrate for these degradation trials. As most critical point, the resin's aromatic, densely crosslinked structure (typical of carbon-fiber reinforced polymer (CFRP) matrices) poses both chemical and steric resistance to enzymatic attack. By milling the resin into fine particles (250 µm range), the available surface area was increased to improve enzyme contact. This pre-processing step proved essential, as it enabled more homogeneous solid–liquid interactions and was a practical compromise between particle size and handling. Using low-molecular-weight model compounds that mimic segments of the epoxy network was another aspect of the approach. This allowed rapid screening of various fungal laccases and provided quantitative measures of their activity on epoxy-like bonds. A clear trend emerged linking enzyme redox potential to oxidative efficacy on the model substrate *N*,*N*-bis(2-hydroxypropyl)-*p*-toluidine (NNBT).

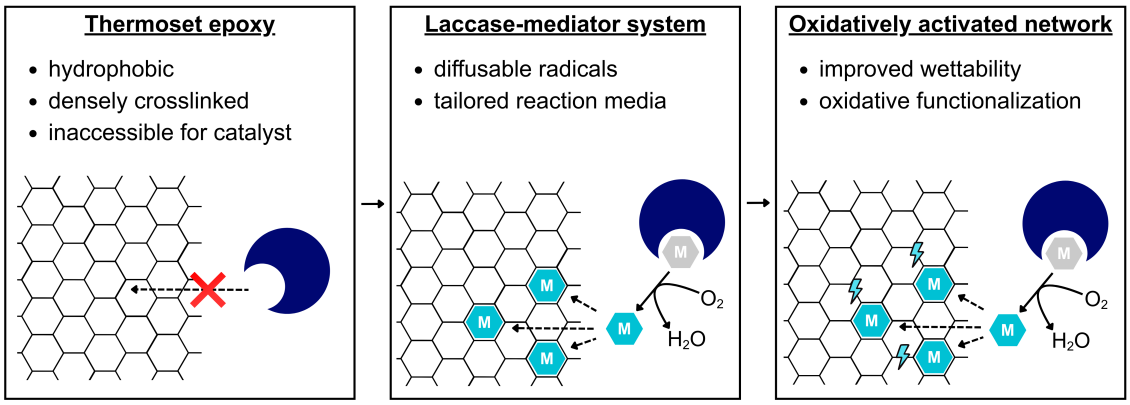

Figure 6.1 Conceptual scheme illustrating the transition from enzyme-inaccessible thermoset epoxy networks to oxidatively activated structures via a laccasemediator system. The illustration is a simplified and stylized representation. Hexagonal symbols denote arbitrary redox mediators.

High-redox-potential laccases (able to abstract electrons from strong C–H or non-phenolic aromatic bonds) outperformed lower-potential enzymes, consistent with the need to attack the inert structures present in the resin [15]. This finding advances the broader understanding of enzymes by demonstrating that electrochemical properties are critical determinants of an enzymes effectiveness in degrading synthetic polymers.

Future enzyme discovery and engineering for polymer degradation should prioritize oxidoreductases with higher redox potentials or those that natively utilize redox mediators. In the latter context, the screening of different redox mediators confirmed that, even though the best-performing laccase from *Funalia trogii* was able to oxidize the model compound on its own, the addition of suitable mediators partly improved conversion. This validates the classical laccasemediator system (LMS) concept in a new application domain, extending its relevance from natural lignin breakdown to man-made epoxy resin waste [248].

Molecular docking studies provided mechanistic insight into why mediators are likely indispensable for attacking a crosslinked epoxy network. The simulations showed that large epoxy oligomers analogous to segments of the cured RTM6 resin cannot easily fit into the enzyme active site due to steric hindrance. Only small molecules, like the mediator 2,2,6,6-tetramethylpiperidinyloxyl (TEMPO) or the model amine substrates, could effectively bind and undergo direct oxidation. These results imply that the laccase must act primarily by first oxidizing a small mediator, which in turn diffuses into the polymer matrix to oxidatively cleave bonds that the enzyme is sterically limited to access on its own.

To find the best suited mediator for that case, electrochemical analysis was conducted to evaluate the stability of the screened mediators alongside their biochemical properties. Among the panel of candidate mediators evaluated electrochemically, TEMPO was identified as the most effective and stable molecule. The mediator analysis by cyclic voltammetry (CV) ensured that the chosen compound could withstand the reaction conditions without extensive autodegradation.

Together, these outcomes underline a general principle for polymer biodegradation, namely, that combining enzymes with synergistic small-molecule mediators can overcome the size and stability barriers of heavily crosslinked plastics. Future research can extend this principle by testing additional redox mediators and enzyme pairings to push degradation efficiency further. For instance, employing mediator cocktails or engineering laccases with expanded substrate spectra could broaden the range of attack on the polymer backbone. Additionally, integrating peroxidases or other oxygenase enzymes, such as lignin peroxidase, that produce radical species might complement laccases and lead to a more pronounced and efficient bond cleavage [249].

The reaction conditions for the LMS were further systematically investigated. Temperature optimization revealed a strong trade-off between stability and thermal activation. While raising the temperature accelerated the oxidation rates, it also reduced enzyme half-life significantly. A moderate temperature of 50 řC was identified as the preferred compromise, enabling substantially faster kinetics than at room temperature without leading to strong thermal deactivation. Additionally, sufficient aeration was critical because oxygen is the terminal oxidant in laccase-catalyzed reactions (Section 2.4). As demonstrated by the stirred-tank experiments, in the absence of oxygen supplementation, there was a rapid decline in dissolved oxygen (DO) levels, which resulted in a decline of the reaction rate. By ensuring adequate aeration, a high catalytic turnover could be maintained, leading to an overall 5-fold increase in oxidation rates.

Applying the optimized laccase-TEMPO system to actual RTM6 epoxy samples demonstrated partial oxidative degradation of the thermoset network. Although complete depolymerization was not achieved under the conditions tested, clear evidence of bond cleavage and oxidative modification was obtained. Attenuated total reflection fourier-transform infrared spectroscopy (ATR-FTIR) spectroscopy of enzyme-treated resin showed new absorption bands (e.g., signals indicative of carbonyl functionalities) that were absent in the untreated control, indicating the introduction of oxygen into the polymer backbone. Elemental analysis further supported an increase in oxygen content of the solid residue. These chemical changes were accompanied by observable physical changes of the material.

The treated resin particles exhibited discoloration, and thermogravimetric analysis (TGA) revealed a reduction in thermal stability relative to the virgin resin. Such alterations are characteristic of partial oxidation and chain scission, and they represent a first step toward breaking the polymer into smaller fragments.

Importantly, even partial degradation can be technologically useful. For instance, oxidatively pretreating the matrix could facilitate fiber recovery from composites or allow subsequent mild hydrolysis to occur more readily. From a bioeconomy perspective, the ability to at least fragment or make the epoxy network more susceptible to further attack could potentially allow to convert a recalcitrant thermoset into oligomeric products that might be revalorized or mineralized by microorganisms, as proposed by Wongwattanarat et al. (2025) [13]. A next set of experiments could therefore be to couple the LMS treatment with consecutive or preceding biodegradation by specialized microbes, to assess if the oxidized fragments can be fully assimilated. Additionally, identifying potential soluble oxidation products could provide further insights into the biochemical oxidation/degradation pathways and foster the development of downstream valorization routes.

In this study, gas chromatography coupled mass spectrometry (GC-MS) analysis of model compound degradation revealed distinct products and plausible pathways (e.g., benzylic alcohols, ketones, and cleavage products). Extending such analysis to real resin digests could uncover whether valuable aromatic chemicals or polyols are being generated, opening the door to recovering these as chemical feedstocks or novel monomers for future polymer applications.

Finally, one of the fundamental hurdles in enzymatic polymer degradation was addressed: the poor wettability and accessibility of hydrophobic plastics in aqueous biocatalytic environments [250, 251]. Epoxy resins like RTM6 are highly hydrophobic and tend to repel water, limiting enzyme contact on their surfaces. To mitigate this, deep eutectic solvent (DES) mixtures were investigated as alternative reaction media. The introduction of DES and aqueous solutions thereof led to a marked improvement in polymer wetting, evidenced by substantially reduced contact angles on epoxy surfaces.

This improved wettability implies that the enzyme solution can spread and penetrate more effectively, potentially accessing internal sites on the polymer particles that were previously unreachable. Moreover, certain DES components can act as gentle swelling agents for polymers, further increasing enzyme accessibility [252]. In experiments involving the model compound NNBT, especially the inclusion of polyol-based DES led to partially increased enzymatic activity against the surrogate and facilitated faster oxidation of the polymeric resin. This effect was achieved without needing a packedbed reactor, since

the DES enhanced substrate suspendability, making the resin easier to disperse in bulk solution.

Future experiments should target the optimization of the composition of DES mixtures to balance improved wetting against any potential enzyme inhibition, or even utilize bio-derived DES components to maintain overall process sustainability. If successful, these solvents coupled with robust enzymes could form the basis of an efficient pretreatment for enzymatic recycling of not just epoxies but other hydrophobic polymer wastes [253].

In summary, the biocatalytic degradation investigations have resulted in a foundational methodology for tackling one of the most recalcitrant classes of polymers, thermoset epoxies, using oxidative enzymes. The work represents a new perspective on the biodegradation of epoxy by proving that laccase systems, when assisted by mediators and process engineering aspects (e.g., packed-bed reactor, alternative solvents), can overcome the barriers that have made the biodegradation of thermosets a largely overlooked field of research. This approach contributes to the broader vision of sustainable materials management, suggesting that even highly crosslinked durable plastics might be repurposed under environmental benign conditions. For technological application, while a fully enzymatic recycling process for epoxy composites is still in early stages, the study indicates which enzyme characteristics are desirable, which process conditions are optimal, and which supplementary strategies (mediators, co-solvents) might be worth pursuing in future. Future research should expand on this by testing real composite systems to evaluate the influence of carbon or glass fibers on the enzymatic reaction system. Additionally, upscaling the reactor system, possibly using fixed- or trickle-bed bioreactors will be crucial. As fiber length is important for the effective end-of-life use of composites, a reaction system is required that can handle these particular demands, as it is not possible to simply use finely ground particles as done in the present work. By continuing to refine enzymemediator formulations and coupling them with additional up- or downstream treatments, the development moves closer to bio-inspired end-of-life strategies for epoxy-based materials, in which biocatalytic degradation pathways play a pivotal role in recycling and waste valorization.

6.2 Chemoenzymatic Synthesis of Epoxidized Linseed Oil as Renewable Epoxy Alternative With Inherent Biodegradability

Complementing the degradation approach, this dissertation also targeted a sustainable synthesis route for epoxy resins, focusing on epoxidized linseed oil (ELO) as a renewable monomer platform for fiber-reinforced applications. The strategy combined enzymatic catalysis with classical chemistry to perform epoxidation of unsaturated plant oils under mild, green conditions. At the core of this process is the use of lipase from *Candida antarctica* (CALB) (immobilized as Novozyme® 435) to generate peroxycarboxylic acids *in situ*. In practical terms, the enzyme catalyzes the reaction of a carboxylic acid such as butyric acid (BA) with H_2O_2 to form a peracid, which then performs *Prileshajev* epoxidation on the C=C double bonds of linseed oil (LO) fatty acid chains. This chemoenzymatic epoxidation (CEE) route circumvents the need for strong mineral acids or metal catalysts and avoids the handling of hazardous peracids separately. The result is an environmentally friendly epoxidation process which operates at low temperatures, produces water as the major by-product, and significantly reduces the risk of side reactions that can occur with traditional, purely chemical processes.

In the context of green chemistry, these features contribute to safer and more sustainable manufacturing of epoxy precursors, aligning with the principles of using renewable feedstocks and biocatalysts. A further key aspect of this work was the integration of real-time analytical monitoring using fourier-transform infrared spectroscopy (FTIR) spectroscopy into the epoxidation process, which addressed the challenge in working with multiphase reaction mixtures.

The reaction mixture for ELO production is complex as it contains a hydrophobic oil phase (substrate and product), aqueous H_2O_2, an organic co-solvent, a co-catalyst (BA), and the solid enzyme particles. These components all have overlapping infrared absorbances, making conventional *inline* monitoring difficult. To overcome this, an *inline* ATR-FTIR probe was employed in combination with a indirect hard modeling (IHM) approach. Specifically, a classical least squares model was constructed from the reference infrared spectra of each key component (LO, ELO, BA, toluene (TOL)), enabling deconvolution of the mixture spectrum. This analytical solution allowed for quantitative tracking of both substrate consumption and product formation in real time, even in the presence of emulsions and dispersion. The validity of the spectroscopic monitoring was confirmed by a strong correlation with *offline* titration data ($R^2 > 0.99$, prediction error < 0.6 % (v/v)).

Using this integrated monitoring, the study employed design of experiments (DoE) to systematically optimize the epoxidation conditions. A BoxBehnken experimental design evaluated the effects of three critical factors enzyme concentration, H_2O_2:C=C ratio, and BA concentration on the extent of epoxidation. The analysis revealed significant two-factor interaction effects, most notably between enzyme loading and co-catalyst amount. At low enzyme loading, increasing the acid beyond a certain point did not result in a higher epoxide yield, likely due to rate limitation in peracid formation. In contrast, at high enzyme loading, the acid amount became a decisive factor for maximizing conversion in the given time frame. The optimal conditions were identified as 6 % (w/w) enzyme, 1.75 mol · mol^{-1} H_2O_2:C=C, and 0.5 mol · mol^{-1} BA:C=C. Under these conditions, the reaction reached complete conversion of unsaturated bonds in under 3 h, achieving an epoxy number (EN) of 25 g · $100\,g^{-1}$ with negligible residual acidity. No side-products were detectable by the end of the reaction, indicating a high selectivity in the optimized process. These results contrast conventional chemical epoxidation of vegetable oils, which often suffer from over-oxidation (yielding diols or glycols) or require much longer reaction times and stronger catalysts [172, 254]. From a technological application viewpoint, achieving quantitative epoxidation in such a short time frame enhances the throughput potential of the process, and the mild conditions help preserve the integrity of the desired epoxide functional groups.

Moving forward, an area of further research could focus on enzyme reuse and stability, for instance, examining how many batches the immobilized lipase can catalyze before activity decreases, or whether enzyme performance can be sustained in a continuous reactor over extended periods. This would directly impact the economic feasibility of scaling up the process. Additionally, exploring other inexpensive short-chain acids, or even acids derived from biowaste streams, as the oxygen carrier for peracid generation could improve the sustainability and cost profile of the epoxidation route. A further promising optimization strategy could involve increasing the effective H_2O_2 concentration at reduced overall water content, in order to enhance peracid formation while minimizing undesired hydrolytic side reactions.

The scalability of the CEE process was demonstrated by transferring the reaction from bench-scale to a 200 mL reactor without loss of performance. A rotating bed reactor (RBR) was used at the larger scale, which houses the immobilized enzyme in a spinning cylindrical cage to ensure efficient mixing and mass transfer [255]. This setup delivered comparable kinetic profiles and final epoxide yields as the small-scale trials, proving that

the process can be scaled at least two orders of magnitude with the mixing time as scale-up criterion. One challenge encountered at higher stirring speeds was the formation of fine emulsions that interfered with the ATR-FTIR baseline. This circumstance was solved by introducing a bypass loop for the FTIR sensor and restored the previous state of the spectroscopic measurement without requiring a new calibration.

This practical solution exemplifies how engineering adjustments can solve scale-up issues while preserving the benefit of real-time monitoring. For industrial translation, such insight is invaluable: it suggests that the core reaction and analytical method are robust, and only minor modifications are needed to maintain performance in larger reactors. As an outlook, the next step is to push the scale further and test the process in larger SpinChem reaction vessel. Alternatively, a continuous reactor, such as a packed-bed system where fresh oil and peroxide can be fed continuously through an Novozyme® 435-packed column, could be tested according to the principles of flow chemistry. Continuous operation could facilitate enzyme reuse and improve space-time yields, moving the technology closer to an economically viable industrial process.

After epoxidation, the downstream processing of the crude ELO was addressed to ensure a high-purity epoxy product and to evaluate its material performance. The main impurity to remove was the residual BA and any derivatives thereof. A simple yet effective liquidliquid extraction protocol was developed using $NaHCO_3$ solution, which reacts with and extracts carboxylic acids as water-soluble salts. Three washes with $0.1\,\mathrm{mol}\cdot\mathrm{L}^{-1}$ $NaHCO_3$ reduced the acid number (AN) of the ELO to below $5\,\mathrm{mg_{KOH}}\cdot\mathrm{g}^{-1}$, with minimal loss of the epoxidized triglycerides.

After purification, the functional performance of the biobased ELO was validated by formulating it into a thermoset resin and evaluating its curing behavior. Using citric acid as bio-derived curing agent, the ELO was crosslinked into a polymer network, thereby creating a fully biobased epoxy resin system. differential scanning calorimetry (DSC) of the curing reaction showed an exothermic peak around 155 řC, with a total enthalpy of $35\,\mathrm{J}\cdot\mathrm{g}^{-1}$ to $37\,\mathrm{J}\cdot\mathrm{g}^{-1}$. These values are in strong agreement with those of a chemically epoxidized linseed oil batch, cured under similar conditions. The similarity in curing exotherm and enthalpy indicates that the epoxide functionality in ELO is comparably reactive and capable of forming crosslinked networks with an efficiency analogous to conventional epoxies.

This successful curing experiment demonstrates that biobased epoxy resins produced via the CEE route can meet the performance benchmarks of chemically epoxidized systems. It

adds to the scientific understanding that plant-oil-derived epoxides, when properly formulated, can transition from being just plasticizer additives to serving as primary resin components for durable materials [132]. From an application perspective, this opens up pathways to develop sustainable composites and coatings, e.g., combining ELO-based resins with natural fiber reinforcements or using them in protective coatings where biodegradability and low toxicity are desired. The next steps would include testing the mechanical properties and long-term stability of the cured ELOcitric resin, to ensure that its promising thermal curing profile translates into sufficient strength, stiffness, and durability for real-world use. Additionally, the concept of *inherent biodegradability* should be empirically verified. Since the crosslinker (citric acid) introduces ester bonds into the network, the cured ELO resin is expected to be more susceptible to hydrolytic enzymatic attack. Future experiments could involve exposing the cured resin to compost or enzyme solutions to measure its degradability.

Overall, the development of the CEE process for LO underscores a significant environmentally friendly shift in how epoxy resins and their precursors can be produced. By combining biocatalysis, *inline* analytical monitoring, and process engineering, this work provided the basis for a scalable method for producing renewable epoxy monomers. In future, the biobased epoxy resin platform could be expanded and refined. For instance, other polyunsaturated oils (from algae, waste cooking oil, or non-edible seeds) could be explored as feedstocks using the same enzymatic epoxidation reaction, potentially tuning the epoxy equivalent weight (EEW) and functionality for different applications.

Likewise, alternative bio-derived co-monomers or crosslinkers, such as itaconic acid, derived from fermentation, could be tested with ELO to increase the variety of fully sustainable resin systems [256]. In line with the enzymatic degradation efforts, this work on biobased epoxy synthesis contributes to a circular economy approach for epoxy polymers from the opposite end of the product life cycle. While the degradation pathway intends to deal with conventional epoxy materials, the biobased synthesis route aims to reduce future waste by creating epoxy resins that are derived from renewable resources and potentially easier to degrade or recycle. The interplay of these two strategies is an important outlook for the research field in general. In the ideal scenario, future epoxy composites will be made from bio-derived monomers and crosslinkers, so that any waste generated can be fed into biocatalytic recycling processes.

In summary, by demonstrating both biocatalytic degradation pathways for current epoxy thermosets and a biobased epoxy synthesis for future materials, this research has

advanced toward closing the loop for epoxy polymers. This study shows that the use of high-performance materials can be made more compatible with environmental sustainability by applying biocatalysis and green process engineering. It also outlines several practical directions for further research in the field of circular polymer systems.

7 Summary

The present study tackled the dual challenge of recycling epoxy thermosets and producing sustainable alternatives, aiming to support circular polymer technologies. It focused on two complementary goals: **(1)** enzymatic depolymerization of high-performance epoxy networks and **(2)** the chemoenzymatic synthesis of biobased epoxides from plant oils, enabling improved recyclability and sustainability of epoxy materials.

Section 5.1 investigated oxidative degradation of an aerospace-grade thermoset epoxy (RTM6) using fungal laccases and small redox mediators. To provide enzyme access, the resin was synthesized in-house, cured, and mechanically milled. Low-molecular-weight model compounds such as N,N-Bis(2-hydroxypropyl)-p-toluidine (NNBT) were used to screen enzyme activity. Laccases alone were partly able to oxidize NNBT, but in combination with TEMPO and other redox mediators, an increase in conversion was achieved. Among several enzymes tested, a high-redox-potential laccase from *Funalia trogii* showed superior activity. *In silico* docking studies supported the role of TEMPO as a diffusible mediator, since bulky polymer fragments could not enter the enzymes active site. Subsequent optimization identified ideal conditions (pH 4, 50 řC, 10 mmol $\cdot$ L^{-1} TEMPO), which were transferred to a packed-bed reactor setup to treat real, polymeric epoxy particles. Spectroscopic, thermal, and elemental analyses all confirmed oxidative modifications to the polymer, such as increased oxygen content, carbonyl and hydroxyl group formation, and decreased thermal stability. These changes were visually reflected in color shifts and elevated char residue in thermal analysis. Collectively, these results demonstrate partial oxidative cleavage of aromatic and amine structures within the epoxy network. The use of DESwater mixtures further improved wetting and enzyme contact, offering a promising strategy to enhance degradation of hydrophobic polymers in future studies.

Section 5.2 focused on the chemoenzymatic epoxidation of linseed oil to produce a renewable epoxy monomer, epoxidized linseed oil, with potential biodegradability. The reaction employed immobilized Novozyme® 435 to catalyze *in situ* formation of peracids from butyric acid and H_2O_2, which subsequently epoxidize C=C bonds in the oil. The process was performed under mild conditions (50 řC) and monitored *inline* via ATR-FTIR spectroscopy in combination with an Indirect Hard Modeling approach, yielding a robust predictive model ($R^2 > 0.99$). A DoE-based optimization (BoxBehnken) identified optimal conditions: 6 % (w/w_{oil}) enzyme, 1.75 mol $\cdot$ mol^{-1} H_2O_2:C=C, and 0.5 mol $\cdot$ mol^{-1} butyric acid:C=C, achieving complete conversion within 3 h and

producing epoxidized linseed oil with an epoxy number of approximately $25\,\mathrm{g} \cdot 100\,\mathrm{g}^{-1}$. The process was further successfully scaled to 200 mL using a SpinChem® reactor with a bypass loop for improved spectral monitoring, opening further options for industrial implementation. For downstream processing of the product, a $NaHCO_3$ washing step removed residual free fatty acid, reducing the acid number of the epoxidized linseed oil below 5 $\mathrm{mg_{KOH}} \cdot \mathrm{g}^{-1}$. The purified epoxidized linseed oil was then cured with citric acid, and DSC analysis revealed curing behavior and enthalpy ($35\,\mathrm{J} \cdot \mathrm{g}^{-1}$ to $37\,\mathrm{J} \cdot \mathrm{g}^{-1}$) comparable to conventional petrochemical epoxy systems, underlining the suitability of the process for demanding applications.

In conclusion, this work presents a holistic approach to advance epoxy circularity: **(1)** enzymatic degradation of existing thermosets using laccasemediator systems and **(2)** a green, scalable synthesis route for renewable epoxy monomers with real-time process control. Together, these approaches contribute to the development of sustainable high-performance materials within a circular polymer economy.

Literature

[1] L. Pardi-Comensoli, M. Tonolla, A. Colpo, Z. Palczewska, S. Revikrishnan, M. Heeb, I. Brunner, and M. Barbezat. „Microbial Depolymerization of Epoxy Resins: A Novel Approach to a Complex Challenge“. en. In: *Applied Sciences* 12.1 (Jan. 2022), p. 466. ISSN: 2076-3417. DOI: 10.3390/app12010466.

[2] M. Dokl, A. Copot, D. Krajnc, Y. V. Fan, A. Vujanovi, K. B. Aviso, R. R. Tan, Z. Kravanja, and L. uek. „Global projections of plastic use, end-of-life fate and potential changes in consumption, reduction, recycling and replacement with bioplastics to 2050“. In: *Sustainable Production and Consumption* 51 (Nov. 2024), pp. 498–518. ISSN: 2352-5509. DOI: 10.1016/j.spc.2024.09.025.

[3] *Plastics the fast Facts 2024 Plastics Europe*. en-GB. 2024.

[4] S. S. Ali, T. Elsamahy, R. Al-Tohamy, D. Zhu, Y. A. .-. Mahmoud, E. Koutra, M. A. Metwally, M. Kornaros, and J. Sun. „Plastic wastes biodegradation: Mechanisms, challenges and future prospects“. In: *Science of The Total Environment* 780 (Aug. 2021), p. 146590. ISSN: 0048-9697. DOI: 10.1016/j.scitotenv.2021.146590.

[5] R. Geyer, J. R. Jambeck, and K. L. Law. „Production, use, and fate of all plastics ever made“. eng. In: *Science advances* 3.7 (2017), e1700782. DOI: 10.1126/sciadv.1700782.

[6] L. Klose, N. Meyer-Heydecke, S. Wongwattanarat, J. Chow, P. Pérez García, C. Carré, W. Streit, G. Antranikian, A. M. Romero, and A. Liese. „Towards Sustainable Recycling of Epoxy-Based Polymers: Approaches and Challenges of Epoxy Biodegradation“. en. In: *Polymers* 15.12 (June 2023), p. 2653. ISSN: 2073-4360. DOI: 10.3390/polym15122653.

[7] Bundesministerium für Wirtschaft und Klimaschutz (BMWK), ed. *Leichtbaustrategie der Bundesregierung*. de. July 2023.

[8] C. Vogiantzi and K. Tserpes. „A Comparative Environmental and Economic Analysis of Carbon Fiber-Reinforced Polymer Recycling Processes Using Life Cycle Assessment and Life Cycle Costing“. en. In: *Journal of Composites Science* 9.1 (Jan. 2025), p. 39. ISSN: 2504-477X. DOI: 10.3390/jcs9010039.

[9] M. Sauer. *Composites Market Report 2024 - The global market for carbon fibers and carbon composites*. Market Report. Berlin: Composites United e.V., Mar. 2025.

[10] B. M. Terra, D. A. de Andrade, and R. N. de Mesquita. „Characterization of polyacrylonitrile thermal stabilization process for carbon fiber production using intelligent algorithms“. en. In: *Polymer Testing* 100 (Aug. 2021), p. 107238. ISSN: 0142-9418. DOI: 10.1016/j.polymertesting.2021.107238.

[11] D. Borjan, . Knez, and M. Knez. „Recycling of Carbon Fiber-Reinforced CompositesDifficulties and Future Perspectives“. In: *Materials* 14.15 (July 2021), p. 4191. ISSN: 1996-1944. DOI: 10.3390/ma14154191.

[12] V. Tournier, S. Duquesne, F. Guillamot, H. Cramail, D. Taton, A. Marty, and I. André. „Enzymes Power for Plastics Degradation“. In: *Chemical Reviews* (Mar. 2023). ISSN: 0009-2665. DOI: 10.1021/acs.chemrev.2c00644.

[13] S. Wongwattanarat, A. Schorn, L. Klose, C. Carré, A. M. Romero, A. Liese, P. Pérez-García, and W. R. Streit. *A Combined Chemo-Enzymatic Treatment for the Oxidation of Epoxy-Based Carbon Fiber-Reinforced Polymers (CFRPs)*. en. June 2025. DOI: 10.1101/2025.06.04.657587.

[14] J. Zampolli, M. Mangiagalli, D. Vezzini, M. Lasagni, D. Ami, A. Natalello, F. Arrigoni, L. Bertini, M. Lotti, and P. Di Gennaro. „Oxidative degradation of polyethylene by two novel laccase-like multicopper oxidases from Rhodococcus opacus R7.“ en. In: *Environmental Technology & Innovation* 32 (Nov. 2023), p. 103273. ISSN: 2352-1864. DOI: 10.1016/j.eti.2023.103273.

[15] C. Yao, W. Xia, M. Dou, Y. Du, and J. Wu. „Oxidative degradation of UV-irradiated polyethylene by laccase-mediator system“. en. In: *Journal of Hazardous Materials* 440 (Oct. 2022), p. 129709. ISSN: 0304-3894. DOI: 10.1016/j.jhazmat.2022.129709.

[16] E. Milchert, K. Malarczyk, and M. Kos. „Technological Aspects of Chemoenzymatic Epoxidation of Fatty Acids, Fatty Acid Esters and Vegetable Oils: A Review“. en. In: *Molecules* 20.12 (Dec. 2015), pp. 21481–21493. ISSN: 1420-3049. DOI: 10.3390/molecules201219778.

[17] R. Dinu and A. Mija. „Bio-based epoxy resins and composites from epoxidized linseed oil crosslinked with different cyclic anhydrides and their combination with lignin“. In: *Cellulose Chemistry and Technology* 54.9-10 (Nov. 2020), pp. 925–938. ISSN: 0576-9787, 2457-9459. DOI: 10.35812/cellulosechemtechnol.2020.54.89.

[18] R. Turco, R. Tesser, V. Russo, T. Cogliano, M. Di Serio, and E. Santacesaria. „Epoxidation of Linseed Oil by Performic Acid Produced In Situ“. en. In: *Industrial & Engineering Chemistry Research* 60.46 (Nov. 2021), pp. 16607–16618. ISSN: 0888-5885, 1520-5045. DOI: 10.1021/acs.iecr.1c02212.

[19] A. Todorovic, Y. BlöSSl, G. Oreski, and K. Resch-Fauster. „High-performance composite with 100% bio-based carbon content produced from epoxidized linseed oil, citric acid and flax fiber reinforcement“. In: *Composites Part A: Applied Science and Manufacturing* 152 (Jan. 2022), p. 106666. ISSN: 1359-835X. DOI: 10.1016/j.compositesa.2021.106666.

[20] C. Ding, P. S. Shuttleworth, S. Makin, J. H. Clark, and A. S. Matharu. „New insights into the curing of epoxidized linseed oil with dicarboxylic acids“. en. In: *Green Chemistry* 17.7 (2015), pp. 4000–4008. ISSN: 1463-9262, 1463-9270. DOI: 10.1039/c5gc00912j.

[21] H. Q. Pham and M. J. Marks. „Epoxy Resins“. en. In: *Ullmann's Encyclopedia of Industrial Chemistry*. Ed. by Wiley-VCH. 1st ed. Wiley, Oct. 2005. ISBN: 978-3-527-30385-4 978-3-527-30673-2. DOI: 10.1002/14356007.a09_547.pub2.

[22] X. Wan, B. Demir, M. An, T. R. Walsh, and N. Yang. „Thermal conductivities and mechanical properties of epoxy resin as a function of the degree of cross-linking“. en. In: *International Journal of Heat and Mass Transfer* 180 (Dec. 2021), p. 121821. ISSN: 0017-9310. DOI: 10.1016/j.ijheatmasstransfer.2021.121821.

[23] J.-P. Pascault and R. J. J. Williams, eds. *Epoxy Polymers: New Materials and Innovations*. en. 1st ed. Wiley, Jan. 2010. ISBN: 978-3-527-32480-4 978-3-527-62870-4. DOI: 10.1002/9783527628704.

[24] M. Weisbrodt, A. Kowalczyk, and K. Kowalczyk. „Structural Adhesives Tapes Based on a Solid Epoxy Resin and Multifunctional Acrylic Telomers“. en. In: *Polymers* 13.20 (Jan. 2021), p. 3561. ISSN: 2073-4360. DOI: 10.3390/polym13203561.

[25] W.-L. Hsu, C.-C. Liu, Y.-C. Shiau, and W.-C. Lin. „Discussion on the Reinforcement of Reinforced Concrete Slab Structures“. en. In: *Sustainability* 11.6 (Jan. 2019), p. 1756. ISSN: 2071-1050. DOI: 10.3390/su11061756.

[26] A. Bajpai, A. K. Kadiyala, and C. M. Ó Brádaigh. „Introduction to Epoxy/Synthetic Fiber Composites“. en. In: *Handbook of Epoxy/Fiber Composites*. Ed. by S. Mavinkere Rangappa, J. Parameswaranpillai, S. Siengchin, and S. Thomas. Singapore: Springer Nature, 2022, pp. 3–34. ISBN: 978-981-19-3603-6. DOI: 10.1007/978-981-19-3603-6_1.

[27] R. Jeyakumar, R. Ramamoorthi, and K. Balasubramanian. „Mechanical and wear characteristics of glass fiber reinforced modified epoxy nano composites A review“. en. In: *Materials Today: Proceedings*. International Conference on Newer Trends and Innovation in Mechanical Engineering: Materials Science

37 (Jan. 2021), pp. 901–907. ISSN: 2214-7853. DOI: 10.1016/j.matpr.2020.06.052.

[28] A. Kausar. „Role of Thermosetting Polymer in Structural Composite“. en. In: *American Journal of Polymer Science & Engineering* 5.1 (2017). ISSN: 2572-5734.

[29] V. Dogra, A. Gaur, C. Kishore, and A. Verma. „11 - Effect of reinforcement materials on the glass transient temperature and viscoelastic properties of polymer composites“. In: *Dynamic Mechanical and Creep-Recovery Behavior of Polymer-Based Composites*. Elsevier, Jan. 2024, pp. 189–202. ISBN: 978-0-443-19009-4. DOI: 10.1016/B978-0-443-19009-4.00011-4.

[30] M. B. Iqbal, A. Khattak, A. Ali, M. H. Raza, N. Ullah, A. A. Alahmadi, and A. Khan. „Influence of Ramped Compression on the Dielectric Behavior of the High-Voltage Epoxy Composites“. en. In: *Polymers* 13.18 (Jan. 2021), p. 3150. ISSN: 2073-4360. DOI: 10.3390/polym13183150.

[31] M. A. Alim, M. Z. Abdullah, M. S. A. Aziz, and R. Kamarudin. „Die attachment, wire bonding, and encapsulation process in LED packaging: A review“. en. In: *Sensors and Actuators A: Physical* 329 (Oct. 2021), p. 112817. ISSN: 0924-4247. DOI: 10.1016/j.sna.2021.112817.

[32] E. Morici and N. T. Dintcheva. „Recycling of Thermoset Materials and Thermoset-Based Composites: Challenge and Opportunity“. In: *Polymers* 14.19 (Oct. 2022), p. 4153. ISSN: 2073-4360. DOI: 10.3390/polym14194153.

[33] E. M. Petrie. *Epoxy Adhesive Formulations*. en. McGraw Hill Professional, Sept. 2005. ISBN: 978-0-07-158908-6.

[34] M. Dornbusch, U. Christ, and R. Rasing. „Epoxy Resins“. en. In: *Epoxy Resins*. Vincentz Network, Apr. 2016. ISBN: 978-3-7486-0030-5. DOI: 10.1515/9783748600305.

[35] A. Al-Lami, P. Hilmer, and M. Sinapius. „Eco-efficiency assessment of manufacturing carbon fiber reinforced polymers (CFRP) in aerospace industry“. In: *Aerospace Science and Technology* 79 (2018), pp. 669–678. ISSN: 12709638. DOI: 10.1016/j.ast.2018.06.020.

[36] J.-P. Pascault, H. Sautereau, J. Verdu, and R. J. J. Williams. *Thermosetting Polymers*. en. 0th ed. CRC Press, Feb. 2002. ISBN: 978-0-203-90840-2. DOI: 10.1201/9780203908402.

[37] M. Y. Khalid, Z. U. Arif, M. Hossain, and R. Umer. „Recycling of wind turbine blades through modern recycling technologies: A road to zero waste“. en. In: *Renewable Energy Focus* 44 (Mar. 2023), pp. 373–389. ISSN: 1755-0084. DOI: 10.1016/j.ref.2023.02.001.

[38] K. Li, N. Huo, X. Liu, J. Cheng, and J. Zhang. „Effects of the furan ring in epoxy resin on the thermomechanical properties of highly cross-linked epoxy networks: A molecular simulation study“. In: *RSC Adv.* 6 (Jan. 2016), pp. 769–777. DOI: 10.1039/C5RA22955C.

[39] J.-E. Ehlers, N. G. Rondan, L. K. Huynh, H. Pham, M. Marks, and T. N. Truong. „Theoretical Study on Mechanisms of the EpoxyAmine Curing Reaction“. In: *Macromolecules* 40.12 (June 2007), pp. 4370–4377. ISSN: 0024-9297. DOI: 10.1021/ma070423m.

[40] H. Q. Pham and M. J. Marks. „Epoxy Resins“. In: *Ullmann's encyclopedia of industrial chemistry*. 7. edition, release 2015. Weinheim; Wiley online library: Wiley-VCH, 2010. ISBN: 3-527-30673-0. DOI: 10.1002/14356007.a09_547.pub2.

[41] W. Ashcroft and B. Ellis. *Chemistry and Technology of Epoxy Resins*. eng. Dordrecht: Springer Netherlands, 1993. ISBN: 978-94-011-2932-9.

[42] F.-L. Jin, X. Li, and S.-J. Park. „Synthesis and application of epoxy resins: A review“. en. In: *Journal of Industrial and Engineering Chemistry* 29 (Sept. 2015), pp. 1–11. ISSN: 1226-086X. DOI: 10.1016/j.jiec.2015.03.026.

[43] L. Lassila, E. Säilynoja, R. Prinssi, P. Vallittu, and S. Garoushi. „Characterization of a new fiber-reinforced flowable composite“. In: *Odontology* 107.3 (2019), pp. 342–352. ISSN: 1618-1247. DOI: 10.1007/s10266-018-0405-y.

[44] S. Maiti, M. R. Islam, M. A. Uddin, S. Afroj, S. J. Eichhorn, and N. Karim. „Sustainable Fiber-Reinforced Composites: A Review“. en. In: *Advanced Sustainable Systems* 6.11 (2022), p. 2200258. ISSN: 2366-7486. DOI: 10.1002/adsu.202200258.

[45] Y. G. Thyavihalli Girijappa, S. Mavinkere Rangappa, J. Parameswaranpillai, and S. Siengchin. „Natural Fibers as Sustainable and Renewable Resource for Development of Eco-Friendly Composites: A Comprehensive Review“. English. In: *Frontiers in Materials* 6 (Sept. 2019). ISSN: 2296-8016. DOI: 10.3389/fmats.2019.00226.

[46] J. Tian, T. Xu, L. An, S. Wang, Y. Tan, and G. Chen. „Study on behavior and mechanism of low-velocity impact and post-impact flexural properties of carbon-aramid/epoxy resin laminated composites“. In: *Composite Structures* 300 (Nov. 2022), p. 116166. ISSN: 0263-8223. DOI: 10.1016/j.compstruct.2022.116166.

[47] S. Tiwari and J. Bijwe. „Surface Treatment of Carbon Fibers - A Review“. In: *Procedia Technology*. 2nd International Conference on Innovations in Automation and Mechatronics Engineering, ICIAME 2014 14 (Jan. 2014), pp. 505–512. ISSN: 2212-0173. DOI: 10.1016/j.protcy.2014.08.064.

[48] E. Cipriani, M. Zanetti, P. Bracco, V. Brunella, M. P. Luda, and L. Costa. „Crosslinking and carbonization processes in PAN films and nanofibers“. In: *Polymer Degradation and Stability* 123 (Jan. 2016), pp. 178–188. ISSN: 0141-3910. DOI: 10.1016/j.polymdegradstab.2015.11.008.

[49] M. S. A. Rahaman, A. F. Ismail, and A. Mustafa. „A review of heat treatment on polyacrylonitrile fiber“. In: *Polymer Degradation and Stability* 92.8 (Aug. 2007), pp. 1421–1432. ISSN: 0141-3910. DOI: 10.1016/j.polymdegradstab.2007.03.023.

[50] Z. Wangxi, L. Jie, and W. Gang. „Evolution of structure and properties of PAN precursors during their conversion to carbon fibers“. In: *Carbon* 41.14 (Jan. 2003), pp. 2805–2812. ISSN: 0008-6223. DOI: 10.1016/S0008-6223(03)00391-9.

[51] P. Bhatt and A. Goe. „Carbon Fibres: Production, Properties and Potential Use“. In: *Material Science Research India* 14.1 (2017), pp. 52–57. ISSN: 09733469. DOI: 10.13005/msri/140109.

[52] X. Huang. „Fabrication and Properties of Carbon Fibers“. In: *Materials* 2.4 (Dec. 2009), pp. 2369–2403. ISSN: 1996-1944. DOI: 10.3390/ma2042369.

[53] K. Bilisik, N. S. Karaduman, and N. E. Bilisik. „Fiber Architectures for Composite Applications“. en. In: *Fibrous and Textile Materials for Composite Applications*. Ed. by S. Rana and R. Fangueiro. Singapore: Springer, 2016, pp. 75–134. ISBN: 978-981-10-0234-2. DOI: 10.1007/978-981-10-0234-2_3.

[54] Q. Govignon, S. Bickerton, and P. Kelly. „6 - Liquid composite molding processes“. en. In: *Advanced Fiber-Reinforced Polymer(FRP) Composites for Structural Applications (Second Edition)*. Ed. by J. Bai. Woodhead Publishing Series in Civil and Structural Engineering. Woodhead Publishing, Jan. 2023, pp. 101–136. ISBN: 978-0-12-820346-0. DOI: 10.1016/B978-0-12-820346-0.00006-X.

[55] N. Uddin. *Blast protection of civil infrastructures and vehicles using composites*. eng. Woodhead publishing in materials. Boca Raton: CRC press, 2010. ISBN: 978-1-4398-2771-0 978-1-84569-399-2.

[56] S. E. Günaslan, A. Karain, and M. E. Öncü. „Properties of FRP materials for strengthening“. In: *International Journal of Innovative Science, Engineering & Technology* 1.9 (2014), pp. 656–660.

[57] I. Shakir Abbood S., S. a. Odaa, K. F. Hasan, and M. A. Jasim. „Properties evaluation of fiber reinforced polymers and their constituent materials used in structures A review“. In: *Materials Today: Proceedings* 43 (2021), pp. 1003–1008. ISSN: 22147853. DOI: 10.1016/j.matpr.2020.07.636.

[58] C. Soutis. „Carbon fiber reinforced plastics in aircraft construction“. In: *Materials Science and Engineering: A* 412.1-2 (2005), pp. 171–176. ISSN: 09215093. DOI: 10.1016/j.msea.2005.08.064.

[59] Y. Wang, S. K. Raman Pillai, J. Che, and M. B. Chan-Park. „High Interlaminar Shear Strength Enhancement of Carbon Fiber/Epoxy Composite through Fiber- and Matrix-Anchored Carbon Nanotube Networks“. In: *ACS Applied Materials & Interfaces* 9.10 (Mar. 2017), pp. 8960–8966. ISSN: 1944-8244. DOI: 10.1021/acsami.6b13197.

[60] J. Zhang, V. S. Chevali, H. Wang, and C.-H. Wang. „Current status of carbon fibre and carbon fibre composites recycling“. In: *Composites Part B: Engineering* 193 (July 2020), p. 108053. ISSN: 1359-8368. DOI: 10.1016/j.compositesb.2020.108053.

[61] S. A. A. N. Nasreen, S. Sundarrajan, S. A. S. Nizar, H. Wei, D. Xuecheng, and S. Ramakrishna. „Pyrolysis, Microwave, Chemical and Biodegradation Methodology in Recycling of Plastic Waste: a Circular Economy Concept“. en. In: *Circular Economy and Sustainability* 2.2 (June 2022), pp. 609–632. ISSN: 2730-5988. DOI: 10.1007/s43615-021-00109-x.

[62] C. A. Navarro, C. R. Giffin, B. Zhang, Z. Yu, S. R. Nutt, and T. J. Williams. „A structural chemistry look at composites recycling“. en. In: *Materials Horizons* 7.10 (2020), pp. 2479–2486. ISSN: 2051-6347, 2051-6355. DOI: 10.1039/D0MH01085E.

[63] B. Parveez, M. I. Kittur, I. A. Badruddin, S. Kamangar, M. Hussien, and M. A. Umarfarooq. „Scientific Advancements in Composite Materials for Aircraft Applications: A Review“. en. In: *Polymers* 14.22 (Nov. 2022), p. 5007. ISSN: 2073-4360. DOI: 10.3390/polym14225007.

[64] C. Tokoro, K. Sato, M. Inutsuka, and T. Koita. „Efficient recovery of carbon fibers from carbon fiber-reinforced polymers using direct discharge electrical pulses“. en. In: *Scientific Reports* 14.1 (Nov. 2024), p. 29762. ISSN: 2045-2322. DOI: 10.1038/s41598-024-76955-0.

[65] A. Merrington. *Applied Plastics Engineering Handbook*. Elsevier, 2011. ISBN: 978-1-4377-3514-7. DOI: 10.1016/C2010-0-67336-6.

[66] P. Kang, S. Yang, S. Bai, and Q. Wang. „Novel Application of Mechanochemistry in Waste Epoxy Recycling via Solid-State Shear Milling“. In: *ACS Sustainable Chemistry & Engineering* 9.35 (Sept. 2021), pp. 11778–11789. DOI: 10.1021/acssuschemeng.1c03221.

[67] P. Yang, Q. Zhou, X.-X. Yuan, J. M. N. van Kasteren, and Y.-Z. Wang. „Highly efficient solvolysis of epoxy resin using poly(ethylene glycol)/NaOH systems“. en. In: *Polymer Degradation and Stability* 97.7 (July 2012), pp. 1101–1106. ISSN: 0141-3910. DOI: 10.1016/j.polymdegradstab.2012.04.007.

[68] R. L. Pérez, C. E. Ayala, M. M. Opiri, A. Ezzir, G. Li, and I. M. Warner. „Recycling Thermoset Epoxy Resin Using Alkyl-Methyl-Imidazolium Ionic Liquids as Green Solvents“. In: *ACS Applied Polymer Materials* 3.11 (Nov. 2021), pp. 5588–5595. DOI: 10.1021/acsapm.1c00896.

[69] A. Ahrens, A. Bonde, H. Sun, N. K. Wittig, H. C. D. Hammershøj, G. M. F. Batista, A. Sommerfeldt, S. Frølich, H. Birkedal, and T. Skrydstrup. „Catalytic disconnection of CO bonds in epoxy resins and composites“. en. In: *Nature* (Apr. 2023), pp. 1–8. ISSN: 1476-4687. DOI: 10.1038/s41586-023-05944-6.

[70] M. Pavlas, M. Tou, L. Bébar, and P. Stehlík. „Waste to energy An evaluation of the environmental impact“. en. In: *Applied Thermal Engineering*. Selected Papers from the 12th Conference on Process Integration, Modelling and Optimisation for Energy Saving and Pollution Reduction 30.16 (Nov. 2010), pp. 2326–2332. ISSN: 1359-4311. DOI: 10.1016/j.applthermaleng.2009.10.019.

[71] V. K. Soni, G. Singh, B. K. Vijayan, A. Chopra, G. S. Kapur, and S. S. V. Ramakumar. „Thermochemical Recycling of Waste Plastics by Pyrolysis: A Review“. In: *Energy & Fuels* 35.16 (Aug. 2021), pp. 12763–12808. ISSN: 0887-0624. DOI: 10.1021/acs.energyfuels.1c01292.

[72] S. J. Pickering. „Recycling technologies for thermoset composite materialscurrent status“. In: *Composites Part A: Applied Science and Manufacturing* 37.8 (2006), pp. 1206–1215. ISSN: 1359835X. DOI: 10.1016/j.compositesa.2005.05.030.

[73] N. Barber. *Polyethylene Terephthalate*. eng. Polymer Science and Technology. Hauppauge: Nova Science Publishers Incorporated, 2017. ISBN: 978-1-5361-1991-6.

[74] A. Singh, N. A. Rorrer, S. R. Nicholson, E. Erickson, J. S. DesVeaux, A. F. Avelino, P. Lamers, A. Bhatt, Y. Zhang, G. Avery, L. Tao, A. R. Pickford, A. C. Carpenter, J. E. McGeehan, and G. T. Beckham. „Techno-economic, life-cycle, and socioeconomic impact analysis of enzymatic recycling of poly(ethylene terephthalate)“. In: *Joule* 5.9 (2021), pp. 2479–2503. ISSN: 25424351. DOI: 10.1016/j.joule.2021.06.015.

[75] M. Srikanth, T. S. R. S. Sandeep, K. Sucharitha, and S. Godi. „Biodegradation of plastic polymers by fungi: a brief review“. In: *Bioresources and Bioprocessing* 9.1 (Apr. 2022), p. 42. ISSN: 2197-4365. DOI: 10.1186/s40643-022-00532-4.

[76] G. A. Rather and M. Raina. „Microbial Modifications and Biochemical Pathway: Mechanism for Ecosystem Decontamination“. en. In: *Microbial Bioremediation: Sustainable Management of Environmental Contamination*. Ed. by R. A. Bhat, M. Butnariu, G. H. Dar, and K. R. Hakeem. Cham: Springer International Publishing, 2023, pp. 109–124. ISBN: 978-3-031-18017-0. DOI: 10.1007/978-3-031-18017-0_6.

[77] A. Amobonye, P. Bhagwat, S. Singh, and S. Pillai. „Plastic biodegradation: Frontline microbes and their enzymes“. In: *Science of The Total Environment* 759 (Mar. 2021), p. 143536. ISSN: 0048-9697. DOI: 10.1016/j.scitotenv.2020.143536.

[78] H. Inderthal, S. L. Tai, and S. T. L. Harrison. „Non-Hydrolyzable Plastics An Interdisciplinary Look at Plastic Bio-Oxidation“. In: *Trends in Biotechnology* 39.1 (Jan. 2021), pp. 12–23. ISSN: 0167-7799. DOI: 10.1016/j.tibtech.2020.05.004.

[79] D. Danso, J. Chow, and W. R. Streit. „Plastics: Environmental and Biotechnological Perspectives on Microbial Degradation“. eng. In: *Applied and environmental microbiology* 85.19 (2019). DOI: 10.1128/AEM.01095-19.

[80] R.-J. Mueller. „Biological degradation of synthetic polyestersEnzymes as potential catalysts for polyester recycling“. In: *Process Biochemistry* 41.10 (2006), pp. 2124–2128. ISSN: 13595113. DOI: 10.1016/j.procbio.2006.05.018.

[81] G. Wang, K. Chai, J. Wu, and F. Liu. „Effect of *Pseudomonas* putida on the degradation of epoxy resin varnish coating in seawater“. In: *International Biodeterioration & Biodegradation* 115 (Nov. 2016), pp. 156–163. ISSN: 0964-8305. DOI: 10.1016/j.ibiod.2016.08.017.

[82] S. Zhang, H. Zheng, W. Chang, Y. Lou, and H. Qian. „Microbiological Deterioration of Epoxy Coating on Carbon Steel by Pseudomonas aeruginosa“. en. In: *Coatings* 13.3 (Mar. 2023), p. 606. ISSN: 2079-6412. DOI: 10.3390/coatings13030606.

[83] J.-D. Gu, C. Lu, K. Thorp, A. Crasto, and R. Mitchell. „Fiber-reinforced polymeric composites are susceptible to microbial degradation“. In: *Journal of Industrial Microbiology and Biotechnology* 18.6 (June 1997), pp. 364–369. ISSN: 1367-5435. DOI: 10.1038/sj.jim.2900401.

[84] M. Dolz, I. Mateljak, D. Méndez-Sánchez, I. Sánchez-Moreno, P. Gomez de Santos, J. Viña-Gonzalez, and M. Alcalde. „Colorimetric High-Throughput Screening Assay to Engineer Fungal Peroxygenases for the Degradation of Thermoset Composite Epoxy Resins“. English. In: *Frontiers in Catalysis* 2 (Apr. 2022). ISSN: 2673-7841. DOI: 10.3389/fctls.2022.883263.

[85] N. Eliaz, E. Z. Ron, M. Gozin, S. Younger, D. Biran, and N. Tal. „Microbial Degradation of Epoxy“. eng. In: *Materials (Basel, Switzerland)* 11.11 (2018). ISSN: 1996-1944. DOI: 10.3390/ma11112123.

[86] S. Deng. „Effect of Bacillus flexus on the Degradation of Epoxy Resin Varnish Coating in Seawater“. In: *International Journal of Electrochemical Science* (2019), pp. 315–328. DOI: 10.20964/2019.01.64.

[87] H. Negi, A. Kapri, M. Zaidi, A. Satlewal, and R. Goel. „Comparative in-vitro biodegradation studies of epoxy and its silicone blend by selected microbial consortia“. In: *International Biodeterioration & Biodegradation* 63.5 (2009), pp. 553–558. ISSN: 09648305. DOI: 10.1016/j.ibiod.2009.03.001.

[88] P. A. Wagner, B. J. Little, K. R. Hart, and R. I. Ray. „Biodegradation of composite materials“. In: *International Biodeterioration & Biodegradation* 38.2 (1996), pp. 125–132. ISSN: 09648305. DOI: 10.1016/S0964-8305(96)00036-4.

[89] S. Dutta, N. Karak, J. P. Saikia, and B. K. Konwar. „Biodegradation of Epoxy and MF Modified Polyurethane Films Derived from a Sustainable Resource“. en. In: *Journal of Polymers and the Environment* 18.3 (Sept. 2010), pp. 167–176. ISSN: 1566-2543, 1572-8900. DOI: 10.1007/s10924-010-0161-8.

[90] A. Liese, K. Seelbach, and C. Wandrey. *Industrial biotransformations*. eng. 2nd, completely revised and extended ed. Weinheim: Wiley-VCH, 2005. ISBN: 978-3-527-31001-2.

[91] R. Debnath and T. Saha. „An insight into the production strategies and applications of the ligninolytic enzyme laccase from bacteria and fungi“. In: *Biocatalysis and Agricultural Biotechnology* 26 (July 2020), p. 101645. ISSN: 1878-8181. DOI: 10.1016/j.bcab.2020.101645.

[92] K. Piontek, M. Antorini, and T. Choinowski. „Crystal Structure of a Laccase from the FungusTrametes versicolor at 1.90-Å Resolution Containing a Full Complement of Coppers *“. English. In: *Journal of Biological Chemistry* 277.40 (Oct. 2002), pp. 37663–37669. ISSN: 0021-9258, 1083-351X. DOI: 10.1074/jbc.M204571200.

[93] H. Wang, L.-X. Tang, Y.-F. Ye, J.-X. Ma, X. Li, J. Si, and B.-K. Cui. „Laccase immobilization and its degradation of emerging pollutants: A comprehensive review“. In: *Journal of Environmental Management* 359 (May 2024), p. 120984. ISSN: 0301-4797. DOI: 10.1016/j.jenvman.2024.120984.

[94] S. Khodaverdian, B. Dabirmanesh, A. Heydari, E. Dashtban-moghadam, K. Khajeh, and F. Ghazi. „Activity, stability and structure of laccase in betaine based natural deep eutectic solvents“. In: *International Journal of Biological Macromolecules* 107 (Feb. 2018), pp. 2574–2579. ISSN: 0141-8130. DOI: 10.1016/j.ijbiomac.2017.10.144.

[95] F. Hollmann, Y. Gumulya, C. Tölle, A. Liese, and O. Thum. „Evaluation of the Laccase from Myceliophthora thermophila as Industrial Biocatalyst for Polymerization Reactions“. en. In: *Macromolecules* 41.22 (Nov. 2008), pp. 8520–8524. ISSN: 0024-9297, 1520-5835. DOI: 10.1021/ma801763t.

[96] D. Brinch and P. Pedersen. „Toxicological Studies on Laccase from Myceliophthora thermophila Expressed in Aspergillus oryzae“. en. In: *Regulatory Toxicology and Pharmacology* 35.3 (June 2002), pp. 296–307. ISSN: 02732300. DOI: 10.1006/rtph.2002.1538.

[97] E. Martin, P. Dubessay, E. Record, F. Audonnet, and P. Michaud. „Recent advances in laccase activity assays: A crucial challenge for applications on complex substrates“. In: *Enzyme and Microbial Technology* 173 (Feb. 2024), p. 110373. ISSN: 0141-0229. DOI: 10.1016/j.enzmictec.2023.110373.

[98] M. Deska and B. Koczak. „Immobilized fungal laccase as "green catalyst" for the decolourization process State of the art“. In: *Process Biochemistry* 84 (Sept. 2019), pp. 112–123. ISSN: 1359-5113. DOI: 10.1016/j.procbio.2019.05.024.

[99] S. Burton. „Laccases and Phenol Oxidases in Organic Synthesis - a Review“. en. In: *Current Organic Chemistry* 7.13 (Sept. 2003), pp. 1317–1331. ISSN: 13852728. DOI: 10.2174/1385272033486477.

[100] P. Baiocco, A. M. Barreca, M. Fabbrini, C. Galli, and P. Gentili. „Promoting laccase activity towards non-phenolic substrates: a mechanistic investigation with some laccase-mediator systems“. eng. In: *Organic & biomolecular chemistry* 1.1 (2003), pp. 191–197. ISSN: 1477-0520. DOI: 10.1039/b208951c.

[101] S. Camarero, D. Ibarra, M. J. Martínez, and Á. T. Martínez. „Lignin-Derived Compounds as Efficient Laccase Mediators for Decolorization of Different Types of Recalcitrant Dyes“. In: *Applied and Environmental Microbiology* 71.4 (Apr. 2005), pp. 1775–1784. DOI: 10.1128/AEM.71.4.1775-1784.2005.

[102] A. Kumar and R. Chandra. „Ligninolytic enzymes and its mechanisms for degradation of lignocellulosic waste in environment“. In: *Heliyon* 6.2 (Feb. 2020), e03170. ISSN: 2405-8440. DOI: 10.1016/j.heliyon.2020.e03170.

[103] R. Hilgers, G. v. Erven, V. Boerkamp, I. Sulaeva, A. Potthast, M. A. Kabel, and J.-P. Vincken. „Understanding laccase/HBT-catalyzed grass delignification at the molecular level“. en. In: *Green Chemistry* 22.5 (2020), pp. 1735–1746. DOI: 10.1039/C9GC04341A.

[104] R. Hilgers, J.-P. Vincken, H. Gruppen, and M. A. Kabel. „Laccase/Mediator Systems: Their Reactivity toward Phenolic Lignin Structures“. eng. In: *ACS Sustainable Chemistry & Engineering* 6.2 (2018), pp. 2037–2046. ISSN: 2168-0485. DOI: 10.1021/acssuschemeng.7b03451.

[105] A. Gazka, U. Jankiewicz, and A. Szczepkowski. „Biochemical Characteristics of Laccases and Their Practical Application in the Removal of Xenobiotics from Water“. en. In: *Applied Sciences* 13.7 (Jan. 2023), p. 4394. ISSN: 2076-3417. DOI: 10.3390/app13074394.

[106] L. P. Christopher, B. Yao, and Y. Ji. „Lignin Biodegradation with Laccase-Mediator Systems“. In: *Frontiers in Energy Research* 2 (Mar. 2014). ISSN: 2296-598X. DOI: 10.3389/fenrg.2014.00012.

[107] G. Marco-Velasco, A. Gálvez-Subiela, R. Jiménez-Robles, M. Izquierdo, A. Cháfer, and J. D. Badia. „A Review on the Application of Deep Eutectic Solvents in Polymer-Based Membrane Preparation for Environmental Separation Technologies“. en. In: *Polymers* 16.18 (Jan. 2024), p. 2604. ISSN: 2073-4360. DOI: 10.3390/polym16182604.

[108] S. Bagder Elmaci, J. Schultz, A. Isci, M. Scherzinger, D. D. Aslanhan, M. D. Cam, O. Sakiyan, and M. Kaltschmitt. „Deep eutectic solvent pretreatment of cork dust Effects on biomass composition, phenolic extraction and anaerobic degradability“. en. In: *Waste Management* 181 (May 2024), pp. 114–127. ISSN: 0956053X. DOI: 10.1016/j.wasman.2024.04.007.

[109] A. P. Abbott, G. Capper, D. L. Davies, R. K. Rasheed, and V. Tambyrajah. „Novel solvent properties of choline chloride/urea mixtures“. en. In: *Chemical Communications* 1 (Jan. 2003), pp. 70–71. ISSN: 1364-548X. DOI: 10.1039/B210714G.

[110] Q. Zhang, K. D. O. Vigier, S. Royer, and F. Jérôme. „Deep eutectic solvents: syntheses, properties and applications“. en. In: *Chemical Society Reviews* 41.21 (Oct. 2012), pp. 7108–7146. ISSN: 1460-4744. DOI: 10.1039/C2CS35178A.

[111] M. Francisco, A. Van Den Bruinhorst, and M. C. Kroon. „New natural and renewable low transition temperature mixtures (LTTMs): screening as solvents for lignocellulosic biomass processing“. en. In: *Green Chemistry* 14.8 (2012), p. 2153. ISSN: 1463-9262, 1463-9270. DOI: 10.1039/c2gc35660k.

[112] M. Pätzold, S. Siebenhaller, S. Kara, A. Liese, C. Syldatk, and D. Holtmann. „Deep Eutectic Solvents as Efficient Solvents in Biocatalysis“. In: *Trends in Biotechnology* 37.9 (Sept. 2019), pp. 943–959. ISSN: 0167-7799. DOI: 10.1016/j.tibtech.2019.03.007.

[113] K. Griebenow and A. M. Klibanov. „On Protein Denaturation in AqueousOrganic Mixtures but Not in Pure Organic Solvents“. In: *Journal of the American Chemical Society* 118.47 (Jan. 1996), pp. 11695–11700. ISSN: 0002-7863. DOI: 10.1021/ja961869d.

[114] V. Stepankova, P. Vanacek, J. Damborsky, and R. Chaloupkova. „Comparison of catalysis by haloalkane dehalogenases in aqueous solutions of deep eutectic and organic solvents“. English. In: *Green Chemistry* 16.5 (2014), pp. 2754–2761. ISSN: 1463-9262. DOI: 10.1039/c4gc00117f.

[115] D. Lindberg, M. de la Fuente Revenga, and M. Widersten. „Deep eutectic solvents (DESs) are viable cosolvents for enzyme-catalyzed epoxide hydrolysis“. In: *Journal of Biotechnology* 147.3 (June 2010), pp. 169–171. ISSN: 0168-1656. DOI: 10.1016/j.jbiotec.2010.04.011.

[116] R. Sánchez-Leija, J. Torres-Lubián, A. Reséndiz-Rubio, G. Luna-Bárcenas, and J. Mota-Morales. „Enzyme-mediated free radical polymerization of acrylamide in deep eutectic solvents“. English. In: *RSC Advances* 6.16 (2016), pp. 13072–13079. ISSN: 2046-2069. DOI: 10.1039/c5ra27468k.

[117] Z. Maugeri and P. Domínguez de María. „Benzaldehyde lyase (BAL)-catalyzed enantioselective CC bond formation in deep-eutectic-solventsbuffer mixtures“. In: *Journal of Molecular Catalysis B: Enzymatic* 107 (Sept. 2014), pp. 120–123. ISSN: 1381-1177. DOI: 10.1016/j.molcatb.2014.06.003.

[118] J. P. Bittner, N. Zhang, L. Huang, P. Domínguez De María, S. Jakobtorweihen, and S. Kara. „Impact of deep eutectic solvents (DESs) and individual DES components on alcohol dehydrogenase catalysis: connecting experimental data and molecular dynamics simulations“. en. In: *Green Chemistry* 24.3 (2022), pp. 1120–1131. ISSN: 1463-9262, 1463-9270. DOI: 10.1039/D1GC04059F.

[119] N. Guajardo and P. Domínguez de María. „Continuous Biocatalysis in EnvironmentallyFriendly Media: A Triple Synergy for Future Sustainable Processes“. en. In: *ChemCatChem* 11.14 (July 2019), pp. 3128–3137. ISSN: 1867-3880, 1867-3899. DOI: 10.1002/cctc.201900773.

[120] L. Weng and M. Toner. „Janus-faced role of water in defining nanostructure of choline chloride/glycerol deep eutectic solvent“. en. In: *Physical Chemistry Chemical Physics* 20.35 (2018), pp. 22455–22462. ISSN: 1463-9076, 1463-9084. DOI: 10.1039/C8CP03882A.

[121] A. E. Ünlü, B. Prasad, K. Anavekar, P. Bubenheim, and A. Liese. „The effect of natural deep eutectic solvents on laccase activity and oligomerization of rutin“. en. In: *Biocatalysis and Biotransformation* 41.5 (Sept. 2023), pp. 353–366. ISSN: 1024-2422, 1029-2446. DOI: 10.1080/10242422.2022.2120391.

[122] A. E. Ünlü, B. Prasad, K. Anavekar, P. Bubenheim, and A. Liese. „Investigation of a green process for the polymerization of catechin“. en. In: *Preparative Biochemistry & Biotechnology* 47.9 (Oct. 2017), pp. 918–924. ISSN: 1082-6068, 1532-2297. DOI: 10.1080/10826068.2017.1365241.

[123] P. Lajtai-Szabó, N. Nemestóthy, and L. Gubicza. „The Role of Water Activity in Terms of Enzyme Activity and Enantioselectivity during Enzymatic Esterification in Non-conventional Media“. In: *Hungarian Journal of Industry and Chemistry* 48.2 (Dec. 2020), pp. 9–12. ISSN: 2450-5102, 0133-0276. DOI: 10.33927/hjic-2020-22.

[124] K. Lin, W. Zhang, X. Fan, X. Li, N. Wang, S. Yu, and L. Lu. „Deep eutectic solvents assisted laccase pretreatment for improving enzymatic hydrolysis of corn stover“. en. In: *Bioprocess and Biosystems Engineering* 48.2 (Feb. 2025), pp. 209–219. ISSN: 1615-7605. DOI: 10.1007/s00449-024-03102-4.

[125] S. Varriale, A. E. Delorme, J.-M. Andanson, J. Devemy, P. Malfreyt, V. Verney, and C. Pezzella. „Enhancing the Thermostability of Engineered Laccases in Aqueous Betaine-Based Natural Deep Eutectic Solvents“. In: *ACS Sustainable Chemistry & Engineering* 10.1 (Jan. 2022), pp. 572–581. DOI: 10.1021/acssuschemeng.1c07104.

[126] M. L. Toledo, M. M. Pereira, M. G. Freire, J. P. A. Silva, J. A. P. Coutinho, and A. P. M. Tavares. „Laccase Activation in Deep Eutectic Solvents“. In: *ACS Sustainable Chemistry & Engineering* 7.13 (July 2019), pp. 11806–11814. DOI: 10.1021/acssuschemeng.9b02179.

[127] J. C. Chan, B. Zhang, M. Martinez, B. Kuruba, J. Brozik, C. Kang, and X. Zhang. „Structural studies of *Myceliophthora* Thermophila Laccase in the presence of deep eutectic solvents“. In: *Enzyme and Microbial Technology* 150 (Oct. 2021), p. 109890. ISSN: 0141-0229. DOI: 10.1016/j.enzmictec.2021.109890.

[128] M. Hatimuria, J. Das, K. Gavvala, S. Bag, and A. Pabbathi. „Recent advances in the use of laccase enzyme in deep eutectic solvents“. In: *Sustainable Chemistry and Pharmacy* 33 (June 2023), p. 101148. ISSN: 2352-5541. DOI: 10.1016/j.scp.2023.101148.

[129] M. Radovi, A. Jurinjak Tuek, T. Reiter, W. Kroutil, M. Cvjetko Bubalo, and I. Radoji Redovnikovi. „Rational design of deep eutectic solvents for the stabilization of dehydrogenases: an artificial neural network prediction approach“. In: *Frontiers in Chemistry* 12 (Aug. 2024), p. 1436049. ISSN: 2296-2646. DOI: 10.3389/fchem.2024.1436049.

[130] L. M. d. S. Mesquita, L. S. Contieri, F. H. B. Sosa, R. S. Pizani, J. Chaves, J. Viganó, S. P. M. Ventura, and M. A. Rostagno. „Combining eutectic solvents and pressurized liquid extraction coupled in-line with solid-phase extraction to recover, purify and stabilize anthocyanins from Brazilian berry waste“. en. In: *Green Chemistry* 25.5 (2023), pp. 1884–1897. DOI: 10.1039/D2GC04347E.

[131] F. H. B. Sosa, D. O. Abranches, A. M. da Costa Lopes, J. A. P. Coutinho, and M. C. da Costa. „Kraft Lignin Solubility and Its Chemical Modification in Deep Eutectic Solvents“. In: *ACS Sustainable Chemistry & Engineering* 8.50 (Dec. 2020), pp. 18577–18589. DOI: 10.1021/acssuschemeng.0c06655.

[132] M. Walter, v. Berg, Karl, Unverfährt, Sven, and Fiedler, Bodo. „Novel Manufacturing Process for Natural Fibre Composites out of Biobased and Biodegradable Materials“. en. In: *Proceedings of the 23th International Conference on Composite Materials*. Belfast, 2023.

[133] M. Walter, M. Neubacher, and B. Fiedler. „Using thermokinetic methods to enhance properties of epoxy resins with amino acids as biobased curing agents by achieving full crosslinking“. en. In: *Scientific Reports* 14.1 (Feb. 2024), p. 4367. ISSN: 2045-2322. DOI: 10.1038/s41598-024-54484-0.

[134] G. Lewandowski, M. Musik, K. Malarczyk-Matusiak, . Saaciski, and E. Milchert. „Epoxidation of Vegetable Oils, Unsaturated Fatty Acids and Fatty Acid Esters: A Review“. en. In: *Mini-Reviews in Organic Chemistry* 17.4 (May 2020), pp. 412–422. ISSN: 1570-193X. DOI: 10.2174/1570193x16666190430154319.

[135] Z. S. Petrovi. „Polyurethanes from Vegetable Oils“. In: *Polymer Reviews* 48.1 (Feb. 2008), pp. 109–155. ISSN: 1558-3724. DOI: 10.1080/15583720701834224.

[136] S. K. Sahoo, V. Khandelwal, and G. Manik. „Development of completely biobased epoxy networks derived from epoxidized linseed and castor oil cured with citric acid“. en. In: *Polymers for Advanced Technologies* 29.7 (July 2018), pp. 2080–2090. ISSN: 1042-7147, 1099-1581. DOI: 10.1002/pat.4316.

[137] M. I. Necolau, C. M. Damian, E. Olaret, H. Iovu, and B. Balanuca. „Comparative Thermo-Mechanical Properties of Sustainable Epoxy Polymer Networks Derived from Linseed Oil“. en. In: *Polymers* 14.19 (Oct. 2022), p. 4212. ISSN: 2073-4360. DOI: 10.3390/polym14194212.

[138] W. Y. Pérez-Sena, T. Salmi, L. Estel, and S. Leveneur. „Thermal risk assessment for the epoxidation of linseed oil by classical Prisleschajew epoxidation and by direct epoxidation by H2O2 on alumina“. en. In: *Journal of Thermal Analysis and Calorimetry* 140.2 (Apr. 2020), pp. 673–684. ISSN: 1588-2926. DOI: 10.1007/s10973-019-08894-2.

[139] V.-M. Popa, A. Gruia, C. Moldovan, D. Bordean, and C. Mateescu. „Fatty acids composition and oil characteristics of linseed (Linum Usitatissimum L.) from Romania“. en. In: *Journal of Agroalimentary Processes and Technologies* (2012).

[140] S. Sun, X. Ke, L. Cui, G. Yang, Y. Bi, F. Song, and X. Xu. „Enzymatic epoxidation of *Sapindus mukorossi* seed oil by perstearic acid optimized using response surface methodology“. In: *Industrial Crops and Products* 33.3 (May 2011), pp. 676–682. ISSN: 0926-6690. DOI: 10.1016/j.indcrop.2011.01.002.

[141] V. M. Abbasov, F. A. Nasirov, and N. S. Rzayeva. „Epoxidated Vegetable Oils: Preparation, Properties and Application“. In: *Polymers and Petrochemistry Review* 19.4 (2018), pp. 427–449.

[142] E. Santacesaria, R. Turco, V. Russo, R. Tesser, and M. Di Serio. „Soybean Oil Epoxidation: Kinetics of the Epoxide Ring Opening Reactions“. en. In: *Processes* 8.9 (Sept. 2020), p. 1134. ISSN: 2227-9717. DOI: 10.3390/pr8091134.

[143] K. Hernandez, A. Berenguer-Murcia, R. C. Rodrigues, and R. Fernandez-Lafuente. „Hydrogen Peroxide in Biocatalysis. A Dangerous Liaison“. en. In: *Current Organic Chemistry* 16.22 (Nov. 2012), pp. 2652–2672. ISSN: 1385-2728. DOI: 10.2174/138527212804004526.

[144] I. Hilker, D. Bothe, J. Prüss, and H. .-. Warnecke. „Chemo-enzymatic epoxidation of unsaturated plant oils“. In: *Chemical Engineering Science*. 16th International Conference on Chemical Reactor Engineering 56.2 (Jan. 2001), pp. 427–432. ISSN: 0009-2509. DOI: 10.1016/S0009-2509(00)00245-1.

[145] C. Orellana-Coca, J. M. Billakanti, B. Mattiasson, and R. Hatti-Kaul. „Lipase mediated simultaneous esterification and epoxidation of oleic acid for the production of alkylepoxystearates“. en. In: *Journal of Molecular Catalysis B: Enzymatic* 44.3-4 (Mar. 2007), pp. 133–137. ISSN: 13811177. DOI: 10.1016/j.molcatb.2006.09.002.

[146] R. D. C. S. Schneider, L. R. S. Lara, T. B. Bitencourt, M. D. G. Nascimento, and M. R. D. S. Nunes. „Chemo-enzymatic epoxidation of sunflower oil methyl esters“. en. In: *Journal of the Brazilian Chemical Society* 20.8 (2009), pp. 1473–1477. ISSN: 0103-5053. DOI: 10.1590/s0103-50532009000800013.

[147] F. Haitz, S. Radloff, S. Rupp, M. Fröhling, T. Hirth, and S. Zibek. „Chemo-Enzymatic Epoxidation of Lallemantia IbericaSeed Oil: Process Development and Economic-Ecological Evaluation“. en. In: *Applied Biochemistry and Biotechnology* 185.1 (May 2018), pp. 13–33. ISSN: 1559-0291. DOI: 10.1007/s12010-017-2630-1.

[148] R. Hiessl, L. Hennecke, C. Plass, J. Kleber, S. Wahlefeld, R. Otter, H. Gröger, and A. Liese. „FTIR based kinetic characterisation of an acid-catalysed esterification of 3-methylphthalic anhydride and 2-ethylhexanol“. en. In: *Analytical Methods* 12.24 (2020), pp. 3137–3144. ISSN: 1759-9660, 1759-9679. DOI: 10.1039/D0AY00686F.

[149] C. Minnich, S. Hardy, and S. Krämer. „Stopping the Babylonian Confusion: An Updated Nomenclature for Process Analyzers in PAT Applications“. en. In: *Chemie Ingenieur Technik* 88.6 (2016), pp. 694–697. ISSN: 1522-2640. DOI: 10.1002/cite.201500188.

[150] M. Park, A. Somborn, D. Schlehuber, V. Keuter, and G. Deerberg. „Raman spectroscopy in crop quality assessment: focusing on sensing secondary metabolites: a review“. In: *Horticulture Research* 10.5 (Apr. 2023), uhad074. ISSN: 2662-6810. DOI: 10.1093/hr/uhad074.

[151] J. I. Kelz, J. L. Uribe, and R. W. Martin. „Reimagining magnetic resonance instrumentation using open maker tools and hardware as protocol“. In: *Journal of Magnetic Resonance Open* 6-7 (June 2021), p. 100011. ISSN: 2666-4410. DOI: 10.1016/j.jmro.2021.100011.

[152] K. B. Be, J. Grabska, Y. Ozaki, M. A. Czarnecki, and C. W. Huck. „Simulated NIR spectra as sensitive markers of the structure and interactions in nucleobases“. en. In: *Scientific Reports* 9.1 (Nov. 2019), p. 17398. ISSN: 2045-2322. DOI: 10.1038/s41598-019-53827-6.

[153] S. G. Kazarian and K. L. Andrew Chan. „ATR-FTIR spectroscopic imaging : recent advances and applications to biological systems“. en. In: *Analyst* 138.7 (2013), pp. 1940–1951. DOI: 10.1039/C3AN36865C.

[154] J. Gebhard, D. Sellin, L. Hilterhaus, and A. Liese. „Online Analysis of Enzymatic Polycondensation Reactions in Bubble Column Reactors by Means of ATRFTIR Spectroscopy“. en. In: *Chemie Ingenieur Technik* 85.7 (July 2013), pp. 1016–1022. ISSN: 0009-286X, 1522-2640. DOI: 10.1002/cite.201200248.

[155] T. Vlek and Z. S. Petrovi. „Optimization of the chemoenzymatic epoxidation of soybean oil“. en. In: *Journal of the American Oil Chemists' Society* 83.3 (2006), pp. 247–252. ISSN: 1558-9331. DOI: 10.1007/s11746-006-1200-4.

[156] M. H. Tavassoli-Kafrani, F. R. van de Voort, and J. M. Curtis. „The use of ATR-FTIR spectroscopy to measure changes in the oxirane content and iodine value of vegetable oils during epoxidation“. en. In: *European Journal of Lipid Science and Technology* 119.7 (2017), p. 1600354. ISSN: 1438-9312. DOI: 10.1002/ejlt.201600354.

[157] M. S. Bhalerao, V. M. Kulkarni, and A. V. Patwardhan. „Ultrasound-assisted chemoenzymatic epoxidation of soybean oil by using lipase as biocatalyst“. In: *Ultrasonics Sonochemistry* 40 (Jan. 2018), pp. 912–920. ISSN: 1350-4177. DOI: 10.1016/j.ultsonch.2017.08.042.

[158] F. Alsmeyer, H.-J. KoSS, and W. Marquardt. „Indirect Spectral Hard Modeling for the Analysis of Reactive and Interacting Mixtures“. EN. In: *Applied Spectroscopy* 58.8 (Aug. 2004), pp. 975–985. ISSN: 0003-7028. DOI: 10.1366/0003702041655368.

[159] P. Beumers. *Physically-based models for the analysis of Raman spectra = Physikalisch basierte Modelle zur Auswertung von Raman Spektren*. eng. 1. Auflage. Aachen: Wissenschaftsverlag Mainz GmbH, 2019. ISBN: 978-3-95886-319-4.

[160] C. E. Eskildsen, S. B. Engelsen, K. R. Dankel, L. E. Solberg, and T. Næs. „Diagnosing indirect relationships in multivariate calibration models“. en. In: *Journal of Chemometrics* 35.9 (2021), e3366. ISSN: 1099-128X. DOI: 10.1002/cem.3366.

[161] C. E. Eskildsen, T. Næs, P. B. Skou, L. E. Solberg, K. R. Dankel, S. A. Basmoen, J. P. Wold, S. S. Horn, B. Hillestad, N. A. Poulsen, M. Christensen, T. Pieper, N. K. Afseth, and S. B. Engelsen. „Cage of covariance in calibration modeling: Regressing multiple and strongly correlated response variables onto a low rank subspace of explanatory variables“. In: *Chemometrics and Intelligent Laboratory Systems* 213 (June 2021), p. 104311. ISSN: 0169-7439. DOI: 10.1016/j.chemolab.2021.104311.

[162] E. Kriesten, D. Mayer, F. Alsmeyer, C. B. Minnich, L. Greiner, and W. Marquardt. „Identification of unknown pure component spectra by indirect hard modeling“. In: *Chemometrics and Intelligent Laboratory Systems* 93.2 (Oct. 2008), pp. 108–119. ISSN: 0169-7439. DOI: 10.1016/j.chemolab.2008.05.002.

[163] D. H. Müller. *In-Line Monitoring and Control of Bioprocesses Using Raman Spectroscopy and Indirect Hard Modeling*. eng. Aachen: Verlag Günter Mainz, 2024. ISBN: 978-3-95886-537-2.

[164] J. Almond, P. Sugumaar, M. N. Wenzel, G. Hill, and C. Wallis. „Determination of the carbonyl index of polyethylene and polypropylene using specified area under band methodology with ATR-FTIR spectroscopy“. en. In: *e-Polymers* 20.1 (Jan. 2020), pp. 369–381. ISSN: 1618-7229. DOI: 10.1515/epoly-2020-0041.

[165] T. Kenzom, P. Srivastava, and S. Mishra. „Structural Insights into 2,2'-Azino-Bis(3-Ethylbenzothiazoline-6-Sulfonic Acid) (ABTS)-Mediated Degradation of Reactive Blue 21 by Engineered Cyathus bulleri Laccase and Characterization of Degradation Products“. In: *Applied and Environmental Microbiology* 80.24 (Dec. 2014), pp. 7484–7495. ISSN: 0099-2240. DOI: 10.1128/AEM.02665-14.

[166] K. Obleser, H. Kalaus, B. Seidl, M. Kozich, C. Stanetty, and M. D. Mihovilovic. „An Organic Chemist's Guide to Mediated Laccase Oxidation“. en. In: *ChemBioChem* 23.23 (2022), e202200411. ISSN: 1439-7633. DOI: 10.1002/cbic.202200411.

[167] L. Klose. *3D-printed cyclic voltammetry cell based on 50 mL laboratory glass bottle*. Dec. 2026. DOI: 10.15480/882.16321.

[168] G. M. Morris, R. Huey, W. Lindstrom, M. F. Sanner, R. K. Belew, D. S. Goodsell, and A. J. Olson. „AutoDock4 and AutoDockTools4: Automated Docking with Selective Receptor Flexibility“. In: *Journal of computational chemistry* 30.16 (Dec. 2009), pp. 2785–2791. ISSN: 0192-8651. DOI: 10.1002/jcc.21256.

[169] I. Matera, A. Gullotto, M. Ferraroni, S. Tilli, F. Briganti, and A. Scozzafava. *Crystal Structure of Blue Laccase from Trametes trogii: 2hrh*. Sept. 2007. DOI: 10.2210/pdb2hrh/pdb.

[170] I. Pardo and S. Camarero. „Laccase engineering by rational and evolutionary design“. en. In: *Cellular and Molecular Life Sciences* 72.5 (Mar. 2015), pp. 897–910. ISSN: 1420-9071. DOI: 10.1007/s00018-014-1824-8.

[171] M. Rüsch gen. Klaas and S. Warwel. „Complete and partial epoxidation of plant oils by lipase-catalyzed perhydrolysis1“. In: *Industrial Crops and Products* 9.2 (Jan. 1999), pp. 125–132. ISSN: 0926-6690. DOI: 10.1016/S0926-6690(98)00023-5.

[172] W. Liu, J. Chen, R. Liu, and Y. Bi. „Revisiting the Enzymatic Epoxidation of Vegetable Oils by Perfatty Acid: Perbutyric Acid Effect on the Oil with Low Acid Value“. en. In: *Journal of the American Oil Chemists' Society* 93.11 (2016), pp. 1479–1486. ISSN: 1558-9331. DOI: 10.1007/s11746-016-2897-3.

[173] ASTM International. *Test Method for Epoxy Content of Epoxy Resins*. en. Tech. rep. D1652-11. West Conshohocken, PA: ASTM International, 2011.

[174] P. C. F. Buchholz, G. Feuerriegel, H. Zhang, P. Perez-Garcia, L.-L. Nover, J. Chow, W. R. Streit, and J. Pleiss. „Plastics degradation by hydrolytic enzymes: The plastics-active enzymes database-PAZy“. eng. In: *Proteins* 90.7 (2022), pp. 1443–1456. DOI: 10.1002/prot.26325.

[175] A. K. S. Kameshwar, R. Barber, and W. Qin. „Comparative modeling and molecular docking analysis of white, brown and soft rot fungal laccases using lignin model compounds for understanding the structural and functional properties of laccases“. en. In: *Journal of Molecular Graphics and Modelling* 79 (Jan. 2018), pp. 15–26. ISSN: 1093-3263. DOI: 10.1016/j.jmgm.2017.10.019.

[176] V. Hämäläinen, T. Grönroos, A. Suonpää, M. W. Heikkilä, B. Romein, P. Ihalainen, S. Malandra, and K. R. Birikh. „Enzymatic Processes to Unlock the Lignin Value“. In: *Frontiers in Bioengineering and Biotechnology* 6 (Mar. 2018), p. 20. ISSN: 2296-4185. DOI: 10.3389/fbioe.2018.00020.

[177] A. Zotti, A. Elmahdy, S. Zuppolini, A. Borriello, P. Verleysen, and M. Zarrelli. „Aromatic Hyperbranched Polyester/RTM6 Epoxy Resin for EXTREME Dynamic Loading Aeronautical Applications“. eng. In: *Nanomaterials (Basel, Switzerland)* 10.2 (2020). ISSN: 2079-4991. DOI: 10.3390/nano10020188.

[178] L. Greiner, P. Kukla, S. Eibl, and M. Döring. „Phosphorus Containing Polyacrylamides as Flame Retardants for Epoxy-Based Composites in Aviation“. eng. In: *Polymers* 11.2 (2019). DOI: 10.3390/polym11020284.

[179] N. Causse, S. Benchimol, L. Martineau, D. Carponcin, A. Lonjon, M. Fogel, J. Dandurand, E. Dantras, and C. Lacabanne. „Polymerization study and rheological behavior of a RTM6 epoxy resin system during preprocessing step“. en. In: *Journal of Thermal Analysis and Calorimetry* 119.1 (Jan. 2015), pp. 329–336. ISSN: 1388-6150, 1588-2926. DOI: 10.1007/s10973-014-4147-y.

[180] M. Euring, K. Ostendorf, M. Rühl, and U. Kües. „Enzymatic Oxidation of Ca-Lignosulfonate and Kraft Lignin in Different Lignin-Laccase-Mediator-Systems and MDF Production“. eng. In: *Frontiers in bioengineering and biotechnology* 9 (2021), p. 788622. ISSN: 2296-4185. DOI: 10.3389/fbioe.2021.788622.

[181] M. Frasconi, H. Boer, A. Koivula, and F. Mazzei. „Electrochemical evaluation of electron transfer kinetics of high and low redox potential laccases on gold electrode surface“. In: *Electrochimica Acta* 56.2 (Dec. 2010), pp. 817–827. ISSN: 0013-4686. DOI: 10.1016/j.electacta.2010.09.056.

[182] H. Lin, Z. Yu, Q. Wang, Y. Liu, L. Jiang, C. Xu, and M. Xian. „Application of Laccase Catalysis in Bond Formation and Breakage: A Review“. en. In: *Catalysts* 13.4 (Apr. 2023), p. 750. ISSN: 2073-4344. DOI: 10.3390/catal13040750.

[183] P. Baldrian. „Fungal laccases occurrence and properties“. en. In: *FEMS Microbiology Reviews* 30.2 (2006), pp. 215–242. ISSN: 1574-6976. DOI: 10.1111/j.1574-4976.2005.00010.x.

[184] V. Hahn, A. Mikolasch, C. Kuhlisch, and F. Schauer. „Laccase-mediated multi-step homo- and heteromolecular reactions of *ortho*-dihydroxylated aromatic compounds and mono- or diaminated substances resulting in CC, CO and CN bonds“. In: *Journal of Molecular Catalysis B: Enzymatic* 122 (Dec. 2015), pp. 56–63. ISSN: 1381-1177. DOI: 10.1016/j.molcatb.2015.08.011.

[185] C. Novoa, G. V. Dhoke, D. M. Mate, R. Martínez, T. Haarmann, M. Schreiter, J. Eidner, R. Schwerdtfeger, P. Lorenz, M. D. Davari, F. Jakob, and U. Schwaneberg. „KnowVolution of a Fungal Laccase toward Alkaline pH“. en. In: *ChemBioChem* 20.11 (2019), pp. 1458–1466. ISSN: 1439-7633. DOI: 10.1002/cbic.201800807.

[186] C. Sandford, M. A. Edwards, K. J. Klunder, D. P. Hickey, M. Li, K. Barman, M. S. Sigman, H. S. White, and S. D. Minteer. „A synthetic chemist's guide to electroanalytical tools for studying reaction mechanisms“. en. In: *Chemical Science* 10.26 (2019), pp. 6404–6422. DOI: 10.1039/C9SC01545K.

[187] N. Elgrishi, K. J. Rountree, B. D. McCarthy, E. S. Rountree, T. T. Eisenhart, and J. L. Dempsey. „A Practical Beginners Guide to Cyclic Voltammetry“. In: *Journal of Chemical Education* 95.2 (Feb. 2018), pp. 197–206. ISSN: 0021-9584. DOI: 10.1021/acs.jchemed.7b00361.

[188] I. O. Hordieieva, O. V. Kushch, T. O. Hordieieva, S. I. Sirobaba, M. O. Kompanets, V. M. Anishchenko, and A. N. Shendrik. „Eco-friendly TEMPO/laccase/O 2 biocatalytic system for degradation of Indigo Carmine: operative conditions and laccase inactivation“. en. In: *RSC Advances* 13.30 (2023), pp. 20737–20747. DOI: 10.1039/D3RA03107A.

[189] K. Krikstopaitis and J. Kulys. „Electrochemical properties of violuric acid and oxidase biosensor preparation“. In: *Electrochemistry Communications* 2.2 (Feb. 2000), pp. 119–123. ISSN: 1388-2481. DOI: 10.1016/S1388-2481(99)00158-7.

[190] E. Aracri, T. Tzanov, and T. Vidal. „Use of Cyclic Voltammetry as an Effective Tool for Selecting Efficient Enhancers for Oxidative Bioprocesses: Importance of pH“. In: *Industrial & Engineering Chemistry Research* 52.4 (Jan. 2013), pp. 1455–1463. ISSN: 0888-5885. DOI: 10.1021/ie3027586.

[191] A. M. Garzillo, M. C. Colao, V. Buonocore, R. Oliva, L. Falcigno, M. Saviano, A. M. Santoro, R. Zappala, R. P. Bonomo, C. Bianco, P. Giardina, G. Palmieri, and G. Sannia. „Structural and kinetic characterization of native laccases from Pleurotus ostreatus, Rigidoporus lignosus, and Trametes trogii“. eng. In: *Journal of Protein Chemistry* 20.3 (Apr. 2001), pp. 191–201. ISSN: 0277-8033. DOI: 10.1023/a:1010954812955.

[192] U. Fillat and M. B. Roncero. „Optimization of laccasemediator system in producing biobleached flax pulp“. In: *Bioresource Technology* 101.1 (Jan. 2010), pp. 181–187. ISSN: 0960-8524. DOI: 10.1016/j.biortech.2009.07.020.

[193] S. Scheiblbrandner, E. Breslmayr, F. Csarman, R. Paukner, J. Führer, P. L. Herzog, S. V. Shleev, E. M. Osipov, T. V. Tikhonova, V. O. Popov, D. Haltrich, R. Ludwig, and R. Kittl. „Evolving stability and pH-dependent activity of the high redox potential Botrytis aclada laccase for enzymatic fuel cells“. en. In: *Scientific Reports* 7.1 (Oct. 2017), p. 13688. ISSN: 2045-2322. DOI: 10.1038/s41598-017-13734-0.

[194] Q. Yin, G. Zhou, C. Peng, Y. Zhang, U. Kües, J. Liu, Y. Xiao, and Z. Fang. „The first fungal laccase with an alkaline pH optimum obtained by directed evolution and its application in indigo dye decolorization“. In: *AMB Express* 9 (Sept. 2019), p. 151. ISSN: 2191-0855. DOI: 10.1186/s13568-019-0878-2.

[195] E. Grassi, P. Scodeller, N. Filiel, R. Carballo, and L. Levin. „Potential of Trametes trogii culture fluids and its purified laccase for the decolorization of different types of recalcitrant dyes without the addition of redox mediators“. en. In: *International Biodeterioration & Biodegradation* 65.4 (July 2011), pp. 635–643. ISSN: 09648305. DOI: 10.1016/j.ibiod.2011.03.007.

[196] D. Huber, A. Ortner, A. Daxbacher, G. S. Nyanhongo, W. Bauer, and G. M. Guebitz. „Influence of Oxygen and Mediators on Laccase-Catalyzed Polymerization of Lignosulfonate“. In: *ACS Sustainable Chemistry & Engineering* 4.10 (Oct. 2016), pp. 5303–5310. DOI: 10.1021/acssuschemeng.6b00692.

[197] A. Ortner, D. Huber, O. Haske-Cornelius, H. K. Weber, K. Hofer, W. Bauer, G. S. Nyanhongo, and G. M. Guebitz. „Laccase mediated oxidation of industrial lignins: Is oxygen limiting?“ In: *Process Biochemistry* 50.8 (Aug. 2015), pp. 1277–1283. ISSN: 1359-5113. DOI: 10.1016/j.procbio.2015.05.003.

[198] M. Lecourt, G. Chietera, B. Blerot, and S. Antoniotti. „Laccase-Catalyzed Oxidation of Allylbenzene Derivatives: Towards a Green Equivalent of Ozonolysis“. en. In: *Molecules* 26.19 (Jan. 2021), p. 6053. ISSN: 1420-3049. DOI: 10.3390/molecules26196053.

[199] I. Matijosyte. „Mechanistic studies of laccase/TEMPO catalyzed aerobic oxidation of alcohols“. Dissertation (TU Delft). Vilnius, Litouwen: JSC Ciklonas, 2008.

[200] H. Clever, R. Battino, H. Miyamoto, Y. Yampolski, and C. Young. „IUPAC-NIST Solubility Data Series. 103. Oxygen and Ozone in Water, Aqueous Solutions, and Organic Liquids (Supplement to Solubility Data Series Volume 7)“. In: *Journal of Physical and Chemical Reference Data* 43 (Sept. 2014), p. 033102. DOI: 10.1063/1.4883876.

[201] R. M. Lindeque and J. M. Woodley. „The Effect of Dissolved Oxygen on Kinetics during Continuous Biocatalytic Oxidations“. In: *Organic Process Research & Development* 24.10 (Oct. 2020), pp. 2055–2063. ISSN: 1083-6160. DOI: 10.1021/acs.oprd.0c00140.

[202] M. Fabbrini, C. Galli, and P. Gentili. „Radical or electron-transfer mechanism of oxidation with some laccase/mediator systems“. In: *Journal of Molecular Catalysis B: Enzymatic* 18.1 (Sept. 2002), pp. 169–171. ISSN: 1381-1177. DOI: 10.1016/S1381-1177(02)00082-6.

[203] I. Bassanini, S. Grosso, C. Tognoli, G. Fronza, and S. Riva. „Studies on the Oxidation of Aromatic Amines Catalyzed by Trametes versicolor Laccase“. en. In: *International Journal of Molecular Sciences* 24.4 (Jan. 2023), p. 3524. ISSN: 1422-0067. DOI: 10.3390/ijms24043524.

[204] J. Dong, E. Fernández-Fueyo, F. Hollmann, C. E. Paul, M. Pesic, S. Schmidt, Y. Wang, S. Younes, and W. Zhang. „Biocatalytic Oxidation Reactions: A Chemist's Perspective“. en. In: *Angewandte Chemie International Edition* 57.30 (2018), pp. 9238–9261. ISSN: 1521-3773. DOI: 10.1002/anie.201800343.

[205] A. Potthast, T. Rosenau, and K. Fischer. „Oxidation of Benzyl Alcohols by the Laccase-Mediator System (LMS) a Comprehensive Kinetic Description“. In: *Holzforschung* 55 (Jan. 2001), pp. 47–56. DOI: 10.1515/HFSG.2001.47.

[206] C. Yang, L. Ma, X. Wang, Y. Xing, and X. Lü. „A Novel Polyphenol Oxidoreductase OhLac from Ochrobactrum sp. J10 for Lignin Degradation“. English. In: *Frontiers in Microbiology* 12 (Oct. 2021). ISSN: 1664-302X. DOI: 10.3389/fmicb.2021.694166.

[207] G. Janusz, E. Skwarek, and A. Pawlik. „Potential of Laccase as a Tool for Biodegradation of Wastewater Micropollutants“. en. In: *Water* 15.21 (Jan. 2023), p. 3770. ISSN: 2073-4441. DOI: 10.3390/w15213770.

[208] L. Zhang, T. You, T. Zhou, L. Zhang, and F. Xu. „Determining Lignin Degradation in White-Rot Fungi-Treated Sacrau Poplar: Lignin Structural Changes and Degradation Compound Analysis“. en. In: *BioResources* 11.2 (Mar. 2016). ISSN: 1930-2126. DOI: 10.15376/biores.11.2.3972-3986.

[209] Y. Jiang, X. Duan, H. Qu, and S. Zheng. „Browning: Enzymatic Browning“. In: *Encyclopedia of Food and Health*. Ed. by B. Caballero, P. M. Finglas, and F. Toldrá. Oxford: Academic Press, Jan. 2016, pp. 508–514. ISBN: 978-0-12-384953-3. DOI: 10.1016/B978-0-12-384947-2.00090-8.

[210] J. Coates. „Interpretation of Infrared Spectra, A Practical Approach“. en. In: *Encyclopedia of Analytical Chemistry*. John Wiley & Sons, Ltd, 2006. ISBN: 978-0-470-02731-8. DOI: 10.1002/9780470027318.a5606.

[211] S. Morsch, Y. Liu, S. B. Lyon, S. R. Gibbon, B. Gabriele, M. Malanin, and K.-J. Eichhorn. „Examining the early stages of thermal oxidative degradation in epoxy-amine resins“. In: *Polymer Degradation and Stability* 176 (June 2020), p. 109147. ISSN: 0141-3910. DOI: 10.1016/j.polymdegradstab.2020.109147.

[212] P. Musto, G. Ragosta, P. Russo, and L. Mascia. „Thermal-Oxidative Degradation of Epoxy and Epoxy-Bismaleimide Networks: Kinetics and Mechanism“. en. In: *Macromolecular Chemistry and Physics* 202.18 (2001), pp. 3445–3458. ISSN: 1521-3935. DOI: 10.1002/1521-3935(20011201)202:18<3445::AID-MACP3445>3.0.CO;2-N.

[213] E. Aracri, A. G. Barneto, and T. Vidal. „Comparative Study of the Effects Induced by Different Laccase-Based Systems on Sisal Cellulose Fibers“. In: *Industrial & Engineering Chemistry Research* 51.10 (Mar. 2012), pp. 3895–3902. ISSN: 0888-5885. DOI: 10.1021/ie2028206.

[214] Y.-C. Chiu, I.-C. Chou, W.-C. Tseng, and C.-C. M. Ma. „Preparation and thermal properties of diglycidylether sulfone epoxy“. en. In: *Polymer Degradation and Stability* 93.3 (Mar. 2008), pp. 668–676. ISSN: 0141-3910. DOI: 10.1016/j.polymdegradstab.2007.12.014.

[215] L. Munk, M. L. Andersen, and A. S. Meyer. „Influence of mediators on laccase catalyzed radical formation in lignin“. In: *Enzyme and Microbial Technology* 116 (Sept. 2018), pp. 48–56. ISSN: 0141-0229. DOI: 10.1016/j.enzmictec.2018.05.009.

[216] B. Xu, M. Wu, Y. Liu, and S. Wei. „Study on Flame Retardancy Behavior of Epoxy Resin with Phosphaphenanthrene Triazine Compound and Organic Zinc Complexes Based on Phosphonitrile“. en. In: *Molecules* 28.7 (Jan. 2023), p. 3069. ISSN: 1420-3049. DOI: 10.3390/molecules28073069.

[217] R. Ménard, C. Negrell, M. Fache, L. Ferry, R. Sonnier, and G. David. „From a bio-based phosphorus-containing epoxy monomer to fully bio-based flame-retardant thermosets“. en. In: *RSC Advances* 5.87 (Aug. 2015), pp. 70856–70867. ISSN: 2046-2069. DOI: 10.1039/C5RA12859E.

[218] Z. Chen, X. Bai, L. A, and C. Wan. „High-Solid Lignocellulose Processing Enabled by Natural Deep Eutectic Solvent for Lignin Extraction and Industrially Relevant Production of Renewable Chemicals“. en. In: *ACS Sustainable Chemistry & Engineering* 6.9 (Sept. 2018), pp. 12205–12216. ISSN: 2168-0485, 2168-0485. DOI: 10.1021/acssuschemeng.8b02541.

[219] National Center for Biotechnology Information. *Formic Acid*. 2025. DOI: https://pubchem.ncbi.nlm.nih.gov/compound/284.

[220] National Center for Biotechnology Information. *Lactic Acid*. 2025. DOI: https://pubchem.ncbi.nlm.nih.gov/compound/612.

[221] National Center for Biotechnology Information. *Ethylene Glycol*. 2025. DOI: https://pubchem.ncbi.nlm.nih.gov/compound/174.

[222] National Center for Biotechnology Information. *N,N-Dimethylformamide*. 2025. DOI: https://pubchem.ncbi.nlm.nih.gov/compound/6228.

[223] National Center for Biotechnology Information. *Choline Chloride*. 2025. DOI: https://pubchem.ncbi.nlm.nih.gov/compound/6209.

[224] National Center for Biotechnology Information. *Betaine*. 2025. DOI: https://pubchem.ncbi.nlm.nih.gov/compound/247.

[225] X. Chen, Q. Liu, B. Li, N. Wang, C. Liu, J. Shi, and L. Liu. „Unveiling the potential of novel recyclable deep eutectic solvent pretreatment: Effective separation of lignin from poplar hydrolyzed residue“. en. In: *International Journal of Biological Macromolecules* 259 (Feb. 2024), p. 129354. ISSN: 01418130. DOI: 10.1016/j.ijbiomac.2024.129354.

[226] D. Zhou, X. Chen, G. Li, M. Zhao, and D. Li. „Effect of deep eutectic solvents on activity, stability, and selectivity of enzymes: Novel insights and further prospects“. In: *International Journal of Biological Macromolecules* 284 (Jan. 2025), p. 138148. ISSN: 0141-8130. DOI: 10.1016/j.ijbiomac.2024.138148.

[227] J. C. Chan. *Interactions Between Deep Eutectic Solvent and Laccase*. eng. Tech. rep. Washington State University, Jan. 2020.

[228] T. Khan, N. Das, S. Bhowmik, K. S. Negi, and P. Sen. „Critical Role of Water beyond the Media to Maintain Protein Stability and Activity in Hydrated Deep Eutectic Solvent“. eng. In: *The Journal of Physical Chemistry. B* 129.1 (Jan. 2025), pp. 162–175. ISSN: 1520-5207. DOI: 10.1021/acs.jpcb.4c07039.

[229] L. Yang, J. Chen, K. Xie, K. He, W. Sheng, M. Zhou, G. Jiang, and Y. Tian. „Effects of deep eutectic solvent on laccase activity and thermal stability“. In: *Bioresource Technology* 436 (Nov. 2025), p. 132992. ISSN: 0960-8524. DOI: 10.1016/j.biortech.2025.132992.

[230] E. Delamarche, A. Mattlet, S. Livi, J.-F. Gérard, R. Bayard, and V. Massardier. „Tailoring Biodegradability of Poly(Butylene Succinate)/Poly(Lactic Acid) Blends With a Deep Eutectic Solvent“. English. In: *Frontiers in Materials* 7 (Feb. 2020). ISSN: 2296-8016. DOI: 10.3389/fmats.2020.00007.

[231] J. A. Brom, R. G. Petrikis, and G. J. Pielak. „How Sugars Protect Dry Protein Structure“. In: *Biochemistry* 62.5 (Feb. 2023), pp. 1044–1052. ISSN: 0006-2960. DOI: 10.1021/acs.biochem.2c00692.

[232] J. Guo, N. Zhao, Y. Zhao, H. Jin, G. Sun, J. Yu, H. Zhang, M. Yu, D. Yang, and Z. Liang. „Effect of Deep Eutectic Solvents on the Activity and Stability of Cellulases and Pectinases“. In: *ACS Omega* 8.48 (Dec. 2023), pp. 45678–45686. DOI: 10.1021/acsomega.3c06088.

[233] F. Z. Ibn Majdoub Hassani, S. Amzazi, and I. Lavandera. „The Versatile Applications of DES and Their Influence on Oxidoreductase-Mediated Transformations“. en. In: *Molecules* 24.11 (Jan. 2019), p. 2190. ISSN: 1420-3049. DOI: 10.3390/molecules24112190.

[234] M.-Q. Ai, F.-F. Wang, and F. Huang. „Purification and Characterization of a Thermostable Laccase from Trametes trogii and Its Ability in Modification of Kraft Lignin“. en. In: *Journal of Microbiology and Biotechnology* 25.8 (Aug. 2015), pp. 1361–1370. ISSN: 1017-7825, 1738-8872. DOI: 10.4014/jmb.1502.02022.

[235] N. Zhang, F. Steininger, L.-E. Meyer, K. Koren, and S. Kara. „Can Deep Eutectic Solvents Sustain Oxygen-Dependent Bioprocesses?Measurements of Oxygen Transfer Rates“. In: *ACS Sustainable Chemistry & Engineering* 9.25 (June 2021), pp. 8347–8353. DOI: 10.1021/acssuschemeng.1c03547.

[236] S. Kumar, S. Krishnan, and K. Prabakaran. „Renewable Resource-Based Epoxy Vitrimer Composites for Future Application: A Comprehensive Review“. In: *ACS Sustainable Resource Management* 1.9 (Sept. 2024), pp. 2086–2107. DOI: 10.1021/acssusresmgt.4c00200.

[237] S. Kern, A. Himmelspach, K. Grammann, O. Thum, and A. Liese. „Process Characterization Studies for Solvent-Free Simultaneous Epoxidation and Transesterification of Fatty Acid Methyl Esters“. en. In: *Organic Process Research & Development* 20.11 (Nov. 2016), pp. 1930–1936. ISSN: 1083-6160, 1520-586X. DOI: 10.1021/acs.oprd.6b00254.

[238] M. Gerlei, H. Pierson, M. Ponçot, C. J. F. Kahn, and M. Linder. „Chemical Composition and Crystallization Behavior of Oil and Fat Blends for Spreadable Fat Applications“. en. In: *Foods* 13.20 (Jan. 2024), p. 3305. ISSN: 2304-8158. DOI: 10.3390/foods13203305.

[239] N. Garti, E. Wellner, and S. Sarig. „Effect of surfactants on crystal structure modification of stearic acid“. In: *Journal of Crystal Growth* 57.3 (May 1982), pp. 577–584. ISSN: 0022-0248. DOI: 10.1016/0022-0248(82)90076-8.

[240] J. Chen, J. Zhou, W. Liu, Y. Bi, and D. Peng. „Enzymatic epoxidation of soybean oil in the presence of perbutyric acid“. en. In: *Chemical Papers* 71.11 (Nov. 2017), pp. 2139–2144. ISSN: 1336-9075. DOI: 10.1007/s11696-017-0206-8.

[241] K. Quast. „The use of zeta potential to investigate the pKa of saturated fatty acids“. In: *Advanced Powder Technology* 27.1 (Jan. 2016), pp. 207–214. ISSN: 0921-8831. DOI: 10.1016/j.apt.2015.12.003.

[242] Y. Liu, E. Lotero, and J. G. Goodwin. „Effect of carbon chain length on esterification of carboxylic acids with methanol using acid catalysis“. In: *Journal of Catalysis* 243.2 (Oct. 2006), pp. 221–228. ISSN: 0021-9517. DOI: 10.1016/j.jcat.2006.07.013.

[243] G. E. P. Box and D. W. Behnken. „Some New Three Level Designs for the Study of Quantitative Variables“. en. In: *Technometrics* 2.4 (Nov. 1960), pp. 455–475. ISSN: 0040-1706, 1537-2723. DOI: 10.1080/00401706.1960.10489912.

[244] M. Nordblad and P. Adlercreutz. „Effects of acid concentration and solvent choice on enzymatic acrylation by *Candida antarctica* lipase B“. In: *Journal of Biotechnology* 133.1 (Jan. 2008), pp. 127–133. ISSN: 0168-1656. DOI: 10.1016/j.jbiotec.2007.09.002.

[245] N. R. Amrutha, P. S. K. Murthy, and J. P. Reddy. „Epoxidized safflower oil: Synthesis and evaluation of its performance as bioplasticizer for polylactic acid films“. In: *Industrial Crops and Products* 224 (Feb. 2025), p. 120360. ISSN: 0926-6690. DOI: 10.1016/j.indcrop.2024.120360.

[246] M. Musik, M. Bartkowiak, and E. Milchert. „Advanced Methods for Hydroxylation of Vegetable Oils, Unsaturated Fatty Acids and Their Alkyl Esters“. en. In: *Coatings* 12.1 (Jan. 2022), p. 13. ISSN: 2079-6412. DOI: 10.3390/coatings12010013.

[247] I. Fuste-Dmoc, R. Dinu, T. Mluan, and A. Mija. „Valorisation of Chitosan Natural Building Block as a Primary Strategy for the Development of Sustainable Fully Bio-Based Epoxy Resins“. en. In: *Polymers* 15.24 (Jan. 2023), p. 4627. ISSN: 2073-4360. DOI: 10.3390/polym15244627.

[248] M. Fujisawa, H. Hirai, and T. Nishida. „Degradation of Polyethylene and Nylon-66 by the Laccase-Mediator System“. en. In: *Journal of Polymers and the Environment* 9.3 (July 2001), pp. 103–108. ISSN: 1572-8900. DOI: 10.1023/A:1020472426516.

[249] I. Mateljak, E. Monza, M. F. Lucas, V. Guallar, O. Aleksejeva, R. Ludwig, D. Leech, S. Shleev, and M. Alcalde. „Increasing Redox Potential, Redox Mediator Activity, and Stability in a Fungal Laccase by Computer-Guided Mutagenesis and Directed Evolution“. en. In: *ACS Catalysis* 9.5 (May 2019), pp. 4561–4572. ISSN: 2155-5435, 2155-5435. DOI: 10.1021/acscatal.9b00531.

[250] H. Lippold, L. Kahle, C. Sonnendecker, J. Matysik, and C. Fischer. „Temporal and spatial evolution of enzymatic degradation of amorphous PET plastics“. en. In: *npj Materials Degradation* 6.1 (Nov. 2022), pp. 1–6. ISSN: 2397-2106. DOI: 10.1038/s41529-022-00305-6.

[251] Y. Zheng, E. K. Yanful, and A. S. Bassi. „A review of plastic waste biodegradation“. eng. In: *Critical reviews in biotechnology* 25.4 (2005), pp. 243–250. ISSN: 0738-8551. DOI: 10.1080/07388550500346359.

[252] F. K. Metze, S. Sant, Z. Meng, H.-A. Klok, and K. Kaur. „Swelling-Activated, Soft Mechanochemistry in Polymer Materials“. In: *Langmuir* 39.10 (Mar. 2023), pp. 3546–3557. ISSN: 0743-7463. DOI: 10.1021/acs.langmuir.2c02801.

[253] S. Krainara, A. N. Mistry, C. Malee, C. Chavananikul, O. Pinyakong, W. Assavalapsakul, S. M. Jitpraphai, B. Kachenchart, and E. Luepromchai. „Development of a plastic waste treatment process by combining deep eutectic solvent (DES) pretreatment and bioaugmentation with a plastic-degrading bacterial consortium“. In: *Journal of Hazardous Materials* 460 (Oct. 2023), p. 132507. ISSN: 0304-3894. DOI: 10.1016/j.jhazmat.2023.132507.

[254] C. Cai, H. Dai, R. Chen, C. Su, X. Xu, S. Zhang, and L. Yang. „Studies on the kinetics of in situ epoxidation of vegetable oils“. en. In: *European Journal of Lipid Science and Technology* 110.4 (2008), pp. 341–346. ISSN: 1438-9312. DOI: 10.1002/ejlt.200700104.

[255] S. Pithani, S. Karlsson, H. Emtenäs, and C. T. Öberg. „Using Spinchem Rotating Bed Reactor Technology for Immobilized Enzymatic Reactions: A Case Study“. In: *Organic Process Research & Development* 23.9 (Sept. 2019), pp. 1926–1931. ISSN: 1083-6160. DOI: 10.1021/acs.oprd.9b00240.

[256] C. Di Mauro, A. Genua, and A. Mija. „Fully bio-based reprocessable thermosetting resins based on epoxidized vegetable oils cured with itaconic acid“. In: *Industrial Crops and Products* 185 (Oct. 2022), p. 115116. ISSN: 0926-6690. DOI: 10.1016/j.indcrop.2022.115116.

Appendix

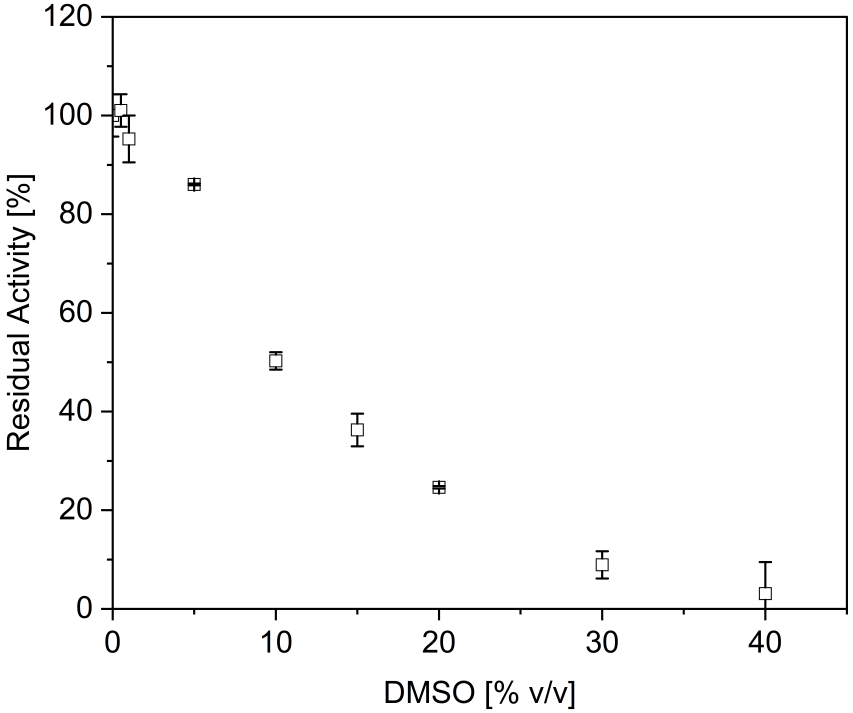

Figure A.1 DMSO tolerance of laccase from *Funalia trogii* (LacF) in 0.1 mol · L^{-1} aqueous citrate-phophate buffer at pH 4. Activity determined according to Section 4.5.

Listing 1 First-order kinetic fit using SciPy.

```
import os
import pandas as pd
import numpy as np
import matplotlib.pyplot as plt
from scipy.optimize import curve_fit
from scipy import stats

# Define the first-order kinetic model function
def first_order_kinetic(t, A, k):
    return A * np.exp(-k * t)

# Calculate R-squared value of the fit
def r_squared(y, y_fit):
    ss_res = np.sum((y - y_fit) ** 2)
    ss_tot = np.sum((y - np.mean(y)) ** 2)
```

```
16      return 1.0 - (ss_res / ss_tot)
17
18  # Calculate the confidence intervals for the fitted parameters
19  def confidence_interval(popt, pcov, alpha=0.1):
20      perr = np.sqrt(np.diag(pcov))
21      t_score = stats.t.ppf(1 - alpha / 2, len(popt) - 1)
22      lower_bound = popt - t_score * perr
23      upper_bound = popt + t_score * perr
24      return lower_bound, upper_bound
25
26  # Create a subfolder called "output" to save the plots
27  output_folder = 'output'
28  os.makedirs(output_folder, exist_ok=True)
29
30  # Replace 'data.xlsx' with the actual filename and path of your
        XLSX file
31  file_path = 'data.xlsx'
32
33  # Load data from the XLSX file into a pandas DataFrame
34  df = pd.read_excel(file_path, sheet_name='Sheet1', engine='openpyxl
        ')
35
36  # Extract the names from the first row (header) of the DataFrame
37  names = df.columns[1::2].tolist() # Skip the first column (Time)
        and take every even column
38
39  # Export the fit curve data
40  for name in names:
41      data_column = name
42      deviation_column = df.columns[df.columns.get_loc(name) + 1] #
        Get the corresponding deviation column
43
44      # Get the time (t), data (y), and deviation (sigma) values for
        the current dataset
45      t = df['Time']
46      y = df[data_column]
47      sigma = df[deviation_column]
48
49      # Guess initial parameter values for the fit
```

```
50      A_guess = np.mean(y) # Starting concentration guess (mean of
    data)
51      k_guess = 1.0 # Rate constant guess
52
53      # Perform the curve fitting
54      popt, pcov = curve_fit(first_order_kinetic, t, y, p0=[A_guess,
    k_guess])
55
56      # Extract the fitted parameters
57      A_fit, k_fit = popt
58
59      # Export the fit curve data
60      t_export = np.arange(0, max(t), 0.1)
61      y_export = first_order_kinetic(t_export, A_fit, k_fit)
62
63      # Save as CSV file
64      export_df = pd.DataFrame({'t': t_export, 'y': y_export})
65      export_df.to_csv(os.path.join(output_folder, f'{name}_fit.csv')
    , index=False)
66
67 # Create a 4x2 grid of subplots for all the plots
68 n_plots = len(names)
69 n_rows = 4
70 n_cols = 2
71 fig, axes = plt.subplots(n_rows, n_cols, figsize=(10, 15))
72
73 # Perform the first-order kinetic fit for each dataset and create
    individual plots
74 for i, name in enumerate(names):
75
76      data_column = name
77      deviation_column = df.columns[df.columns.get_loc(name) + 1] #
    Get the corresponding deviation column
78
79      # Get the time (t), data (y), and deviation (sigma) values for
    the current dataset
80      t = df['Time']
81      y = df[data_column]
82      sigma = df[deviation_column]
```

```
83
84      # Guess initial parameter values for the fit
85      A_guess = np.mean(y) # Starting concentration guess (mean of
        data)
86      k_guess = 1.0 # Rate constant guess
87
88      # Perform the curve fitting without taking deviation into
        account
89      popt, pcov = curve_fit(first_order_kinetic, t, y, p0=[A_guess,
        k_guess])
90
91      # Extract the fitted parameters
92      A_fit, k_fit = popt
93
94      # Calculate the fitted curve using the fitted parameters
95      y_fit = first_order_kinetic(t, A_fit, k_fit)
96
97      # Calculate the standard error of the fitted parameters
98      k_std_err = np.sqrt(pcov[1, 1])
99
100     # Calculate the R-squared value of the fit
101     r2 = r_squared(y, y_fit)
102
103     # Calculate the confidence intervals for the fitted curve
104     lower_bound, upper_bound = confidence_interval(popt, pcov)
105
106     # Create the individual plot for each dataset without the
        matrix
107     plt.figure()
108     plt.errorbar(t, y, yerr=sigma, marker='o', linestyle='', label=
        'NNBT Concentration [mM]')
109     plt.errorbar(t, y, yerr=sigma, marker='', linestyle='', ecolor=
        '#1f77b4')
110     t_fit = np.linspace(0, 200, 100) # Set x-axis limit to start
        from 0 and have a maximum value of 190
111     y_fit = first_order_kinetic(t_fit, A_fit, k_fit)
112     plt.plot(t_fit, y_fit, label=f'Fit: k={k_fit:.4f}, R^2={r2:.4f}
        ')
```

```
113     plt.fill_between(t_fit, first_order_kinetic(t_fit, *lower_bound
    ), first_order_kinetic(t_fit, *upper_bound), alpha=0.2)
114     plt.xlim(0, 200)
115     plt.ylim(0, 6)
116     plt.xlabel('Time [min]')
117     plt.ylabel('NNBT Concentration [mM]')
118     plt.title(f'{data_column}')
119     plt.legend()
120     plt.grid(True)
121     plt.savefig(os.path.join(output_folder, f'plot_{data_column}.
    png'))
122     plt.close()
123 
124     # Plot the data points (with error bars for deviation) in the
    matrix plot
125     row = i % n_rows
126     col = i // n_rows
127     axes[row, col].errorbar(t, y, yerr=sigma, marker='o', linestyle
    ='', label='NNBT Concentration [mM]')
128     axes[row, col].errorbar(t, y, yerr=sigma, marker='', linestyle=
    '', ecolor='#1f77b4')
129     t_fit = np.linspace(0, 200, 100)
130     y_fit = first_order_kinetic(t_fit, A_fit, k_fit)
131     axes[row, col].plot(t_fit, y_fit, label=f'Fit: k={k_fit:.4f}
    +/- {k_std_err:.4f}, R^2={r2:.4f}')
132     axes[row, col].fill_between(t_fit, first_order_kinetic(t_fit, *
    lower_bound), first_order_kinetic(t_fit, *upper_bound), alpha
    =0.2)
133     axes[row, col].set_xlim(0, 200)
134     axes[row, col].set_ylim(0, 6)
135     axes[row, col].set_xlabel('Time [min]')
136     axes[row, col].set_ylabel('NNBT Concentration [mM]')
137     axes[row, col].set_title(f'{data_column}')
138     axes[row, col].legend()
139     axes[row, col].grid(True)
140 
141 # Hide any empty plots in the matrix plot
142 for i in range(n_plots, n_rows * n_cols):
143     row = i % n_rows
```

```
144     col = i // n_rows
145     axes[row, col].axis('off')
146 
147 # Adjust the layout of the matrix plot and save it in the "output"
    subfolder
148 plt.tight_layout()
149 plt.savefig(os.path.join(output_folder, 'matrix_plot.png'))
150 
151 # Show all the individual plots
152 plt.show()
```

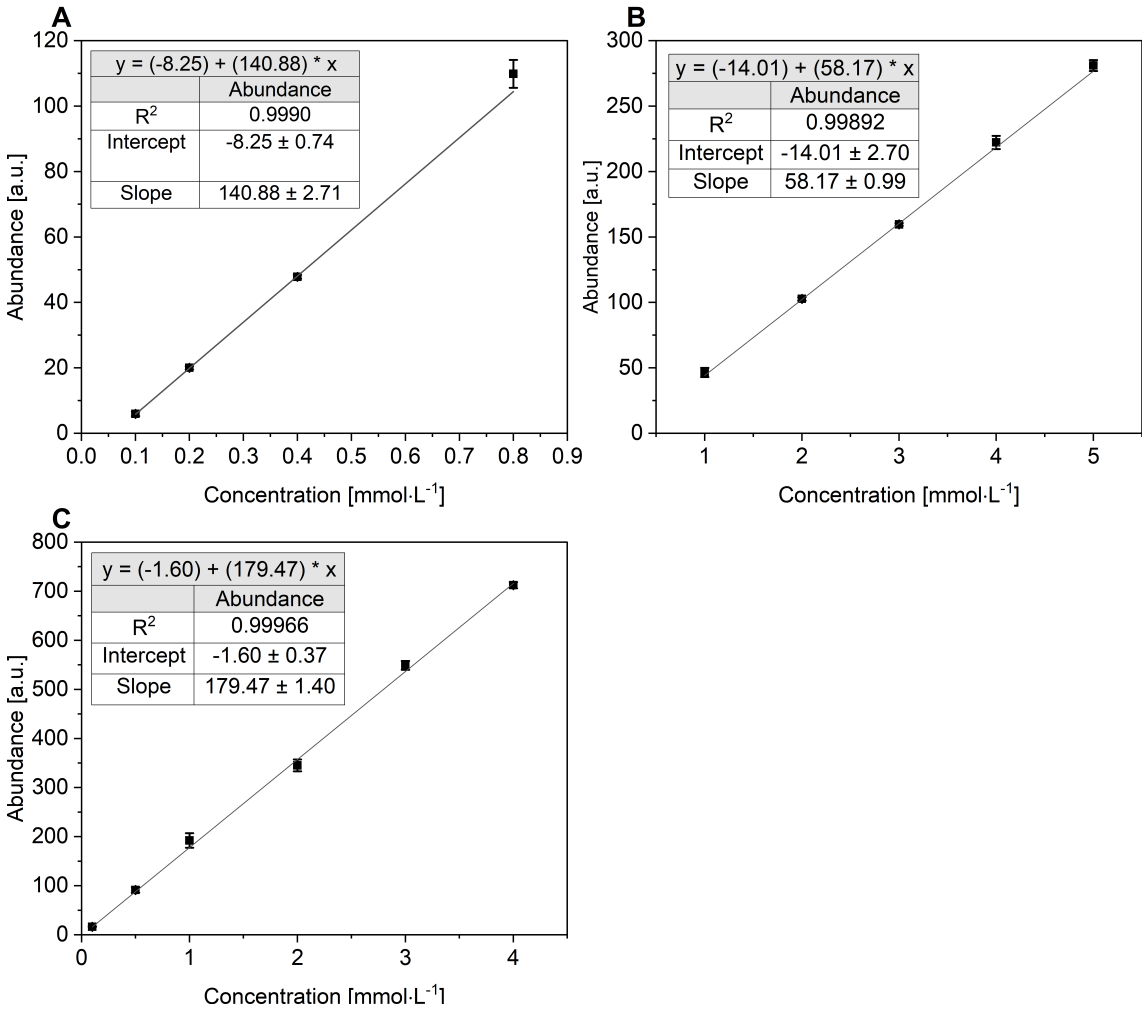

Figure A.2 Gas chromatography coupled flame ionization detector (GC-FID) calibrations for **(A)** *N*,*N*-bis(2-hydroxypropyl)-*p*-toluidine (NNBT) range from 0.1 mmol · L^{-1} to 0.8 mmol · L^{-1}, **(B)** NNBT range from 1 mmol · L^{-1} to 5 mmol · L^{-1} and **(C)** Michlers base (MB) range from 0.1 mmol · L^{-1} to 4 mmol · L^{-1}.

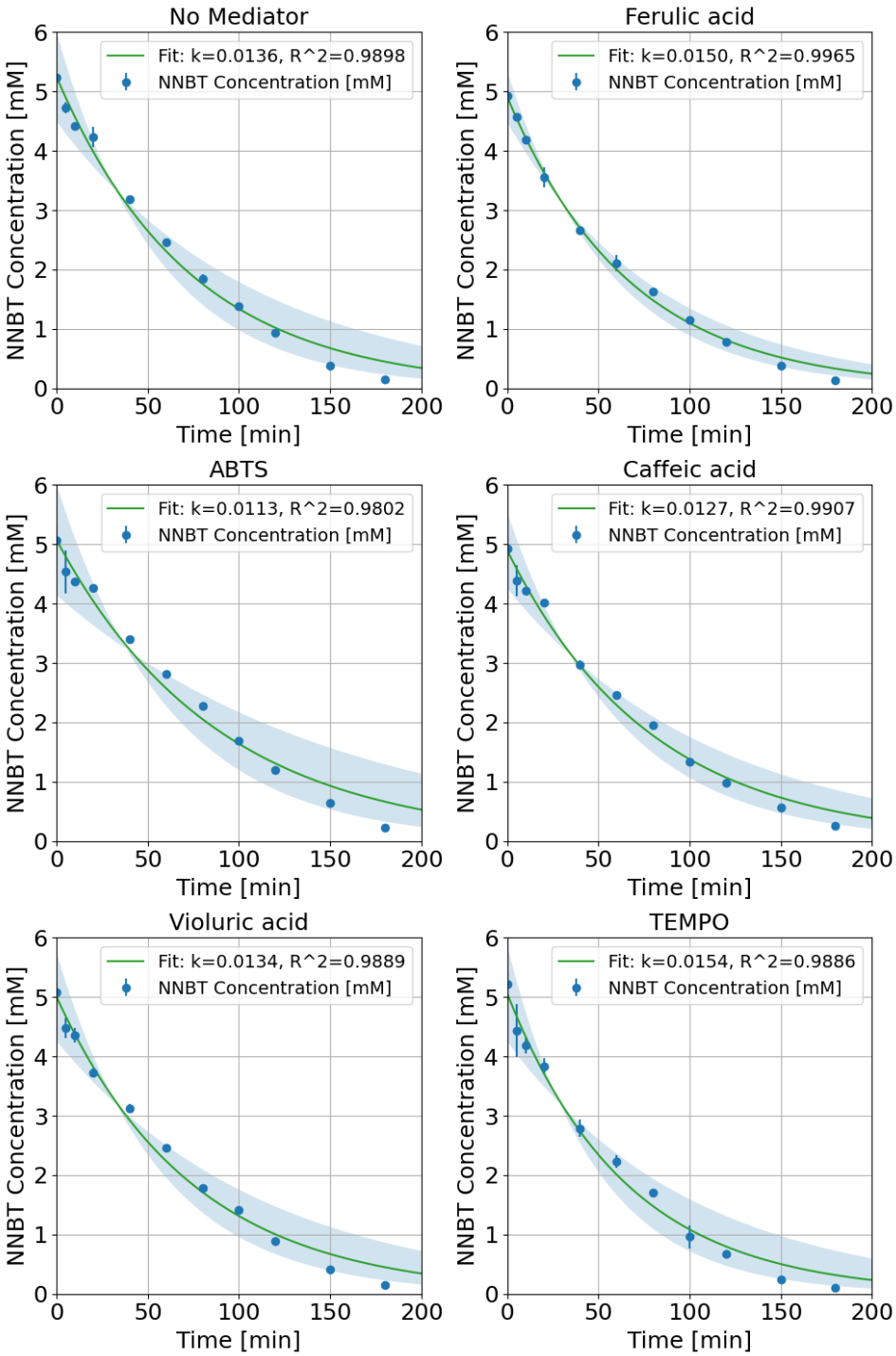

Figure A.3 Kinetic analysis of NNBT oxidation by laccasemediator system (LMS). First-order kinetic fitting was done with the `scipy.optimize.curve_fit` (NumPy library) function (all $R^2 > 0.98$). Reaction conditions: 0.1 U · mL^{-1} LacF, 5 mmol · L^{-1} NNBT, 1.5 mmol · L^{-1} mediator, 750 rpm, pH 4.5 (0.1 mol · L^{-1} citrate-phosphate-citrate buffer), 30 řC.

Certificate of Analysis

Item number: 9338

Linseed oil

native, cold-pressed

batch: 474355285

CAS No.:	8001-26-1	print date:	22.11.2024
formula:		recommended retest date:	31.10.2025
density:	0,93	release date:	21.11.2024
molecular weight:			

	Type analysis	batch results
Appearance	clear, gold-yellow or brownish to greenish-yellow oil	complies
Density (20 °C)	~0.931	0.930
Water	≤0.1 %	< 0.1 %
Cadmium (Cd)	≤0.00005 %	< 0.00005 %
Refractive index n_D^{20}	~1.480	1.4807
Acid value	≤4.5	1.6
Peroxide value	≤15	1.2
Iodine value	160-200	179
Saponification value	188-195	192
Unsaponifiable matter	≤1.5 %	< 1.5 %
Fatty acid compound	complies	complies

Our products are tested for laboratory use only.
The stated information refers to the current status of product quality.
We reserve the right to implement necessary changes.

S. Lindenfelser
Quality Control

K. Weber
Quality Assurance

This document is computer printout and has therefore not been signed by hand.

Carl Roth GmbH + Co. KG
Schoemperlenstraße 3-5
76185 Karlsruhe

Telefon 0721/5606-0
Telefax 0721/5606-149
E-Mail: info@carlroth.de

Figure A.4 Analysis certificate of linseed oil batch used in epoxidation reactions.

180°C mono-component epoxy system for Resin Transfer Moulding and Infusion technologies

Neat Resin Properties

	Tensile	Flexure
Strength (MPa)	75	132
Modulus (MPa)	2890	3300
Strain (%)	3.4	
Standard specifications	ASTM D638	ASTM D790

Uncured resin density: 1.11 g/cm³ at 25°C
Cured resin density: 1.14 g/cm³ at 25°C
Fracture toughness (G_{1C}/ASTM D 5045): 89 J/m²
Coefficient of Thermal Expansion: 52.7 e-6 /K

Properties on Composite Laminate

Composition of the laminate: Injectex® G0926: 5H Satin weave of 370g/m², HR 6K
Epoxy powdered fabric
Fibre volume fraction: 57%
HexFlow® RTM 6 resin
Inject the resin under vacuum/low pressure (1 to 5 bar)
Cure cycle 120 min at 180°C - no postcure

Dry/RT Properties

	Tensile Warp	I.L.S. Warp	Compression Warp	In Plane Shear
Strength (MPa)	860	62	680	95
Modulus (GPa)	67	-	60	4.3
Standard specifications	EN 2597 B	EN 2563	EN 2850 A1	EN 6031

Values obtained for G0926 SD (AS4C J) E01 RTM6

Figure A.5 Excerpt from datasheet of HexFlow® RTM6 resin.

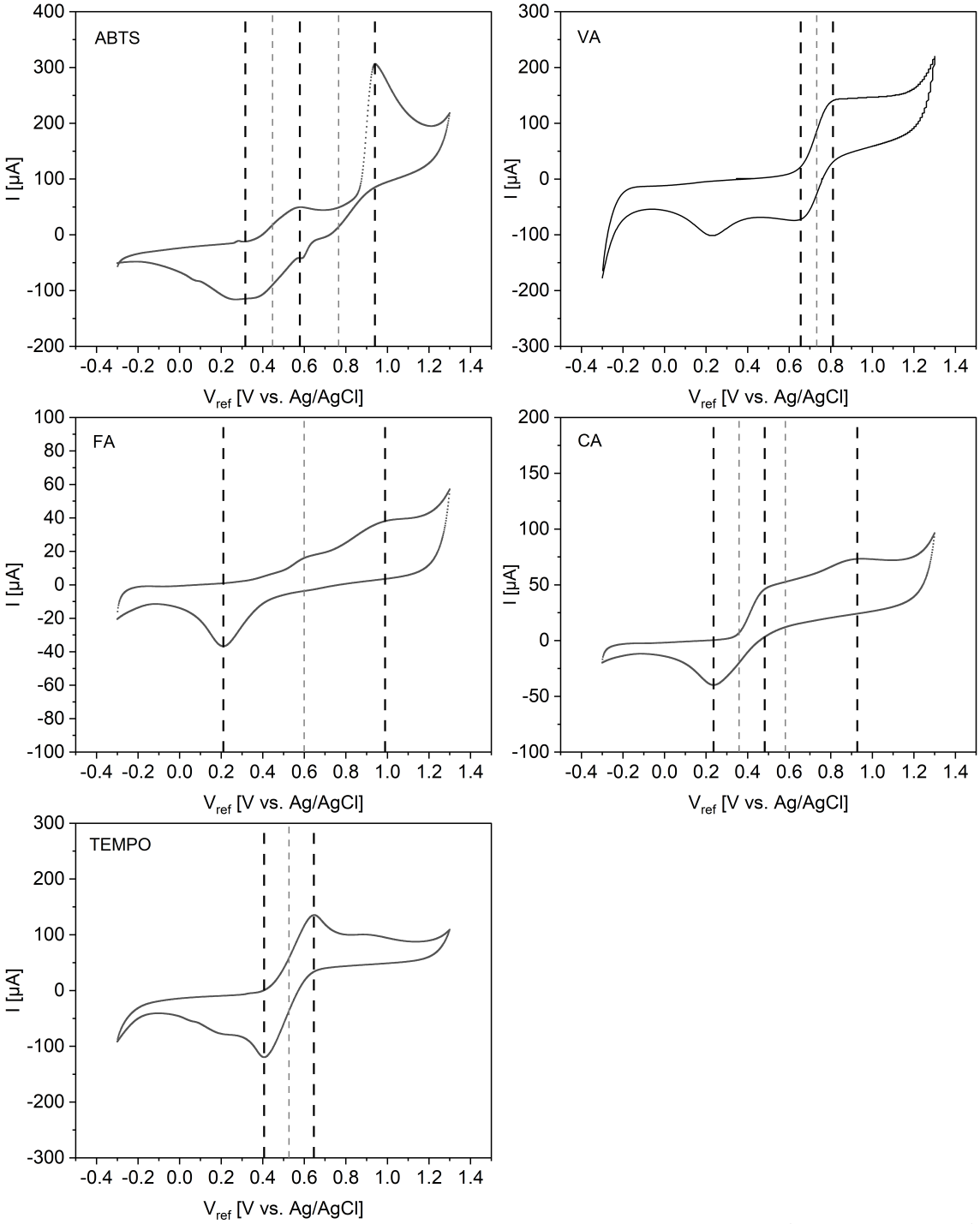

Figure A.6 Cyclic voltammograms of mediators recorded at 50 mV · s^{-1} in 0.1 mol · L^{-1} citrate-phosphate buffer (pH 4). Analyte concentration: 10 mmol · L^{-1}, −0.3 V to 1.3 V, working electrode: 99.95 % platinum plate (1 mm thickness, 9 mm^2 surface area), reference electrode: Ag/AgCl, solution was sparged with N_2.

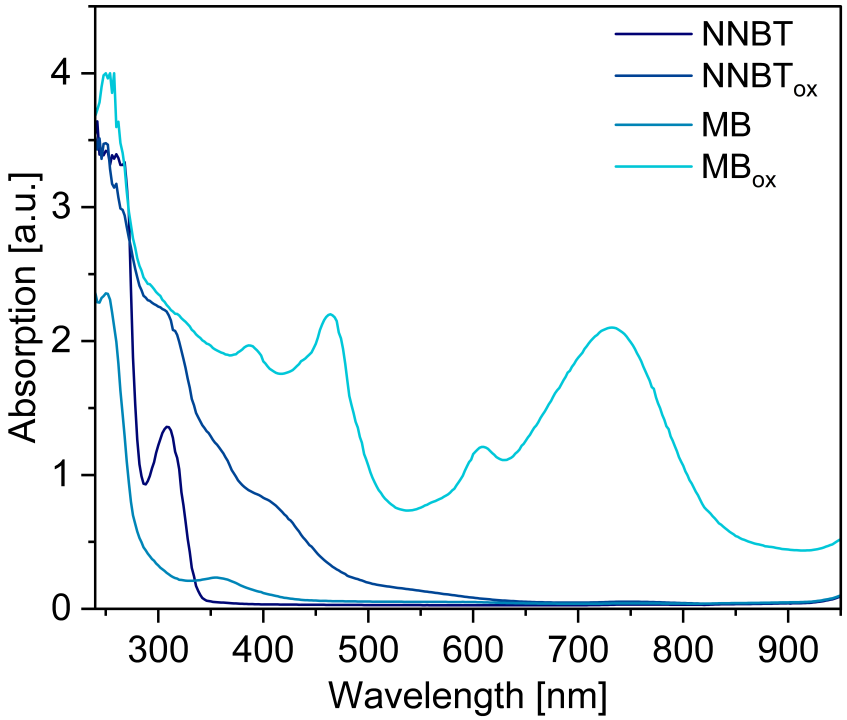

Figure A.7 Ultraviolet-visible light (UV/VIS) spectra of NNBT and MB in their native and enzymatically oxidized form from 240 nm to 950 nm.